

Springer Theses

Recognizing Outstanding Ph.D. Research

Aims and Scope

The series “Springer Theses” brings together a selection of the very best Ph.D. theses from around the world and across the physical sciences. Nominated and endorsed by two recognized specialists, each published volume has been selected for its scientific excellence and the high impact of its contents for the pertinent field of research. For greater accessibility to non-specialists, the published versions include an extended introduction, as well as a foreword by the student’s supervisor explaining the special relevance of the work for the field. As a whole, the series will provide a valuable resource both for newcomers to the research fields described, and for other scientists seeking detailed background information on special questions. Finally, it provides an accredited documentation of the valuable contributions made by today’s younger generation of scientists.

Theses are accepted into the series by invited nomination only and must fulfill all of the following criteria

- They must be written in good English.
- The topic should fall within the confines of Chemistry, Physics, Earth Sciences, Engineering and related interdisciplinary fields such as Materials, Nanoscience, Chemical Engineering, Complex Systems and Biophysics.
- The work reported in the thesis must represent a significant scientific advance.
- If the thesis includes previously published material, permission to reproduce this must be gained from the respective copyright holder.
- They must have been examined and passed during the 12 months prior to nomination.
- Each thesis should include a foreword by the supervisor outlining the significance of its content.
- The theses should have a clearly defined structure including an introduction accessible to scientists not expert in that particular field.

More information about this series at <http://www.springer.com/series/8790>

Bastian Ebeling

Smart Nanohybrids of RAFT Polymers and Inorganic Particles

Doctoral Thesis accepted by
the Georg-August-University Göttingen, Germany

Author

Dr. Bastian Ebeling
Institute of Physical Chemistry
Georg-August-University Göttingen
Göttingen
Germany

Supervisor

Prof. Dr. Philipp Vana
Institute of Physical Chemistry
Georg-August-University Göttingen
Göttingen
Germany

Present Address

CPE Lyon, Laboratoire de Chimie,
Catalyse, Polymères et Procédés
(C2P2), Equipe LCPP
University of Lyon 1
Villeurbanne
France

Additional material to this book can be downloaded from <http://extras.springer.com>.

ISSN 2190-5053

Springer Theses

ISBN 978-3-319-38630-0

DOI 10.1007/978-3-319-15245-5

ISSN 2190-5061 (electronic)

ISBN 978-3-319-15245-5 (eBook)

Springer Cham Heidelberg New York Dordrecht London

© Springer International Publishing Switzerland 2015

Softcover reprint of the hardcover 1st edition 2015

This work is subject to copyright. All rights are reserved by the Publisher, whether the whole or part of the material is concerned, specifically the rights of translation, reprinting, reuse of illustrations, recitation, broadcasting, reproduction on microfilms or in any other physical way, and transmission or information storage and retrieval, electronic adaptation, computer software, or by similar or dissimilar methodology now known or hereafter developed.

The use of general descriptive names, registered names, trademarks, service marks, etc. in this publication does not imply, even in the absence of a specific statement, that such names are exempt from the relevant protective laws and regulations and therefore free for general use.

The publisher, the authors and the editors are safe to assume that the advice and information in this book are believed to be true and accurate at the date of publication. Neither the publisher nor the authors or the editors give a warranty, express or implied, with respect to the material contained herein or for any errors or omissions that may have been made.

Printed on acid-free paper

Springer International Publishing AG Switzerland is part of Springer Science+Business Media
(www.springer.com)

Previous publications

Parts of this thesis have been published in the following journal articles:

- “Ideal Molecular Weight Distributions of Multiblock Copolymers Prepared via RAFT Polymerization”
B. Ebeling, M. Eggers, P. Vana, *Macromolecules* **2010**, 43(24), 10283–10290.
- “Multiblock Copolymers of Styrene and Butyl Acrylate via Polytrithiocarbonate-Mediated RAFT Polymerization”
B. Ebeling, P. Vana, *Polymers* **2011**, 3(2), 719–739.
- “RAFT-Polymers with Single and Multiple Trithiocarbonate Groups as Uniform Gold-Nanoparticle Coatings”
B. Ebeling, P. Vana, *Macromolecules* **2013**, 46(12), 4862–4871.
- “Spherical Gold-Nanoparticle Assemblies with Tunable Interparticle Distances Mediated by Multifunctional RAFT Polymers”
C. Rossner, B. Ebeling, P. Vana, *ACS Macro Letters* **2013**, 2, 1073–1076.
- “Oberflächen nach Maß”
B. Ebeling, F. Ehlers, P. Vana, *Nachrichten aus der Chemie* **2014**, 62, 24–28.
- “Flipping the Pressure- and Temperature-Dependent Cloud-Point Behavior in the Cononsolvency System of Poly-(*N*-isopropylacrylamide) in Water and Ethanol”
B. Ebeling, S. Eggers, M. Hendrich, A. Nitschke, P. Vana, *Macromolecules* **2014**, 47(4), 1462–1469.
- “Comparison of Monomethoxy-, Dimethoxy-, and Trimethoxysilane Anchor Groups for Surface-Initiated RAFT Polymerization from Silica Surfaces”
D. Hübner, V. Koch, B. Ebeling, J. Mechau, J. E. Steinhoff, P. Vana, *Journal of Polymer Science, Part A: Polymer Chemistry* **2014**, 53(1), 103–113.
- “Design Strategies for the Fabrication of Tailored Nanocomposites via RAFT Polymerization”
C. Rossner, B. Ebeling, P. Vana, *ACS Symposium Series* **2015**, in press.

Supervisor's foreword

Reversible deactivation radical polymerization (RDRP), formerly also known as controlled radical polymerization or living radical polymerization, has become one of the most prominent methods in polymer science for tailoring the architecture of synthetic polymers. Reversible Addition–Fragmentation chain Transfer (RAFT) Polymerization is one of these RDRP processes and has the distinct advantage of being extremely versatile with respect to monomer choice and reaction conditions. As a consequence, RAFT has become a standard method for synthesizing polymers with complex topology and demanding functional groups, which can be produced with this method with relative ease.

RAFT polymerization, however, also shows great potential for functionalizing surfaces with well-defined polymers, which can either directly be formed upon the surface via linking the controlling RAFT agents to a specific surface or via grafting preformed polymer obtained by RAFT. Both strategies have their benefits and disadvantages, but provide pathways to unique surface structures which cannot easily be obtained with alternative methods. Surface-bound star polymers, polymer loops, block copolymers, and network structures are currently being developed, demonstrating the rising complexity of these materials. For obtaining functional materials, however, the choice of the partner that provides the solid surface is often of equal importance. Nanoparticles have attracted much attention in this context, as they provide a large surface area and unfold specific functionalities that are not accessible with larger particles. The field of functional nanocomposites made of tailored polymer and nanoparticles of various natures is thus a very vivid one and many materials with new properties are currently emerging.

Gold nanoparticles are one of the most prominent nanoparticles in this respect and they are used as (bio)sensors, in medical applications, for catalysis, and in many industrial applications (e.g., cosmetics, food packaging, lubricants). Gold and RAFT were long considered to be completely incompatible, as sulfur—the main active element of any RAFT agent—is known to strongly interact with gold surfaces. Bastian Ebeling decided to tackle this problem and chose the development of nanocomposites made of gold nanoparticles and functional polymer—namely the thermoresponsive poly(NIPAm)—made via RAFT polymerization as topic for his PhD thesis. The goal of the project was to evenly disperse gold nanoparticles

in the functional polymer matrix in order to arrive at new sensor materials, in which surface plasmon resonance signals can be used as a measure for interparticle distances that respond to external stimuli. The probability of success for this project appeared to be rather low in the beginning, but Bastian Ebeling showed real commitment by turning many obvious disadvantages of the system into benefits and exploiting the specific characteristics of the system, leading the project to a superb completion. He designed these nanocomposites directly from scratch, developing and exploring all building blocks individually in an extremely systematic way. The very well investigated components were finally combined to generate astonishingly regular nanocomposites, which not only constitute a new class of materials, but also provide a system that can be used for probing macromolecular structures of the matrix polymer. By investigating the responsiveness of the polymer matrix, he also made substantial contributions to the thermodynamic understanding of the LCST behavior of poly(NIPAm). The experimental approaches for linking polymer to gold nanoparticles, which he developed during his thesis, are invaluable for further progress in this field and have already sparked new material design strategies, such as planet-satellite structures, which have not been accessible before.

The PhD thesis by Bastian Ebeling is in every essence outstanding: It describes excellent science, is enjoyable to read, and also looks great. It was a real pleasure and privilege for me to supervise Bastian during his doctorate and I am deeply convinced that we will see many more excellent publications by him. I wish him the very best for his future.

Göttingen, 27.11.2014

Prof. Dr. Philipp Vana

Preface and acknowledgements

This book is the final revised version of the thesis for which I obtained the “Doktorgrad (Doctor rerum naturalium)” from the “Georg-August-Universität Göttingen”. It summarizes the research I performed in the Macromolecular Chemistry Group of Prof. Dr. Philipp Vana at the “Institut für Physikalische Chemie” from 2010 to 2014. I am honored that this thesis was also awarded the Richard-Zsigmondy prize for Göttingen’s best chemistry thesis in 2014.

The underlying work would have been impossible to complete without receiving support and help in a number of different ways. Rather than hiding the acknowledgements at the end of this book, I feel that the only appropriate place to recognize several special people is in the very first pages.

First of all, I want to extend my sincerest thanks to my main supervisor Prof. Dr. Philipp Vana for his extraordinary scientific guidance, his incredible motivational capabilities, and for showing perpetual confidence in my skills.

I also want to thank my co-supervisor Prof. Dr. Hans-Ulrich Krebs for his friendly personal support and also as a representative for his group and the whole “Institut für Materialphysik”. The interdisciplinary cooperation was extremely valuable for me. It was especially helpful that I was given the opportunity to regularly work with their transmission electron microscope. Within the course of the presented studies, I took a large number of micrographs, several of which can be seen in this thesis and significantly contribute to the informative value of this work (most notably in Sections 4.1 and 5.1 and in Chapter 8.2). Dr. Peter-Joachim Wilbrandt and Matthias Hahn particularly helped me by offering plenty of assistance with the instrument and thoroughly refreshing my understanding in optics.

I would like to express my gratitude to Prof. Dr. Michael Buback for valuable and interesting discussions and for the opportunity to work with the high-pressure apparatus (Chapter 6). Concerning these experiments, Dr. Hans-Peter Vögele provided indispensable technical advice and Sandra Lotze and Heike Rohmann offered great practical support, for which I am also very grateful.

I thank Martin Eggers for his assistance in the creation of the script for the processing of AFM images (Section 4.2). The background of this thesis’ original cover illustration (Figure 1) is actually a real microscopic image of polymer-coated gold nanocrystals on a glass surface (Section 8.3.2.1) that was converted into a 3-

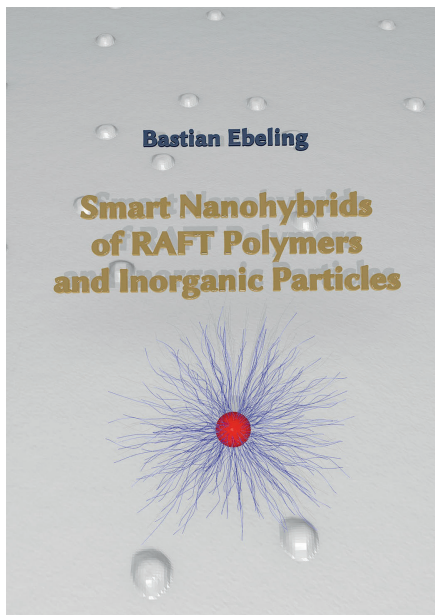


Fig. 1: Original cover of this thesis.

dimensional mesh using this script. The original scene is approximately 200 times smaller in width than a human hair.

I consider myself very lucky to have supervised a couple of highly talented students, that contributed practically to some of the experiments presented here: Stefan Ringe (double-anchor RAFT agent, Sections 5.2.1 and 7.1), Jannik Mechau (mono-functional silyl anchor, Sections 5.2.2 and 7.2), and Annika Nitschke (high-pressure cloud points, Chapter 6) worked in our lab in the framework of their bachelor theses. Steffen Eggers and Michael Hendrich (also high-pressure cloud points) did their practical lab course under my supervision. My special thanks go to all of them.

It was very pleasant to be able to work in the friendly, supportive, and productive atmosphere of the Vana/Buback group. I warmly thank all of my former colleagues and representatively list the people with whom I spent more time in the office: Cathrin Conrad, Nadja Förster, Hendrik Kattner, Vanessa Koch, Joachim Morick, Wibke Meiser, and Katharina Tietz.

I would also like to acknowledge Samuel J. Pearson, Ming Liang Koh, Dennis Hübner, Hendrik Kattner, Julia Möhrke, and Christian Roßner for diligent proofreading of this work, and Marc Janisse for answering lots of language-related questions.

Also, financial support by the “Deutsche Forschungsgemeinschaft” and the “Georg-August-Universität Göttingen” is gratefully acknowledged.

I want to express my deepest gratitude to my fellow students Jakob Hey, Stefan Jackenkroll, Reent Michel, Adam Walli, and Arne Wolpers for their friendship.

Finally, I want to thank, with all of my heart, my family for unconditionally supporting me in any possible way and keeping me balanced. This includes my exceptionally understanding partner Sarah. The promise of our common future always motivated me on this exciting journey.

At this point, I would also like to give some general remarks on this thesis. It is generally subdivided into three main parts: An introductory part, where the most important theoretical concepts are reviewed, the experimental part, featuring a detailed description of the methods, and the major results part, in which the acquired data are presented and discussed. Additional information can be found in the appendices. Some more orientation guides are placed on the introductory page of each part and at the beginning of the chapters.

Although all figures were newly created for this thesis, some of them feature data which have already been presented in peer-reviewed publications which I (co)authored.^[1–8] Any partial reproduction of these data is done with permission from the original publisher and indicated at the end of the figure’s caption.

I kept my research organized using the fantastic ORG-MODE^[9,10] for EMACS^[11] (founded by *Prof. Dr. Carsten Dominik*), which I highly recommend to everybody.

I truly hope some people will find the reading of this thesis helpful. Please do not hesitate to contact me if you have any comments or questions.

All the best to every reader of this text.

Göttingen/Lyon, 2014

Bastian Ebeling

References

- (1) Ebeling, B., Eggers, M., Vana, P., *Macromolecules* **2010**, 43 (24), 10283–10290.
- (2) Ebeling, B., Vana, P., *Polymers* **2011**, 3 (2), 719–739.
- (3) Ebeling, B., Vana, P., *Macromolecules* **2013**, 46 (12), 4862–4871.
- (4) Rossner, C., Ebeling, B., Vana, P., *ACS Macro Lett.* **2013**, 2, 1073–1076.
- (5) Ebeling, B., Ehlers, F., Vana, P., *Nachr. Chem.* **2014**, 62, 24–28.
- (6) Ebeling, B., Eggers, S., Hendrich, M., Nitschke, A., Vana, P., *Macromolecules* **2014**, 47 (4), 1462–1469.
- (7) Hübner, D., Koch, V., Ebeling, B., Mechau, J., Steinhoff, J. E., Vana, P., *J. Polym. Sci., Part A: Polym. Chem.* **2014**, 53 (1), 103–113.
- (8) Rossner, C., Ebeling, B., Vana, P., *ACS Symp. Ser.* **2015**, in press.
- (9) Schulte, E., Davison, D., *Comput. Sci. Eng.* **2011**, 13 (3), 66–73.
- (10) Schulte, E., Davison, D., Dye, T., Dominik, C., *J. Stat. Soft.* **2012**, 46 (3), 1–24.
- (11) Stallman, R. M., *ACM SIGOA Newsletter* **1981**, 2 (1–2), 147–156.

Abbreviations, symbols, labels

Abbreviations and acronyms

AF(M)	atomic force (m icroscopy)
ACVA	4,4'- a zobis(4-cyanovaleric acid)
AIBN	2,2'- a zobis(<i>i</i> so- b utyronitrile)
ATRP	<i>a</i> tom <i>t</i> ransfer <i>r</i> adical <i>p</i> olymerization
AuNP(s)	gold n anoparticle(s)
BA	<i>n</i> - b utyl acrylate
BET	B runauer– E mmett– T eller method
bs	b road singlet
CC BY-SA 3.0	Creative Commons Attribution-ShareAlike 3.0 Unported (http://creativecommons.org/licenses/by-sa/3.0/deed.en)
CCD	charge-coupled d evice
CP	cloud p oint
CSIRO	Commonwealth Scientific and Industrial R esearch O rganisation
d	d oublet
DCC	1,3- d icyclohexylcarbodiimide
DDQ	2,3- d ichloro-5,6- d icyano-1,4-benzo q uinone
DFG	D eutsche F orschungsb e gemeinschaft (German Research Foundation)
DMAEA	2-(d imethylamino)ethyl acrylate
DMAc	<i>N,N</i> - d imethylacetamide
DMAP	4-(d imethylamino)pyridine
DMF	<i>N,N</i> - d imethylformamide
DMSO	d imethyl sulfoxide
DNA	d eoxyribonucleic acid

DSC	d ifferential scanning calorimetry
DTT	d ithiothreitol (Cleland's reagent)
DVD	D igital V ersatile D isc
EA	e lemental a nalysis
EDX	e nergy- d ispersive X -ray
ESI	e lectrospray ionization
<i>et al.</i>	and others (et alii)
EU	E uropean U nion
fcc	f ace c entered c ubic
Fig.	F igure
GNU	G NU's N ot U nix!
GPC	g el- p ermeation chromatography
GRK	G raduiertenkolleg (Graduate School)
HPLC	h igh- p erformance liquid chromatography
IUPAC	I nternational U nion of P ure and A ppplied C hemistry
LCST	l ower c ritical s olution t emperature
m	m ultiplet
M	m olecule
MA	m ethyl a crylate
MBP	m ultiblock p olymer
MADIX	M acromolecular D esign via the I nterchange of X anthates
Me	m ethyl
MMA	m ethyl m ethacrylate
MS	m ass spectrometry
NIPAm	N -isopropylacrylamide
NMP	n itroxide m ediated radical p olymerization
NMR	n uclear m agnetic r esonance
no.	n umber
OS	o perating s ystem
p...	p oly...

PDI	p oly d ispersity index
q	q uartet
quin	q uintett
RAFT	r eversible a ddition– f ragmentation chain t ransfer (polymerization)
RI	r efractive index
s	s inglet
SDV	s tyrene– d ivinylbenzene copolymer network
SE(C)	s ize- e xclusion (c hromatography)
SE(M)	s canning e lectron (m icroscopy)
t	t riplet
Tab.	T able
TCEP	t ris(2- c arboxy e thyl) p hosphine hydrochloride
TE(M)	t ransmission e lectron (m icroscopy)
TERP	organot e llurium-mediated r adical p olymerization
TGA	t hermo g ravimetric a nalysis
THF	t etra h ydro f uran
TOC	t otal o rganic carbon (in purified water)
UCST	u pper c ritical solution t emperature
UK	U nited K ingdom
UV	u ltraviolet (radiation)
vis	v isible
XPS	X -ray p hotoelectron s pectroscopy
z	v ertical axis

Formula symbols and variables

\propto	proportional to
a	lattice constant, Mark–Houwink parameter
A	area, absorbance
b	number of blocks in multiblock polymers
\dot{b}	number of end blocks of a multiblock polymer
\ddot{b}	number of middle blocks of a multiblock polymer
\dot{B}	total number of end blocks
\ddot{B}	total number of middle blocks
B	total number of blocks
β	molecule density
c	concentration
C	circularity
\bar{D}	dispersity = $\frac{\bar{M}_w}{\bar{M}_n}$
d	interparticle distance
D	diameter
δ	chemical shift, density
Δ	difference
e	Euler's number
e^-	electron
E	electric field strength
\vec{E}	electric field vector
\in	...is element of...
g	number of trithiocarbonate groups in multiblock polymers, gravitational constant
G	total number of trithiocarbonate groups
ε^*	mass attenuation coefficient
η	viscosity
h	Miller index
H	enthalpy

i	natural number
I	intensity, integral
j	natural number
J	coupling constant
k	natural number, Miller index, force constant
\vec{k}	wave vector
k_d	rate coefficient of initiator decay
k_i	rate coefficient of initiation
k_p	rate coefficient of propagation
k_{tr}	rate coefficient of radical transfer
k_t	rate coefficient of termination
K	Mark–Houwink parameter
κ	curvature
l	natural number, length, Miller index
L	perimeter
\lim	limit of a sequence/function
λ	wavelength
m	mass, natural number
\dot{m}	mass of end blocks
\ddot{m}	mass of middle blocks
M	molar mass, total number of molecules
\overline{M}_n	number-weighted mean of a distribution function
\overline{M}_w	mass-weighted mean of a distribution function
${}^n\mu_v$	ν^{th} moment about the mean value of a distribution function
n	natural number
N	number-weighted distribution function, total number of data points, atoms, ...
ν	expectation value, (tapping) frequency
ω	mass fraction
p	degree of polymerization, pressure
π	Ludolph's number
s	solidity

S	surface area
σ	standard deviation
t	reaction time
θ	temperature, diffraction angle
r	radius
$r_{\bar{m}/\bar{m}}$	mass ratio of middle and end blocks
R_f	retardation factor in chromatography
ρ	density, resistivity
T	temperature
V	(elution) volume
w	full width at half maximum
W	mass-weighted distribution function
x	distribution function, mole fraction
X	conversion
z	number of elementary charges
\mathbb{Z}	set of integers
$\bar{\square}^*$	mean value
$\bar{\square}$	normalized variable
$\bar{\square}^o$	end blocks count only half
\square_0	...prior to the reation
\square_1	...after the reation
\square^A	...for distribution function A
\square_{Au}	...for gold
\square^B	...for distribution function B
\square_c	...of a polymer with the concentration c
\square_c	...of the clouding, of the container
\square_C	...of the carbon
\square_{cl}	...determined by cleavage of the polymers
\square_{con}	convex
\square_{fus}	...of the fusion

*The “ \square ” symbol stands for any variable.

\square_g	...by gravimetry
\square_G	Gaussian
\square_h	hydrodynamic
\square_m	...of mixing, molar, mean
\square_l	liquid
\square_m	specific
\square_M	...of the monomer
\square_{NMR}	...by NMR
\square_p	...per particle, planar, at the peak, of the polymer
\square_s	solid
\square_S	...of the (pure) solvent, ...on the surface
\square_{SEC}	...of the SE chromatograms
\square_{SiO_2}	...for silica
\square_{RAFT}	...of the RAFT agent
\square_{red}	reduced
$[\square]$	intrinsic

Unit symbols

%	percent (10^{-2})
A	ampere
Å	Ångström (10^{-10} m)
eq.	equivalent
°C	degree Celsius
CFU	colony forming units (in purified water)
d	day
eV	electron volt
g	gram
h	hour
H	proton equivalents in ^1H -NMR
Hz	hertz
L	liter
mesh	mesh
m	meter
min	minute
mol	mole
N	normal (equivalents per liter), newton
ppm	parts per million (10^{-6})
s	second
V	volt
W	watt

Unit prefixes

M	mega	(10 ⁶)
k	kilo	(10 ³)
d	deci	(10 ⁻¹)
c	centi	(10 ⁻²)
m	milli	(10 ⁻³)
μ	micro	(10 ⁻⁶)
n	nano	(10 ⁻⁹)
p	pico	(10 ⁻¹²)

Guide to substance identifiers

Substance identifiers are generally typeset completely **in upright and bold** and explained when they first occur in the text. The Greek letters indicate the type of substance. The number at the end is unique for each sample type. The super- and subscripts are only additional markers for higher clarity, but are not necessary for differentiation.

π	polymer
ρ	RAFT agent
P	RAFT agent immobilized on surface
ν	nanoparticles
λ	ligand for gold
κ	polymer–nanoparticle nanohybrid
σ	other reagent

Abstract

Within the work presented here, the special features of reversible addition–fragmentation chain transfer (RAFT) polymerization were exploited to explore pathways for the production of novel nanohybrids composed of polymers and inorganic particles. Surface-confined radical polymerizations were carried out employing RAFT agents tethered to silica surfaces via methoxysilyl moieties located at the end of their stabilizing Z-groups. The RAFT agents were adaptively designed to meet the special demands imposed by different types of silica substrates. A doubly anchored RAFT agent led to polymer loops on the surface of fumed silica through a polymerization mechanism in which the propagating radicals as well as the mediating groups remain attached to the surface. By the use of a RAFT agent with an anchor group only capable of forming a single covalent bond (rather than three as for the first RAFT agent), the crosslinking of colloiddally dispersed carrier particles of silica ($\varnothing \approx 50$ nm) during the immobilization process could successfully be prevented.

Poly(*N*-isopropylacrylamide) (pNIPAm) samples with distinct molar masses were prepared in the presence of a trithiocarbonate RAFT agent. By analyzing aqueous solutions of these multiresponsive polymers in an optical autoclave cell up to pressures of 3 000 bar and down to temperatures of -20 °C, a completely new aspect of their phase behavior was found. It was demonstrated that the addition of several organic cononsolvents in low concentrations leads to an increasing solubility of the polymer in the low-temperature/high-pressure region, while, on the contrary, the solvents reduce the solubility of the polymer and therefore its cloud temperature at atmospheric pressure. It was found that the phase-separation behavior is gradually and completely inverted, regarding both its pressure- and temperature-dependence, when the mole fraction of added ethanol is increased over the whole cononsolvency range. As a special case, at a mole fraction of $x = 0.23$, the system clears up independent of temperature at a constant pressure of about 1 000 bar. In terms of solvent–solvent or solvent–polymer interactions, these findings support the assumption of substantially different clouding mechanisms for the high-temperature and the low-temperature regions.

The pNIPAm samples were grafted to gold nanoparticles (AuNPs, $\varnothing \approx 14$ nm) obtained from the reduction of gold ions with sodium citrate. In a survey of different liquid-chemical AuNP synthesis methods, these particles had been found

to be especially well suited for the production of nanohybrids, owing to their homogeneity, their very reactive surface, the reproducibility of the reaction, and the very pronounced plasmon resonance signal. The ability that the trithiocarbonate groups incorporated into the RAFT polymers fulfill the second function of anchor units for gold was thereby capitalized on, which turned out to be essential for long-term AuNP stabilization. The products were analyzed via transmission electron microscopy (TEM), revealing self-assembled hexagonal lattices of gold cores. The interparticle distances in these lattices increased significantly with the molar mass of the coating macromolecules, providing a universal calibration function. The close-to-linear shape of this curve indicated a high polymer grafting density. By atomic force microscopy (AFM), the decorating polymer was mainly found lying laterally around the polymer cores in the deposited nanohybrids.

By performing the radical polymerizations in the presence of RAFT agents with multiple trithiocarbonate groups, pNIPAm samples composed of several homogeneous blocks interconnected by these functional groups were obtained. In contrast to the conventional method of producing polymers of this structure—the coupling reaction of functionalized prepolymers—the strategy employed here enables a generally higher extent of control over the product properties, with regard to the number of trithiocarbonate groups per polymer chain and the lengths of the individual blocks. Moreover, it could be shown that the strategy used here theoretically leads to a more even distribution of trithiocarbonate groups among the macromolecules.

When these multifunctional polymers were employed in an analogous coating reaction of AuNPs in the above-described manner, the same hexagonal lattices were observed by TEM. The employed polymers possessed distinctly differing molar masses and numbers of trithiocarbonate groups. The interparticle spacings in the self-assembled lattices, however, were constant for all samples and, moreover, significantly lower than would have been expected based on the calibration function for the nanohybrids composed of polymers with single trithiocarbonate groups. This proved that the multifunctional polymers are wrapped around the AuNPs with several gold–trithiocarbonate junctions—a conclusion which was also supported by results from AFM and size-exclusion chromatography. Absolutely no crosslinking was found. These novel and promising nanohybrids constitute yet another pathway for polymer loops on surfaces.

Courtesy of the responsive properties of the pNIPAm shells in combination with the optical characteristics of the AuNP cores, a reversible color change of the water-soluble nanohybrids could be externally triggered, promising a great potential for sensor applications.

Contents

Previous publications	iii
Supervisor's foreword	v
Preface and acknowledgements	vii
References	x
Abbreviations, symbols, labels	xi
Formula symbols and variables	xiv
Unit symbols	xviii
Unit prefixes	xix
Guide to substance identifiers	xix
Abstract	xxi
Contents	xxiii
I Introductory part	1
1 Introduction and background	3
1.1 Introduction	3
1.2 Theoretical background	7
1.2.1 Polymers	7
1.2.2 Poly(<i>N</i> -isopropylacrylamide)	18
1.2.3 Nanosciences	27
1.2.4 Polymers on surfaces	35
References for Chapter 1	39

II	Experimental	53
2	Instrumentation	55
2.1	Centrifugation	55
2.2	Chromatography	55
2.2.1	Column chromatography	55
2.2.2	Size-exclusion chromatography (SEC)	55
2.2.3	Thin-layer chromatography	56
2.3	Cloud-point measurements	57
2.3.1	Cloud-point determination at atmospheric pressure	57
2.3.2	Cloud-point determination at high pressures	57
2.4	Determination of pH values	60
2.5	Electrospray-ionization mass spectrometry (ESI-MS)	60
2.6	Elemental analysis	60
2.7	Microscopy	60
2.7.1	Atomic force microscopy (AFM)	60
2.7.2	Transmission electron microscopy	61
2.7.3	Scanning electron microscopy (SEM)	62
2.8	Spectroscopy	62
2.8.1	Nuclear magnetic resonance (NMR) spectroscopy	62
2.8.2	UV/vis spectroscopy	62
2.9	Thermogravimetric analysis	62
2.10	Ultrasonication	63
2.11	Water purification	63
2.12	Further equipment	63
	References for Chapter 2	64
3	Substances	65
3.1	Commercially acquired substances	65
3.1.1	Monomers	67
3.1.2	Initiators	67
3.1.3	RAFT agents	67
3.1.4	Polymers	68
3.1.5	Nanoparticles	68
3.2	Synthesis of substances	69
3.2.1	Synthesis of a RAFT agent with two anchor groups	69
3.2.2	Synthesis of RAFT agent with a monofunctional anchor group	70
3.2.3	Synthesis of the alkyne RAFT agent	72

3.2.4	Synthesis of the azidothiol	72
3.2.5	Synthesis of the Dess–Martin periodinane	75
3.2.6	Polymers	75
3.2.7	Synthesis of AuNPs	86
3.2.8	Functionalization reactions	87
	References for Chapter 3	91

III Results 93

4	Analysis of microscopic images	95
4.1	Analysis of TEM images	95
4.1.1	General information obtained by TEM	95
4.1.2	Alteration of samples in the microscope	100
4.1.3	Self-assembly of nanoparticles in TE micrographs	102
4.1.4	Semi-automatic particle size and shape analysis	103
4.2	Analysis of AFM images	110
	References for Chapter 4	114
5	Building-block design	115
5.1	Preparation of gold nanoparticles	115
5.1.1	General remarks on AuNP synthesis strategies	115
5.1.2	AuNPs via reduction by citrate ions	117
5.1.3	The Brust–Schiffrin method	129
5.1.4	Reduction by a long-chain amine	135
5.1.5	Conclusions on the AuNP syntheses	136
5.2	Synthesis of special RAFT agents	139
5.2.1	Synthesis of a RAFT agent with two anchor groups	139
5.2.2	Synthesis of a RAFT agent with a monofunctional anchor group	140
5.2.3	Synthesis of a “clickable” RAFT agent	142
5.3	Synthesis of the azidothiol	143
5.4	Preparation of <i>N</i> -isopropylacrylamide polymers	145
5.4.1	Experimental polymerization conditions	146
5.4.2	Determination of monomer conversion	146
5.4.3	SEC analysis	151
5.4.4	Multiblock poly(<i>N</i> -isopropylacrylamide)	152
5.4.5	Cleavage of trithiocarbonate groups	157
	References for Chapter 5	160

6	High-pressure phase behavior of aqueous pNIPAm solutions	171
6.1	Current state of research regarding the high-pressure experiments	171
6.2	Experimental acquisition of cloud-point curves	175
6.2.1	Acquisition of cloud points at elevated pressures	175
6.2.2	Acquisition of cloud points at atmospheric pressure	179
6.3	Finding reference conditions	181
6.3.1	Polymer concentration for the measurements	181
6.3.2	Influence of the polymer chain-length	183
6.4	Effect of additives	185
6.4.1	Effect of additives at low concentrations	185
6.4.2	The cononsolvency region	189
6.5	Conclusions from the cloud-point experiments	192
	References for Chapter 6	195
7	Nanocomposites via polymerization from silica	199
7.1	Polymer nanoloops on fumed silica	200
7.1.1	The substrate fumed silica	200
7.1.2	Immobilization of the RAFT agent	200
7.1.3	Surface polymerization	202
7.1.4	Analysis of the produced nanocomposites	204
7.2	Polymers with single covalent bonds to silica nanoparticles	207
7.2.1	The substrate silica nanoparticles	207
7.2.2	Immobilization of the RAFT agent	207
7.2.3	Surface polymerization	210
7.2.4	Analysis of the produced nanocomposites	211
	References for Chapter 7	213
8	Nanohybrids of gold particles	215
8.1	Different ligands on AuNPs	215
8.1.1	Functionalization of Brust–Schiffrin gold nanocrystals	215
8.2	Functionalization of citrate-prepared gold nanocrystals	220
8.2.1	Non-polymeric ligands onto citrate-prepared AuNPs	222
8.3	Grafting of polymers to citrate AuNPs	226
8.3.1	Grafting of polymers without sulfur to citrate AuNPs	228
8.3.2	Grafting of polymers with trithiocarbonate groups to citrate AuNPs	229
	References for Chapter 8	250

9	Future perspectives	255
	References for Chapter 9	261
10	Conclusions	263
 Appendices		 265
A	Code of the conversion script	267
B	Index	275
 About the author		 289
	Curriculum vitae	289
	Publications	290
	Contributions to conferences and workshops	291

Part I

Introductory part

This part gives a theoretical introduction to the subjects of this thesis. After the general introduction, which also contains the main objectives for the performed work, the current state of research of the underlying field and the basics for the easy understanding of the results in the main part are outlined in the section “Theoretical background”. The key topics here are polymers, in particular RAFT polymerization, the very special properties of pNIPAm, and the relevant concepts of nanosciences, including the general pathways for the surface functionalization of nanomaterials with polymers.

Chapter 1

Introduction and background

1.1 Introduction

The nanoscale (from the ancient Greek *νᾶνος*, meaning dwarf) refers to structures with at least one dimension sized from 1 to 100 nm.^[1] Substances in this size regime can exhibit peculiar properties that are dramatically different from the bulk solids as well as from the individual molecules, such as a lower melting point, a higher conductivity, a greater elasticity or strength, a higher reactivity, catalytic capacities, or a different color.^[2] As opposed to the typical lustrous color of gold bars, colloidal solutions of spherical gold nanocrystals appear vividly red, owing to the collective oscillation of the confined conduction electrons being in resonance with the incident light.^[3]

Materials containing nanosized subunits are termed nanomaterials. Their macroscopic properties are governed by the large interface area per unit volume. Over the last several decades, there has been an ever-rising surge of scientific activities on nanomaterials.^[4] They can be employed in a vast range of applications, for instance in medicine, electronics, optics, biology, catalysis, and energy production,^[5] and are found more and more in commercial products.^[6] Major driving forces behind this boost were the emergence and improvement of advanced microscopic techniques and the craving of modern technologies for a rampant miniaturization.^[7] It is forecast by many that we are on the verge of an era where nanomaterials will reshape our daily life just as steel did in the industrial age.^[8]

Although synthetic polymers are usually not regarded as nanoscaled objects by themselves, they are ideal and cheap candidates for uniting with inorganic nanoparticles.^[9–11] The formed organic–inorganic hybrid materials, or nanohybrids, can adopt the best properties of both constituents,^[12] in exact analogy to the mythological creatures combining body parts of more than one species. Because of the outstanding property combinations, this class of composite materials holds significant promise in a variety of fields. The polymer component can impart long-term

colloidal stabilization, solubility, reduced protein adhesion, or an even dispersion. By synergistic effects, completely new properties can also emerge.^[13] Of the range of different nanohybrid structures that can be designed, layered nanoparticles with an inorganic core and a polymer shell are typical examples.^[14,15]

Conversely, the performance of a polymer matrix, regarding process ability, strength, stiffness, wear resistance, appearance, or simply the cost, can be greatly enhanced by capitalizing on the nature and properties of an embedded nanoparticulate filler.^[16–20] Thanks to their low-price, universality, ubiquity, and their non-toxicity, nanosized silica particles are often used for this task. Natural archetypes for the formed synthetic nanostructured materials with an interstitial organic phase are, for example, bone and nacre.

With a view to potential sensor, actuation, drug-delivery, or catalytic applications, polymers which react to external stimuli with a drastic change in their properties, so-called “smart polymers”, are especially promising candidates for components of multifunctional nanohybrids. By far the most prominent representative of this class is poly(*N*-isopropylacrylamide) (pNIPAm). Its abrupt precipitation from aqueous solutions can be triggered by temperature, additives, and pressure. It is, with this regard, also regarded as a model system for the conformational behavior of proteins.

The precise control of the polymer characteristics is essential for the effective design of nanohybrids with a defined structure.^[21] For many applications, it is also mandatory to incorporate a functional group into the polymer chains, through which they can be linked covalently to the inorganic substrate, rather than relying on weak polymer physisorption. The synthesis of polymers, which fulfill these conditions, from common industrial monomers has been enabled by the advent of reversible-deactivated radical polymerization (RDRP) techniques in the late nineties. This has meant a huge leap forward in polymer science. By the use of special mediating agents, these techniques allow for the facile large-scale production of macromolecules with defined molar masses and complex architectures. Suitable anchor groups for the grafting of the polymer chains to a surface can be easily introduced as part of the controlling molecules. Alternatively, it is also possible to directly tether the mediating agent to the surface. Polymerizations in the presence of surfaces functionalized in this way usually lead to higher grafting densities. Reversible addition–fragmentation chain transfer (RAFT) polymerization is arguably the most versatile representative of RDRP techniques. It proceeds via a degenerative chain-transfer mechanism which induces an equilibrium between propagating macroradicals and dormant mediating agents carrying dithio moieties, for example trithiocarbonate groups. In addition to the characteristics shared with other important RDRP techniques, the RAFT process inherently possesses three unique

features, which render it particularly promising for employment in the production of sophisticated nanohybrid materials:^[22,23]

- The RAFT agent can be immobilized on a solid substrate via its stabilizing Z-group, leading to the peculiar mechanistic situation that in surface-confined polymerizations, the polymer chains propagate unattached in the interstitial solution phase. Hence, at the end of the polymerization, no irreversibly terminated polymer chains are linked to the surface.^[24,25]
- The sulfur-containing mediating RAFT groups themselves are capable of being anchored to gold surfaces. Therefore, after controlling the radical polymerization, they can also fulfill a second purpose.^[26]
- Polymers carrying multiple RAFT groups along the backbone chain are synthetically accessible with exceptional ease.^[27] The possibility to form several links to gold can give rise to novel nanostructures.

The scientific goals of this work were to exploit these special features and the versatility of the RAFT process for the production of new and advanced nanohybrids containing inorganic particles. As the first step, synthetic pathways to the following suitable components for nanocomposites were intended for exploration:

- Gold nanoparticles of different sizes, which can be easily functionalized with RAFT agents or polymers, either via an accessible and reactive gold surface, or via suitable functional groups on the decorating ligands.
- Specially designed RAFT agents carrying one or more suitable functional anchor groups, with which they can be irreversibly immobilized on nano-sized silica particles of different types or the produced functionalized gold nanoparticles via their Z-group. (The direct coating of gold nanoparticles with RAFT agents is impeded by the fact that all RAFT groups themselves are susceptible to chemisorption on gold.)
- Polymers of *N*-isopropylacrylamide carrying single terminal trithiocarbonate end groups or multiple trithiocarbonate groups evenly distributed along their main chain. Samples varying molar masses and numbers of trithiocarbonate groups were planned to be synthesized to enable comparative experiments.

In a modular way, these building blocks were intended to then be used to produce organic-inorganic nanohybrids, either by carrying forward the principle of surface-confined Z-RAFT polymerization, probing the suitability of the designed RAFT agents on different substrates, or by direct assembly of the different types of polymers

and gold nanocrystals. A special focus was planned for the production of surface-bound polymer nanoloops, which are usually considered especially challenging to generate.

Since the color of colloidal gold crystals depends on the interparticle spacings,^[28] it was envisaged that the combination with the smart pNIPAm would lead to a material, in which the response to outer stimuli would go along with a change in the color of the nanohybrids.^[29] For the targeted sensor applications,^[30,31] the responsive behavior of the pNIPAm component was intended to be analyzed individually under high pressures. Because of the entailed experimental effort, this is an often neglected aspect, which nevertheless does not make it any less important.

In the experiments of grafting polymers to gold nanocrystals, an especially intriguing question was which kind of structures result when polymers with multiple trithiocarbonate anchor groups are employed.

To complete the studies, viable analysis methods to help answer this question and characterize the produced nanohybrids were hoped to be found.

1.2 Theoretical background

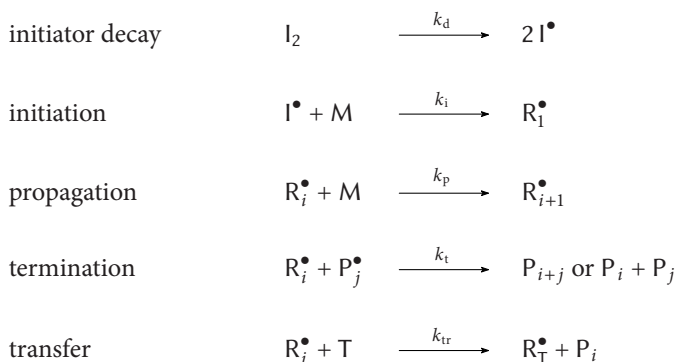
1.2.1 Polymers

Polymers consist of macromolecules, in which many self-repeating and covalently linked subunits, called monomers, are incorporated. Natural biopolymers which are produced by living organisms—polynucleotides, polypeptides, and polysaccharides (sugars)—are the basis of life and constitute the majority of organic material on this planet. Since the foundation of modern macromolecular science by the pioneering works of Hermann Staudinger in the beginning of the 20th century,^[32] artificially created synthetic polymers have assumed an ever-increasing role for the modern society and shape the appearance of our civilization. Steady worldwide research has led to the emergence of tailored materials with a huge range of applications, spanning domains such as packaging, clothing, infrastructure, paints, medical equipment, electronics, sports and musical equipment, and the automotive, aircraft, and space industries.^[33] The polymer properties are mainly directed by the choice of monomer and their topology.^[34]

1.2.1.1 Radical polymerization

Radical polymerization is arguably the most widely used method for the production of synthetic polymers, both in industry and academic laboratories.^[35] A great variety of vinyl monomers are amenable to this technique, including (meth-)acrylates, styrenes, (meth-)acrylamides, butadiene, and vinyl acetate, and it is generally very tolerant towards most functional groups and a wide range of reaction conditions. Radical polymerization can be performed with very low experimental effort and is therefore in most cases more efficient than other techniques. Since it belongs to the group of *chain-growth polymerizations*, where unsaturated monomer molecules add onto the active site (here the radical function) on a growing polymer chain one at a time, high degrees of polymerization are even achieved at low monomer-to-polymer conversions. (For the other principal polymerization technique, the *step-growth polymerization*, where the monomer molecules first form dimers, which then in turn couple to longer oligomers and eventually to polymers, the mechanism demands a very high extent of reaction and stoichiometry to achieve high molecular weights.)

Conventional radical polymerization Scheme 1.1 shows the five elementary reactions of conventional radical polymerization. It is called “conventional” to indicate that no other substances but the basic ingredients which are necessary for



Scheme 1.1: Elementary reactions of conventional radical polymerization. I denotes an initiator fragment, M a monomer molecule, R is a radical, P a polymer chain, and T a radical transfer partner. The chain-lengths are indicated by the indices i and j . Hence, R_1 is a monomeric radical, and $R_{i,j}$ are macroradicals. The variables k_d , k_i , k_p , k_{tr} , and k_t denote the rate coefficients of initiator dissociation, initiation, propagation, radical transfer, and termination.

the polymerization are contained in the system. In industry, most radical polymerizations are performed in the conventional way. The first step of the mechanistic scheme is the production of radicals. In most cases, this is achieved by the thermally, chemically, photochemically, or redox-activated decay of initiator molecules. Radicals can also be generated without designated initiator molecules by high-energy radiation, plasma, or the self-initiation of certain monomers (e. g. styrene). The thus produced radical then adds to a monomer molecule and starts the polymerization (initiation). By addition of further monomer molecules to the active chain end, the radical chain continues to grow (propagation) until the radical function is transferred to another species (monomer molecule, polymer chain, solvent, ...), which can in turn continue or re-initiate the polymerization,* or the radical function is terminated by combination or disproportionation with another radical.^[36]

Both transfer and termination reactions lead to the production of non-active, so-called *dead* chains, which can no longer participate in the polymerization. The life-time of active chains does not exceed the range of a few seconds and only a very small fraction of polymer chains grow simultaneously.^[37] For these two reasons, the molar mass and the chemical composition of the polymer material are very difficult

* Specifically added agents which form very stable radicals and can therefore bring the polymerization to a stop are called *inhibitors*.

to control and the resulting polymers therefore possess very broad molar-mass distributions ($\mathcal{D} \geq 1.5$, see section 1.2.1.2). Furthermore, it is often impossible to incorporate functional groups into the polymer backbone or to produce complex architectures, such as block-, star- or comb-polymers.

The advantages of conventional radical polymerization lie in its high tolerance towards impurities like water, its high reaction rate and its cost efficiency.

Reversible-deactivated radical polymerization In 1956, the term *living polymerization*^[38] was coined by Szwarc for polymerizations in which the growth of all polymer chains starts simultaneously and neither transfer nor termination reactions take place.^[39,40] Since this leads to all chains having the same life-time, the resulting molar-mass distribution is very narrow (see section 1.2.1.2) and the average molar mass can be controlled by the stoichiometry of the system or the reaction time. After completion of the polymerization, the active center remains at the macromolecular chain ends and the reaction can be continued with additional monomer molecules. In the case of a different type of monomer, the production of block copolymers is possible.^[41]

Originally, Szwarc had referred this denomination only to *anionic polymerization*. Over the following years, this concept of living polymerization could be successfully expanded also to *cationic*,^[42] *coordinative*,^[43] *ring-opening*,^[44] and *group-transfer polymerization*.^[45]

Given the universality, ease, and efficiency of conventional radical polymerization, it goes without saying that it had been a covetable objective in polymer chemistry to find ways of performing a radical polymerization which exhibits living characteristics. But it was only in 1982 that this concept could at least in part be realized, when so-called *iniferters* were intensively examined by Otsu.^[46–48] Iniferters are compounds which are able to simultaneously act as *initiators* and *transfer* and *terminating* agents in a radical polymerization. Because of slow initiation, these systems still lack control over the obtained average molecular weight as well as the molar-mass distribution.

In the late nineties, polymerization techniques were finally established which could truly combine the versatility of radical polymerization with the control of living polymerization, which were then termed *controlled (or “living”) radical polymerizations*.^[35,49] Nowadays, the term *reversible-deactivated radical polymerization* (RDRP) is recommended by the International Union of Pure and Applied Chemistry (IUPAC)^[50] and should therefore be used preferably.^[51] The control of these techniques is in general based on one of two major principles which mechanistically govern the polymerization by inducing a dynamic equilibrium between

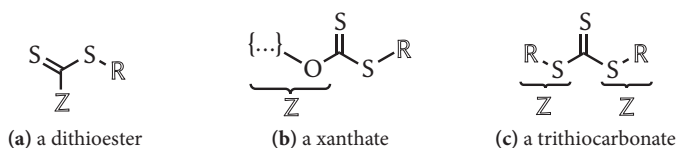


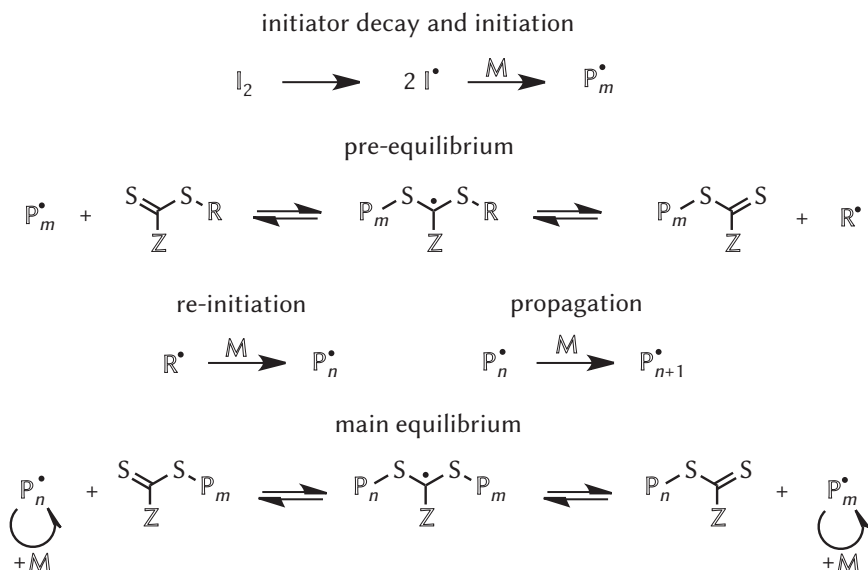
Fig. 1.1: Chemical structures of important types of RAFT agents. Z denotes the stabilizing group, R the re-initiating leaving group. The ellipses express that a fraction of a larger molecule is shown. Note that not all trithiocarbonates are symmetrical and have two leaving groups as shown in c.

dormant chains and propagating radicals: *reversible termination* or *reversible chain transfer*.

The most important examples of polymerizations based on reversible termination are the *atom transfer radical polymerization (ATRP)*^[35,52–56] and the *nitroxide mediated radical polymerization (NMP)*.^[57–60] These systems require adapted initiators (alkyl halides for ATRP, alkoxyamines for NMP). These initiators and the derived dormant chains reversibly produce (macro)radicals by direct activation via either a redox dissociation mechanism (ATRP, usually involving the use of a copper-based transition-metal complex catalyst) or via thermal dissociation (NMP). Both the radical concentration and the concentration of obtained living macromolecules is therefore directly determined by the concentration of the respective initiator (stoichiometric polymerization).

The most important examples for the second category—the reversible chain transfer—are the *reversible addition–fragmentation chain transfer (RAFT) polymerization*^[61–64] and the *organotellurium-mediated radical polymerization (TERP)*.^[65–67] These systems require the use of reversible chain-transfer agents along with the continuous production of radicals resulting from the dissociation of a classical radical initiator introduced in low concentration with respect to the control agent. Here, the chain transfer agent only determines the concentration of obtained living chains. The dormant chains are activated by an exchange mechanism with the propagating macroradicals. In the case of TERP, this exchange takes place directly; in the case of RAFT, via an addition–fragmentation step. Since the latter occupies a central role in this work, it is presented in more detail in a separate section.

RAFT polymerization The reversible addition–fragmentation chain transfer (RAFT) process was first presented in the year 1998 by the Australian *Commonwealth Scientific and Industrial Research Organisation (CSIRO)*.^[68–70] The contemporaneously presented *Macromolecular Design via the Interchange of Xanthates*



Scheme 1.2: Elementary reactions in a RAFT polymerization. Z denotes the stabilizing group, R the re-initiating group, I an initiator fragment, M a monomer molecule, and P a polymer chain.

(MADIX)^[71,72] polymerisation proceeds with the same reaction mechanism, but refers exclusively to xanthates (xanthic acid esters, see Figure 1.1b) as mediating agents.

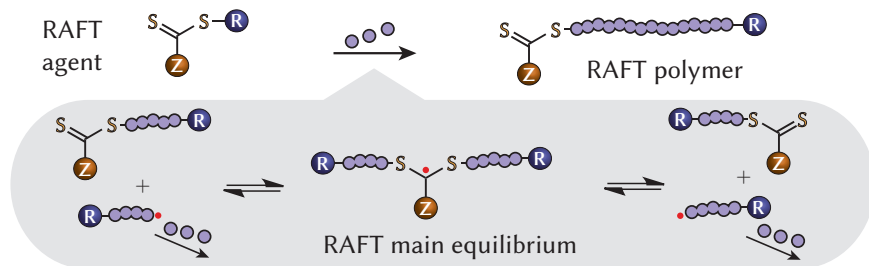
RAFT polymerization is arguably the most versatile RDRP technique: It can be performed in almost all solvents, including aqueous solutions^[73,74] and supercritical fluids,^[75] over a wide temperature^[76,77] and pressure^[78] range. The high tolerance towards functional groups^[79,80] enables all common monomers which are amenable to radical polymerization (see Section 1.2.1.1) to be used for RAFT polymerizations as well,^[81–83] allowing for the synthesis of a wide variety of polymeric structures with defined molar-mass distributions (see Section 1.2.1.2).^[22,84–87]

As control agents^[88] in RAFT polymerizations, usually compounds of the group of *dithioesters*,^[89,90] including xanthates, trithiocarbonates, and dithiocarbamate compounds,^[91,92] are employed. The generic chemical structure is shown in Figure 1.1a. In this figure, Z denotes the *stabilizing group*, and R the *re-initiating group*. The active group between Z- and R- group in a RAFT agent is often termed the *RAFT group*. All other components in a RAFT polymerization are identical to a conventional radical polymerization system (see Section 1.2.1.1).

In Scheme 1.2, all elementary reaction steps of the generally accepted mechanism of RAFT polymerization are presented.^[93] As in the case of conventional radical polymerization, the polymerization is started by the addition of a radical to a monomer molecule (initiation). The radicals are shown here as derived from a thermal initiator, but also other initiation methods are possible.^[94,95] The growing polymer chains quickly add to the reactive carbon–sulfur double bond of the RAFT agent and a tertiary radical intermediate is formed (*pre-equilibrium*). The stability of this intermediate radical is affected by the Z-group. Strongly stabilizing Z-groups promote the formation of the tertiary radical and hence increase the reactivity of the carbon–sulfur double bond.^[96] This stabilization, however, must not be too strong, since the formed radical must be able to easily decompose in the next step. A typical stabilizing Z-group which is suitable for the controlled polymerization of many different monomer types is the phenyl group.^[97,98] In principle, there exist two possible decomposition pathways for the intermediate RAFT-centered radical: Either the reverse reaction of the described addition takes place, which simply regenerates the initial RAFT agent and the polymer radical, or the R-group is split off and a macromolecular RAFT agent is obtained. The R-group can then re-initiate the polymerization by addition to a monomer molecule and start another growing polymer chain, which in turn adds to a RAFT agent or a macromolecular RAFT agent. The R-group must therefore be a fast-fragmenting leaving group with respect to the polymer chain, but the formed radical must also be reactive enough to quickly re-initiate the polymerization. Therefore, both Z- and R-groups must be rationally chosen in a RAFT agent to enable the polymerization of a given monomer.^[99] The phase of the polymerization in which a rapid exchange of growing polymer chains and those bound to a macromolecular RAFT agent takes place is called *main equilibrium*. This exchange reaction leads to all polymer chains having approximately the same probability to grow. The result is a narrow molar-mass distribution.

At the end of the polymerization, a large majority of macromolecular chains possess the RAFT (and Z-) group at one end and the R-group at the other end.^[100,101] The overarching consequence is that in a RAFT polymerization, the polymer is evenly inserted into all RAFT agents between their RAFT and R-groups. This net reaction is illustrated in Scheme 1.3 along with the underlying control mechanism in the main equilibrium. The produced macro-RAFT agents can be employed in a second radical polymerization to produce block copolymers.^[102–106]

Assuming that all RAFT-agent molecules take part in the reaction and neglecting the radical chains carrying fragments of the radical initiator,^[107,108] the theoretical



Scheme 1.3: Net reaction of a RAFT polymerization: the polymer chain is inserted between the RAFT group and the re-initiating group. Control over this reaction is provided by the RAFT main equilibrium. Z denotes the stabilizing group, R the re-initiating group. See Scheme 1.2 for the detailed elementary reactions.

number-weighted mean of the molar masses $\overline{M}_{n,theo}$ of polymers from a RAFT polymerization can be predicted for any monomer conversion X_M via the equation:

$$\overline{M}_{n,theo} = \frac{c_M \times M_M \times X_M}{c_{RAFT}} + M_{RAFT}. \quad (1.1)$$

Here, c_M and c_{RAFT} are the concentrations of the monomer and the RAFT agent, M_M and M_{RAFT} are the respective molar masses. For polymerizations in bulk, the product of the monomer's concentration and molar mass approximately coincides with its density δ_M :

$$c_M \times M_M \approx \delta_M. \quad (1.2)$$

Insertion of (1.2) into (1.1) gives:

$$\overline{M}_{n,theo} \approx \frac{\delta_M \times X_M}{c_{RAFT}} + M_{RAFT}. \quad (1.3)$$

The trithiocarbonate group Trithiocarbonates (Figure 1.1c) are among the most commonly used RAFT agents. They are relatively easy to synthesize and very versatile—they control polymerizations with a variety of monomers.^[61,109] Trithiocarbonates are unique RAFT agents in the sense that they are inherently bifunctional, so that a polymer chain can be inserted on both sides of the functional group when it is connected to two good leaving groups, and the trithiocarbonate group will be found in the middle of the formed polymer chains.^[110] Triblock copolymers can thus be prepared in just two polymerization steps.^[111,112]

Organic trithiocarbonates are typically synthesized by reaction of thiols with carbon disulfide in alkaline medium.^[113–116] An alternative method is the reaction of trithiocarbonate anions with alkyl halogenides^[117–120] or alkyl tosylates^[121] in the presence of bases,^[122,123] phase-transfer catalysts,^[124,125] or elevated temperatures.^[126] The trithiocarbonate anion for these reactions, which follow the mechanism of a nucleophilic substitution, can be prepared *in situ* by treatment of carbon disulfide with bases.^[127] In this work, most of the used RAFT agents are of trithiocarbonate type.

1.2.1.2 Molar-mass distributions

The degrees of polymerization (and therefore also the molar masses) in polymer materials are not identical for all macromolecules, but distributed over a certain range. In order to describe this distribution of chain lengths, usually a *distribution function*^{*} is given, by which the relative frequency of respective molecules can be calculated for all chain lengths in the material. Because the molar mass can only assume certain values, all these functions are discreet.

It is advisable to give any distribution function in normalized form, in order to render it independent of the number of macromolecules, which means that the sum over all function values \underline{M}_i must be equal to 1:

$$\sum_{i=1}^{\infty} \underline{M}_i = 1. \quad (1.4)$$

To transform any distribution function $x(M)$ into the normalized form $\underline{x(M)}$, it has to be divided by the sum of all possible function values, the normalization factor N :

$$\underline{x(M)} = \frac{x(M)}{N}, \quad (1.5)$$

$$N = \sum_{i=1}^{\infty} M_i. \quad (1.6)$$

Distribution functions are often stated in terms of the degree of polymerization p , rather than the molar mass M . The degree of polymerization is the proportionality factor between the molar mass M of the complete polymer chain and the molar

^{*}This should not be confused with the *cumulative distribution function* in statistics which describes the probability that a random variable will be found at a value less than or equal to the corresponding function variable. The term “distribution function” is strictly used in the sense of a *probability mass function* in this work.

mass of the monomeric unit M_M , so that a given distribution function can be easily converted into a *chain-length distribution function* using the following equation:

$$M = p \times M_M. \quad (1.7)$$

For a chain-growth polymerization, for which the assumptions can be made that the number of growing chains remains constant, the addition of monomer molecules does not depend on the chain length, and that the growth of all chains is stated at the same time—this holds true for reversible-deactivated radical polymerizations—the molar mass distribution of the produced macromolecules can be expressed by a *Poisson distribution*.^[128] The (normalized) Poisson distribution N_p^P as a function of the degree of polymerization p with an expectation value of v_p is

$$N_p^P = \frac{v_p^p \times e^{-v_p}}{p!}, \quad p = 1, 2, 3, \dots \quad (1.8)$$

Characterization of molar mass distributions Statistical quantitative key measures of distribution functions are generally expressed as the *moments* of these distributions. The v^{th} *moment about the mean* ${}^n\mu_v$ (or v^{th} *central moment*) of an integer-valued random variable i with the distribution function N_i is defined as

$${}^n\mu_v \equiv \sum_{i=1}^k N_i \times M_i^v, \quad v \in \mathbb{Z}, \quad (1.9)$$

k being the highest occurring value. The zeroth central moment ${}^n\mu_0$ of a normalized distribution function is 1, otherwise it coincides with the normalization factor N (see Equation (1.6)).

The quotient of the first and the zeroth moment of a molar mass distribution equals the arithmetic mean of all molar masses M_i , which are weighted by their absolute frequencies n_i . This mean value is called *number average* \overline{M}_n of the molar mass,

$$\overline{M}_n \equiv \frac{{}^n\mu_1}{{}^n\mu_0} \stackrel{(1.9)}{=} \frac{\sum_{i=1}^k N_i M_i}{\sum_{i=1}^k N_i}. \quad (1.10)$$

It is accessible experimentally, for example, by osmometry.

The mean value of all molar masses of a sample, which are weighted by the corresponding mass m_i , is the so-called *mass average* \overline{M}_w of the molar mass,

$$\overline{M}_w \equiv \frac{\sum_{i=1}^k m_i M_i}{\sum_{i=1}^k m_i}. \quad (1.11)$$

The absolute mass m_i corresponds to the product of the number n_i of macromolecules and their molar mass M_i :

$$m_i = n_i M_i. \quad (1.12)$$

Insertion of (1.12) in (1.11) shows that the mass average \overline{M}_w is the quotient of the second and the first moment of the number-weighted molar mass distribution:

$$\overline{M}_w = \frac{\sum_{i=1}^k n_i M_i^2}{\sum_{i=1}^k n_i M_i} = \frac{\sum_{i=1}^k N_i M_i^2}{\sum_{i=1}^k N_i M_i} \stackrel{(1.9)}{=} \frac{{}^n\mu_2}{{}^n\mu_1}. \quad (1.13)$$

In the case where all macromolecules possess the same mass, the number average and the mass average of the molar mass distribution are identical. Otherwise, the mass average is always higher:

$$\overline{M}_w \geq \overline{M}_n. \quad (1.14)$$

A method which gives access to the mass average is static light scattering.

An important indicator for the characterization of the width of molar mass distributions is the *dispersity* \mathcal{D} (formerly called *polydispersity index*, *PDI*). It is defined as the quotient of mass average and number average of the molar mass distribution:*

$$\mathcal{D} \equiv \frac{\overline{M}_w}{\overline{M}_n} \stackrel{(1.10)}{=} \frac{{}^n\mu_2}{{}^n\mu_1} \stackrel{(1.13)}{=} \frac{{}^n\mu_2}{{}^n\mu_1^2}, \quad \mathcal{D} \geq 1. \quad (1.15)$$

A narrow molar mass distribution possesses a low \mathcal{D} , which is desirable for most purposes.

For the Poisson distribution, the mean value of the number distribution \overline{M}_n^p coincides with its expectation value ν_p :

$$\overline{M}_n^p = \nu_p. \quad (1.16)$$

* Due to the proportionality of molar mass and degree of polymerization, the dispersity \mathcal{D} can as well be calculated by inserting distribution functions of the degree of polymerization here.

The mass average M_w^P of the Poisson distribution is

$$\overline{M}_n^P = \nu_p + 1. \quad (1.17)$$

The dispersity \mathcal{D}^P of the Poisson distribution is therefore

$$\mathcal{D}^P \stackrel{(1.15)}{=} \frac{\overline{M}_w^P}{\overline{M}_n^P} \stackrel{(1.16)}{\stackrel{(1.17)}}{=} \frac{\nu_p + 1}{\nu_p} = 1 + \frac{1}{\nu_p}. \quad (1.18)$$

With growing expectation value, the dispersity of the Poisson distribution decreases and converges to the value of $\mathcal{D} = 1$.

Size-exclusion chromatography The most important method for the determination of molar mass distributions of polymers is *size-exclusion chromatography*^[129,130] (SEC), also termed *gel-permeation chromatography*^[131,132] (GPC) when organic solvents are used. It is a form of liquid chromatography, performed as column chromatography.

The stationary phase consists in a porous, swollen polymer network with a broad distribution of pore sizes. The fractionation is based on the different hydrodynamic volume V_h of the analytes, which can be calculated from the intrinsic viscosity $[\eta]$ and the molar mass M by

$$V_h = [\eta] \times M. \quad (1.19)$$

Polymers dissolved in a solvent increase its viscosity. The reduced viscosity η_{red} expresses the contribution of the polymer to the total viscosity:

$$\eta_{\text{red}} = \frac{\eta_c - \eta_s}{\eta_s}. \quad (1.20)$$

Here, c is the polymer's concentration, η_c the viscosity of a polymer solution with the concentration c , and η_s the viscosity of the pure solvent. Extrapolation to very low concentrations yields the intrinsic viscosity $[\eta]$, which is also called *Staudinger index*:

$$\lim_{c \rightarrow 0} \eta_{\text{red}} = [\eta]. \quad (1.21)$$

The higher the hydrodynamic volume of the analyte particle, the lower is its retention time in the column.

SEC is a relative method and any instrument has therefore to be calibrated with calibration samples having very narrow and known molar mass distributions.^[133] When no calibration data are available for a given substance, it is possible to use

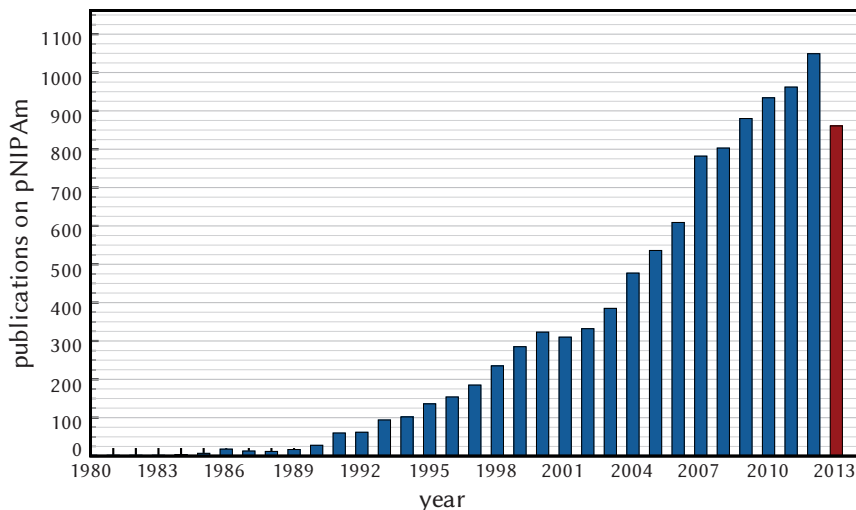


Fig. 1.2: Temporal development of the number of new publications on pNIPAm per year. The data were obtained from WEB OF KNOWLEDGE running a search for the name of the polymer and all common acronyms in the title or the keywords. The search was performed in November 2013.

a universal calibration, when the *Mark-Houwink parameters* are known.^[134] The results of SEC measurements are typically either given as mass-weighted molar-mass distributions in logarithmic form $W(\log M)$, when a calibration could be applied,^[135] or as the directly obtained chromatograms as a function of the retention time.

1.2.2 Poly(*N*-isopropylacrylamide) (pNIPAm)

The central role for the presented work of *poly(N-isopropylacrylamide)* (pNIPAm) and its special characteristic features in aqueous solution, namely thermoresponsive properties (Section 1.2.2.1) and cononsolvency (Section 1.2.2.2), justify dedicating a stand-alone theoretical section to this polymer.

PNIPAm is typically prepared from the respective monomer (see Figure 5.11) by radical polymerization.^[136] The polymer is the topic of over 10 000 publications, mostly from polymer and materials science and chemistry, but also in great part from other fields like physics, biology, medicine and pharmacology. The number of publications per year is thereby steadily increasing. It already exceeded 1000 in 2012 and the increase does not seem to have peaked yet, as it can be seen in the

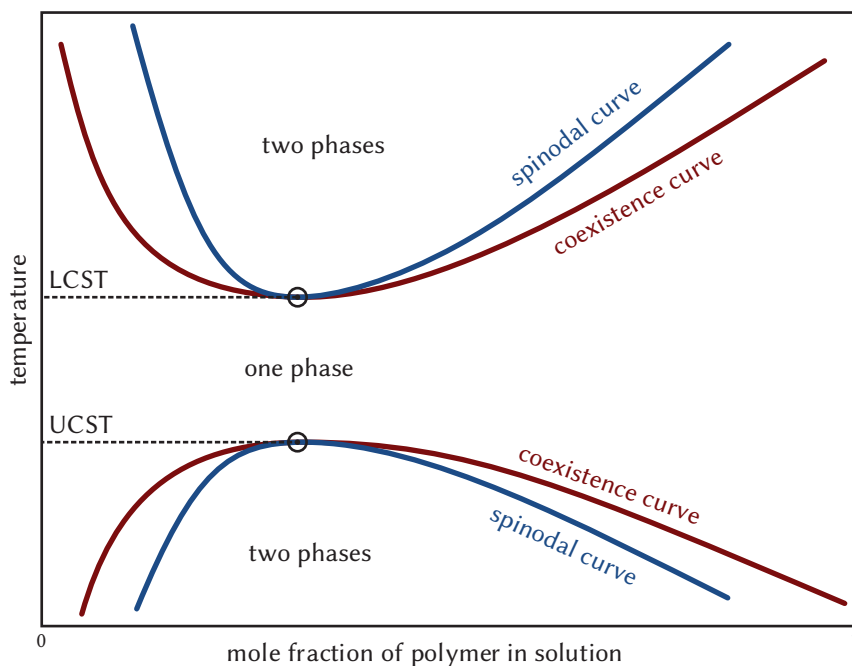


Fig. 1.3: Exemplified schematic phase plot of a typical polymer binary solution phase behavior featuring both a lower critical solution temperature (LCST) and an upper critical solution temperature (UCST). The coexistence curve is also termed “binodal curve”.

plot in Figure 1.2. In some of these studies, pNIPAm was just used because of its solubility in water and almost all polar organic solvents. Other studies cover practical applications of pNIPAm, such as tissue engineering,^[137] electrophoresis,^[138] or chromatography.^[139] The majority of studies, however, deal with the very special behavior of the polymer in aqueous solutions, which is contrary to most other polymers and described in the following.

1.2.2.1 PNIPAm as a smart polymer

Solubility of polymers in general First of all, the effect of the temperature on the solubility of polymers shall be discussed in general. Figure 1.3 shows a schematic temperature-dependent phase diagram of a polymer binary solution exhibiting two characteristic features: The system is miscible at all compositions

at medium temperatures, but the polymer precipitates when the temperature is raised or decreased. Two special points are marked in this diagram: The lowest temperature at which the system is miscible for all possible compositions is called *upper critical solution temperature (UCST)* and the highest temperature at which the system is miscible independent of the composition is called *lower critical solution temperature (LCST)*.^[140] Describing these phenomena in thermodynamic terms, it can be stated that for the components of a system to be miscible, the increment of the free enthalpy (Gibbs energy) of mixing ΔG_{mix} has to be negative:

$$\Delta G_{\text{mix}} = \Delta H_{\text{mix}} - T\Delta S_{\text{mix}} < 0. \quad (1.22)$$

ΔH_{mix} and ΔS_{mix} are the increments of the enthalpy and entropy of mixing, T is the absolute temperature.

In the case of a UCST, this expression becomes negative with increasing temperature. That means that both the increments of the enthalpy and the entropy of mixing necessarily have to be positive:

$$\text{UCST:} \quad \Delta H_{\text{mix}} > 0, \Delta S_{\text{mix}} > 0. \quad (1.23)$$

In the case of an LCST, the increments of the enthalpy and the entropy of mixing both have to be negative:

$$\text{LCST:} \quad \Delta H_{\text{mix}} < 0, \Delta S_{\text{mix}} < 0. \quad (1.24)$$

For completeness, also the two remaining possibilities shall be considered. If

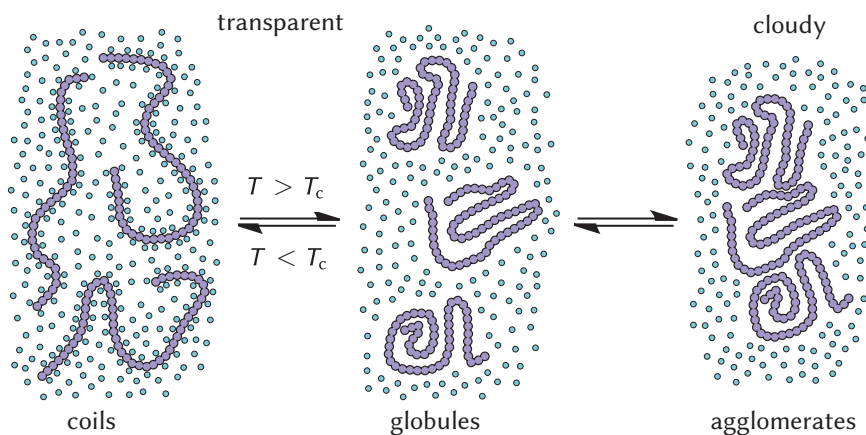
$$\Delta H_{\text{mix}} < 0, \text{ and } \Delta S_{\text{mix}} > 0, \quad (1.25)$$

the polymer is soluble at all temperatures, and if

$$\Delta H_{\text{mix}} > 0, \text{ and } \Delta S_{\text{mix}} < 0, \quad (1.26)$$

the polymer is insoluble at all temperatures, obviously given that ΔH_{mix} and ΔS_{mix} are themselves temperature-independent.

A UCST behavior is the standard behavior in organic solvents with undirected intermolecular forces and clearly more common for polymer solutions than an LCST behavior. In fact, the existence of an LCST is counterintuitive since it requires a negative entropy of mixing, that is, the system becoming more “ordered” upon mixing. The key of understanding here is the low *orientation entropy*^[141] in the solution. Highly ordered structures are formed by the solvent molecules around the polymer chains, driven by their enthalpy of formation. When the polymer



Scheme 1.4: Schematic illustration of the clouding of a polymer solution by the coil-to-globule transition. The aggregation of the globules causes the solution to appear opaque.

precipitates endothermically, these aggregates collapse, accompanied by an increase of the total entropy.^[142] It goes without saying that this behavior is almost exclusively observed for solutions with very polar solvents (usually water) which are able to have specific (directed) interactions with the polymer, namely oriented hydrogen bonds.

Of course, in principle most systems would show mixing and demixing at some point, but in practice, with many systems one does not observe phase separation upon cooling, because the solvent solidifies before it becomes sufficiently poor to induce demixing. Analogously, the solvent often boils at atmospheric pressure before the two-phase state is reached.

Coil-to-globule transition of pNIPAm It has been known since 1968^[143] that aqueous solutions of pNIPAm exhibit an LCST at around 32 °C (atactic polymer with $\bar{M}_n > 10^4 \text{ g mol}^{-1}$ ^[144] at atmospheric pressure).^[145,146] Below that temperature, the polymer chains are in the hydrated state. Water molecules are associated with the amide groups by hydrogen-bonding,^[147] and additionally form cage-like structures^[148] around the hydrophobic isopropyl groups along the polymer chain.^[149] Because the polymer cannot form hydrogen bonds with itself, the dissolution is energetically favored. The solution appears completely transparent.

When the cloud temperature* T_c is exceeded, the expanded polymer coils collapse to shrunken globules in an endothermic coil-to-globule transition.^[151,152] The segregated polymer globules subsequently aggregate. This in turn renders the solution turbid, due to the different refractive indices of the components, or potentially even visible flocks and a two-phase system are formed. (The coil-to-globule transition itself does not change the visual appearance of the solution.) The clouding of a pNIPAm solution above the cloud temperature is illustrated schematically in Figure 1.4. The major driving force for the coil-to-globule transition is the dehydration of the hydrophobic moieties.^[153] In solution, there are around 8–15 water molecules per monomer unit associated with the polymer chain.^[154–156] Above the cloud temperature, this number drastically drops to almost zero—the polymer becomes hydrophobic.

Strictly speaking, the LCST is only the *critical* temperature at the minimum of the two-phase region for a certain polymer concentration, the temperature below which the components of a mixture are miscible for all compositions. But in the case of pNIPAm in water, the spinodal curve (see Figure 1.3) is very flat and increases only a few degrees, when going from the minimum concentration at which the turbidity is still observable up to very high concentrations.^[157] (So flat, it is very hard to give an exact composition corresponding to the LCST. It is around 5–10 % by weight.)^[147] Consequently, people often refer to the transition temperature at any composition as the LCST. This is nevertheless a bad habit and should be avoided.

Due to the abruptness and reversibility of the thermoresponsive transition, pNIPAm is counted among the group of *smart polymers*,^[158,159] also termed *stimuli-responsive*,^[160,161] *intelligent*,^[139] or *environmentally sensitive*.^[162] These polymers react to one or more external physical (temperature, pressure, radiation), chemical (pH value, signaling molecules) or biological (enzymes) stimuli with drastic changes in their chemical and physical properties. Important features are that these changes are drastic, discontinuous, and reversible. That means that the changes occur abruptly at a certain point, but the material returns to its initial state upon application of a counter-trigger. Aqueous pNIPAm solutions are arguably the most prominent representative of the class of smart polymers and have been established as the standard model system to study the coil-to-globule transition,^[163,164] which is of great importance for biology because of the presence of coil-globule transitions of proteins, nucleic acids and other biopolymers.^[165] These natural macromolecules are stable in solution over a wide range of stimuli, but react at a certain point with drastic conformational alteration and concomitant changes of their properties.^[166] Another

*This term is preferred over “transition temperature” because it refers to the observable phenomenon of the clouding of the solution, which is generally taken as optical indicator for the determination of this temperature.^[150]

thermoresponsive polymer is for instance poly(*N*-vinylcaprolactam).^[167] Examples of pH-responsive polymers are poly(2-(diethylamino)ethyl methacrylate)^[168] and poly(2-(dimethylamino)ethyl acrylate) (pDMAEA).^[169] The reactions of smart polymers to their external stimuli can be fine-tuned by factors such as the concentration, the chain-length distribution, the topology, or additives. For pNIPAM, most additives to the aqueous solution lower the cloud temperature.^[170–173] For inorganic salts, the lowering effect can be correlated with the Hofmeister series,^[174] in which the ions were originally sorted according to their strength in precipitating (“salting out”) proteins from aqueous solutions.^[175,176] By the synthesis of block copolymers, the desirable properties of two different types of polymers can often be combined.^[177]

PNIPAm can be crosslinked to form a hydrogel. Typical crosslinkers are *N,N'*-methylene-*bis*-acrylamide and *N,N'*-cystamine-*bis*-acrylamide.^[178,179] Here, heating and cooling lead to the reversible collapsing or swelling of the hydrogels.^[179] The transition still occurs at a temperature approximately identical to the cloud temperature of isolated chains—coined the “volume phase transition temperature” for hydrogels. That means that most results obtained for isolated chains can be applied correspondingly to crosslinked pNIPAm.^[180] These hydrogels show great potential for applications in medicine,^[158] in particular for drug delivery^[181–183] in biomedical engineering because the transition occurs just below the human body temperature and accompanied by an expulsion of any absorbed therapeutics.^[160,161]

1.2.2.2 Cononsolvency

The second very particular feature of aqueous pNIPAm solutions is the very rare phenomenon of *cononsolvency*, which shall be explained in the following. The term derives from the clearly more common phenomenon of *cosolvency*^[184,185] (also called *mixed* or *true* cosolvency) which was found and coined independently by Wolf and Molinari^[186] (1973) and Cowie and McEwen^[187] (1974) for the ternary system polystyrene in acetone and diethyl ether. Another example is the system of poly(methyl methacrylate) (pMMA) in water and methanol. The IUPAC gives the following definition for cosolvency of polymers* in the “IUPAC Gold Book”:^[188]

Co-solvency (in polymers):

The dissolution of a polymer in a solvent comprising more than one

*It should be noted that the definition is different in pharmaceuticals, where the word cosolvent is used for a solvent which also dissolves the drug in pure form. Also, cosolvency is just the special case for mixtures of one solid and two liquid substances. A more general term would be co-miscibility, although that term is very uncommon.

component, each component of which by itself is a non-solvent for the polymer.*

Cononsolvency is simply the contrary phenomenon—the formation of a nonsolvent for a polymer by mixing two solvents.^[189]

For pNIPAm, it was first reported for by Winnik, Ringsdorf, and Venzmer^[190] in a communication in 1990 (although the equivalent effect for pNIPAm hydrogels was already known by then).^[180,191,192] In reading an article by Schild and Tirell^[193] on the measurement of the cloud temperature of pNIPAm with calorimetry and they stumbled over a sentence in the experimental section where the precipitation of the polymer from the aqueous polymerization solution was mentioned:

Precipitation was carried out by dropwise addition of the polymerization mixture to 800 mL of methanol.

It surprised them that the precipitation of pNIPAm was performed by its addition to the even better solvent methanol, which probably goes against the natural intuition of any synthetic chemist. (In terms of solubility in mixtures of water and methanol, pNIPAm is just the opposite to the above-mentioned pMMA.) After reproduction of the experiment with different mole fractions of methanol, they published the aforementioned communication and were thus even faster with their publication than the authors of the paper they had originally read, who published the same results, albeit with more detailed experiments, shortly after.^[194]

In the following years, this anomaly was analyzed in further detail by different scientists in over 100 publications, varying lots of different factors.^[195,196] It was found for example that, unlike for the cloud temperature of pure aqueous pNIPAm solutions, the cononsolvency area does depend very strongly on the polymer's molar masses.^[197] This is important to note since before the advent of RDRP (see Section 1.2.1.1), only samples with very ill-defined molar masses from conventional radical polymerization were accessible for research, so that only quite inaccurate results were achievable which could not be easily aligned with theoretical expectations.

The miscibility gap in the system with methanol as cononsolvent is treated in the majority of studies,^[198–200] but also several other common organic solvents act as cononsolvents for aqueous solutions of pNIPAm, including other alcohols,^[191,201] dimethyl sulfoxide (DMSO),^[202] *N,N*-dimethylformamide (DMF),^[203] dioxane^[204] tetrahydrofuran (THF),^[205] acetone, and others.^[201] In some of these cases, the LCST behavior can be retained over the whole composition range, as for methanol or

*The spelling is retained in the quote, although it differs from the (more commonly used) spelling in this work.

acetone as cononsolvents. In contrast, the phase-separation curve in a temperature–mole fraction phase diagram can also be flipped for higher mole fractions of the organic cononsolvent, such that heating of the mixture leads to the solution clearing up (UCST behavior). Examples for this behavior are DMSO or ethanol as cononsolvents.^[206] As for the temperature-induced clouding described above, the results regarding cononsolvency of linear pNIPAm chains directly apply to the crosslinked polymer as well.^[207] The hydrogels shrink upon addition of a cononsolvent and expel the absorbed molecules.

Possible explanations for the cononsolvency of these systems are still vigorously discussed in the scientific community. In essence, it is categorically disputed whether this intriguing anomaly can be mainly traced to polymer–solvent or to solvent–solvent interactions. Both models, which are mutually incompatible, have strengths and weaknesses in explaining and predicting the behavior:

Polymer–solvent interactions: According to this first theory, the cononsolvent competes with the water for the hydrogen–bond positions,^[208] preferentially binds to the polymer,^[195,209,210] and replaces the associated water molecules. In these aggregates, the hydrophobic part of the cononsolvents points towards the solution, making the polymer hydrophobic overall and therefore insoluble until the solvent mixture becomes hydrophobic enough to enable solvency by nonspecific interactions after further addition of the cononsolvent.^[211] This explanation seems most reasonable for cononsolvents like alcohols, which are able to actively form hydrogen-bonds and possess a hydrophobic tail. In fact, this model of competitive hydrogen bonding refers in most cases to the system pNIPAm/water/methanol.^[195] Here, it is supported by several theoretical calculations.^[197,212,213]

Solvent–solvent interactions: According to the second model of solvent–solvent interactions, energetically favorable complexation forms network or cluster structures^[214,215] in the liquid mixture.^[151] For the system pNIPAm/water/methanol, it is for example speculated that water pentamers are formed with methanol by hydrogen bonding,^[216] but most of the formed structures have only been predicted theoretically, since they are very hard to detect experimentally with currently used methods.^[214,217] These structures are then assumed to be poorer solvents for the polymer than the two pure solvents.^[216,218–220] Put simply, there are just less water molecules available to hydrate the polymer.^[206] This model is very well compatible with the finding that the solvency increases again when ions are added which are known to destroy the postulated solvent–solvent complexes.^[196] On the other hand, it also displays some shortcomings, as it fails for example to explain findings

like the high influence of the polymer's molecular weight on the expansion of the miscibility gap found for methanol as cononsolvent.^[197] According to this model, the solubility of polymer chains should be rather independent of their lengths.

Models involving ternary complexation interactions with structures formed by both solvents and the polymer^[180,191,192] can be excluded since the transition also occurs in extremely diluted polymer solutions at the same mole fraction of cononsolvent.^[149,151] Also, concentration fluctuations can be neglected as reason for cononsolvency, since, as a good approximation, most solvent mixtures can be considered as homogeneous. They can only play a major role for solvent pairs with bad miscibility.^[221] It is, of course, possible that different mechanisms or combined mechanisms are responsible for the cononsolvency of different systems.

Aqueous solutions of pNIPAm are by far the best known and most studied system regarding cononsolvency. Together with the coil-to-globule transition, this makes them the number one model system for two different phenomena and underlines again the great importance of this polymer in modern research.^[196]

Only very few other systems that exhibit cononsolvency behavior are known. Most of the examined systems comprise copolymers of NIPAm and other monomers with a very high content of pNIPAm,^[222] but there are also a few other examples:

- poly(*N*-isopropylmethacrylamide) in water and ethanol,^[223]
- poly(2-methacryloxyethyl phosphorylcholine) in water and ethanol^[224] or 2-propanol,^[225]
- poly(vinyl alcohol)^[226,227] and poly(*N,N*-diethylacrylamide) in water and DMSO^[192] or methanol,^[228]
- poly(*N,N*-dimethylacrylamide) in water and organic solvents,^[229]
- poly(vinyl methyl ether) in water and alcohols^[230] or THF,^[231]
- poly(vinylpyrrolidone) in water and methanol,^[232]
- poly(oligo(ethylene glycol)-phenyl ether acrylate) in water and ethanol,^[233]
- cellulose acetate in acetic acid and aniline,^[190]
- polystyrene in DMF and cyclohexane,^[189]
- poly(ether imide) in *N*-methyl-2-pyrrolidinone and methylene chloride^[234]

- poly(methyl methacrylate) in chlorobutane^[235] and amyl acetate and in pyridine and formic acid,^[236]
- poly(η -caprolactone) in pyridine and formic acid.^[236]

Many of these systems, especially the latter non water-soluble polymers, exhibit only a UCST-style cononsolvency behavior that is totally different from the LCST-cononsolvency behavior of pNIPAm.^[204,229] Often, the type of behavior is not even discussed or examined. Moreover, the solution does not necessarily become turbid at the structural transition of the polymer.^[232] Again, this highlights the particularity of pNIPAm in polymer science.

1.2.3 Nanosciences

Nanosciences is the generic term for any aspect of science in which objects with features on the multi-nanometer length scale are synthesized or studied. When speaking about the macroscopic properties of such substances, people often refer to them as *nanomaterials*. A more functionality-based definition of nanomaterials, which is dependent on the type of the respective substance, is that their properties scale with the size of their components. Nanoparticles, the fragments of nanomaterials, are tiny in comparison to our macroscopic world, but gigantic with respect to the atoms and molecules which are at the center of traditional chemistry. Consequently, in their properties, they are fundamentally distinct and unique, giving rise to a wide range of potential applications (also see the Introduction, Section 1.1).

It should also be mentioned at this point that, as is arguably the case for any emerging technology, nanosciences raise many concerns in parts of our society, ranging from worries about the environmental impact and the toxicity of nanomaterials^[237–241] through to apocalyptic doomsday scenarios, such as the fear of an earth-consuming “gray goo”, composed of self-replicating nanorobots gone out of control.^[1] On the other hand, people have in principle been unknowingly using nanotechnology since ancient times. A good example (other than the gold-stained glass objects in Figure 1.4) was recently presented by Reibold *et al.*^[242] (2006). They were able to show that the mythical quality of blades made of “Damascus steel”, produced in ancient India using high-carbon steel and first encountered by the crusaders when fighting against Muslims, can—at least in part—be traced to incorporated carbon nanotubes and cementite nanowires, which had formed within the historical, but today no longer replicable, production process.

1.2.3.1 General strategies for the synthesis of nanomaterials

Very broadly, there are two general approaches to reach the nanoscale: the *bottom-up* and the *top-down* approach.^[243] The terms *synthesizing-up* and *engineering-down* are also in use within this context. Not only are the latter terms more figurative, they are also more specific because they exclusively refer to nanosciences. Engineering down to the nanoscale involves using the same methods which an engineer or artisan performs on the macroscopic scale, but using the latest in modern specialized techniques in order to miniaturize. A typical example is the production of electronic components with ever-decreasing sizes by lithographic etching of silicon semiconductors. Modern microchips can be made so compact that several billion transistors fit on an area as small as 1 cm^2 . The width of each conducting line in these integrated circuits has already dropped below 100 nm. The fabrication of microchips has therefore reached the domain of nanotechnology by going smaller and smaller, following an engineering-down strategy. In contrast, the synthesizing-up approach is modeled on biology, where nanostructures are typically reached by self-assembly of yet smaller building units. Following this approach, these building units are generally sought to be synthesized by chemical reactions, often starting from very small molecules or even individual atoms or atomic ions. To stick with the example of modern computing, the first reports of molecular computing based on supramolecular species have already begun to appear.^[244]

Applying the above definitions, all synthesis strategies of nanostructures followed in this thesis can strictly be allocated to the field of bottom-up synthesis.

1.2.3.2 Gold nanoparticles

Gold nanoparticles (AuNPs)^[249–251] is the generic but vague umbrella term for a variety of nanosized gold objects with greatly differing chemical and physical properties, such as color, bonding and aggregation characteristics, electronic structure, stability, dispersability, and interactions with biological systems. Most importantly, these properties depend on their size. In this regard, AuNPs can be roughly classified into *gold nanoclusters* and *gold nanocrystals*.^[252,253] The terms reflect the fact that the AuNP structure becomes crystalline when the diameter exceeds a value of approximately 2 nm. The characteristic properties of the two types of nanosized gold particles are confronted in Table 1.1. Put simply, gold nanoclusters behave more like large molecules and gold nanocrystals are more comparable to tiny gold lumps.

While Michael Faraday^[254] (1857) is generally regarded as the inventor of AuNP synthesis,^[255] colloidal gold has been used since ancient times as a means for staining glass (see next section). In Figure 1.4, three photographs of historical gold-stained

Tab. 1.1: Comparison of typical characteristic properties of gold nanoclusters and gold nanocrystals.

characteristic	gold nanoclusters	gold nanocrystals
diameter	< 2 nm	2.5–100 nm
number of atoms	10–100, preferentially “magic numbers”	> 200
structure	molecular-like	metallic nature (face-centered cubic)
optical spectrum	discrete electronic transitions, “fingerprint”	broad localized plasmon resonance absorption peak
resulting color	brown, yellow	red to blue (if spherical)
shapes	defined, polyhedral	many different shapes: spheres, rods, ^[245] cubes, ^[246] plates, cages, ^[247] rosettes, ^[248] ...

glass objects are shown. Photograph (a) shows the Lycurgus cup, a 4th century Roman chalice made of dichroic* glass impregnated with gold and silver nanoparticles (approximately 70 nm),^[256] today on display at the British Museum, London, UK. When the Lycurgus cup is viewed under normal lighting conditions, it appears green, but when light is shone through the glass, only the characteristic crimson color is let through. The photograph is taken in a way that both colors can be seen at the same time. Photograph (b) in Figure 1.4 shows a stained glass window from the 14th or the 15th century in the Basilica di Santa Maria del Fiore, Florence, Italy. In photograph (c), a gold ruby cup from the treasury chamber of the Wittelsbacher (Munich Residenz) can be seen. It is attributed to the German chemist and apothecary Johannes Kunckel.

On a side note, Chen *et al.*^[257] (2008) have found very recently that gold-stained glass is not only pleasant to look at, but actually environmentally beneficial as well, because the enhanced magnetic field around the embedded nanoparticles' surface, which is enhanced by the irradiation with light (see next section) greatly accelerates

* A *dichroic* material causes visible light to be split up into two distinct beams of different wavelengths.

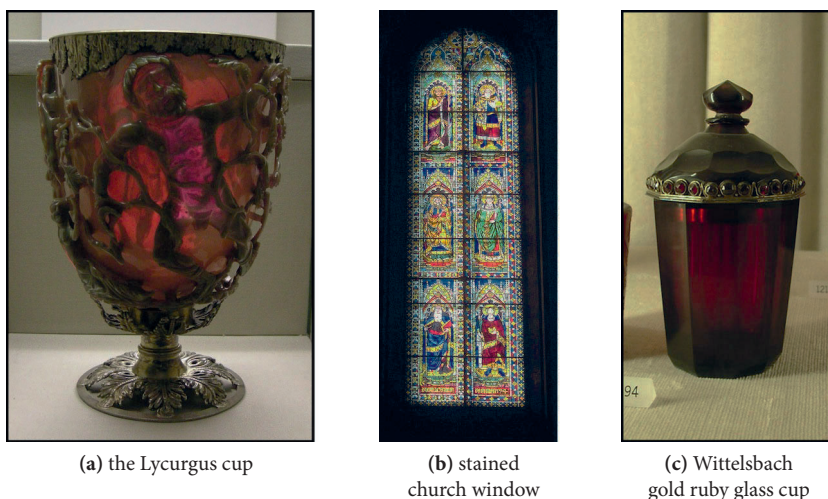


Fig. 1.4: Photographs of historic glass objects stained with colloidal gold; photo (a) by “Sailko”, photo (b) by “JoJan”, photo (c) by “Schtone”, Wikimedia Commons under CC BY-SA 3.0.

the decomposition reaction of volatile organic pollutant compounds in the air even at ambient temperatures, therefore effectively leading to a cleansing of the air.

AuNPs are usually protected by an outer ligand layer. The typical link between the particle and the organic ligand molecules is the gold–thiolate bond.^[260,261] Thanks to the higher stability of gold nanoclusters with certain “magic numbers” of gold atoms, Jadzinsky *et al.*^[258] (2007) and Zhu *et al.*^[259] (2008) managed to obtain gold nanoclusters in pure form, crystallize them, and determine the crystal structures by X-ray diffraction. These two structures are depicted in Figure 1.5, because they give a clear image of the type of the bond to the thiols: The sulfur atoms equally bind to two gold atoms and the ligands do not stand perpendicular on the surface. In the structure shown in Figure 1.5b ($\text{Au}_{25}\text{SR}_{18}$ with $\text{SR} = \text{phenylethanethiol}$), the 25 gold atoms are arranged in the following way: A central gold atom is surrounded by 12 other core gold atoms without bonds to a ligand. They constitute the vertices of an icosahedron, whose edges are colored in blue for visualization purposes. 12 of the 20 faces are capped centrally by a peripheral gold atom ($12 + 12 + 1 = 25$). All peripheral gold atoms are bonded to 2 thiolate molecules, the gold atoms constituting the blue icosahedron only to one thiolate molecule ($\frac{1}{2} \times [2 \times 12 + 1 \times 12] = 18$). Although

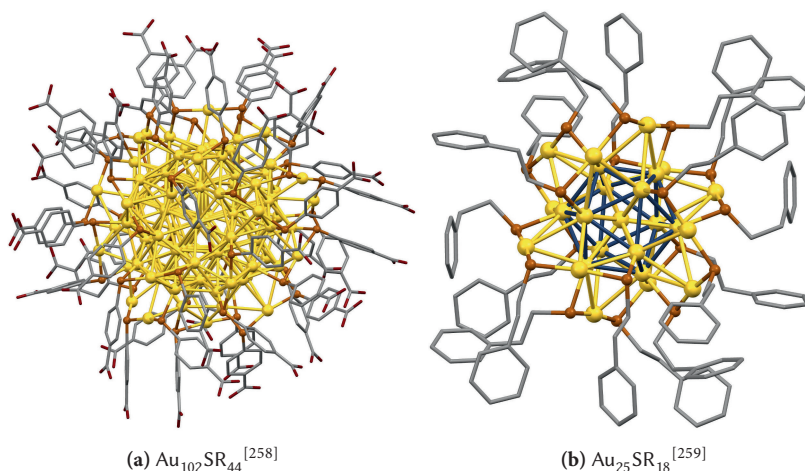


Fig. 1.5: The first two obtained crystal structures of thiolate-protected gold nanoclusters. a) SR = *para*-mercaptobenzoic acid, b) SR = phenylethanethiol. These illustrations were created with the software MERCURY 3.1.1 by the CAMBRIDGE CRYSTALLOGRAPHIC DATA CENTRE using the crystallographic data provided by the authors of the referenced publications. Hydrogen atoms are omitted for clarity.

the gold–sulfur bonding mode might not be absolutely identical on the surface of larger gold nanocrystals, the structures shown here give a basic visual idea.

Although the gold–thiolate link is generally regarded as the most stable bond with gold surfaces, the bonding strength is still so low that it is known to be reversibly cleaved at temperatures over 60–80 °C.^[262,263] Even at room temperature in organic solvents without an excess of thiols, the half-life of the bond is only about one day.^[264]

Optical properties of gold nanoparticles The optical properties of AuNPs are a very important feature, since (i) optical spectroscopy is a powerful and convenient AuNP analysis method and (ii) most of the major AuNP applications are based on these special properties. Because the optical properties are directly related to the AuNP structure, gold nanoclusters and gold nanoparticles have different optical features. Both form very intensely colored colloidal solutions.

Gold nanoclusters exhibit molecular-like discrete electronic properties with single-electron transitions between quantized energy states at distinct wavelengths,

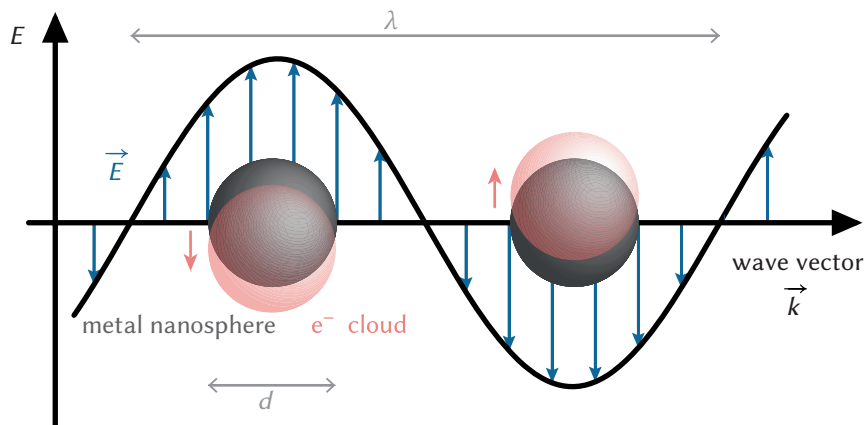


Fig. 1.6: Schematic illustration of the interaction of incident light with the confined conduction electrons of metal nanoparticles.

reminiscent of semiconductor quantum dots, at the lower end of the visible range.^[265] The colloidal solutions are, depending on the gold concentration, dark brown or yellow. The photographs in Figure 1.7a show a colloidal solution of gold nanoclusters in methanol, which has been gradually diluted. In the case that only gold nanoclusters of a single size are present in the sol, distinct transition peaks can be seen in the optical spectrum.^[266] Mostly, the nanoparticle sizes are distributed over a certain range and the signals overlap (see Figure 5.8 for an exemplary spectrum).

The optical excitations of crystalline AuNPs, on the contrary, are of a collective nature. The incident light excites the oscillation of conduction electrons against the restoring force of the positive gold nuclei,^[267,268] as illustrated schematically in Figure 1.6 for a metal nanosphere with the diameter d . E is the electric field strength, λ is the wavelength of the absorbed light. The effect is called *localized surface plasmon resonance*. (A plasmon is the quasiparticle corresponding to the quantized plasma oscillations.) The dependence on the wavelength of the incoming light is relatively weak, so that the plasmon resonance signal is relatively broad. In the case of gold nanospheres, it occurs at around 520 nm (see Figure 5.8 for an exemplary spectrum)—the colloidal solutions are vividly red. The photographs in Figure 1.7b show a colloidal solution of commercial gold nanospheres in methanol with increasing dilution.

The position and shape of the plasmon resonance peak is affected by the following factors:

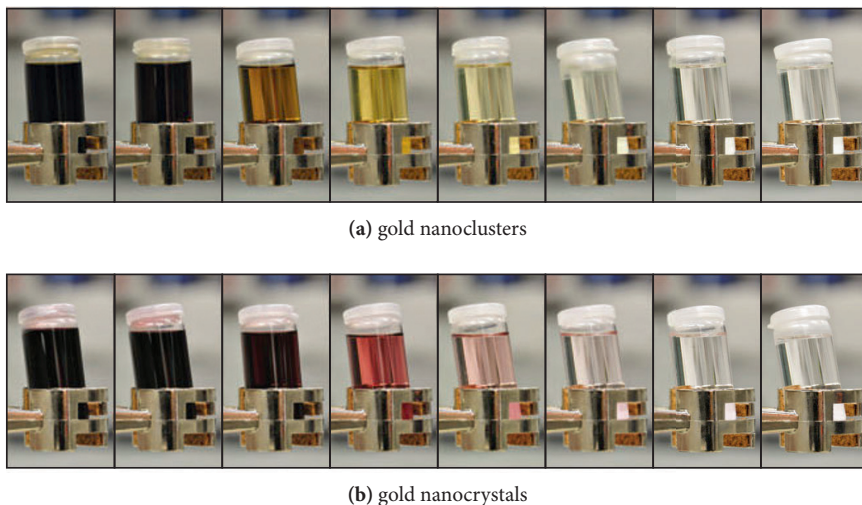


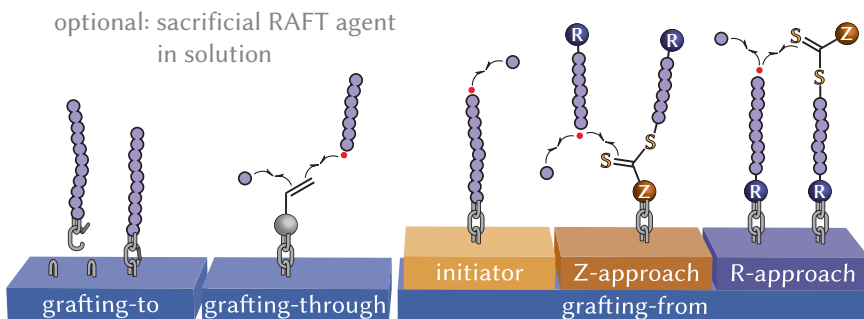
Fig. 1.7: Photographs of gold nanosphere sols in methanol. The upper row shows gold nanoclusters (sample $\text{Au}^{\text{Ibs}}\sqrt{\text{OH}}-6$, see Section 5.1.3.2), the lower row shows gold nanocrystals (acquired commercially from ALDRICH). The concentrations are equal for photographs in the same column. From left to right they are: 1.1 g mL^{-1} , 0.37 g mL^{-1} , 0.12 g mL^{-1} , 41 mg L^{-1} , 14 mg L^{-1} , 4.6 mg L^{-1} , 1.5 mg L^{-1} , and 0.76 mg L^{-1} .

Particle shape: Non-spherical gold nanocrystals form colloidal solutions of completely different colors. Gold nanorods, for instance, exhibit two plasmon resonance peaks—a lateral and a transversal signal.^[269,270] The following points refer mainly to spherical particles, as studied in this work.

Particle size: Larger particle sizes lead to a more pronounced plasmon resonance signal.^[271] Up to a diameter of approximately 25 nm, the absorption band becomes narrower, after which it widens up again. The peak maximum is also shifted to longer wavelengths.^[272] Hence, a more heterogeneous size distribution is reflected in a broader plasmon absorption peak.^[273]

Refractive index of the surrounding medium: A high refractive index (or relative permittivity) of the solvent also shifts the peak to longer wavelengths.^[267,268,274]

Type of the ligands: In addition to the ligands' effect on the refractive index around the AuNP, electron-withdrawing ligands lead to a similar effect as a smaller particle size.



Scheme 1.5: General synthesis strategies for the production of covalently bound polymer brushes using radical polymerization. The grafting-from approach is shown for the special case of RAFT polymerization. Z denotes the stabilizing group, R the re-initiating group in RAFT polymerization.

Temperature: A higher temperature leads to a slightly less pronounced plasmon signal.^[273,275]

Mutual approaching: The plasmon modes are very sensitive to the interparticle distances. Mutual approaching to distances in the dimension of the resonance wavelength gives rise to additional resonances^[276] at longer wavelengths—the effect of “plasmon coupling”.^[277–279] The dispersion turns blue.

Applications of AuNPs Thanks to the dependence of the plasmon resonance signal on the interparticle distances, AuNPs hold great potential for (bio)sensing applications.^[280–284]

Their manifold medical applications^[285,286] include the diagnosis of diseases,^[287] photothermal anti-cancer therapy,^[288,289] drug and gene delivery,^[290] and the use as labels in electron microscopy “immunogold staining”^[291] or contrast agents for computed tomography.^[292] Some of these applications can be enabled by coating the AuNPs with polymers, in order to make them resistant to protein adsorption^[293] and mask them from the body’s reticuloendothelial system.^[294]

Other applications of AuNPs are catalysis,^[295–299] surface-enhanced Raman scattering,^[300,301] staining,^[302] and their employment as compatibilizers in polymer blends.^[303]

AuNPs are already widely used in industrial consumer products, such as cosmetics, food packaging, lubricants, beverages, automobiles, and toothpaste.^[304,305]

1.2.4 Polymers on surfaces

A classic polymer coating—a traditional varnish—is applied on surfaces from solution in a quickly evaporating solvent or from a polymer melt. The varnish can be hardened by—typically UV-radiation induced—crosslinking. However, in all these conventional films, the polymer chains are only physisorbed, weakly attached by van-der-Waals forces, and lying flat on the surface. Only certain, hard, polymers can be used for such coatings. Furthermore, the polymer film is very thick, up to millimeters, which makes it impossible to reach the nanoscale with this approach.

In polymer brushes,^[306–308] the macromolecular chains are linked to the surface through covalent bonds, formed by incorporated functional anchor groups.^[309] The thickness of these brushes coincides with the length of the polymer chains and can therefore be fine-tuned with almost nanometer precision, enabling very fine surface patterning^[310] and the coating of nanoparticles for the production of sophisticated nanohybrids. The coating of surfaces by polymer brushes with special properties can equip them with hydrophobicity,^[311] protein repellence,^[312,313] and antibacterial properties.^[314] Also, parameters like roughness, biocompatibility, toughness, electrical conductivity, pH-compatibility, or heat resistivity can be specifically adjusted.^[265,315–321]

Modern RDRP techniques (see Section 1.2.1.1) render it possible to employ radical polymerization for the production of covalently bound polymer brushes on surfaces. The three general synthesis strategies therefore are shown in Scheme 1.5:

Grafting-to: Preformed polymer chains with an incorporated functional group are grafted to the surface.^[322] Such polymers can also be obtained from conventional radical polymerization using a radical initiator carrying the functionality.^[323] Depending on the type of surface, it can be necessary to prefunctionalize it with complementary groups. Because of the steric hindrance entailed within the grafting-to strategy, it is difficult to achieve high grafting densities.^[324]

Grafting-through: Molecules carrying unsaturated units are immobilized on the surface^[325,326] and then built into the polymer chains propagating in solution.^[327] This is by far the least used strategy of the three and does not necessarily rely on RDRP techniques either.

Grafting-from: The surface is first functionalized with a radical initiator^[328,329] or an RDRP control agent,^[330–332] so that the growing radical chains are directly bound to the surface at one end.^[333,334] Here, a high extent of termination events can only be prevented when a mediating agent, rather than a radical initiator, is immobilized on the surface.

A typical group for anchoring molecules onto surfaces with hydroxyl groups (silica, quartz, aluminosilicates) is the trimethoxysilyl group.^[335]

1.2.4.1 RAFT polymerization from surfaces

Regarding the grafting-to approach to gold surfaces, a special feature of RAFT polymerization is that the active RAFT groups themselves are highly susceptible to chemisorption.^[26,336] The RAFT group can therefore fulfill a second function after completion of the polymerization.

The grafting-from approach, in the case of RAFT polymerization, can be further subdivided into three fundamental strategies (see Scheme 1.5):

Bound initiator: This was historically the first performed approach. Only the radical initiator is tethered to the surface.^[337–339] Although the RAFT agent in solution induces some control over the polymerization, in terms of control, this approach is clearly inferior to the other two. Note that the initiator-terminated polymer chains are usually neglected in an ideal RAFT polymerization (see Section 1.2.1.1).

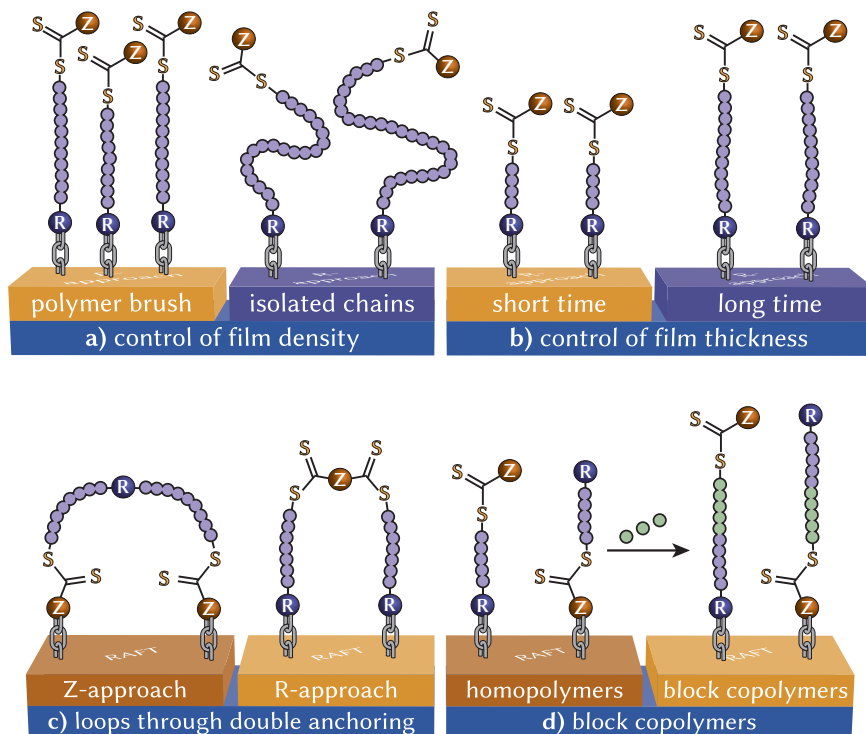
Z-approach: The Z-approach is a unique feature of RAFT polymerization. Hereby, the RAFT agent is covalently bound to the surface with its stabilizing Z-group.^[24,25] The radical chains propagate unattached in solution and return to the surface.* With this approach, only living polymer will eventually reside on the surface—an ideal condition for the production of block copolymers.^[340,341]

R-approach: The RAFT agent is covalently bound to the surface via a link at its R-group.^[342–344] The polymer chains then grow from the surface and the RAFT end group is interchanged between the chains and remains accessible in the periphery.^[345] Since even irreversibly terminated polymer chains will remain on the surface, a maximum grafting density can be achieved.

Even for the R- and the Z-approach, a so-called “sacrificial” RAFT agent is often added to the solution, in order to enhance the overall control.^[346,347]

Scheme 1.6 gives an overview of the different methods of control that can be utilized in surface-confined RAFT polymerizations according to the grafting-from approach:

* Because of these characteristics, the Z-approach could also be regarded as a grafting-to technique.



Scheme 1.6: Ways of control in grafting-from surface polymerizations. Z denotes the stabilizing group, R the re-initiating group in RAFT polymerization.

Scheme 1.6a: The grafting density of the polymer can be adjusted prior to the polymerization by immobilizing the RAFT agents in the desired concentration. In the case of high grafting densities, a polymer brush is formed.^[348] When the grafting density is lower, the polymer chains assume mushroom-like shapes.

Scheme 1.6b: The thickness of the polymer film increases linearly with the monomer conversion and can thus be specifically tuned.

Scheme 1.6c: Polymer loops can be created by anchoring both ends of a RAFT agent to the surface.^[349–351] This can be done for the Z- (left) or the R- approach (right). Both halves of the RAFT agent remain connected to the

surface throughout the course of the polymerization. Due to steric hindrance, polymer loops cannot be produced with the grafting-to strategy.

Scheme 1.6d: Block copolymers on the surface can be formed via a sequential radical polymerization with another monomer.^[352] If the order of monomer addition is dictated by their reactivity, both sequences are still accessible by using either the Z- or the R-approach.

References for Chapter 1

- (1) Drexler, K. E., *Engines of Creation 2.0 – The Coming Era of Nanotechnology*, 20th anniversary ed., **2006**.
- (2) Roduner, E., *Chem. Soc. Rev.* **2006**, 35 (7), 583–592.
- (3) McFarland, A. D., Haynes, C. L., Mirkin, C. A., Van Duyne, R. P., Godwin, H. A., *J. Chem. Ed.* **2004**, 81 (4), 544A.
- (4) Chomoucka, J., Drbohlavova, J., Masarik, M., Ryvolova, M., Huska, D., Prasek, J., Horna, A., Trnkova, L., Provaznik, I., Adam, V., Hubalek, J., Kizek, R., *Int. J. Nanotechnol.* **2012**, 9 (8-9), 746–783.
- (5) Bandyopadhyay, A. K., *Nano Materials*; New Age International: **2008**.
- (6) *Growth Market Nanotechnology - An Analysis of Technology and Innovation*; Norbert Malanowski Thomas Heimer, W. L., Werner, M., Eds.; WILEY-VCH: **2006**.
- (7) Mappes, T., Jahr, N., Csaki, A., Vogler, N., Popp, J., Fritzsche, W., *Angew. Chem., Int. Ed.* **2012**, 51 (45), 11208–11212.
- (8) Ramsden, J., *Essentials of Nanotechnology*; Ventus Publishing: **2009**.
- (9) Balazs, A. C., Emrick, T., Russell, T. P., *Science* **2006**, 314 (5802), 1107–1110.
- (10) Paul, D., Robeson, L., *Polymer* **2008**, 49 (15), 3187–3204.
- (11) Perrier, T., Saulnier, P., Benoit, J.-P., *Chem.—Eur. J.* **2010**, 16 (38), 11516–11529.
- (12) *Multifunctional Polymer Nanocomposites*; Leng, J., Lau, A. K. T., Eds.; CRC Press: Boca Raton, Florida, **2011**.
- (13) Bansal, A., Yang, H., Li, C., Cho, K., Benicewicz, B. C., Kumar, S. K., Schadler, L. S., *Nat. Mater.* **2005**, 4 (9), 693–698.
- (14) Stenzel, M. H., *Macromol. Rapid Commun.* **2009**, 30 (19), 1603–1624.
- (15) Ghosh Chaudhuri, R., Paria, S., *Chem. Rev.* **2012**, 112 (4), 2373–2433.
- (16) *Nanocomposites and Polymers with Analytical Methods*; Cuppoletti, J., Ed.; InTech: Rijeka, Croatia, **2011**.
- (17) Ash, B. J., Rogers, D. F., Wiegand, C. J., Schadler, L. S., Siegel, R. W., Benicewicz, B. C., Apple, T., *Polym. Compos.* **2002**, 23 (6), 1014–1025.
- (18) Kickelbick, G., *Prog. Polym. Sci.* **2003**, 28 (1), 83–114.
- (19) Ash, B. J., Siegel, R. W., Schadler, L. S., *Macromolecules* **2004**, 37 (4), 1358–1369.
- (20) Moniruzzaman, M., Winey, K. I., *Macromolecules* **2006**, 39 (16), 5194–5205.
- (21) Natte, K., Österle, W., Friedrich, J. F., von Klitzing, R., Orts-Gil, G., *Macromol. Chem. Phys.* **2012**, 213 (22), 2412–2419.
- (22) Boyer, C., Stenzel, M. H., Davis, T. P., *J. Polym. Sci., Part A: Polym. Chem.* **2011**, 49 (3), 551–595.
- (23) Kumar, S. K., Jouault, N., Benicewicz, B., Neely, T., *Macromolecules* **2013**, 46 (9), 3199–3214.
- (24) Zhao, Y., Perrier, S., *Macromolecules* **2006**, 39 (25), 8603–8608.
- (25) Peng, Q., Lai, D. M. Y., Kang, E. T., Neoh, K. G., *Macromolecules* **2006**, 39 (16), 5577–5582.

- (26) Duwez, A.-S., Guillet, P., Colard, C., Gohy, J.-F., Fustin, C.-A., *Macromolecules* **2006**, 39 (8), 2729–2731.
- (27) Ebeling, B., Vana, P., *Polymers* **2011**, 3 (2), 719–739.
- (28) Lu, Y., Mei, Y., Ballauff, M., Drechsler, M., *J. Phys. Chem. B* **2006**, 110 (9), 3930–3937.
- (29) Caseri, W., *J. Mater. Chem.* **2010**, 20 (27), 5582–5592.
- (30) Uehara, N., *Anal. Sci.* **2010**, 26 (12), 1219–1228.
- (31) Choi, I., Choi, Y., *IEEE J. Quantum Electron.* **2012**, 18 (3), 1110–1121.
- (32) Staudinger, H., Muntwyler, O., Kupfer, O., *Helv. Chim. Acta* **1922**, 5 (5), 756–767.
- (33) Tsitsilianis, C., *Macromolecular Engineering: Precise Synthesis, Materials Properties, Applications*, 1st ed.; Matyjaszewski, K., Gnanou, Y., Leibler, L., Eds.; Wiley-VCH: **2007**; Vol. 2 Elements of Macromolecular Structural Control.
- (34) Lechner, M. D., Gehrke, K., Nordmeier, E. H., *Makromolekulare Chemie*, 3rd edition; Birkhäuser Verlag: Basel, **2003**.
- (35) *Handbook of Radical Polymerization*; Matyjaszewski, K., Davis, T. P., Eds.; Wiley-Interscience: Hoboken, New Jersey, **2002**.
- (36) Vana, P., Davis, T. P., Barner-Kowollik, C., *Macromol. Rapid Commun.* **2002**, 23 (16), 952–956.
- (37) Buback, M., *Makromol. Chem.* **1990**, 191 (7), 1575–1587.
- (38) Webster, O. W., *Science* **1991**, 251 (4996), 887–893.
- (39) Szwarc, M., Levy, M., Milkovich, R., *J. Am. Chem. Soc.* **1956**, 78 (11), 2656–2657.
- (40) Szwarc, M., *Nature* **1956**, 178 (4543), 1168–1169.
- (41) Matsushita, Y., Mogi, Y., Mukai, H., Watanabe, J., Noda, I., *Polymer* **1994**, 35 (2), 246–249.
- (42) Kennedy, J., *J. Polym. Sci., Part A: Polym. Chem.* **1999**, 37 (14), 2285–2293.
- (43) Grubbs, R., Tumas, W., *Science* **1989**, 243 (4893), 907–915.
- (44) Schrock, R. R., *Acc. Chem. Res.* **2002**, 23 (5), 158–165.
- (45) Webster, O. W., Hertler, W. R., Sogah, D. Y., Farnham, W. B., RajanBabu, T. V., *J. Am. Chem. Soc.* **1983**, 105 (17), 5706–5708.
- (46) Otsu, T., Yoshida, M., *Macromol. Rapid Commun.* **1982**, 3 (2), 127–132.
- (47) Otsu, T., Yoshida, M., Tazaki, T., *Macromol. Rapid Commun.* **1982**, 3 (2), 133–140.
- (48) Nicolaÿ, R., Kwak, Y., Matyjaszewski, K., *Macromolecules* **2008**, 41 (13), 4585–4596.
- (49) *Controlled and Living Polymerizations—Methods and Materials*; Müller, A. H., Matyjaszewski, K., Eds.; Weinheim; Wiley-VCH: **2009**.
- (50) Jenkins, A. D., Jones, R. G., Moad, G., *Pure Appl. Chem.* **2010**, 82 (2), 483–491.
- (51) Shipp, D. A., *Polym. Rev.* **2011**, 51 (2), 99–103.
- (52) Kato, M., Kamigaito, M., Sawamoto, M., Higashimura, T., *Macromolecules* **1995**, 28 (5), 1721–1723.
- (53) Wang, J.-S., Matyjaszewski, K., *J. Am. Chem. Soc.* **1995**, 117 (20), 5614–5615.
- (54) Matyjaszewski, K., Patten, T. E., Xia, J., *J. Am. Chem. Soc.* **1997**, 119 (4), 674–680.

- (55) Matyjaszewski, K., Xia, J., *Chem. Rev.* **2001**, 101 (9), 2921–2990.
- (56) *Macromolecular Engineering: Precise Synthesis, Materials Properties, Applications*; Matyjaszewski, K., Gnanou, Y., Leibler, L., Eds.; Wiley-VCH: Weinheim, **2007**; Vol. 1.
- (57) Moad, G., Rizzardo, E., Solomon, D. H., *Macromolecules* **1982**, 15 (3), 909–914.
- (58) Hawker, C. J., Bosman, A. W., Harth, E., *Chem. Rev.* **2001**, 101 (12), 3661–3688.
- (59) Grubbs, R. B., *Polym. Rev.* **2011**, 51 (2), 104–137.
- (60) Nicolas, J., Guillauneuf, Y., Lefay, C., Bertin, D., Gignes, D., Charleux, B., *Prog. Polym. Sci.* **2012**, 38 (1), 63–235.
- (61) Moad, G., Rizzardo, E., Thang, S. H., *Aust. J. Chem.* **2005**, 58 (6), 379–410.
- (62) Moad, G., Rizzardo, E., Thang, S. H., *Aust. J. Chem.* **2006**, 59 (10), 669–692.
- (63) Moad, G., Rizzardo, E., Thang, S. H., *Aust. J. Chem.* **2009**, 62 (11), 1402–1472.
- (64) Moad, G., Rizzardo, E., Thang, S. H., *Aust. J. Chem.* **2012**, 65 (8), 985–1076.
- (65) Yamago, S., Iida, K., Yoshida, J.-i., *J. Am. Chem. Soc.* **2002**, 124 (12), 2874–2875.
- (66) Yamago, S., *J. Polym. Sci., Part A: Polym. Chem.* **2006**, 44 (1), 1–12.
- (67) Kumar, S., Changez, M., Murthy, C. N., Yamago, S., Lee, J.-S., *Macromol. Rapid Commun.* **2011**, 32 (19), 1576–1582.
- (68) Chiefari, J., Chong, Y. K., Ercole, F., Krstina, J., Jeffery, J., Le, T. P. T., Mayadunne, R. T. A., Meijs, G. F., Moad, C. L., Moad, G., Rizzardo, E., Thang, S. H., *Macromolecules* **1998**, 31 (16), 5559–5562.
- (69) Chong, Y. K., Le, T. P. T., Moad, G., Rizzardo, E., Thang, S. H., *Macromolecules* **1999**, 32 (6), 2071–2074.
- (70) Moad, G., Thang, S. H., *Aust. J. Chem.* **2009**, 62 (11), 1379–1381.
- (71) Charmot, D., Corpart, P., Adam, H., Zard, S. Z., Biadatti, T., Bouhadir, G., *Macromol. Symp.* **2000**, 150 (1), 23–32.
- (72) Taton, D., Wilczewska, A. Z., Destarac, M., *Macromol. Rapid Commun.* **2001**, 22 (18), 1497–1503.
- (73) McCormick, C. L., Lowe, A. B., *Acc. Chem. Res.* **2004**, 37 (5), 312–325.
- (74) O'Donnell, J. M., *Chem. Soc. Rev.* **2012**, 41 (8), 3061–3076.
- (75) Arita, T., Beuermann, S., Buback, M., Vana, P., *Macromol. React. Eng.* **2005**, 290 (4), 283–293.
- (76) Arita, T., Buback, M., Vana, P., *Macromolecules* **2005**, 38 (19), 7935–7943.
- (77) Quinn, J. F., Davis, T. P., Barner, L., Barner-Kowollik, C., *Polymer* **2007**, 48 (22), 6467–6480.
- (78) Arita, T., Buback, M., Janssen, O., Vana, P., *Macromol. Rapid Commun.* **2004**, 25 (15), 1376–1381.
- (79) Mori, H., Matsuyama, M., Sutoh, K., Endo, T., *Macromolecules* **2006**, 39 (13), 4351–4360.
- (80) ten Cate, M. G. J., Rettig, H., Bernhardt, K., Borner, H. G., *Macromolecules* **2005**, 38 (26), 10643–10649.
- (81) Perrier, S., Takolpuckdee, P., *J. Polym. Sci., Part A: Polym. Chem.* **2005**, 43 (22), 5347–5393.
- (82) Nguyen, D. H., Wood, M. R., Zhao, Y., Perrier, S., Vana, P., *Macromolecules* **2008**, 41 (19), 7071–7078.

- (83) Barner-Kowollik, C., Perrier, S., *J. Polym. Sci., Part A: Polym. Chem.* **2008**, *46* (17), 5715–5723.
- (84) Moad, G., Mayadunne, R. T. A., Rizzardo, E., Skidmore, M., Thang, S. H., *Macromol. Symp.* **2003**, *192* (1), 1–12.
- (85) Alam, M. Z., Shibahara, A., Ogata, T., Kurihara, S., *Polymer* **2011**, *52* (17), 3696–3703.
- (86) Boschmann, D., Mänz, M., Pöppler, A.-C., Sörensen, N., Vana, P., *J. Polym. Sci., Part A: Polym. Chem.* **2008**, *46* (21), 7280–7286.
- (87) Moad, G., Chen, M., Haussler, M., Postma, A., Rizzardo, E., Thang, S. H., *Polym. Chem.* **2011**, *2* (3), 492–519.
- (88) Benaglia, M., Chieffari, J., Chong, Y. K., Moad, G., Rizzardo, E., Thang, S. H., *J. Am. Chem. Soc.* **2009**, *131* (20), 6914–6915.
- (89) Chong, Y. K., Krstina, J., Le, T. P. T., Moad, G., Postma, A., Rizzardo, E., Thang, S. H., *Macromolecules* **2003**, *36* (7), 2256–2272.
- (90) Moad, G., Rizzardo, E., Thang, S. H., *Polym. Int.* **2011**, *60* (1), 9–25.
- (91) Thang, S. H., Chong, (Y. K., Mayadunne, R. T. A., Moad, G., Rizzardo, E., *Tetrahedron Lett.* **1999**, *40* (12), 2435–2438.
- (92) Schilli, C., Lanzendorfer, M. G., Muller, A. H. E., *Macromolecules* **2002**, *35* (18), 6819–6827.
- (93) Barner-Kowollik, C., Davis, T. P., Heuts, J. P. A., Stenzel, M. H., Vana, P., Whittaker, M., *J. Polym. Sci., Part A: Polym. Chem.* **2003**, *41* (3), 365–375.
- (94) You, Y., Hong, C., Bai, R., Pan, C., Wang, J., *Macromol. Chem. Phys.* **2002**, *203* (3), 477–483.
- (95) Ran, R., Yu, Y., Wan, T., *J. Appl. Polym. Sci.* **2007**, *105* (2), 398–404.
- (96) Perrier, S., Barner-Kowollik, C., Quinn, J. F., Vana, P., Davis, T. P., *Macromolecules* **2002**, *35* (22), 8300–8306.
- (97) Chieffari, J., Mayadunne, R. T. A., Moad, C. L., Moad, G., Rizzardo, E., Postma, A., Thang, S. H., *Macromolecules* **2003**, *36* (7), 2273–2283.
- (98) Buback, M., Meiser, W., Vana, P., *Aust. J. Chem.* **2009**, *62* (11), 1484–1487.
- (99) Vana, P., *Macromol. Symp.* **2007**, *248* (1), 71–81.
- (100) Perrier, S., Takolpuckdee, P., Mars, C. A., *Macromolecules* **2005**, *38* (6), 2033–2036.
- (101) Moad, G., Chong, Y., Postma, A., Rizzardo, E., Thang, S. H., *Polymer* **2005**, *46* (19), 8458–8468.
- (102) Davis, K. A., Matyjaszewski, K., *Statistical, Gradient, Block, and Graft Copolymers by Controlled/Living Radical Polymerizations*; Advances in Polymer Science, Vol. 159; Springer: Berlin/Heidelberg, **2002**.
- (103) De Brouwer, H., Schellekens, M. A. J., Klumperman, B., Monteiro, M. J., German, A. L., *J. Polym. Sci., Part A: Polym. Chem.* **2000**, *38* (19), 3596–3603.
- (104) Krasia, T., Soula, R., Borner, H. G., Schlaad, H., *Chem. Commun.* **2003**, *4*, 538–539.
- (105) Convertine, A. J., Sumerlin, B. S., Thomas, D. B., Lowe, A. B., McCormick, C. L., *Macromolecules* **2003**, *36* (13), 4679–4681.
- (106) Keddie, D. J., *Chem. Soc. Rev.* **2014**, *43* (2), 496–505.
- (107) Konkolewicz, D., Hawket, B. S., Gray-Weale, A., Perrier, S., *Macromolecules* **2008**, *41* (17), 6400–6412.

- (108) Konkolewicz, D., Siau, M., Gray-Weale, A., Hawket, B. S., Perrier, S., *J. Phys. Chem. B* **2009**, *113* (20), 7086–7094.
- (109) Gaillard, N., Guyot, A., Claverie, J., *J. Polym. Sci., Part A: Polym. Chem.* **2003**, *41* (5), 684–698.
- (110) Mayadunne, R. T. A., Rizzardo, E., Chiefari, J., Krstina, J., Moad, G., Postma, A., Thang, S. H., *Macromolecules* **2000**, *33* (2), 243–245.
- (111) Motokuchio, S., Sudo, A., Sanda, F., Endo, T., *Chem. Commun.* **2002**, *17*, 1946–1947.
- (112) Lai, J. T., Filla, D., Shea, R., *Macromolecules* **2002**, *35* (18), 6754–6756.
- (113) Frank, R. L., Drake, S., Smith, P., Stevens, C., *J. Polym. Sci.* **1948**, *3* (1), 50–57.
- (114) Godt, H. C., Wann, R. E., *J. Org. Chem.* **1961**, *26* (10), 4047–4051.
- (115) Braun, D., Kiessel, M., *Monatsh. Chem.* **1965**, *96* (2), 631–641.
- (116) Soga, K., Sato, M., Imamura, H., Ikeda, S., *J. Polym. Sci., Part C: Polym. Lett.* **1975**, *13* (3), 167–171.
- (117) Husemann, A., *Liebigs Ann. Chem.* **1862**, *123* (1), 64–83.
- (118) Husemann, A., *Liebigs Ann. Chem.* **1863**, *126* (3), 269–298.
- (119) Aoyagi, N., Ochiai, B., Mori, H., Endo, T., *Synlett* **2006**, *4*, 636–638.
- (120) Aoyagi, N., Endo, T., *J. Polym. Sci., Part A: Polym. Chem.* **2009**, *47* (14), 3702–3709.
- (121) Chaturvedi, D., Mishra, N., Chaturvedi, A. K., Mishra, V., *Monatsh. Chem.* **2008**, *139* (12), 1467–1470.
- (122) Movassagh, B., Soleiman-Beigi, M., Nazari, M., *M. Chem. Lett.* **2008**, *37* (1), 22–23.
- (123) Movassagh, B., Soleiman-Beigi, M., *Monatsh. Chem.* **2008**, *139* (8), 927–930.
- (124) Lee, A. W. M., Chan, W. H., Wong, H. C., *Synth. Commun.* **1988**, *18* (13), 1531–1536.
- (125) Leung, L. M., Chan, W. H., Leung, S. K., *J. Polym. Sci., Part A: Polym. Chem.* **1993**, *31* (7), 1799–1806.
- (126) Leung, M., Hsieh, D. T., Lee, K. H., Liou, J. C., *J. Chem. Res., Synop.* **1995**, *11*, 478–479.
- (127) Wertheim, E., *J. Am. Chem. Soc.* **1926**, *48* (3), 826–830.
- (128) Sun, S. F., *Physical Chemistry of Macromolecules*, 2. edition; Wiley-Interscience: **2004**; Chapter 3: Distribution of Molecular Weight, pp 52–66.
- (129) Lathe, G. H., Ruthven, C. R., *Biochem. J.* **1956**, *62* (4), 665–674.
- (130) Determann, H., *Angew. Chem., Int. Ed.* **1964**, *3* (9), 608–617.
- (131) Moore, J. C., *J. Polym. Sci., Part A: Polym. Chem.* **1964**, *2* (2), 835–843.
- (132) Johnson, J., *Polym. Rev.* **1966**, *1* (2), 393–434.
- (133) Tung, L. H., *Sep. Sci. Technol.* **1970**, *5* (3), 339–347.
- (134) Scholte, T. G., Meijerink, N. L. J., Schoffeleers, H. M., Brands, A. M. G., *J. Appl. Polym. Sci.* **1984**, *29* (12), 3763–3782.
- (135) Hutchinson, R. A., Aronson, M. T., Richards, J. R., *Macromolecules* **1993**, *26* (24), 6410–6415.
- (136) Ito, S., *Kobunshi Ronbunshu* **1989**, *46* (7), 437–443.
- (137) Ohya, S., Nakayama, Y., Matsuda, T., *Biomacromolecules* **2001**, *2* (3), 856–863.

- (138) Liang, D., Song, L., Zhou, S., Zaitsev, V. S., Chu, B., *Electrophoresis* **1999**, 20 (14), 2856–2863.
- (139) Kikuchi, A., Okano, T., *Prog. Polym. Sci.* **2002**, 27 (6), 1165–1193.
- (140) Siow, K. S., Delmas, G., Patterson, D., *Macromolecules* **1972**, 5 (1), 29–34.
- (141) Walker, J. S., Vause, C. A., *Sci. Am.* **1987**, 256 (5), 98–195.
- (142) Patterson, D., *Macromolecules* **1969**, 2 (6), 672–677.
- (143) Heskins, M., Guillet, J. E., *J. Macromol. Sci. Chem.* **1968**, 2 (8), 1441–1455.
- (144) Tiktopulo, E. I., Uversky, V. N., Lushchik, V. B., Klenin, S. I., Bychkova, V. E., Ptitsyn, O. B., *Macromolecules* **1995**, 28 (22), 7519–7524.
- (145) Cheng, H., Shen, L., Wu, C., *Macromolecules* **2006**, 39 (6), 2325–2329.
- (146) Deshmukh, S. A., Sankaranarayanan, S. K. R. S., Suthar, K., Mancini, D. C., *J. Phys. Chem. B* **2012**, 116 (9), 2651–2663.
- (147) Okada, Y., Tanaka, F., *Macromolecules* **2005**, 38 (10), 4465–4471.
- (148) Cho, E. C., Lee, J., Cho, K., *Macromolecules* **2003**, 36 (26), 9929–9934.
- (149) Schild, H., *Prog. Polym. Sci.* **1992**, 17 (2), 163–249.
- (150) Boutris, C., Chatzi, E., Kiparissides, C., *Polymer* **1997**, 38 (10), 2567–2570.
- (151) Zhang, G., Wu, C., *J. Am Chem. Soc.* **2001**, 123 (7), 1376–1380.
- (152) Ye, X., Lu, Y., Shen, L., Ding, Y., Liu, S., Zhang, G., Wu, C., *Macromolecules* **2007**, 40 (14), 4750–4752.
- (153) Kujawa, P., Winnik, F. M., *Macromolecules* **2001**, 34 (12), 4130–4135.
- (154) Shibayama, M., Mizutani, S.-y., Nomura, S., *Macromolecules* **1996**, 29 (6), 2019–2024.
- (155) Kogure, H., Nanami, S., Masuda, Y., Toyama, Y., Kubota, K., *English Colloid Polym. Sci.* **2005**, 283 (11), 1163–1171.
- (156) Ono, Y., Shikata, T., *J. Am. Chem. Soc.* **2006**, 128 (31), 10030–10031.
- (157) Gomez de Azevedo, R., Rebelo, L. P. N., Ramos, A. M., Szydlowski, J., Sousa, H. C. de, Klein, J., *Fluid Phase Equilib.* **2001**, 185 (1-2), 189–198.
- (158) *Smart Polymers – Applications in Biotechnology and Biomedicine*, 2nd edition; Galaev, I., Mattiasson, B., Eds.; CRC Press: **2008**.
- (159) Hoffman, A. S., Stayton, P. S., Bulmus, V., Chen, G., Chen, J., Cheung, C., Chilkoti, A., Ding, Z., Dong, L., Fong, R., Lackey, C. A., Long, C. J., Miura, M., Morris, J. E., Murthy, N., Nabeshima, Y., Park, T. G., Press, O. W., Shimoboji, T., Shoemaker, S., Yang, H. J., Monji, N., Nowinski, R. C., Cole, C. A., Priest, J. H., Harris, J. M., Nakamae, K., Nishino, T., Miyata, T., *J. Biomed. Mater. Res.* **2000**, 52 (4), 577–586.
- (160) Cabane, E., Zhang, X., Langowska, K., Palivan, C. G., Meier, W., *English Biointerphases* **2012**, 7 (1–4), 1–27.
- (161) Hoffman, A. S., *Adv. Drug Delivery Rev.* **2013**, 65 (1), 10–16.
- (162) Qiu, Y., Park, K., *Adv. Drug Delivery Rev.* **2001**, 53 (3), 321–339.
- (163) Kubota, K., Fujishige, S., Ando, I., *J. Phys. Chem.* **1990**, 94 (12), 5154–5158.
- (164) Kubota, K., Hamano, K., Kuwahara, N., Fujishige, S., Ando, I., *Polymer J.* **1990**, 22 (12), 1051–1057.

- (165) Jeong, B., Gutowska, A., *Trends Biotechnol.* **2002**, 20 (7), 305–311.
- (166) Kumar, A., Srivastava, A., Galaev, I. Y., Mattiasson, B., *Prog. Polym. Sci.* **2007**, 32 (10), 1205–1237.
- (167) Webster, M., Miao, J., Lynch, B., Green, D., Jones-Sawyer, R., Linhardt, R. J., Mendenhall, J., *Macromol. Mater. Eng.* **2013**, 298 (4), 447–453.
- (168) Liu, L., Wu, C., Zhang, J., Zhang, M., Liu, Y., Wang, X., Fu, G., *J. Polym. Sci., Part A: Polym. Chem.* **2008**, 46 (10), 3294–3305.
- (169) Li, Z., Serelis, A. K., Reed, W. F., Alb, A. M., *Polymer* **2010**, 51 (21), 4726–4734.
- (170) Freitag, R., Garret-Flaudy, F., *Langmuir* **2002**, 18 (9), 3434–3440.
- (171) Hofmann, C., Schönhoff, M., *Colloid Polym. Sci.* **2009**, 287 (12), 1369–1376.
- (172) Du, H., Wickramasinghe, R., Qian, X., *J. Phys. Chem. B* **2010**, 114 (49), 16594–16604.
- (173) Patel, T., Ghosh, G., Yusa, S.-i., Bahadur, P., *J. Dispersion Sci. Technol.* **2011**, 32 (8), 1111–1118.
- (174) Zhang, Y., Furry, S., Sagle, L. B., Cho, Y., Bergbreiter, D. E., Cremer, P. S., *J. Phys. Chem. C* **2007**, 111 (25), 8916–8924.
- (175) Hofmeister, F., *German Arch. Exp. Pathol. Pharmacol.* **1888**, 25 (1), 1–30.
- (176) Kunz, W., Henle, J., Ninham, B., *Curr. Opin. Colloid Interface Sci.* **2004**, 9 (1–2), 19–37.
- (177) He, C., Kim, S. W., Lee, D. S., *J. Controlled Release* **2008**, 127 (3), 189–207.
- (178) Pelton, R., Chibante, P., *Colloids Surf.* **1986**, 20 (3), 247–256.
- (179) Asano, M., Winnik, F. M., Yamashita, T., Horie, K., *Macromolecules* **1995**, 28 (17), 5861–5866.
- (180) Hirotsu, S., *J. Chem. Phys.* **1988**, 88 (1), 427–431.
- (181) Chung, J., Yokoyama, M., Yamato, M., Aoyagi, T., Sakurai, Y., Okano, T., *J. Controlled Release* **1999**, 62 (1–2), 115–127.
- (182) Soppimath, K., Aminabhavi, T., Dave, A., Kumbar, S., Rudzinski, W., *Drug Dev. Ind. Pharm.* **2002**, 28 (8), 957–974.
- (183) Gil, E. S., Hudson, S. M., *Prog. Polym. Sci.* **2004**, 29 (12), 1173–1222.
- (184) Scott, R. L., *J. Chem. Phys.* **1949**, 17 (3), 268–279.
- (185) Wolf, B. A., Blaum, G., *J. Polym. Sci., Polym. Phys. Ed.* **1975**, 13 (6), 1115–1132.
- (186) Wolf, B. A., Molinari, R. J., *Makromol. Chem.* **1973**, 173 (1), 241–245.
- (187) Cowie, J. M. G., McEwen, I. J., *J. Chem. Soc., Faraday Trans. I* **1974**, 70, 171–177.
- (188) McNaught, A. D., Wilkinson, A., *Compendium of Chemical Terminology: IUPAC Recommendations: Gold Book (IUPAC Chemical Nomenclature Series)*, 2nd edition; IUPAC International Union of Pure and Applied Chem: **1997**.
- (189) Wolf, B. A., Willms, M. M., *Makromol. Chem.* **1978**, 179 (9), 2265–2277.
- (190) Winnik, F. M., Ringsdorf, H., Venzmer, J., *Macromolecules* **1990**, 23 (8), 2415–2416.
- (191) Amiya, T., Hirokawa, Y., Hirose, Y., Li, Y., Tanaka, T., *J. Chem. Phys.* **1987**, 86 (4), 2375–2379.
- (192) Katayama, S., Hirokawa, Y., Tanaka, T., *Macromolecules* **1984**, 17 (12), 2641–2643.
- (193) Schild, H. G., Tirrell, D. A., *J. Phys. Chem.* **1990**, 94 (10), 4352–4356.
- (194) Schild, H. G., Muthukumar, M., Tirrell, D. A., *Macromolecules* **1991**, 24 (4), 948–952.

- (195) Winnik, F. M., Ottaviani, M. F., Bossmann, S. H., Garcia-Garibay, M., Turro, N. J., *Macromolecules* **1992**, 25 (22), 6007–6017.
- (196) López-León, T., Bastos-González, D., Ortega-Vinuesa, J. L., Elaïssari, A., *ChemPhysChem* **2010**, 11 (1), 188–194.
- (197) Tanaka, F., Koga, T., Kojima, H., Xue, N., Winnik, F. M., *Macromolecules* **2011**, 44 (8), 2978–2989.
- (198) Arndt, M. C., Sadowski, G., *Macromolecules* **2012**, 45 (16), 6686–6696.
- (199) Heppner, I. N., Islam, M. R., Serpe, M. J., *Macromol. Rapid Commun.* **2013**, 34 (21), 1708–1713.
- (200) Mukherji, D., Kremer, K., *Macromolecules* **2013**, 46 (22), 9158–9163.
- (201) Crowther, H. M., Vincent, B., *English Colloid Polym. Sci.* **1998**, 276 (1), 46–51.
- (202) Yamauchi, H., Maeda, Y., *J. Phys. Chem. B* **2007**, 111 (45), 12964–12968.
- (203) Zhu, P. W., Napper, D. H., *Chem. Phys. Lett.* **1996**, 256 (1–2), 51–56.
- (204) Dalkas, G., Pagonis, K., Bokias, G., *Polymer* **2006**, 47 (1), 243–248.
- (205) Winnik, F. M., Ottaviani, M. F., Bossmann, S. H., Pan, W., Garcia-Garibay, M., Turro, N. J., *Macromolecules* **1993**, 26 (17), 4577–4585.
- (206) Costa, R. O., Freitas, R. F., *Polymer* **2002**, 43 (22), 5879–5885.
- (207) Richtering, W., Pich, A., *Soft Matter* **2012**, 8 (45), 11423–11430.
- (208) Shankar, R., Klossner, R. R., Weaver, J. T., Koga, T., Zanten, J. H. van, Krause, W. E., Colina, C. M., Tanaka, F., Spontak, R. J., *Soft Matter* **2009**, 5 (2), 304–307.
- (209) Hofmann, C. H., Plamper, F. A., Scherzinger, C., Hietala, S., Richtering, W., *Macromolecules* **2013**, 46 (2), 523–532.
- (210) Kojima, H., Tanaka, F., Scherzinger, C., Richtering, W., *J. Polym. Sci., Part B: Polym. Phys.* **2013**, 51 (14), 1100–1111.
- (211) Walter, J., Sehr, J., Vrabec, J., Hasse, H., *J. Phys. Chem. B* **2012**, 116 (17), 5251–5259.
- (212) Tanaka, F., Koga, T., Winnik, F. M., *Phys. Rev. Lett.* **2008**, 101 (2), 028302.
- (213) Tanaka, F., Koga, T., Kojima, H., Winnik, F. M., *Macromolecules* **2009**, 42 (4), 1321–1330.
- (214) Dixit, S., Crain, J., Poon, W. C. K., Finney, J. L., Soper, A. K., *Nature* **2002**, 416 (6883), 829–832.
- (215) Yang, C., Li, W., Wu, C., *J. Phys. Chem. B* **2004**, 108 (31), 11866–11870.
- (216) Liu, G., Zhang, G., *Langmuir* **2005**, 21 (5), 2086–2090.
- (217) Mashimo, S., Miura, N., *J. Chem. Phys.* **1993**, 99 (12), 9874–9881.
- (218) Liu, M., Bian, F., Sheng, F., *Eur. Polym. J.* **2005**, 41 (2), 283–291.
- (219) Zhang, G., Wu, C., *Phys. Rev. Lett.* **2001**, 86 (5), 822–825.
- (220) Kyriakos, K., Philipp, M., Adelsberger, J., Jaksch, S., Berezkin, A. V., Lugo, D. M., Richtering, W., Grillo, I., Miasnikova, A., Laschewsky, A., Müller-Buschbaum, P., Papadakis, C. M., *Macromolecules* **2014**, 47 (19), 6867–6879.
- (221) Hao, J., Cheng, H., Butler, P., Zhang, L., Han, C. C., *J. Chem. Phys.* **2010**, 132 (15), 154902.
- (222) Wang, H., An, Y., Huang, N., Ma, R., Shi, L., *J. Colloid Interface Sci.* **2008**, 317 (2), 637–642.
- (223) Maeda, Y., Nakamura, T., Ikeda, I., *Macromolecules* **2001**, 34 (23), 8246–8251.

- (224) Matsuda, Y., Kobayashi, M., Annaka, M., Ishihara, K., Takahara, A., *Polym. J.* **2008**, *40* (5), 479–483.
- (225) Edmondson, S., Nguyen, N. T., Lewis, A. L., Armes, S. P., *Langmuir* **2010**, *26* (10), 7216–7226.
- (226) Young, T.-H., Chuang, W.-Y., *J. Membrane Sci.* **2002**, *210* (2), 349–359.
- (227) Takahashi, N., Kanaya, T., Nishida, K., Kaji, K., *Polymer* **2003**, *44* (15), 4075–4078.
- (228) Scherzinger, C., Lindner, P., Keerl, M., Richtering, W., *Macromolecules* **2010**, *43* (16), 6829–6833.
- (229) Pagonis, K., Bokias, G., *Polymer* **2004**, *45* (7), 2149–2153.
- (230) Maeda, Y., Yamamoto, H., Ikeda, I., *Langmuir* **2004**, *20* (17), 7339–7341.
- (231) Bergé, B., Koningsveld, R., Berghmans, H., *Macromolecules* **2004**, *37* (21), 8082–8090.
- (232) Guettari, M., Gomati, R., Gharbi, A., *J. Macromol. Sci. Part B Phys.* **2010**, *49* (3), 552–562.
- (233) Roth, P. J., Collin, M., Boyer, C., *Soft Matter* **2013**, *9* (6), 1825–1834.
- (234) Young, T.-H., Tao, C.-T., Lai, P.-S., *Polymer* **2003**, *44* (5), 1689–1695.
- (235) Fernández-Pirola, I., Horta, A., *English Polym. Bull.* **1980**, *3* (5), 273–278.
- (236) Nandi, A., Sen, U., Bhattacharyya, S., Mandal, B., *Eur. Polym. J.* **1983**, *19* (4), 283–286.
- (237) Sellers, K., Mackay, C., Bergeson, L. L., Clough, S. R., Hoyt, M., Chen, J., Henry, K., Hamblen, J., *Nanotechnology and the Environment*; CRC Press: Boca Raton, **2009**.
- (238) Khlebtsov, N., Dykman, L., *Chem. Soc. Rev.* **2011**, *40* (3), 1647–1671.
- (239) Sharifi, S., Behzadi, S., Laurent, S., Laird Forrest, M., Stroeve, P., Mahmoudi, M., *Chem. Soc. Rev.* **2012**, *41* (6), 2323–2343.
- (240) Elsaesser, A., Howard, C. V., *Adv. Drug Delivery Rev.* **2012**, *64* (2), 129–137.
- (241) Labouta, H. I., Schneider, M., *Nanomed. Nanotechnol. Biol. Med.* **2013**, *9* (1), 39–54.
- (242) Reibold, M., Paufler, P., Levin, A. A., Kochmann, W., Patzke, N., Meyer, D. C., *Nature* **2006**, *444* (7117), 286–286.
- (243) Yu, H.-D., Regulacio, M. D., Ye, E., Han, M.-Y., *Chem. Soc. Rev.* **2013**, *42* (14), 6006–6018.
- (244) Collier, C. P., Wong, E. W., Belohradský, M., Raymo, F. M., Stoddart, J. F., Kuekes, P. J., Williams, R. S., Heath, J. R., *Science* **1999**, *285* (5426), 391–394.
- (245) Lohse, S. E., Murphy, C. J., *Chem. Mater.* **2013**, *25* (8), 1250–1261.
- (246) Gagner, J. E., Qian, X., Lopez, M. M., Dordick, J. S., Siegel, R. W., *Biomaterials* **2012**, *33*, 8503–8516.
- (247) Zeng, J., Ma, Y., Jeong, U., Xia, Y., *J. Mater. Chem.* **2010**, *20* (12), 2290–2301.
- (248) Shin, H.-S., Hong, J.-Y., Huh, S., *ACS Appl. Mater. Interfaces* **2013**, *5* (4), 1429–1435.
- (249) Daniel, M.-C., Astruc, D., *Chem. Rev.* **2004**, *104* (1), 293–346.
- (250) Zhou, J., Ralston, J., Sedev, R., Beattie, D. A., *J. Colloid Interface Sci.* **2009**, *331* (2), 251–262.
- (251) Sardar, R., Funston, A. M., Mulvaney, P., Murray, R. W., *Langmuir* **2009**, *25* (24), 13840–13851.
- (252) Jin, R., *Nanoscale* **2010**, *2* (3), 343–362.
- (253) Jin, R., Zhu, Y., Qian, H., *Chem.—Eur. J.* **2011**, *17* (24), 6584–6593.

- (254) Faraday, M., *Philos. Trans. R. Soc. London* **1857**, 147, 145–181.
- (255) Thompson, D., *Gold Bull.* **2007**, 40 (4), 267–269.
- (256) Steed, J. W., Atwood, J. L., *Supramolecular Chemistry*, 2nd edition; Wiley: **2009**.
- (257) Chen, X., Zhu, H.-Y., Zhao, J.-C., Zheng, Z.-F., Gao, X.-P., *Angew. Chem. Int. Ed.* **2008**, 47 (29), 5353–5356.
- (258) Jadzinsky, P. D., Calero, G., Ackerson, C. J., Bushnell, D. A., Kornberg, R. D., *Science* **2007**, 318 (5849), 430–433.
- (259) Zhu, M., Aikens, C. M., Hollander, F. J., Schatz, G. C., Jin, R., *J. Am. Chem. Soc.* **2008**, 130 (18), 5883–5885.
- (260) Yarzhevsky, V., Battocchio, C., *Russ. J. Inorg. Chem.* **2011**, 56 (14), 2147–2159.
- (261) Pensa, E., Cortés, E., Corthey, G., Carro, P., Vericat, C., Fonticelli, M. H., Benítez, G., Rubert, A. A., Salvarezza, R. C., *Acc. Chem. Res.* **2012**, 45 (8), 1183–1192.
- (262) Shah, R. R., Merceyeyes, D., Husemann, M., Rees, I., Abbott, N. L., Hawker, C. J., Hedrick, J. L., *Macromolecules* **2000**, 33 (2), 597–605.
- (263) Bain, C. D., Troughton, E. B., Tao, Y. T., Evall, J., Whitesides, G. M., Nuzzo, R. G., *J. Am. Chem. Soc.* **1989**, 111 (1), 321–335.
- (264) Schlenoff, J. B., Li, M., Ly, H., *J. Am. Chem. Soc.* **1995**, 117 (50), 12528–12536.
- (265) Alivisatos, A. P., *Science* **1996**, 271 (5251), 933–937.
- (266) Wu, Z., Suhan, J., Jin, R., *J. Mater. Chem.* **2009**, 19 (5), 622–626.
- (267) Garcia, M. A., *J. Phys. D: Appl. Phys.* **2011**, 44 (28), 283001.
- (268) Garcia, M. A., *J. Phys. D: Appl. Phys.* **2012**, 45 (38), 389501.
- (269) Sharma, V., Park, K., Srinivasarao, M., *Mater. Sci. Eng., R* **2009**, 65 (1–3), 1–38.
- (270) Chen, H., Shao, L., Li, Q., Wang, J., *Chem. Soc. Rev.* **2013**, 42 (7), 2679–2724.
- (271) Liu, X., Atwater, M., Wang, J., Huo, Q., *Colloids Surf., B* **2007**, 58 (1), 3–7.
- (272) Ringe, E., Langille, M. R., Sohn, K., Zhang, J., Huang, J., Mirkin, C. A., Van Duyne, R. P., Marks, L. D., *J. Phys. Chem. Lett.* **2012**, 3 (11), 1479–1483.
- (273) Link, S., El-Sayed, M. A., *J. Phys. Chem. B* **1999**, 103 (21), 4212–4217.
- (274) Mulvaney, P., *Langmuir* **1996**, 12 (3), 788–800.
- (275) Ghosh, S. K., Pal, T., *Chem. Rev.* **2007**, 107 (11), 4797–4862.
- (276) Quinten, M., Kreibig, U., *Surf. Sci.* **1986**, 172 (3), 557–577.
- (277) Halas, N. J., *Nano Lett.* **2010**, 10 (10), 3816–3822.
- (278) Collier, C. P., Saykally, R. J., Shiang, J. J., Henrichs, S. E., Heath, J. R., *Science* **1997**, 277 (5334), 1978–1981.
- (279) Barrow, S. J., Funston, A. M., Gómez, D. E., Davis, T. J., Mulvaney, P., *Nano Lett.* **2011**, 11 (10), 4180–4187.
- (280) Zeng, S., Yong, K.-T., Roy, I., Dinh, X.-Q., Yu, X., Luan, F., *Plasmonics* **2011**, 6 (3), 491–506.
- (281) Upadhyayula, V. K., *Anal. Chim. Acta* **2012**, 715, 1–18.

- (282) Doria, G., Conde, J., Veigas, B., Giestas, L., Almeida, C., Assunção, M., Rosa, J., Baptista, P. V., *Sensors* **2012**, *12* (2), 1657–1687.
- (283) Yeh, Y.-C., Creran, B., Rotello, V. M., *Nanoscale* **2012**, *4* (6), 1871–1880.
- (284) Lu, F., Doane, T. L., Zhu, J.-J., Burda, C., *Inorg. Chim. Acta* **2012**, *393*, 142–153.
- (285) Dreaden, E. C., Alkilany, A. M., Huang, X., Murphy, C. J., El-Sayed, M. A., *Chem. Soc. Rev.* **2012**, *41* (7), 2740–2779.
- (286) Dykman, L., Khlebtsov, N., *Chem. Soc. Rev.* **2012**, *41* (6), 2256–2282.
- (287) Kumar, A., Boruah, B. M., Liang, X.-J., *J. Nanomater.* **2011**, 202187.
- (288) Dreaden, E. C., Mackey, M. A., Huang, X., Kang, B., El-Sayed, M. A., *Chem. Soc. Rev.* **2011**, *40* (7), 3391–3404.
- (289) Baffou, G., Quidant, R., *Laser Photonics Rev.* **2013**, *7* (2), 171–187.
- (290) Pissuwan, D., Niidome, T., Cortie, M. B., *J. Controlled Release* **2011**, *149* (1), 65–71.
- (291) Faulk, W. P., Taylor, G. M., *Immunochemistry* **1971**, *8* (11), 1081–1083.
- (292) Lee, N., Choi, S. H., Hyeon, T., *Adv. Mater.* **2013**, *25* (19), 2641–2660.
- (293) Chapman, R. G., Ostuni, E., Takayama, S., Holmlin, R. E., Yan, L., Whitesides, G. M., *J. Am. Chem. Soc.* **2000**, *122* (34), 8303–8304.
- (294) Gibson, J. D., Khanal, B. P., Zubarev, E. R., *J. Am. Chem. Soc.* **2007**, *129* (37), 11653–11661.
- (295) Christensen, C. H., Nørskov, J. K., *Science* **2010**, *327* (5963), 278–279.
- (296) Della Pina, C., Falletta, E., *Catal. Sci. Technol.* **2011**, *1* (9), 1564–1571.
- (297) Zhou, X., Liu, G., Yu, J., Fan, W., *J. Mater. Chem.* **2012**, *22* (40), 21337–21354.
- (298) Gucci, L., Beck, A., Pászti, Z., *Catal. Today* **2012**, *181* (1), 26–32.
- (299) Friend, C. M., Hashmi, A. S. K., *Acc. Chem. Res.* **2014**, *47* (3), 729–730.
- (300) Lim, D.-K., Jeon, K.-S., Kim, H. M., Nam, J.-M., Suh, Y. D., *Nat. Mater.* **2010**, *9* (1), 60–67.
- (301) Yajima, T., Yu, Y., Futamata, M., *Phys. Chem. Chem. Phys.* **2011**, *13* (27), 12454–12462.
- (302) Johnston, J., Lucas, K., *Gold Bull.* **2011**, *44* (2), 85–89.
- (303) Kwon, T., Kim, T., Ali, F. b., Kang, D. J., Yoo, M., Bang, J., Lee, W., Kim, B. J., *Macromolecules* **2011**, *44* (24), 9852–9862.
- (304) Sabella, S., Brunetti, V., Vecchio, G., Galeone, A., Maiorano, G., Cingolani, R., Pompa, P., *J. Nanopart. Res.* **2011**, *13* (12), 6821–6835.
- (305) Sung, J. H., Ji, J. H., Park, J. D., Song, M. Y., Song, K. S., Ryu, H. R., Yoon, J. U., Jeon, K. S., Jeong, J., Han, B. S., Chung, Y. H., Chang, H. K., Lee, J. H., Kim, D. W., Kelman, B. J., Yu, I. J., *Part. Fibre Toxicol.* **2011**, *8*.
- (306) Milner, S. T., *Science* **1991**, *251* (4996), 905–914.
- (307) Barbey, R., Lavanant, L., Paripovic, D., Schüwer, N., Sugnaux, C., Tugulu, S., Klok, H.-A., *Chem. Rev.* **2009**, *109* (11), 5437–5527.
- (308) Bünsow, J., Kelby, T. S., Huck, W. T. S., *Acc. Chem. Res.* **2009**, *43* (3), 466–474.
- (309) Ebeling, B., Ehlers, F., Vana, P., *Nachr. Chem.* **2014**, *62*, 24–28.

- (310) Kaholek, M., Lee, W.-K., Ahn, S.-J., Ma, H., Caster, K. C., LaMattina, B., Zauscher, S., *Chem. Mater.* **2004**, *16* (19), 3688–3696.
- (311) Husemann, M., Morrison, M., Benoit, D., Frommer, J., Mate, C. M., Hinsberg, W. D., Hedrick, J. L., Hawker, C. J., *J. Am. Chem. Soc.* **2000**, *122* (8), 1844–1845.
- (312) Li, L., Chen, S., Zheng, J., Ratner, B. D., Jiang, S., *J. Phys. Chem. B* **2005**, *109* (7), 2934–2941.
- (313) Ma, H., Li, D., Sheng, X., Zhao, B., Chilkoti, A., *Langmuir* **2006**, *22* (8), 3751–3756.
- (314) Ramstedt, M., Cheng, N., Azzaroni, O., Mossialos, D., Mathieu, H. J., Huck, W. T. S., *Langmuir* **2007**, *23* (6), 3314–3321.
- (315) Bauer, F., Ernst, H., Decker, U., Findeisen, M., Gläsel, H.-J., Langguth, H., Hartmann, E., Mehnert, R., Peuker, C., *Macromol. Chem. Phys.* **2000**, *201* (18), 2654–2659.
- (316) Edmondson, S., Osborne, V., Huck, W., *Chem. Soc. Rev.* **2004**, *33* (1), 14–22.
- (317) Zhou, F., Zheng, Z., Yu, B., Liu, W., Huck, W. T. S., *J. Am. Chem. Soc.* **2006**, *128* (50), 16253–16258.
- (318) Zhou, F., Huck, W. T. S., *Phys. Chem. Chem. Phys.* **2006**, *8* (33), 3815–3823.
- (319) Costa, A. C., Composto, R. J., Vlček, P., *Macromolecules* **2003**, *36* (9), 3254–3260.
- (320) Raviv, U., Giasson, S., Kampf, N., Gohy, J.-F., Jerome, R., Klein, J., *Nature* **2003**, *425* (6954), 163–165.
- (321) Ma, H., Hyun, J., Stiller, P., Chilkoti, A., *Adv. Mater.* **2004**, *16* (4), 338–341.
- (322) Huang, Y., Liu, Q., Zhou, X., Perrier, S., Zhao, Y., *Macromolecules* **2009**, *42* (15), 5509–5517.
- (323) Bamford, C. H., Jenkins, A. D., Johnston, R., *Trans. Faraday Soc.* **1959**, *55* (1), 179–184.
- (324) Zajac, R., Chakrabarti, A., *Phys. Rev. E* **1995**, *52* (6), 6536–6549.
- (325) Sobani, M., Haddadi-Asl, V., Salami-Kalajahi, M., Roghani-Mamaqani, H., Mirshafiei-Langari, S.-A., Khezri, K., *English J. Sol-Gel Sci. Technol.* **2013**, *66* (2), 337–344.
- (326) Sarsabili, M., Parvini, M., Salami-Kalajahi, M., Ganjeh-Anzabi, P., *Adv. Polym. Technol.* **2013**, *32* (4), 21372.
- (327) Grande, C., Tria, M., Felipe, M., Zuluaga, F., Advincula, R., *English Eur. Phys. J. E* **2011**, *34* (2), 1–10.
- (328) Prucker, O., Ruhe, J., *Macromolecules* **1998**, *31* (3), 592–601.
- (329) Prucker, O., Ruhe, J., *Macromolecules* **1998**, *31* (3), 602–613.
- (330) Werne, T. von, Patten, T. E., *J. Am. Chem. Soc.* **1999**, *121* (32), 7409–7410.
- (331) Matyjaszewski, K., Miller, P. J., Shukla, N., Immaraporn, B., Gelman, A., Luokala, B. B., Siclován, T. M., Kickelbick, G., Vallant, T., Hoffmann, H., Pakula, T., *Macromolecules* **1999**, *32* (26), 8716–8724.
- (332) Yamago, S., Yahata, Y., Nakanishi, K., Konishi, S., Kayahara, E., Nomura, A., Goto, A., Tsujii, Y., *Macromolecules* **2013**, *46* (17), 6777–6785.
- (333) Boven, G., Oosterling, M. L., Challa, G., Schouten, A. J., *Polymer* **1990**, *31* (12), 2377–2383.
- (334) Kickelbick, G., Schubert, U., *English Monatsh. Chem.* **2001**, *132* (1), 13–30.
- (335) Zou, H., Wu, S., Shen, J., *Chem. Rev.* **2008**, *108* (9), 3893–3957.

- (336) Fustin, C.-A., Duwez, A.-S., *J. Electron Spectrosc. Relat. Phenom.* **2009**, 172 (1-3, Sp. Iss. SI), 104–106.
- (337) Baum, M., Brittain, W. J., *Macromolecules* **2002**, 35 (3), 610–615.
- (338) Yoshikawa, C., Goto, A., Tsujii, Y., Fukuda, T., Yamamoto, K., Kishida, A., *Macromolecules* **2005**, 38 (11), 4604–4610.
- (339) Titirici, M.-M., Sellergren, B., *Chem. Mater.* **2006**, 18 (7), 1773–1779.
- (340) Perrier, S., Takolpuckdee, P., Mars, C. A., *Macromolecules* **2005**, 38 (16), 6770–6774.
- (341) Nguyen, D. H., Vana, P., *Polym. Adv. Technol.* **2006**, 17 (9–10), 625–633.
- (342) Skaff, H., Emrick, T., *Angew. Chem., Int. Ed.* **2004**, 43 (40), 5383–5386.
- (343) Li, C., Han, J., Ryu, C. Y., Benicewicz, B. C., *Macromolecules* **2006**, 39 (9), 3175–3183.
- (344) Yang, Q., Wang, L., Xiang, W., Zhou, J., Tan, Q. hua, *Polymer* **2007**, 48 (12), 3444–3451.
- (345) Rowe-Konopacki, M. D., Boyes, S. G., *Macromolecules* **2007**, 40 (4), 879–888.
- (346) Rowe, M. D., Hammer, B. A. G., Boyes, S. G., *Macromolecules* **2008**, 41 (12), 4147–4157.
- (347) Nguyen, D. H. *RAFT-Polymerisation an Oberflächen*, Ph.D. thesis, Georg-August-Universität Göttingen, **2007**.
- (348) Azzaroni, O., *J. Polym. Sci., Part A: Polym. Chem.* **2012**, 50 (16), 3225–3258.
- (349) Rotzoll, R. *Oberflächegebundene Polymerschlaufen durch kontrollierte radikalische RAFT-Polymerisation*, thesis, Georg-August-Universität Göttingen, **2007**.
- (350) Rotzoll, R., Vana, P., *J. Polym. Sci., Part A: Polym. Chem.* **2008**, 46 (23), 7656–7666.
- (351) Rotzoll, R., Vana, P., *Aust. J. Chem.* **2009**, 62 (11), 1473–1478.
- (352) Husseman, M., Malmstrom, E. E., McNamara, M., Mate, M., Mecerreyes, D., Benoit, D. G., Hedrick, J. L., Mansky, P., Huang, E., Russell, T. P., Hawker, C. J., *Macromolecules* **1999**, 32 (5), 1424–1431.

Part II

Experimental

In this part, all experiments are described in a detailed way that allows for their reproduction. It is divided into the instrumental Chapter 2 and the Chapter 3 “Substances”, where mainly the experimental protocols and spectroscopic and polymerization data are given. Readers who are mainly interested in the results and the discussion can safely jump directly to Part III and only refer to the following two chapters as a reference for experimental details.

Chapter 2

Instrumentation

2.1 Centrifugation

For centrifugation, either a SIGMA 2-16KC or a SIGMA 2-16PK centrifuge was used. Both instruments were equipped with a SIGMA 12151 angle rotor for 6 tubes and could be cooled to specified temperatures. Centrifugation was performed at the indicated temperatures in 50 mL or 15 mL polypropylene centrifuge tubes. The rotation frequency was 9 000 revolutions per minute corresponding to an accelerating force of 8 603 *g*.

2.2 Chromatography

2.2.1 Column chromatography

Column chromatography was performed using silica gel 60 (70–230 mesh, 60 Å, ALDRICH or MERCK).

2.2.2 Size-exclusion chromatography (SEC)

All samples were filtered through a 25 mm VWR syringe filter containing a 0.45 µm porous polytetrafluoroethylene membrane prior to injection.

2.2.2.1 SEC with dimethylacetamide

SEC characterization with *N,N*-dimethylacetamide (DMAc) containing 0.1 % (by mass) of lithium bromide as the eluent was performed using an AGILENT 1260 INFINITY system. It was composed of an autosampler, an isocratic solvent pump, a PSS GRAM (polyester copolymer network) precolumn (8 × 50 mm), three PSS GRAM separation columns (8 × 300 mm, nominal particle size = 10 µm; pore sizes =

30 Å, 10^3 Å, and 10^3 Å) maintained at 45 °C in a column compartment, an 80 Hz UV detector (set to a wavelength of 310 nm for the RAFT polymers and to 520 nm for the polymer-functionalized AuNPs), and a refractive index (RI) detector. The flow rate of the mobile phase was 8×10^{-4} L min⁻¹. The whole setup was calibrated with a total of 12 PSS poly(methyl methacrylate) standards ($M_p = 0.8$ –1820 kg mol⁻¹) of low dispersity with toluene as the internal standard. The concentration of the polymer samples was 4.5 g L⁻¹ and the gold concentration of the polymer-functionalized AuNPs was approximately 1 g L⁻¹ (based on the attenuation at 520 nm).

2.2.2.2 SEC with tetrahydrofuran

SEC characterizations with THF as eluent were performed using another AGILENT 1260 INFINITY system. This one consisted of an autosampler, an isocratic HPLC pump, a PSS SDV (styrene–divinylbenzene copolymer–network) precolumn (8 × 50 mm), three PSS SDV separation columns (8 × 300 mm, particle size = 10 µm, pore sizes = 10^6 Å, 10^5 Å, and 10^3 Å), maintained at 35 °C in a column compartment, an 80 Hz UV detector (set to a wavelength of 310 nm) and an RI detector. The flow rate of the mobile phase was 1 mL min⁻¹. The SEC setup was calibrated with low-dispersity PSS standards ($M_p = 0.5$ –2520 kg mol⁻¹) with toluene as the internal standard. Molar masses of poly(*n*-butyl acrylate) (pBA) were determined according to the principle of universal calibration using the Mark–Houwink parameters for the linear polymer ($K = 1.22 \times 10^{-4}$ dL g⁻¹, $a = 0.700$).^[1] The concentration of the samples was 3 g L⁻¹.

The chromatograms for the determination of the degree of polymerization of the multifunctional RAFT agents $\rho^{\text{MB}}\text{-7}$, $\rho^{\text{MB}}\text{-8}$, and $\rho^{\text{MB}}\text{-9}$ were measured in THF with a different setup, which has been reported before.^[2,3]

2.2.3 Thin-layer chromatography

Precoated silica plates of the type MERCK “KIESELGEL F₂₅₄” were used for thin-layer chromatography. Staining was accomplished with basic potassium permanganate, ethanolic ninhydrin (2,2-dihydroxyindane-1,3-dione), or methanol/acetic acid/vanilline staining solutions.

2.3 Cloud-point measurements

2.3.1 Cloud-point determination at atmospheric pressure

The cloud points of the aqueous pNIPAm solutions at atmospheric pressure were determined by optical absorption spectroscopy. The measurements were carried out with a CARY 300 SCAN spectrophotometer against ultrapure water under constant rapid stirring using HELMA quartz cuvettes with a path length of 10 mm. The temperature in the cuvette was measured and logged on the connected computer via a thermocouple dipping into the solution. The temperature could be raised by an integrated heating. In the case of the measurement starting at a temperature below room temperature, the solution was cooled to approximately 10 °C below this respective temperature with an ice-filled plastic bag before starting the experiment. The occurring turbidity causes an increased extinction over the whole range of wavelengths. For the actual measurements, only the wavelength of $\lambda = 400 \text{ nm}$ was monitored, thus obtaining a higher time-resolution (12 min^{-1}) and signal-to-noise ratio. The cloud points were determined by heating the solutions from a temperature significantly lower than the cloud temperature to a temperature clearly above with a rate of approximately $2 \text{ }^{\circ}\text{C min}^{-1}$. A solution was considered turbid once the attenuation had reached 10 % of its maximum value. Another program was used to log the temperature values as a function of the time. The time values were then converted to temperature values using this log file and performing linear regression between the logged time points. The whole measurement took approximately 45 min.

2.3.2 Cloud-point determination at high pressures

2.3.2.1 The cloud-point determination setup

The cloud points at increased pressures were determined with a special discontinuously operated high-pressure apparatus. The heart of the experimental set-up is an optical high-pressure cell with variable internal volume, manufactured in the institute's workshop. Figure 2.1 shows a crosscut through this autoclave cell. The hollow-cylindrical cell body (1) of 171 mm length and of 22 mm inner and 80 mm outer diameter is made from stainless steel containing nickel (ARBED-SAARSTAHL). With the given cell dimensions, this material allows for the operation of the cell up to pressures of 3 000 bar at 300 °C. It is sealed conically from both sides with steel plugs (3, 9) through flanges (2) with six bolts (7) on either side. The opening angles of the cones are 78°, while the opening angles of the plugs are 75°, so that the plugs are tightening against the inner edges of the cell body. The steel which had been

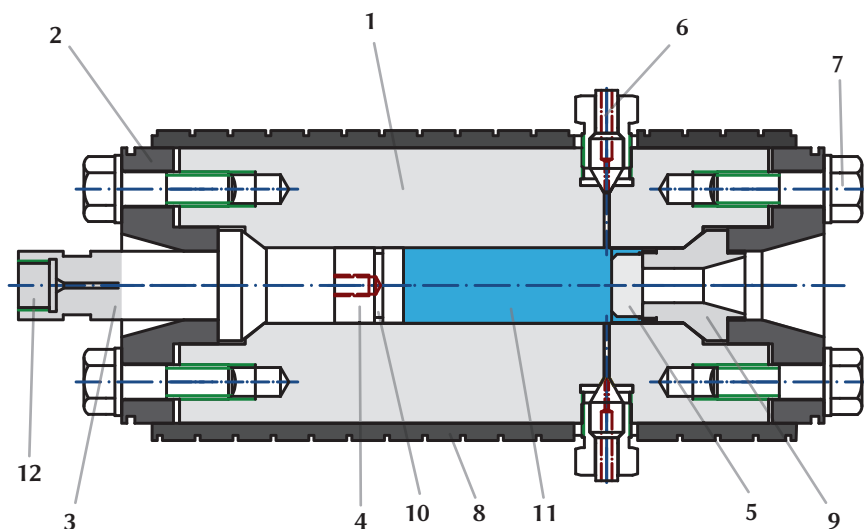


Fig. 2.1: Technical sketch of the high-pressure cell for cloud-point determinations. 1) Stainless-steel cell body, 2) flange, 3) steel plug, 4) movable piston, 5) sapphire window, 6) sheathed thermocouple, 7) bolts, 8) temperature-control shell, 9) steel plug, 10) O-ring, 11) internal volume, 12) connecting bore to the pressurizing system. (Reprinted and adapted with permission from a previous publication.^[4] Copyright 2014 American Chemical Society.)

used for the production of the plugs is softer than the material of the cell body so that abrasion will predominantly occur at the easier replaceable parts. A transparent window made of a synthetic sapphire monocrystal (5, 18 mm outer diameter, 10 mm length, UV grade, RODITI, UNION CARBIDE), optically polished on both sides to reduce reflection and scattering on its surface, is fitted into one of the plugs (9), allowing to monitor the inside of the cell optically using a borescope camera (21.2 mm aperture, OPTIKON) with a halogen light source (TECHNO 150, OPTIKON). This part of the cell is sealed by a 12 μm thick polytetrafluoroethylene foil between the plug and the window—a type of sealing which gets tighter with increasing pressure.^[5] The camera's image is permanently displayed on a screen with an overlay from the computer (added with a VIDEONICS MX-1 video mixer) showing the associated pressure (measured with a strain gauge as pressure transducer within ± 6 bar, HBM-MESSTECHNIK, calibrated against a precision manometer, WIKA as reference) and temperature values inside the cell and in the shell, measured within ± 0.3 °C via a sheathed thermocouple (6, chromel–alumel, CIA S250, CGE ALSTHOM) which sits in the investigated solution, in real time and recorded using a hard-disc recorder

that allows for burning of the movies to DVD for more detailed analyses after the experiments. For measurements at very high temperatures, the borescope camera can be cooled with compressed air, which is also connected to the HPLC pump. The other plug (3) is connected (12) to a high-pressure capillary (1.6 mm inner and 6.4 mm outer diameter, AUTOCLAVE ENGINEERS) which leads to the pressure-generating part of the set-up. Here, the pressurizing fluid *n*-heptane can be pressed into the cell via a syringe pump (12 cm³), this way regulating the pressure inside the cell. A movable metal piston (4, 20.1 mm length and 21.9 mm diameter) separates the inside of the cell in the sample volume (11) and the volume for the pressurizing medium. The flat piston surface which faces the sapphire window is polished to assist the observation of the sample solution. A polytetrafluoroethylene O-ring (10) is used as piston seal and discarded after each measurement. For the temperature control, the cell is covered with a hollow brass shell (8) which is connected to a cryostatic temperature regulator. For the constant agitation of the sample solution, a polytetrafluoroethylene-coated magnetic stirring bar (NEOLAB) inside the sample volume is driven through the non-magnetic cell wall by four magnetic coils positioned outside around the non-magnetic cell with an adjustable frequency. With the computer, the temperature and pressure data can be processed, recorded, and visualized as overlay on the connected screen during the measurements.

A general schematic presentation of the whole set-up is shown in Figure 6.1.

2.3.2.2 Experimental procedure

An amount of 50 mL (or more) of the pNIPAm sample solution was prepared using ultrapure water. This solution and the stirring bar were placed into the cell and it was sealed with the plug tightening the six bolts of the flange with a torque of 30 N m, the piston being equipped with an unused polytetrafluoroethylene O-ring. The cell was encased with the temperature control shell, placed in the apparatus, and the high-pressure capillary for the pressurizing fluid *n*-heptane, the thermocouples and the borescope camera were connected. Each run was started at the lowest desired temperature at a starting pressure of around 1700 bar to be sure that the solution would not freeze. Once the respective temperature was reached, the pressure was increased until a clouding could be observed. A turbid solution appears completely dark through the borescope camera (see Figure 6.2). As cloud pressure, the point was chosen, where the homogeneous mixture turns opaque and the screw on the flat piston surface and the magnetic stirring bar could no longer be seen.^[6] Then, the pressure was decreased until the solution was fully transparent again. At the next, approximately 2 °C higher temperature the measurement was repeated until the highest temperature of interest had been reached. In regions where the cloud

curves exhibited an especially high slope, the intervals were reduced to 1 °C. If not enough *n*-heptane was remaining in the syringe pump (and the part behind), it could be refilled with the HPLC pump. During all measurements, the solution was stirred magnetically with 300 revolutions per minute. When re-opening the cell, it was impossible to prevent *n*-heptane from getting into contact with water so that the solution had to be disposed of and could not be used again.

2.4 Determination of pH values

All pH measurements were performed with a METTLER TOLEDO SEVENMULTI pH meter with a glass electrode. It was calibrated before each measurement if it had not been calibrated earlier at the day of measurement using three buffer solutions.

2.5 Electrospray-ionization mass spectrometry (ESI-MS)

ESI-MS measurements were performed with a BRUKER DALTONIK MICROTOF ESI–time of flight–mass-spectrometer at a spray voltage of 4.5 kV and a capillary temperature of 180 °C. All given values in this work were obtained in positive mode.

2.6 Elemental analysis

Elemental analysis of the carbon, hydrogen, nitrogen, and sulfur content of the sample was performed using an ELEMENTAR “VARIO EL” combustion analyzer in the analytic laboratory of the University’s Institute for Inorganic Chemistry.

2.7 Microscopy

2.7.1 Atomic force microscopy (AFM)

Atomic force microscopy (AFM) here was carried out in an argon-filled glove box (oxygen content below 1 ppm) on a BRUKER MULTIMODE 8 microscope in peak force tapping mode. The instrument was equipped with a silicon nitride cantilever ($k = 0.4 \text{ N m}^{-1}$, $\nu_0 = 50 - 90 \text{ kHz}$). Samples were spin-coated (approximately 1200 revolutions per minute) from solution in methanol on PLANO glass discs with a LAURELL WS-650-23NPP spin coater (gold concentration based on optical

attenuation approximately $2 \times 10^{-2} \text{ g L}^{-1}$). The glass disks had been cleaned for 30 min (100 W) in a ZEPTO plasma cleaner by DIENER ELECTRONIC. The AFM measurements were directed using the software NANOSCOPE 8.15 on a connected computer. Further processing of the data is described in Section 4.2.

2.7.2 Transmission electron microscopy

2.7.2.1 The instrument

All transmission electron microscopy (TEM) measurements were performed with a PHILIPS CM 12 (scanning) transmission electron microscope operating at an acceleration voltage of 120 kV and an emission current of 3–4 μA . The focused electron spot on the sample had a diameter of 1 μm . A 50 μm aperture was used in the condenser lens and—unless stated otherwise—all scattered electrons were blocked with a 20 μm aperture in the focal plane of the objective lens. The instrument was equipped with a goniometer specimen stage, an OXFORD INSTRUMENTS X-MAX 80 mm^2 *energy-dispersive X-ray spectroscopy (EDX)* detector, and an Olympus 1376×1032 pixel charge-coupled device (CCD) camera.

2.7.2.2 Sample preparation

All samples were applied on PLANO 200 mesh copper TEM grids with a diameter of 3.05 mm holding an amorphous carbon film with a thickness of 10–15 nm by drop-casting. The TEM grids were placed on a laboratory paper tissue and one drop of a very diluted (concentration typically 0.1 g L^{-1}) sample solution was placed onto them with a glass pipet. The TEM grid was immediately covered with a plastic cup until all solvent had evaporated. The solvent for the sample preparation was methanol, if not indicated otherwise.

2.7.2.3 Execution of measurements

The TEM grid was then locked into the microscope on a single-tilt specimen holder. Prior to the recording of a micrograph, the following steps were performed: alignment of the illumination system (gun tilt, condenser aperture), finding eucentric sample height, rotation center correction, astigmatism correction, (optionally) insertion of additional apertures, finding a good spot and setting focus and exposure. No further modification of the obtained micrographs other than tonal value correction and cropping was performed.

2.7.3 Scanning electron microscopy (SEM)

Scanning electron microscopy was performed on a LEO SUPRA 35, operating with a voltage of 3 kV, at the Institute of Materials Physics. The samples were glued on specimen holders and coated with a gold film (approximately 8 nm) by sputter coating prior to the measurements.

2.8 Spectroscopy

2.8.1 Nuclear magnetic resonance (NMR) spectroscopy

^1H -NMR, ^{13}C -NMR, and ^{29}Si -NMR spectra were measured at room temperature with tetramethylsilane as external and the residual solvent protons as internal standard using a BRUKER AMX-300, a VARIAN MERCURY 300, or a VARIAN UNITY 300 spectroscope. The concentration of the substances was approximately 50 g L^{-1} . Chemical shifts are given in parts per million (ppm) on the tetramethylsilane scale.

2.8.2 UV/vis spectroscopy

The UV/vis absorption/attenuation spectra of solutions were acquired with a CARY 300 SCAN spectrophotometer against the pure solvent, using HELMA quartz cuvettes with a thickness of 10 mm or, when the solutions were too intensely colored, with a thickness of 1 mm. The spectra were recorded in the wavelength range between 300 nm and 900 nm in steps of 0.5 nm with a scan rate of 60 nm min^{-1} . The instrument was equipped with a stirring and heating function with one thermocouple dipping into the examined solution. Unless stated otherwise, the measurements were performed at 21°C .

2.9 Thermogravimetric analysis

Thermogravimetric analysis was carried out with a NETZSCH "STA 409 PC" apparatus in the analytic laboratory of the University's Institute for Inorganic Chemistry. The samples were heated from 30°C to 800°C with a rate of $10^\circ\text{C min}^{-1}$ under nitrogen (30 mL min^{-1}).

2.10 Ultrasonication

Ultrasonication was performed using a water-filled ELMA S30H ultrasonic bath operating at a frequency of 37 kHz and an effective power of 80 W (320 W peak power) at room temperature.

2.11 Water purification

Deionized water was obtained from the institute's water deionization system (ion exchange columns). Additional purification to type 1 water was performed using a MILLIPORE SIMPLICITY UV water purification system. In this instrument, deionized water is pumped with a flow rate of 0.5 L min^{-1} through a UV chamber, where organic molecules in water are ionized by the UV radiation. All ions are then removed in a ion exchange cartridge. Finally, particles and bacteria with a size greater than 50 nm are removed by a cellulose filter. The total organic carbon (TOC) concentration of the output water is below $5 \mu\text{g L}^{-1}$, the number of micro-organism is below 0.1 CFU mL^{-1} (colony forming units). It was constantly checked that the water had a resistivity of $\rho > 18.2 \text{ M}\Omega \text{ cm}$ (at 25°C). This treatment of the water was performed immediately before use.

2.12 Further equipment

Masses were determined with a SARTORIUS ANALYTIC AC 210 S scale. For degassing of the polymerization solutions, an EDWARDS EXC 120 or a PFEIFFER TMH 071 turbo molecular pump was used. The glovebox was a MBRAUN LABMASTER 120 with an oxygen content below 4 ppm. The vacuum drying was carried out in a THERMO ELECTRON "THERMO SCIENTIFIC" drying cabinet connected to a rotary vane pump. The heating block was a KLEINFELD MBT 250-2 or a ROTH ROTILABO® H250.

References for Chapter 2

- (1) Beuermann, S., Paquet, D. A., McMin, J. H., Hutchinson, R. A., *Macromolecules* **1996**, 29 (12), 4206–4215.
- (2) Ebeling, B. *Multiblock-Copolymere durch RAFT-Polymerisation*, thesis, Georg-August-Universität Göttingen, **2009**.
- (3) Ebeling, B., Vana, P., *Polymers* **2011**, 3 (2), 719–739.
- (4) Ebeling, B., Eggers, S., Hendrich, M., Nitschke, A., Vana, P., *Macromolecules* **2014**, 47 (4), 1462–1469.
- (5) Poulter, T. C., *Phys. Rev.* **1932**, 40 (5), 860–871.
- (6) Hasch, B. M., Meilchen, M. A., Lee, S.-H., McHugh, M. A., *J. Polym. Sci., Part B: Polym. Phys.* **1992**, 30 (12), 1365–1373.

Chapter 3

Substances

3.1 Commercially acquired substances

Acetic acid ($\geq 99.7\%$, ALDRICH), acetone (99.98 %, FISHER SCIENTIFIC), AMBER-LITE IRA-67 (free base, FLUKA), ammonium molybdate tetrahydrate ($\geq 99.0\%$, FLUKA), benzyl mercaptan (99 %, ALDRICH), 11-bromo-1-undecanol ($\geq 99.0\%$, FLUKA), 1-butanol ($\geq 98.0\%$, FLUKA), carbon disulfide ($\geq 99.9\%$, ALDRICH), ((chloromethyl)phenylethyl)trimethoxysilane (mixed *meta* and *para* isomers, purity not specified, ABCR), 3-chloropropyldimethylmethoxysilane (95 %, ABCR), di-*n*-decyldisulfide $S_2\lambda-10$ ($> 90\%$, ABCR), 1,4-diacetylbenzene (99 %, ALDRICH), 1,11-dibromoundecane ($\geq 98\%$, ALDRICH), 2,3-dichloro-5,6-dicyano-1,4-benzoquinone (DDQ, 98 %, ALDRICH), 1,3-dicyclohexylcarbodiimide (99 %, ALDRICH), 4-(dimethylamino)pyridine (99 %, ALDRICH), dithiothreitol (DTT, Cleland's reagent, no purity specified, ABCR), 1-dodecanethiol $^{SH}\lambda-2$ ($\geq 98\%$, ALDRICH), ethanol ($\geq 99.8\%$, ACROS ORGANICS, water-free, denatured with 1 % 2-butanone and 0.0001 % denatonium benzoate), gold(III) bromide ($> 99.99\%$, ABCR), hydrochloric acid ($\geq 37\%$, ALDRICH), hydrofluoric acid ($\geq 48\%$, ALDRICH), hydrogen tetrachloroaurate(III) trihydrate ($> 99.9\%$, ALDRICH or $> 99.99\%$, ABCR, must not get in contact with a metal spatula), lithium bromide ($\geq 99\%$, ALDRICH), maleic acid anhydride ($> 99.9\%$, FLUKA), 3-mercapto-1-propanol (95 %, ALDRICH), 11-mercaptopundecanol $^{SH}\lambda^{OH}-7$ (97 %, ALDRICH), 2-mercaptoethanol ($\geq 99.0\%$, ALDRICH), 6-mercaptohexanol $^{SH}\lambda^{OH}-6$ (97 %, ALDRICH), 4-mercaptophenol $^{SH}\lambda^{OH}-4$ (97 %, ALDRICH), (11-mercaptopundecyl)tetra(ethylene glycol) $^{SH}\lambda^{OH}-8$ (95 %, ALDRICH), methane sulfonyl chloride ($\geq 99.7\%$, ALDRICH), methanol ($\geq 99.9\%$, FISHER CHEMICAL), ninhydrine ($\geq 95.0\%$, ALDRICH), *N,N*-dimethylacetamide (DMAc, $\geq 99.9\%$, ALDRICH), *N,N*-dimethylformamide (DMF, $\geq 99.8\%$, ACROS ORGANICS, extra dry over molecular sieves), *n*-butylamine ($\geq 98\%$, FLUKA), *n*-heptane ($\geq 99.0\%$, MERCK-SCHUCHARDT), octadecylamine $^{NH_2}\lambda-11$ ($\geq 99.0\%$, ALDRICH), oleylamine $^{NH_2}\lambda-12$ (technical grade, 70.0 %, ALDRICH or technical grade 80–90 %, ALDRICH).

ACROS ORGANICS), 1-pentanol ($\geq 99.0\%$, ALDRICH), 2-phenylethanethiol $^{SH}\lambda-1$ ($\geq 99\%$, ALDRICH), potassium carbonate ($\geq 99.0\%$, ALDRICH), potassium permanganate ($\geq 99.0\%$, ALDRICH), potassium thioacetate (98%, ABCR), 1-propanethiol ($\geq 98.5\%$, FLUKA), 1-propanol ($\geq 99.0\%$, MERCK), 2-propanol ($\geq 99.8\%$, ROTH), propargyl alcohol (99%, FLUKA), sodium azide ($\geq 99\%$, ROTH), sodium borohydride ($\geq 96\%$, ALDRICH), sodium chloride ($\geq 99\%$, ALDRICH), sodium citrate tribasic dihydrate ($\geq 99.0\%$, ALDRICH), sodium hydrogencarbonate ($\geq 95\%$, ALDRICH), sodium hydroxide ($\geq 98.0\%$, ALDRICH), sodium iodide ($\geq 99\%$, ALDRICH), sodium methoxide ($\geq 97\%$, FLUKA), sodium methoxide solution (25% in methanol, ALDRICH), sodium sulfate ($> 99.7\%$, ALDRICH), sulfur ($\geq 99.5\%$, ALDRICH), *tert*-tetradecanethiol $^{SH}\lambda-3$ (mixture of isomers, no purity specified, ABCR), tetra-*n*-octylammonium bromide $^{N^+}\lambda-13$ (98%, ABCR), thionyl chloride ($\geq 99\%$, ALDRICH), triethylamine ($\geq 99\%$, ALDRICH), and tris(2-carboxyethyl)-phosphine hydrochloride (TCEP, 98.0%, ABCR) were obtained from the respective suppliers and used as received. The chemical structures of the substances with a sample identifier can be found in 8.5. Dry solvents were obtained by standard drying methods.^[1] Deuterated solvents (chloroform-*d*, acetone-*d*₆, DMSO-*d*₆, DMF-*d*₇) for NMR spectroscopy were provided by the NMR laboratory. Throughout this section, “water” or “deionized water” refer to water from the institute’s deionization system. “Ultrapure water” refers to type 1 water (see Section 2.11).

For easier understanding of the NMR spectra of synthesized substances, some NMR spectra of commercial substances are reported here.

$^1\text{H-NMR}$ (3-chloropropyldimethylmethoxysilane, 300 MHz, CDCl_3): $\delta = 3.52$ (t, $J = 7$ Hz, 2 H, $\text{CH}_2\text{-CH}_2\text{-Cl}$), 3.43 (s, 3 H, O-CH_3), 1.88–1.76 (m, 2 H, $\text{CH}_2\text{-CH}_2\text{-CH}_2$), 0.75–0.68 (m, 2 H, $\text{CH}_2\text{-CH}_2\text{-Si}$), 0.12 (s, 6 H, $2 \times \text{Si-CH}_3$) ppm.

$^1\text{H-NMR}$ ($^{SH}\lambda^{\text{OH}}-4$, 300 MHz, acetone-*d*₆): $\delta = 7.43\text{--}6.66$ (m, 4 H, $4 \times \text{-CH=}$), 3.92 (s, 1 H, -SH) ppm.

$^1\text{H-NMR}$ (11-bromo-1-undecanol, 300 MHz, CDCl_3): $\delta = 3.62$ (t, $J = 7$ Hz, 2 H, $\text{CH}_2\text{-OH}$), 2.51 (q, $J = 7$ Hz, 2 H, $\text{CH}_2\text{-SH}$), 1.65–1.49 (m, 4 H, $\text{CH}_2\text{-CH}_2\text{-OH}$ and $\text{CH}_2\text{-CH}_2\text{-SH}$), 1.40–1.21 (m, 14 H, $\text{OH-CH}_2\text{-CH}_2\text{-(CH}_2)_7$) ppm.

$^1\text{H-NMR}$ (propargyl alcohol, 300 MHz, CDCl_3): $\delta = 4.25$ (d, $J = 2$ Hz, 2 H, $\text{CH}_2\equiv$), 2.46 (t, $J = 2$ Hz, 1 H, $\equiv\text{CH}$), 2.40 (bs, 1 H, $\text{CH}_2\text{-OH}$) ppm.

3.1.1 Monomers

N-isopropylacrylamide (NIPAm, $\geq 99\%$, ALDRICH, or $\geq 99\%$, ACROS ORGANICS) was recrystallized twice from toluene : *n*-hexane = 1 : 3 and dried under high vacuum giving colorless needles. *n*-Butyl acrylate (BA, $\geq 99\%$, containing 10–60 ppm 4-methoxyphenol as inhibitor, ALDRICH) and styrene ($\geq 99\%$, stabilized with 0.002 % 4-*tert*-butylcatechol, ALDRICH) were passed through a column containing aluminum oxide (basic, Brockmann I, 150 mesh, ALDRICH) before use. For the structural formulas of BA, NIPAm, and styrene see Figure 5.11. All purified monomers were stored at 3 °C until use.

3.1.2 Initiators

2,2'-Azobis(*iso*-butyronitrile) (AIBN, 98 %, AKZO NOBEL) was recrystallized twice from methanol, giving colorless needles. 4,4'-Azobis(4-cyanovaleric acid) (ACVA, $\geq 98\%$, ALDRICH) was used as received without further purification. For the structural formulas of AIBN and ACVA see Figure 5.13. The initiators were stored at 8 °C until use.

3.1.3 RAFT agents

2-(Dodecylthiocarbonothioylthio)-2-methylpropanoic acid **p-4** (98 %, ALDRICH) and 4-cyano-4-[(dodecylsulfanylthiocarbonyl)sulfanyl]pentanoic acid **p-5** (97 %, ALDRICH) were used as received without further purification.

¹H-NMR (p-4, 300 MHz, CDCl₃): δ = 3.27 (t, J = 7 Hz, 2 H, CH₂-SCS₂), 1.70 (s, 6 H, S₂CS-C-(CH₃)₂), 1.69–1.60 (m, 2 H, CH₂-CH₂-SCS₂), 1.40–1.20 (m, 18 H, CH₃-(CH₂)₉) 0.86 (t, J = 7 Hz, 3 H, CH₃-CH₂) ppm.

The RAFT agent benzyl(3-trimethoxysilylpropyl)trithiocarbonate **p³-1** (see Figure 5.12) was kindly provided by Robert Rotzoll who has already reported the synthesis protocol.^[2–4] Its integrity was checked by NMR spectroscopy immediately prior to use.

¹H-NMR (300 MHz, CDCl₃): δ = 7.04–7.30 (m, 4 H, 4 × -CH=), 4.60–4.50 (2 × s, 2 H, S-CH₂-C₆H₄ of *meta*- and *para*-isomers), 3.54 (s, 9 H, 3 × Si-O-CH₃), 3.38–3.28 (m, 2 H, S-CH₂-CH₂-CH₃), 2.78–2.60 (m, 2 H, Si-CH₂-CH₂), 1.80–1.65 (m, 2 H, S-CH₂-CH₂-CH₃), 1.05–0.90 (m, 5 H, Si-CH₂ and Si-CH₂-CH₂-CH₃) ppm.

^{13}C -NMR (75 MHz, CDCl_3): $\delta = 223.8$ ($\text{C}=\text{S}$), 126.6, 127.2, 128.1, 128.65, 128.70, 129.2, 132.2, 134.9, 143.9, and 144.9 (C_6H_4 of *meta*- and *para*-isomers), 50.5 ($\text{Si}-\text{O}-\text{CH}_3$), 41.2 and 41.5 ($\text{S}-\text{CH}_2-\text{C}_6\text{H}_4$ of *meta*- and *para*-isomers), 38.8 ($\text{S}-\text{CH}_2-\text{CH}_2-\text{CH}_3$), 28.3 and 28.5 ($\text{Si}-\text{CH}_2-\text{CH}_2$ of *meta*- and *para*-isomers), 21.5 ($\text{S}-\text{CH}_2-\text{CH}_2-\text{CH}_3$), 13.4 ($\text{Si}-\text{CH}_2-\text{CH}_2-\text{CH}_3$), 11.1 ($\text{Si}-\text{CH}_2$) ppm.

The polyfunctional RAFT agents $\rho^{\text{MB}}\text{-7}$, $\rho^{\text{MB}}\text{-8}$, and $\rho^{\text{MB}}\text{-9}$ had already been prepared in previous work by polycondensation of 2,6-dibromoheptanedioate and trithiocarbonate anions on an anionic phase transfer catalyst. The synthesis protocol has already been reported.^[5,6] Their integrity was checked by NMR spectroscopy immediately prior to use. See Figure 5.12 for the structural formulas of these RAFT agents.

^1H -NMR (300 MHz, CDCl_3): $\delta = 1.40\text{--}1.70$ (m, $\text{CH}_2-\text{CH}_2-\text{CH}_2$), 1.85–2.14 (m, $\text{CH}_2-\text{CH}_2-\text{CH}_2$), 3.75 (s, COOCH_3), 4.14–4.24 (m, $\text{CH}-\text{Br}$), 4.59–4.79 (m, $\text{CH}-\text{S}$) ppm.

^{13}C -NMR (75 MHz, CDCl_3): $\delta = 22.1$ ($\text{CH}_2-\text{CH}_2-\text{CH}_2$), 30.5 ($\text{CH}-\text{CS}_3$), 44.8 ($\text{CH}-\text{Br}$), 53.0 ($\text{COO}-\text{CH}_3$, $\text{CH}-\text{SCS}_2$), 170.4 ($\text{COO}-\text{CH}_3$), 219.2 ($\text{S}-\text{CS}-\text{S}$) ppm.

3.1.4 Polymers

The pNIPAm star polymer $\pi^*\text{-19}$ ($\overline{M}_n = 2.07 \times 10^5 \text{ g mol}^{-1}$) was kindly provided by Nadja Förster who has already reported the protocol.^[7,8] See Figure 9.1 for the chemical structure.

The water-soluble polymers polysorbate 20 (TWEEN 20, poly(ethylene glycol) sorbitan monolaurate, 1228 g mol^{-1} , SIGMA), poly(ethylene glycol) ($570\text{--}630 \text{ g mol}^{-1}$, FLUKA), poly(acrylic acid) ($\overline{M}_w = 4.5 \times 10^5 \text{ g mol}^{-1}$, ALDRICH), polyvinylpyrrolidone ($\overline{M}_n = 4 \times 10^4 \text{ g mol}^{-1}$, ALDRICH), poly(methacrylic acid) ($\overline{M}_w \approx 10^5 \text{ g mol}^{-1}$, POLYSCIENCES EUROPE), poly(acrylic acid) ($\overline{M}_w \approx 3 \times 10^6 \text{ g mol}^{-1}$, ALDRICH), were purchased commercially and used as received.

3.1.5 Nanoparticles

The fumed silica $\text{SiO}_2^{\text{fs}}\text{-v-1}$ (ALDRICH) is a mesoporous material produced by the aggregation of primary particles with a diameter of approximately 7 nm. According to the manufacturer's data, the specific surface is $S_m = 390 \pm 40 \text{ m}^2 \text{ g}^{-1}$ and the

planar density of hydroxyl groups is approximately $\rho_p = 2.5 \text{ nm}^{-2}$ (see Section 4.1). The material is a white powder and was used without any pretreatment.

Colloidal silica $\text{SiO}_2^{\text{np}}\mathbf{v-2}$ in methanol ("ORGANOSILICASOL" MA-ST-L) was purchased from NISSAN CHEMICALS and stored at room temperature. The mass fraction of silica was $\omega_{\text{SiO}_2} = 0.43 \pm 0.02$, respectively, as determined gravimetrically.

3.2 Synthesis of substances

3.2.1 Synthesis of RAFT agent $\rho^{2\times}\mathbf{-2}$ with two anchor groups

The whole synthesis is depicted in Figure 5.2.

3.2.1.1 Synthesis of 1,4-bis(hydroxyethyl)benzene $\sigma\mathbf{-4}$

To a solution of 1,4-diacetylbenzene (5.02 g, 31.0 mmol, 1 eq.) in 50 mL of THF was slowly added sodium borohydride (2.53 g, 67.0 mmol, 2.2 eq.). The solution was stirred for 24 h at 40 °C before hydrochloric acid (3 mol L⁻¹, 25 mL) was added. The aqueous phase was extracted with dichloromethane (1 × 100 mL, 2 × 50 mL). The combined organic phases were dried over sodium sulfate and the solvent was removed by rotary evaporation. After purification by column chromatography over silica (ethyl acetate), the title compound $\sigma\mathbf{-4}$ was obtained in the form of yellow crystals (4.52 g, 27.2 mmol, 88 %).

¹H-NMR (300 MHz, CDCl₃): δ = 7.33 (m, 4 H, 4 × C–CH=C), 4.87 (q, J = 7 Hz, 2 H, 2 × CHOH–CH₃), 1.86 (s, 2 H, 2 × OH), 1.47 (d, J = 7 Hz, 6 H, 2 × CHOH–CH₃) ppm.

3.2.1.2 Synthesis of 1,4-bis(1-chloroethyl)benzene $\sigma\mathbf{-5}$

To a solution of 1,4-bis(hydroxyethyl)benzene (4.48 g, 27.0 mmol, 1 eq.) in 50 mL of dichloromethane, a solution of thionyl chloride (4.09 mL, 56.0 mmol, 2.1 eq.) in 25 mL dichloromethane was added dropwise in a nitrogen atmosphere and under constant stirring. The solution was then stirred overnight at room temperature and 25 mL of a saturated aqueous solution of sodium sulfate was added. The aqueous phase was extracted with dichloromethane (3 × 25 mL) and the combined organic phases were dried over sodium sulfate. Removing the solvent under reduced pressure and purification by column chromatography over silica (*n*-pentane :

ethyl acetate = 20 : 1) yielded the title substance σ -5 as greenish-yellow solid (3.64 g, 17.9 mmol, 66 %).

$^1\text{H-NMR}$ (300 MHz, CDCl_3): δ = 7.39 (m, 4 H, $4 \times \text{C-CH=C}$), 5.07 (q, J = 6 Hz, 2 H, $2 \times \text{CHCl-CH}_3$), 1.83 (s, 6 H, $2 \times \text{CHCl-CH}_3$) ppm.

3.2.1.3 Synthesis of sodium (1-trimethoxysilyl)ethylthiobenzoate σ -6

To a suspension of elemental sulfur (470 mg, 15 mmol, 2.0 eq.) in 30 mL of methanol, a solution of sodium methoxide (810 mg, 15 mmol, 2.0 eq.) in 3 mL of methanol was added dropwise. ((Chloromethyl)phenylethyl)trimethoxysilane (mixed *m/p* isomers, 1.81 mL, 7.4 mmol, 1 eq.) was added and the solution was stirred overnight at 80 °C. By filtration of the mixture and removal of the solvent under reduced pressure, the title compound σ -6 was obtained as brown solid. The product was employed in the next reaction step without further purification or analysis.

3.2.1.4 Coupling to the final RAFT agent ρ^{2x} -2

To a refluxing solution of 1,4-bis(1-chloroethyl)benzene (500 mg, 2.5 mmol, 1 eq.) in 10 mL of dry acetonitrile, a solution of sodium (1-trimethoxysilyl)ethylthiobenzoate (complete product of the reaction in Section 3.2.1.3, estimated: 3 eq.) was added dropwise. The solution was stirred for another 4 h under reflux and then filtered. The solvent was removed under reduced pressure. Purification by column chromatography over silica (*n*-pentane : ethyl acetate = 20 : 1) yielded the RAFT agent 1,1'-(1,4-phenylene)-bis(ethane-1,1-diyl)-bis(3/4-(2-(trimethoxysilyl)ethyl)benzodithioate), compound ρ^{2x} -2 (no yield could be calculated because the purification was done in several steps), as red solid.

$^1\text{H-NMR}$ (300 MHz, CDCl_3): δ = 7.95–7.05 (m, 12 H, $12 \times \text{C-CH=C}$), 5.22 (q, J = 6 Hz, 2 H, $2 \times \text{CHS-CH}_3$), 3.55 (s, 18 H, $6 \times \text{OCH}_3$), 2.73 (m, 4 H, $2 \times \text{Si-CH}_2\text{-CH}_2$), 1.76 (d, J = 6 Hz, 6 H, $2 \times \text{CHS-CH}_3$), 1.00 (m, 4 H, $2 \times \text{Si-CH}_2\text{-CH}_2$) ppm.

3.2.2 Synthesis of RAFT agent ρ^1 -3 with a monofunctional anchor group

The convergent reaction scheme is shown in Scheme 5.3.

3.2.2.1 Synthesis of the precursor 3-iodopropyldimethylmethoxysilane σ -7

3-Chloropropyldimethylmethoxysilane (0.58 mL, 0.55 g, 3.5 mmol, 1 eq.) was added to a solution of sodium iodide (5.25 g, 35.0 mmol, 10 eq.) in 30 mL of dry acetone. The solution was stirred for 72 h at 45 °C. The solvent was removed under reduced pressure and chloroform was added to the residue. The colorless precipitate was filtered off. By drying the filtrate by rotary evaporation, the title compound σ -7 was obtained as orange liquid (0.839 g, 3.25 mmol, 93 %).

$^1\text{H-NMR}$ (300 MHz, CDCl_3): δ = 3.42 (s, 3 H, O-CH₃), 3.20 (t, J = 7 Hz, 2 H, CH₂-CH₂-I), 1.80–1.92 (m, 2 H, CH₂-CH₂-CH₂), 0.66–0.73 (m, 2 H, CH₂-CH₂-Si), 0.11 (s, 6 H, 2 × Si-CH₃) ppm.

3.2.2.2 Synthesis of σ -8 and coupling to the final RAFT agent ρ^1 -3

Benzyl mercaptan (0.77 mL, 816 mg, 6.57 mmol, 1 eq.) was added dropwise to a solution of sodium methoxide (355 mg, 6.57 mmol, 1 eq.) in 20 mL of methanol. After stirring for 2 h at room temperature, carbon disulfide (0.62 mL, 10.3 mmol, 1.57 eq.) was added. The mixture was stirred for another 2 h at room temperature. Then, 3-iodopropyldimethylmethoxysilane σ -7 (1.70 g, 6.57 mmol, 1 eq.) was added and the solution was stirred for 16 h at room temperature. The solvent was removed under reduced pressure, chloroform was added and the precipitate was removed by filtration. After removing the chloroform under reduced pressure, the RAFT agent ρ^1 -3 (1.82 g, 5.52 mmol, 84 %) was obtained as orange liquid.

$^1\text{H-NMR}$ (300 MHz, CDCl_3): δ = 7.37–7.27 (m, 5 H, 5 × -CH=), 4.63 (d, J = 2 Hz, 2 H, S₂CS-CH₂-C), 3.44 (s, 3 H, O-CH₃), 3.42–3.37 (m, 2 H, CH₂-CH₂-SCS₂), 1.83–1.71 (m, 2 H, CH₂-CH₂-CH₂), 0.78–0.71 (m, 2 H, CH₂-CH₂-Si), 0.13 (s, 6 H, 2 × Si-CH₃) ppm.

$^{13}\text{C-NMR}$ (75 MHz, CDCl_3): δ = 224.8, 223.9, 222.9 (SCS₂), 136.3, 136.2 (C-CH-C), 129.6, 129.5 (2 × C-CH-C), 129.1, 129.0 (2 × C-CH-C), 128.3, 128.1 (C-CH-C), 50.6 (O-CH₃), 41.8, 41.7 (C-CH₂-SCS₂), 40.3, 40.2 (CH₂-CH₂-SCS₂), 22.6 (CH₂-CH₂-CH₂), 15.9 (Si-CH₂-CH₂), -2.4 (Si-CH₃) ppm.

$^{29}\text{Si-NMR}$ (60 MHz, CDCl_3): δ = 18.9 ppm.

MS (ESI): $\frac{m}{z}$ = 317.1 [M - Me + 2 H]⁺, 331.1 [M + H]⁺, 339.1 [M - Me + H + Na]⁺, 353.1 [M + Na]⁺.

3.2.3 Synthesis of the alkyne RAFT agent $\rho^{\equiv}-6$

This Steglich^[9] esterification reaction was performed twice with different absolute (but identical relative) amounts of the substances. By way of example, only the values of one single reaction are noted here. The reaction is shown in Scheme 5.4.

A solution of 2-(dodecylthiocarbonothioylthio)-2-methylpropanoic acid $\rho-4$ (2.37 g, 6.5 mmol, 1 eq.) in 30 mL of dry dichloromethane was cooled to 0 °C. Subsequently, 4-(dimethylamino)pyridine (63.5 mg, 520 μ mol, 0.08 eq.), propargyl alcohol (1.70 mL, 1.64 g, 29.3 mmol, 4.5 eq.), and 1,3-dicyclohexylcarbodiimide (1.48 g, 7.15 mmol, 1.1 eq.) were added slowly under stirring. The precipitation of a white salt was observed. The cooling was removed and the reaction mixture was stirred for 3 d at room temperature. The precipitate was filtered off and the filtrate was concentrated by rotary evaporation and redissolved in 50 mL of dichloromethane. This solution was filtrated again, washed with 0.5 N hydrochloric acid (3 \times 50 mL) and a saturated solution of sodium hydrogencarbonate (3 \times 50 mL) and dried over sodium sulfate. The solvent was removed via rotary evaporation. After drying under high vacuum, the title compound $\rho^{\equiv}-6$ was obtained (2.25 g, 5.60 mmol, 86 %) as a yellow solid.

¹H-NMR (300 MHz, CDCl₃): δ = 4.69 (d, J = 2 Hz, 2 H, CH₂ \equiv), 3.27 (t, J = 7 Hz, 2 H, CH₂-SCS₂), 2.46 (t, J = 2 Hz, 1 H, \equiv CH), 1.71 (s, 6 H, S₂CS-C-(CH₃)₂), 1.69–1.60 (m, 2 H, CH₂-CH₂-SCS₂), 1.40–1.20 (m, 18 H, CH₃-(CH₂)₉) 0.86 (t, J = 7 Hz, 3 H, CH₃-CH₂) ppm.

Elemental analysis: calculated: 59.65 % C, 23.89 % S, 7.95 % O, 8.51 % H; found: 60.27 % C, 22.61 % S, 8.73 % H.

3.2.4 Synthesis of the azidothiol $^{\text{SH}}\lambda^{\text{N}_3}-9$

The whole synthesis is depicted in Scheme 5.5. A pathway^[10,11] from literature was followed with some modifications, especially in the last step.

3.2.4.1 Synthesis of 1-azidoundecane-11-ol $\sigma-1$

This reaction was performed three times with different absolute (but identical relative) amounts of the substances. By way of example, only the values of one single reaction are noted here.

To 150 mL of dimethyl formamide, which had been bubbled with argon for 5 min, 11-bromo-1-undecanol (10.8 g, 43.1 mmol, 1 eq.) and sodium azide (3.08 g,

47.4 mmol, 1.1 eq.) were added under exclusion of air. The solution was stirred for 24 h under reflux in an argon atmosphere. After the reaction mixture had cooled down to room temperature, 150 mL of water were added. This mixture was extracted with diethyl ether (3×130 mL). The combined organic phases were subsequently washed with water (3×130 mL) and dried over magnesium sulfate. By evaporation of the solvent under reduced pressure and drying of the residue under high vacuum, the title compound σ -1 (8.11 g, 47.4 mmol, 88 %) was obtained as a pale brownish-yellow oil.

$^1\text{H-NMR}$ (300 MHz, CDCl_3): δ = 3.62 (t, J = 7 Hz, 2 H, $\text{CH}_2\text{-OH}$), 3.25 (t, J = 7 Hz, 2 H, $\text{CH}_2\text{-N}_3$), 1.65–1.50 (m, 4 H, $\text{CH}_2\text{-CH}_2\text{-OH}$ and $\text{CH}_2\text{-CH}_2\text{-N}_3$), 1.42–1.22 (m, 14 H, $\text{N}_3\text{-CH}_2\text{-CH}_2\text{-(CH}_2)_7$) ppm.

3.2.4.2 Synthesis of 1-azidoundecane-11-methylsulfonate σ -2

This reaction was performed twice with different absolute (but identical relative) amounts of the substances. By way of example, only the values of one single reaction are noted here.

1-Azidoundecane-11-ol σ -1 (3.30 g, 15.4 mmol, 1 eq.) and methanesulfonyl chloride (3.10 mL, 4.59 g, 40.0 mmol, 2.6 eq.) were added to 100 mL of freshly dried (distillation over calcium hydride) tetrahydrofuran and the mixture was bubbled with argon for 5 min. Under constant stirring, a solution of triethylamine (5.37 mL, 3.90 g, 38.5 mmol, 2.5 eq.) in freshly distilled tetrahydrofuran was added dropwise over 5 min. The reaction mixture was further stirred for 2 h. During this time, the precipitation of a colorless salt was observed. Then the reaction was quenched by addition of 100 mL of ice-cold water. The mixture was extracted with diethyl ether (2×100 mL). The organic phases were combined and washed with 1 M hydrochloric acid (3×100 mL), water (3×100 mL), a saturated aqueous solution of sodium hydrogencarbonate (3×100 mL), and again with water (3×100 mL), and dried over sodium sulfate. The solvent was removed via rotary evaporation and the residue was dried under high vacuum, yielding the title compound σ -2 (3.80 g, 13.0 mmol, 84 %) as a pale yellow oil.

$^1\text{H-NMR}$ (300 MHz, CDCl_3): δ = 4.22 (t, J = 7 Hz, 2 H, $\text{CH}_2\text{-O-SO}_3\text{-CH}_3$), 3.25 (t, J = 7 Hz, 2 H, $\text{CH}_2\text{-N}_3$), 3.00 (s, 3 H, $\text{SO}_3\text{-CH}_3$), 1.75 (quin, J = 7 Hz, 2 H, $\text{CH}_2\text{-CH}_2\text{-O}$), 1.64–1.54 (m, 2 H, $\text{CH}_2\text{-CH}_2\text{-N}_3$), 1.43–1.24 (m, 14 H, $\text{N}_3\text{-CH}_2\text{-CH}_2\text{-(CH}_2)_7$) ppm.

3.2.4.3 Synthesis of 1-azidoundecane-11-thioacetate σ -3

This reaction was performed twice with different absolute (but identical relative) amounts of the substances. By way of example, only the values of one single reaction are noted here.

1-Azidoundecane-11-methylsulfonate σ -2 (0.965 g, 3.30 mmol, 1 eq.) and potassium thioacetate (0.754 g, 25.8 mmol, 2.0 eq) were dissolved in 30 mL of methanol. The reaction mixture was refluxed for 3 h under constant stirring in an argon atmosphere. After cooling to room temperature, the reaction solution was concentrated via rotary evaporation and 30 mL of ice-cold water were added. The mixture was extracted with diethyl ether (3×30 mL). The organic phases were combined, washed with water (3×30 mL), and dried over sodium sulfate. The solvent was removed by rotary evaporation and the residue was dried under high vacuum. Thus, the title compound σ -3 (0.862 g, 3.16 mmol, 96 %) was obtained as a pale yellow oil.

$^1\text{H-NMR}$ (300 MHz, CDCl_3): δ = 3.25 (t, J = 7 Hz, 2 H, $\text{CH}_2\text{-N}_3$), 2.85 (t, J = 7 Hz, 2 H, $\text{CH}_2\text{-S-CO-CH}_3$), 2.31 (s, 3 H, CO-CH_3), 1.72–1.53 (m, 4 H, $\text{CH}_2\text{-CH}_2\text{-N}_3$ and $\text{CH}_2\text{-CH}_2\text{-S-CO}$), 1.42–1.23 (m, 14 H, $\text{N}_3\text{-CH}_2\text{-CH}_2\text{-(CH}_2)_7$) ppm. (And signals of already present thiol and disulfide, see Section 3.2.4.4.)

3.2.4.4 Synthesis of 1-azidoundecane-11-thiol $^{\text{SH}}\lambda^{\text{N}_3}\text{-9}$

This reaction was performed twice with different absolute (but identical relative) amounts of the substances. By way of example, only the values of one single reaction are noted here.

A solution of 1-azidoundecane-11-thioacetate σ -3 (0.861 g, 3.16 mmol, 1 eq.) and 60 mL of methanol was bubbled with argon for 5 min and 3 mL of concentrated hydrochloric acid were added. The solution was refluxed under constant stirring in an argon atmosphere for 4.5 h and then stirred overnight at room temperature. Subsequently, 60 mL of water were added. The resulting mixture was extracted with diethyl ether (2×60 mL). The organic phases were combined, washed with water (3×65 mL), and dried over sodium sulfate. The solvent was removed by rotary evaporation. Purification via column chromatography over silica [petrol ether : ethyl acetate = 100 : 1 \rightarrow 50 : 1; R_f = 0.65 (petrol ether : ethyl acetate = 9 : 1)] and drying under high vacuum yielded the title compound $^{\text{SH}}\lambda^{\text{N}_3}\text{-9}$ (0.509 g, 2.21 mmol, 70 %) as a colorless oil, containing impurities of the corresponding disulfide $^{\text{S}_2}\lambda^{\text{N}_3}\text{-9'}$ (approximately $1/5$ of the total number according to NMR integrals).

$^1\text{H-NMR}$ (thiol, 300 MHz, CDCl_3): see Section 3.2.4.5.

$^1\text{H-NMR}$ (disulfide, 300 MHz, CDCl_3): $\delta = 3.25$ (t, $J = 7$ Hz, 4 H, $2 \times \text{CH}_2\text{-N}_3$), 2.67 (q, $J = 7$ Hz, 4 H, $2 \times \text{CH}_2\text{-S-S}$), 1.67–1.53 (m, 8 H, $2 \times \text{CH}_2\text{-CH}_2\text{-N}_3$ and $2 \times \text{CH}_2\text{-CH}_2\text{-S-S}$), 1.42–1.23 (m, 28 H, $2 \times \text{N}_3\text{-CH}_2\text{-CH}_2\text{-(CH}_2)_7$) ppm.

3.2.4.5 Reduction of bis-(1-azidoundecane) disulfide $\text{S}_2\lambda\text{N}_3\text{-9'}$ to 1-azidoundecane-11-thiol $^{\text{SH}}\lambda\text{N}_3\text{-9}$

A solution of the azidothiol $^{\text{SH}}\lambda\text{N}_3\text{-9}$ (59.6 μL , 57.4 mg, 250 μmol , 1 eq.) containing impurities of the bis-(1-azidoundecane) disulfide $\text{S}_2\lambda\text{N}_3\text{-9'}$ (approximately $1/5$ of the total number according to NMR integrals) in a mixture of 15 mL of methanol and 5 mL of tetrahydrofuran was bubbled 5 min with argon. Under constant stirring, triethylamine (104 μL , 75.9 mg, 750 μmol , 3 eq.) and dithiothreitol (116 mg, 750 μmol , 3 eq.) were added slowly. The solution was further stirred overnight at room temperature and then 20 mL of a 4 % aqueous citric acid solution were added. This mixture was extracted with diethyl ether (2×20 mL). The combined organic phases were washed with water (3×40 mL) and dried over magnesium sulfate. After drying under high vacuum, the pure azidothiol $^{\text{SH}}\lambda\text{N}_3\text{-9}$ (57.4 mg, 250 μmol , quantitative yield) was obtained.

$^1\text{H-NMR}$ (300 MHz, CDCl_3): $\delta = 3.25$ (t, $J = 7$ Hz, 2 H, $\text{CH}_2\text{-N}_3$), 2.51 (q, $J = 7$ Hz, 2 H, $\text{CH}_2\text{-SH}$), 1.67–1.53 (m, 4 H, $\text{CH}_2\text{-CH}_2\text{-N}_3$ and $\text{CH}_2\text{-CH}_2\text{-SH}$), 1.42–1.23 (m, 14 H, $\text{N}_3\text{-CH}_2\text{-CH}_2\text{-(CH}_2)_7$) ppm.

Elemental analysis: calculated: 57.34 % C, 18.24 % N, 13.92 % S, 10.50 % H; found: 57.97 % C, 18.59 % N, 13.87 % S, 10.20 % H.

3.2.5 Synthesis of the Dess–Martin periodinane $\sigma\text{-9}$

The Dess–Martin periodinane,^[12] 1,1,1-triacetoxy-1,1-dihydro-1,2-benziodoxol-3(1H)-one, was synthesized according to the standard literature procedure^[13] and stored at -18°C prior to use.

3.2.6 Polymers

3.2.6.1 Polymerizations

Depending on the quantity, the polymerizations were performed in two different ways.

Polymers $\pi\text{-1}$, $\pi\text{-2}$, $\pi\text{-3}$, $\pi\text{-4}$, $\pi^{\text{MB}}\text{-11}$, $\pi^{\text{MB}}\text{-12}$, $\pi^{\text{MB}}\text{-13}$, $\pi^{\text{MB}}\text{-14}$, $\pi^{\text{MB}}\text{-15}$, $\pi^{\text{MB}}\text{-16}$, $\pi^{\text{MB}}\text{-17}$, and $\pi^{\text{MB}}\text{-18}$ were obtained by dissolving the monomer NI-PAm, the respective RAFT agent, and the initiator AIBN dissolved in DMF in a glass

vial with a septum and degassing the solution thoroughly via bubbling with dried argon. The polymerizations were then conducted in a heated oil-bath of 60 °C in an argon atmosphere with constant magnetic stirring. After the indicated amounts of time, the samples were taken with a syringe.

Polymers π -5, π -6, π -7, π -8, π -9, and π -10 were obtained by degassing the polymerization mixtures containing NIPAm, the respective RAFT agent and initiator in DMF via three freeze–pump–thaw cycles and then portioning it into several capped glass vials in an argon-filled glovebox, which were subsequently placed in a heating block which had been preheated to the polymerization temperature. After the indicated periods of time, the polymerizations were stopped by exposure of the solution to air.

All polymers were then precipitated in large amounts of diethyl ether and collected by centrifugation of the mixture and decantation of the supernatant. It was waited until the remaining diethyl ether had evaporated and the polymers were dry. Then, they were redissolved in a small amount of acetone and the described precipitation–centrifugation process was repeated. After a total of three consecutive precipitation steps, the isolated polymers were dried in a vacuum oven at 55 °C and thus obtained as pale yellow solids. SEC showed that all residual monomer was removed by the work-up (no signal at low molar masses).

The amounts of the used substances and the polymerization conditions for the individual reactions are listed in the Tables 3.1 to 3.18. See Section 5.4 for the explanations of the variables used in these tables.

3.2.6.2 Defunctionalization via aminolysis and Michael-addition sealing

This reaction is based on the protocols published by Qiu and Winnik^[14] (2006) and Lei *et al.*^[15] (2006).

The trithiocarbonate-group containing polymer (10 mg) and a very small amount of tris(2-carboxyethyl) phosphine hydrochloride (TCEP-HCl) were dissolved in 6 mL of THF and *n*-butyl amine (0.20 mL, 2.0 mmol) was added. The solution was shaken for 36 h and *n*-butyl acrylate (BA, 0.2 mL, 1.4 mmol) was added. Colorless polymers were obtained after drying for 1 d under high vacuum at 75 °C.

3.2.6.3 Cleavage via reaction with excess radicals

The trithiocarbonate-group containing polymer (10 mg) and AIBN (10 mg, 60 μ mol) were dissolved in 1 mL of THF. The solution was heated to 85 °C for 5 h. Colorless polymers were obtained after drying under high vacuum at 85 °C for 1 h and sub-

Tab. 3.1: Polymerization data for π -1.

number	π -1	T	60 °C
solvent	DMF	n_M/n_S	1/4
monomer	NIPAm	c_M	3.23 mol L ⁻¹
RAFT agent	ρ -4	c_{RAFT}	6.46×10^{-3} mol L ⁻¹
initiator	AIBN	c_{ini}	2.44×10^{-3} mol L ⁻¹

π -1	t in h	$X_{M,g}$	RI detector		UV detector	
			\overline{M}_n in $\frac{g}{mol}$	\mathcal{D}	\overline{M}_n in $\frac{g}{mol}$	\mathcal{D}
b	1.87	0.380	5.16×10^4	1.08	5.33×10^4	1.06
c	3.50	0.800	5.48×10^4	1.19	5.34×10^4	1.20
d	5.50	0.970	5.50×10^4	1.23	5.02×10^4	1.32
e	7.57	1.000	5.62×10^4	1.23	5.26×10^4	1.31

Tab. 3.2: Polymerization data for π -2.

number	π -2	T	60 °C
solvent	DMF	n_M/n_S	1/3.1
monomer	NIPAm	c_M	4.17 mol L ⁻¹
RAFT agent	ρ -4	c_{RAFT}	5.00×10^{-3} mol L ⁻¹
initiator	AIBN	c_{ini}	2.52×10^{-3} mol L ⁻¹

π -2	t in h	$X_{M,g}$	RI detector		UV detector	
			\overline{M}_n in $\frac{g}{mol}$	\mathcal{D}	\overline{M}_n in $\frac{g}{mol}$	\mathcal{D}
a	2.67	0.350	4.74×10^4	1.15	4.64×10^4	1.14
b	4.47	0.700	6.77×10^4	1.19	6.48×10^4	1.21
c	5.50	0.750	7.26×10^4	1.19	7.14×10^4	1.21
d	6.95	0.720	7.44×10^4	1.22	7.03×10^4	1.29
e	8.17	0.930	6.76×10^4	1.28	5.95×10^4	1.37

Tab. 3.3: Polymerization data for π -3 .

number	π -3	T	60 °C
solvent	DMF	n_M/n_S	1/3
monomer	NIPAm	c_M	4.30 mol L ⁻¹
RAFT agent	ρ -4	c_{RAFT}	1.72×10^{-3} mol L ⁻¹
initiator	AIBN	c_{ini}	1.64×10^{-3} mol L ⁻¹

π -3		RI detector			UV detector	
	t in h	$X_{M,g}$	\overline{M}_n in $\frac{g}{mol}$	\mathcal{D}	\overline{M}_n in $\frac{g}{mol}$	\mathcal{D}
a	2.00	0.490	1.22×10^5	1.31	9.42×10^4	1.52

Tab. 3.4: Polymerization data for π -4 .

number	π -4	T	60 °C
solvent	DMF	n_M/n_S	1/3
monomer	NIPAm	c_M	4.30 mol L ⁻¹
RAFT agent	ρ -4	c_{RAFT}	2.58×10^{-3} mol L ⁻¹
initiator	AIBN	c_{ini}	1.08×10^{-3} mol L ⁻¹

π -4		RI detector			UV detector	
	t in h	$X_{M,g}$	\overline{M}_n in $\frac{g}{mol}$	\mathcal{D}	\overline{M}_n in $\frac{g}{mol}$	\mathcal{D}
c	4.50	1.000	1.09×10^5	1.38	8.50×10^4	1.57
d	6.08	0.750	8.16×10^4	1.59	4.18×10^4	2.10
e	8.00	1.000	9.75×10^4	1.49	5.87×10^4	1.95

Tab. 3.5: Polymerization data for π -5.

number	π -5	T	60 °C
solvent	DMF	n_M/n_S	1/2.86
monomer	NIPAm	c_M	4.51 mol L ⁻¹
RAFT agent	ρ -4	c_{RAFT}	2.86×10^{-3} mol L ⁻¹
initiator	AIBN	c_{ini}	1.58×10^{-3} mol L ⁻¹

π -5			RI detector		UV detector	
	t in h	$X_{\text{M,NMR}}$	\overline{M}_n in $\frac{\text{g}}{\text{mol}}$	\mathcal{D}	\overline{M}_n in $\frac{\text{g}}{\text{mol}}$	\mathcal{D}
b	2.00	0.050	1.26×10^4	1.92	–	–
c	3.00	0.160	3.29×10^4	1.58	–	–
d	5.00	0.350	8.04×10^4	1.38	5.23×10^4	1.77
e	7.00	0.590	7.96×10^4	1.53	3.16×10^4	2.59
f	10.0	0.650	7.71×10^4	1.66	4.02×10^4	2.26

Tab. 3.6: Polymerization data for π -6.

number	π -6	T	70 °C
solvent	DMF	n_M/n_S	1/2.90
monomer	NIPAm	c_M	4.46 mol L ⁻¹
RAFT agent	ρ -4	c_{RAFT}	2.82×10^{-3} mol L ⁻¹
initiator	ACVA	c_{ini}	1.41×10^{-3} mol L ⁻¹

π -6			RI detector		UV detector	
	t in h	$X_{\text{M,NMR}}$	\overline{M}_n in $\frac{\text{g}}{\text{mol}}$	\mathcal{D}	\overline{M}_n in $\frac{\text{g}}{\text{mol}}$	\mathcal{D}
a	1.00	0.420	6.75×10^4	1.46	4.84×10^4	1.71
b	2.00	0.660	6.17×10^4	1.67	2.85×10^4	2.29
c	3.00	0.850	6.36×10^4	1.70	2.56×10^4	2.45
d	5.00	0.900	5.48×10^4	1.87	1.96×10^4	2.60
e	7.00	0.950	6.10×10^4	1.86	1.85×10^4	2.83
f	10.0	0.970	5.03×10^4	2.09	1.64×10^4	3.07

Tab. 3.7: Polymerization data for π -7.

number	π -7	T	65 °C
solvent	DMF	n_M/n_S	1/2.88
monomer	NIPAm	c_M	4.48 mol L ⁻¹
RAFT agent	ρ -4	c_{RAFT}	8.89×10^{-3} mol L ⁻¹
initiator	ACVA	c_{ini}	1.54×10^{-3} mol L ⁻¹

π -7			RI detector		UV detector	
	t in h	$X_{\text{M,NMR}}$	\overline{M}_n in $\frac{\text{g}}{\text{mol}}$	\mathcal{D}	\overline{M}_n in $\frac{\text{g}}{\text{mol}}$	\mathcal{D}
a	1.00	0.420	3.79×10^4	1.14	3.74×10^4	1.13
b	2.00	0.660	4.33×10^4	1.19	4.08×10^4	1.24
c	4.00	0.850	3.82×10^4	1.34	3.02×10^4	1.60
d	5.00	0.900	3.67×10^4	1.39	3.21×10^4	1.54
e	7.00	0.950	4.06×10^4	1.34	2.95×10^4	1.67
f	10.0	0.970	4.72×10^4	1.37	3.35×10^4	1.78

Tab. 3.8: Polymerization data for π -8.

number	π -8	T	65 °C
solvent	DMF	n_M/n_S	1/2.89
monomer	NIPAm	c_M	4.47 mol L ⁻¹
RAFT agent	ρ -4	c_{RAFT}	2.31×10^{-2} mol L ⁻¹
initiator	ACVA	c_{ini}	1.61×10^{-3} mol L ⁻¹

π -8			RI detector		UV detector	
	t in h	$X_{\text{M,NMR}}$	\overline{M}_n in $\frac{\text{g}}{\text{mol}}$	\mathcal{D}	\overline{M}_n in $\frac{\text{g}}{\text{mol}}$	\mathcal{D}
b	2.00	0.370	1.49×10^4	1.20	1.44×10^4	1.20
c	3.00	0.670	2.20×10^4	1.21	2.21×10^4	1.20
d	5.00	0.750	2.58×10^4	1.15	2.52×10^4	1.16
e	7.00	0.880	2.79×10^4	1.16	2.63×10^4	1.23
f	10.0	0.930	2.62×10^4	1.26	2.46×10^4	1.34

Tab. 3.9: Polymerization data for π -9 .

number	π -9	T	65 °C			
solvent	DMF	n_M/n_S	1/3.21			
monomer	NIPAm	c_M	4.02 mol L ⁻¹			
RAFT agent	ρ -5	c_{RAFT}	1.87 × 10 ⁻²	mol L ⁻¹		
initiator	ACVA	c_{ini}	2.57 × 10 ⁻³	mol L ⁻¹		
π -9		RI detector		UV detector		
	t in h	$X_{\text{M,NMR}}$	\overline{M}_n in $\frac{\text{g}}{\text{mol}}$	\mathcal{D}	\overline{M}_n in $\frac{\text{g}}{\text{mol}}$	\mathcal{D}
a	5.00	0.580	2.74 × 10 ⁴	1.16	2.68 × 10 ⁴	1.18

Tab. 3.10: Polymerization data for π -10 .

number	π -10	T	65 °C			
solvent	DMF	n_M/n_S	1/2.97			
monomer	NIPAm	c_M	4.35 mol L ⁻¹			
RAFT agent	ρ -5	c_{RAFT}	2.08 × 10 ⁻²	mol L ⁻¹		
initiator	ACVA	c_{ini}	1.50 × 10 ⁻³	mol L ⁻¹		
π -10		RI detector		UV detector		
	t in h	$X_{\text{M,NMR}}$	\overline{M}_n in $\frac{\text{g}}{\text{mol}}$	\mathcal{D}	\overline{M}_n in $\frac{\text{g}}{\text{mol}}$	\mathcal{D}
a	6.00	0.820	3.17 × 10 ⁴	1.10	3.21 × 10 ⁴	1.10

Tab. 3.11: Polymerization data for $\pi^{\text{MB}}\text{-11}$.

number	$\pi^{\text{MB}}\text{-11}$	T	60 °C
solvent	DMF	$n_{\text{M}}/n_{\text{S}}$	1/3
monomer	NIPAm	c_{M}	4.30 mol L ⁻¹
RAFT agent	$\rho^{\text{MB}}\text{-8}$	c_{RAFT}	8.61×10^{-4} mol L ⁻¹
initiator	AIBN	c_{ini}	2.37×10^{-3} mol L ⁻¹

$\pi^{\text{MB}}\text{-11}$		RI detector			UV detector		
	t in h	$X_{\text{M,g}}$	\overline{M}_{n} in $\frac{\text{g}}{\text{mol}}$	\mathcal{D}	\overline{M}_{n} in $\frac{\text{g}}{\text{mol}}$	\mathcal{D}	\overline{b}_{cl}
b	3.05	0.460	9.08×10^4	1.68	9.00×10^4	1.71	3.00
c	4.63	0.760	8.46×10^4	1.82	8.58×10^4	1.77	–
d	6.92	0.880	7.35×10^4	1.78	7.19×10^4	1.83	–
e	8.63	0.940	7.63×10^4	1.70	7.59×10^4	1.73	1.65

Tab. 3.12: Polymerization data for $\pi^{\text{MB}}\text{-12}$.

number	$\pi^{\text{MB}}\text{-12}$	T	60 °C
solvent	DMF	$n_{\text{M}}/n_{\text{S}}$	1/3
monomer	NIPAm	c_{M}	4.30 mol L ⁻¹
RAFT agent	$\rho^{\text{MB}}\text{-8}$	c_{RAFT}	4.30×10^{-4} mol L ⁻¹
initiator	AIBN	c_{ini}	2.15×10^{-3} mol L ⁻¹

$\pi^{\text{MB}}\text{-12}$		RI detector			UV detector		
	t in h	$X_{\text{M,g}}$	\overline{M}_{n} in $\frac{\text{g}}{\text{mol}}$	\mathcal{D}	\overline{M}_{n} in $\frac{\text{g}}{\text{mol}}$	\mathcal{D}	\overline{b}_{cl}
b	3.45	0.340	1.03×10^5	1.39	9.77×10^4	1.54	–
c	5.22	0.590	1.10×10^5	1.66	1.10×10^5	1.64	1.89
d	6.63	0.660	1.02×10^5	1.68	1.02×10^5	1.70	1.74
e	7.80	0.640	1.01×10^5	1.63	1.03×10^5	1.67	1.66

Tab. 3.13: Polymerization data for $\pi^{\text{MB}}\text{-13}$.

number	$\pi^{\text{MB}}\text{-13}$	T	60 °C				
solvent	DMF	$n_{\text{M}}/n_{\text{S}}$	1/3.5				
monomer	NIPAm	c_{M}	3.69 mol L ⁻¹				
RAFT agent	$\rho^{\text{MB}}\text{-8}$	c_{RAFT}	1.84×10^{-3} mol L ⁻¹				
initiator	AIBN	c_{ini}	1.84×10^{-3} mol L ⁻¹				

$\pi^{\text{MB}}\text{-13}$		RI detector			UV detector		
	t in h	$X_{\text{M,g}}$	\overline{M}_{n} in $\frac{\text{g}}{\text{mol}}$	\mathcal{D}	\overline{M}_{n} in $\frac{\text{g}}{\text{mol}}$	\mathcal{D}	\overline{b}_{cl}
a	2.00	–	1.05×10^4	1.68	9.55×10^3	1.90	–
b	5.00	–	9.04×10^4	1.90	9.18×10^4	1.84	3.62
c	8.35	–	6.95×10^4	1.69	7.12×10^4	1.67	–

Tab. 3.14: Polymerization data for $\pi^{\text{MB}}\text{-14}$.

number	$\pi^{\text{MB}}\text{-14}$	T	60 °C				
solvent	DMF	$n_{\text{M}}/n_{\text{S}}$	1/2.5				
monomer	NIPAm	c_{M}	5.12 mol L ⁻¹				
RAFT agent	$\rho^{\text{MB}}\text{-8}$	c_{RAFT}	4.13×10^{-3} mol L ⁻¹				
initiator	AIBN	c_{ini}	2.07×10^{-3} mol L ⁻¹				

$\pi^{\text{MB}}\text{-14}$			RI detector		UV detector		
	t in h	$X_{\text{M,NMR}}$	\overline{M}_{n} in $\frac{\text{g}}{\text{mol}}$	\mathcal{D}	\overline{M}_{n} in $\frac{\text{g}}{\text{mol}}$	\mathcal{D}	\overline{b}_{cl}
b	3.08	0.070	7.98×10^3	1.49	8.33×10^3	1.43	–
c	5.00	0.490	4.60×10^4	2.09	4.60×10^4	2.15	–

Tab. 3.15: Polymerization data for $\pi^{\text{MB}}\text{-15}$.

number	$\pi^{\text{MB}}\text{-15}$	T	60 °C				
solvent	DMF	$n_{\text{M}}/n_{\text{S}}$	1/2.5				
monomer	NIPAm	c_{M}	5.17 mol L ⁻¹				
RAFT agent	$\rho^{\text{MB}}\text{-8}$	c_{RAFT}	4.13×10^{-3} mol L ⁻¹				
initiator	AIBN	c_{ini}	2.07×10^{-3} mol L ⁻¹				

$\pi^{\text{MB}}\text{-15}$			RI detector		UV detector		\bar{b}_{cl}
	t in h	$X_{\text{M,NMR}}$	\bar{M}_{n} in $\frac{\text{g}}{\text{mol}}$	\mathcal{D}	\bar{M}_{n} in $\frac{\text{g}}{\text{mol}}$	\mathcal{D}	
a	2.60	0.050	6.35×10^3	1.73	6.29×10^3	1.79	–
b	5.53	0.120	1.79×10^4	1.33	1.84×10^4	1.33	–
c	9.87	0.530	4.38×10^4	2.21	4.03×10^4	2.36	4.02

Tab. 3.16: Polymerization data for $\pi^{\text{MB}}\text{-16}$.

number	$\pi^{\text{MB}}\text{-16}$	T	60 °C				
solvent	DMF	$n_{\text{M}}/n_{\text{S}}$	1/2				
monomer	NIPAm	c_{M}	6.46 mol L ⁻¹				
RAFT agent	$\rho^{\text{MB}}\text{-7}$	c_{RAFT}	7.75×10^{-3} mol L ⁻¹				
initiator	AIBN	c_{ini}	2.58×10^{-3} mol L ⁻¹				

$\pi^{\text{MB}}\text{-16}$			RI detector		UV detector		\bar{b}_{cl}
	t in h	$X_{\text{M,NMR}}$	\bar{M}_{n} in $\frac{\text{g}}{\text{mol}}$	\mathcal{D}	\bar{M}_{n} in $\frac{\text{g}}{\text{mol}}$	\mathcal{D}	
a	2.62	0.330	7.11×10^4	1.73	6.92×10^4	1.77	2.92
b	5.65	0.770	8.87×10^4	1.79	9.17×10^4	1.78	–
c	9.87	0.880	9.34×10^4	1.71	9.83×10^4	1.67	1.78

Tab. 3.17: Polymerization data for $\pi^{\text{MB}}\text{-17}$.

number	$\pi^{\text{MB}}\text{-17}$	T	60 °C				
solvent	DMF	$n_{\text{M}}/n_{\text{S}}$	1/6				
monomer	NIPAm	c_{M}	2.15 mol L^{-1}				
RAFT agent	$\rho^{\text{MB}}\text{-8}$	c_{RAFT}	$1.29 \times 10^{-3} \text{ mol L}^{-1}$				
initiator	AIBN	c_{ini}	$8.61 \times 10^{-4} \text{ mol L}^{-1}$				

$\pi^{\text{MB}}\text{-17}$		RI detector			UV detector		
	t in h	$X_{\text{M,g}}$	\overline{M}_{n} in $\frac{\text{g}}{\text{mol}}$	\mathcal{D}	\overline{M}_{n} in $\frac{\text{g}}{\text{mol}}$	\mathcal{D}	\overline{b}_{cl}
a	4.23	0.040	1.13×10^4	3.44	7.79×10^3	1.91	–
b	7.97	0.360	5.41×10^4	1.78	5.63×10^4	1.75	5.45
c	14.7	0.710	5.54×10^4	1.72	5.54×10^4	1.79	3.19

Tab. 3.18: Polymerization data for $\pi^{\text{MB}}\text{-18}$.

number	$\pi^{\text{MB}}\text{-18}$	T	60 °C				
solvent	DMF	$n_{\text{M}}/n_{\text{S}}$	1/6				
monomer	NIPAm	c_{M}	2.15 mol L^{-1}				
RAFT agent	$\rho^{\text{MB}}\text{-9}$	c_{RAFT}	$1.29 \times 10^{-3} \text{ mol L}^{-1}$				
initiator	AIBN	c_{ini}	$8.61 \times 10^{-4} \text{ mol L}^{-1}$				

$\pi^{\text{MB}}\text{-18}$		RI detector			UV detector		
	t in h	$X_{\text{M,g}}$	\overline{M}_{n} in $\frac{\text{g}}{\text{mol}}$	\mathcal{D}	\overline{M}_{n} in $\frac{\text{g}}{\text{mol}}$	\mathcal{D}	\overline{b}_{cl}
a	4.23	0.380	5.95×10^4	1.60	5.66×10^4	1.65	4.22
b	7.97	0.420	5.20×10^4	1.68	5.20×10^4	1.76	2.28
c	14.7	0.480	5.17×10^4	1.48	5.41×10^4	1.48	2.18

jected directly to SEC analysis. For polymer samples π -1c and π -2 d, the reaction was scaled up by the factor of 4. Here, the work-up was done by repeated precipitation and redissolving as described above for the polymerizations.

3.2.7 Synthesis of AuNPs

3.2.7.1 Gold nanocrystals $_{\text{Au}}^{\text{ci}}\mathbf{v-3}$ by reduction with citrate

Several batches of gold sol were prepared in principle according to the literature-known procedure.^[16,17] The reaction was performed in different scales but identical relative amounts. Below, the values for 630 mL of $_{\text{Au}}^{\text{ci}}\mathbf{v-3}$ are given.

All glassware (including stoppers and stirring bar) was cleaned very thoroughly with aqua regia and then rinsed repeatedly with ultrapure water before use. Then a solution of hydrogen tetrachloroaurate trihydrate (118 mg, 0.300 mmol, 1 eq.) in 600 mL of ultrapure water (prepared by diluting a stock solution of higher concentration) was boiled under reflux for 30 min under vigorous stirring (1200 revolutions per minute). Then a hot ($\approx 90^\circ\text{C}$) solution of sodium citrate tribasic dihydrate (344 mg, 1.17 mmol, 3.9 eq.) in 30 mL of ultrapure water was added, leading to characteristic changes in color (from yellow to colorless, to dark blue, and to orange red). After 30 min of further stirring, the reaction was allowed to cool to room temperature. After every reaction, an optical spectrum was measured and the AuNP from 5 mL of the prepared sol were extracted into chloroform containing octadecylamine following the procedure described in Section 3.2.8.1 and analyzed via TEM, in order to be sure that AuNP with the same quality and size distribution were obtained in each batch. The colloidal gold sols were stored in polypropylene centrifuge tubes in the dark at room temperature.

3.2.7.2 Two-phase Brust–Schiffrin synthesis of 2-phenylethanethiolate-protected gold nanoclusters $_{\text{Au}}^{2\text{bs}}\mathbf{v-5}$

The low-temperature protocol from Zhu *et al.*^[18] (2008) was followed, only scaled up by the factor of 5. A dark-brown solid was obtained. (Attention: 2-phenylethanethiol has an extremely aggressive odor!)

3.2.7.3 One-phase Brust–Schiffrin synthesis of hydroxyl-functionalized gold nanoclusters $_{\text{Au}}^{1\text{bs}}\mathbf{v}^{\text{OH}}\mathbf{-6}$

This reaction resembles in principle the original one-phase Brust–Schiffrin synthesis protocol.^[19]

Hydrogen tetrachloroaurate(III) trihydrate (1.20 g, 3.05 mmol, 1 eq.) was dissolved in 1 L of methanol. 4-mercaptophenol $^{\text{SH}}\lambda^{\text{OH}}\text{-4}$ (916 mg, 7.26 mmol, 2.38 eq.) and 12 mL of acetic acid were added. Then, a solution of sodium borohydride (1.81 g, 47.9 mmol, 15.7 eq.) in 80 mL of ultrapure water was added dropwise under vigorous stirring at room temperature. The solution turned dark brown. After stirring for 50 min, the solvent was removed by rotary evaporation not exceeding the temperature of 40 °C. The dark brown residue was redissolved in a mixture of 80 mL of methanol and 450 mL of acetaldehyde and washed with ultrapure water (3 × 800 mL). The organic phase was dried over sodium sulfate, concentrated by rotary evaporation, and washed with copious amounts of diethyl ether on a fritted-glass funnel. The thus obtained gold nanoclusters $^{\text{lbs}}_{\text{Au}}\nu^{\text{OH}}\text{-6}$ were stored in dry form (dark brown wax) at -18 °C.

The identical reaction was repeated thrice with varying amounts of 3-mercapto-1-propanol (2.1 eq. or 2.5 eq.) as thiol without formation of a stable colloid.

$^1\text{H-NMR}$ (300 MHz, acetone- d_6): $\delta = 7.43\text{--}6.66$ (m, 4 H, $4 \times -\text{CH=}$) ppm.

Elemental analysis: 18.45 % C, 7.47 % S, 1.48 % H
(pure $^{\text{SH}}\lambda^{\text{OH}}\text{-4}$: 57.11 % C, 25.41 % S, 4.79 % H).

3.2.7.4 One-phase Brust–Schiffrin synthesis of 2-phenylethanethiolate-protected gold nanoclusters $^{\text{lbs}}_{\text{Au}}\nu\text{-7}$

The protocol from Wu *et al.*^[20] (2009) was followed, only scaled up by the factor of 2. A dark-brown solid was obtained.

3.2.7.5 Synthesis of gold nanocrystals $^{\text{NH}_2}_{\text{Au}}\nu\text{-8}$ with oleylamine

This reaction was performed several times with different absolute, but identical relative amounts of reagents. By way of example, one exemplary reaction procedure is given here. It resembles in principle the reaction presented by Hiramatsu and Osterloh^[21] (2004). The amounts of oleylamine were corrected based on the purity indication of the supplier.

To a solution of oleylamine (5.43 mL, 3.31 g, 16.5 mmol, 55 eq.) in 98 mL toluene, boiling under reflux, a solution of hydrogen tetrachloroaurate trihydrate (118 mg, 0.300 mmol, 1 eq.) and oleylamine (2.96 mL, 2.41 g, 9.00 mmol, 30 eq.) in 2 mL of toluene was added. The mixture was further stirred under reflux for 165 min. The color changed from colorless to pink and eventually to deep red. The reaction mixture was then cooled to room temperature.

3.2.8 Functionalization reactions

3.2.8.1 Amine-functionalization and transfer of citrate AuNP $_{\text{Au}}^{\text{ci}}\mathbf{v}^{\text{oda}}\text{-4}$

This reaction was originally presented by Karg *et al.*^[22] (2011).

A certain volume of the gold sol $_{\text{Au}}^{\text{ci}}\mathbf{v}\text{-3}$ prepared by citrate reduction (see Section 3.2.7.1) was added to $2/3$ of that volume of a 0.75 mmol L^{-1} solution of octadecylamine in chloroform in a sealable container. The container was closed and directly heavily shaken for 1 min. Hereafter, the aqueous phase had turned colorless and the organic phase had turned deep red. The aqueous phase was separated and discarded.

This reaction was performed several times with different absolute amounts. Typically, 5 mL of gold sol $_{\text{Au}}^{\text{ci}}\mathbf{v}\text{-3}$ were used for the TEM analyses and up to 700 mL of gold sol $_{\text{Au}}^{\text{ci}}\mathbf{v}\text{-3}$ were used to prepare the amine-functionalized AuNPs as precursor for functionalization reactions. When indicated in the text, this reaction was performed with toluene instead of chloroform, but otherwise identically.

3.2.8.2 Immobilization of $\rho^{2\text{x}}\text{-2}$ on $_{\text{SiO}_2}^{\text{fs}}\mathbf{v}\text{-1}$

The same procedure was performed which had been used in previous work.^[23,24] The fumed silica (10 g) was dissolved in 300 mL of toluene. A solution of the RAFT agent $\rho^{2\text{x}}\text{-2}$ (0.66 mmol) in toluene was added dropwise. After addition of a small amount of maleic anhydride in water, the mixture was stirred for 3 h at room temperature. The solvent was removed under reduced pressure and the product $_{\text{Si}}^{\text{fs}}\mathbf{P}^{2\text{x}}\text{-1}$ was washed with dichloromethane in a Soxhlet apparatus.

3.2.8.3 Immobilization of $\rho^3\text{-1}$ and $\rho^1\text{-3}$ on $_{\text{SiO}_2}^{\text{np}}\mathbf{v}\text{-2}$

The silica nanoparticles $_{\text{SiO}_2}^{\text{np}}\mathbf{v}\text{-2}$ (1 g) were transferred from methanol to 50 mL of 1,2-dimethoxyethane by centrifugation and redispersion. The RAFT agent $\rho^3\text{-1}$ with a trimethoxysilyl group (0.165 mg, 0.5 mmol) or the RAFT agent $\rho^1\text{-3}$ with a monofunctional anchor group (0.165 mg, 0.5 mmol) was added dropwise under vigorous stirring. Then, a small amount of maleic anhydride was added and the mixture was stirred for 36 h at room temperature. The functionalized nanoparticles $_{\text{Si}}^{\text{np}}\mathbf{P}^3\text{-2}$ and $_{\text{Si}}^{\text{np}}\mathbf{P}^1\text{-3}$ were purified by repeated centrifugation and redispersion in acetone ($3 \times$).

3.2.8.4 *Ex-situ* two-phase Brust–Schiffrin synthesis

This protocol is based on publications by Manna *et al.*^[25] (2003) and Zhou *et al.*^[26]

(2007). The absolute amounts for the reactions with each ligand were different. The absolute values given here refer to one reaction with **p-4**. For the other reactions the equivalents of the respective ligands are given.

To a solution of hydrogen tetrachloroaurate trihydrate (236 mg, 600 μmol , 1 eq.) in 100 mL of ultrapure water was added a solution of tetraoctylammoniumbromide (1.31 g, 2.40 mmol, 4 eq.) in 100 mL of toluene. The mixture was stirred vigorously for 30 min at room temperature. Hereafter, the previously yellow aqueous phase had turned colorless and the upper organic phase had turned deep red. The lower aqueous phase was removed with a syringe. Under vigorous stirring, a solution of sodium borohydride (0.182 g, 4.80 mg, 8 eq.) in 25 mL of ultrapure water was added drop by drop. The solution was stirred for another 3 h in an argon atmosphere at room temperature and then washed with ultrapure water (3×100 mL). Afterwards, the organic phase was added to a solution of 2-(dodecylthiocarbonothioylthio)-2-methylpropanoic acid **p-4** (438 mg, 1.20 mmol, 5 eq.) or 5 eq. of 11-mercaptoundecanol $\text{SH}\lambda^{\text{OH}}\text{-7}$ or 5 eq. of 1-azidoundecane-11-thiol $\text{SH}\lambda^{\text{N}_3}\text{-9}$ or 0.1 eq. of polyfunctional RAFT agent $\text{p}^{\text{MB}}\text{-8}$ in 100 mL of toluene under sonication and the reaction mixture was stirred overnight in an argon atmosphere at room temperature. The solvent was removed under reduced pressure and the black solid residue was washed with methanol ($\text{SH}\lambda^{\text{OH}}\text{-7}$: toluene) on a glass frit. The AuNPs were redispersed in chloroform ($\text{SH}\lambda^{\text{OH}}\text{-7}$: DMF) and the solution was centrifuged for 3 h to remove potentially existing larger aggregates. The thus prepared AuNPs ${}^{\text{2ebs}}\text{V}_{\text{Au}}^{\text{TTC}}\text{-11}$, ${}^{\text{2ebs}}\text{V}_{\text{Au}}^{\text{OH}}\text{-9}$, ${}^{\text{2ebs}}\text{V}_{\text{Au}}^{\text{N}_3}\text{-10}$, and ${}^{\text{2ebs}}\text{V}_{\text{Au}}^{\text{MB}}\text{-12}$ were stored in dried form at -18°C .

3.2.8.5 Thiols on citrate gold nanoparticles ${}^{\text{ci}}\text{V}_{\text{Au}}\text{-3}$

This procedure is described exemplarily for $\text{SH}\lambda^{\text{OH}}\text{-8}$ as ligand.

To 8 mL of the as-prepared citrate gold sol ${}^{\text{ci}}\text{V}_{\text{Au}}\text{-3}$ (containing approximately 0.7 mg gold) in a polypropylene centrifuge tube, a solution of (11-mercaptoundecyl)-tetra(ethylene glycol) (6.9 mg, 18 μmol) in 1 mL of ultrapure water was added. The mixture was incubated overnight in the dark and the functionalized AuNPs were purified by three centrifugation–redispersion steps (first step, ultrapure water, 8 h, 0°C ; second and third step, methanol, 8 h, -5°C).

3.2.8.6 Polymers on citrate gold nanoparticles ${}^{\text{ci}}\text{V}_{\text{Au}}\text{-3}$

The functionalization reactions were conducted in 50-mL polypropylene tubes under sonication at room temperature. A solution of 30 mg of the respective polymer (see Tables 8.1, 8.2, and 8.3) in 10 mL of ultrapure water (${}^{\text{AuK}}\text{MB}\text{-19}$, in 15 mL of

ultrapure water; $\text{AuK}^{\text{MB}}\text{-18}$, in a mixture of 5 mL of ultrapure water and 5 mL of methanol) was added to 40 mL of gold sol $\text{Au}^{\text{ci}}\text{v-3}$ (containing approximately 3.8 mg of gold) and incubated overnight in the dark at room temperature. The polymer-functionalized AuNP were separated from excess polymer and sodium citrate by three centrifugation–redispersion steps (first step, ultrapure water, 8 h, 0 °C; second and third step, methanol, 8 h, –5 °C). In some cases, the redispersion needed to be aided by sonication. The functionalized AuNP were stored in methanol in the dark at room temperature. For the SEC analyses, the same functionalization procedure was carried out, only that methanol was replaced with DMAc.

3.2.8.7 Surface polymerizations

The procedure was identical to the second described way in Section 3.2.6.1. The polymer-functionalized fumed silica $\text{fs}_{\text{si}}\text{K}^{2\text{x}}\text{-1}$ was isolated from solution polymer by Soxhlet extraction. The polymer-functionalized silica nanoparticles $\text{np}_{\text{si}}\text{K}^1\text{-2}$ were isolated by repeated centrifugation and redispersion in acetone. The detailed polymerization conditions can be found in Tables 7.1 and 7.2.

Recovery of the surface-bound polymer Samples $\text{fs}_{\text{si}}\text{K}^{2\text{x}}\text{-1}$ (a–f) and samples $\text{np}_{\text{si}}\text{K}^1\text{-2}$ (b, c, and e) were dispersed in THF in plastic tubes. Hydrofluoric acid (40 % solution in water) was added and the mixture was stirred for 3 h. The mixtures were poured in aluminum dishes. After they had dried, the samples were redispersed in THF, filtered, and subjected to SEC analysis.^[27]

References for Chapter 3

- (1) Becker, H. G. O., Berger, W., Domschke, G., Fanghänel, E., Faust, J., Fischer, M., Gentz, F., Gewald, K., Gluch, R., Mayer, R., Müller, K., Pavel, D., Schmidt, H., Schollberg, K., Schwetlick, K., Seiler, E., Zeppenfeld, G., *Organikum*, 21th edition; Wiley-VCH: Weinheim, **2001**.
- (2) Rotzoll, R., Vana, P., *Macromol. Rapid Commun.* **2009**, 30 (23, Sp. Iss. SI), 1989–1994.
- (3) Schwabe, M., Rotzoll, R., Kuechemann, S., Nadimpalli, K., Vana, P., Samwer, K., *Macromol. Chem. Phys.* **2010**, 211 (15), 1673–1677.
- (4) Rotzoll, R. *Tailored Silica–Polymer Composites and ABA Type Copolymers: Polymerization Kinetics, Structural Design, and Mechanical Properties*, Ph.D. thesis, Georg-August-Universität Göttingen, **2011**.
- (5) Ebeling, B. *Multiblock-Copolymere durch RAFT-Polymerisation*, thesis, Georg-August-Universität Göttingen, **2009**.
- (6) Ebeling, B., Vana, P., *Polymers* **2011**, 3 (2), 719–739.
- (7) Förster, N. *Nano-Carrier Synthesis via Z-RAFT Star Polymerisation*, Ph.D. thesis, Georg-August-Universität Göttingen, **2012**.
- (8) Förster, N., Pöppler, A.-C., Stalke, D., Vana, P., *Polymers* **2013**, 5 (2), 706–729.
- (9) Neises, B., Steglich, W., *Angew. Chem., Int. Ed.* **1978**, 17 (7), 522–524.
- (10) Shon, Y.-S., Kelly, K. F., Halas, N. J., Lee, T. R., *Langmuir* **1999**, 15 (16), 5329–5332.
- (11) Collman, J. P., Devaraj, N. K., Chidsey, C. E. D., *Langmuir* **2004**, 20 (4), 1051–1053.
- (12) Dess, D. B., Martin, J. C., *J. Am. Chem. Soc.* **1991**, 113 (19), 7277–7287.
- (13) Dess, D. B., Martin, J. C., *J. Org. Chem.* **1983**, 48 (22), 4155–4156.
- (14) Qiu, X.-P., Winnik, F. M., *Macromol. Rapid Commun.* **2006**, 27 (19), 1648–1653.
- (15) Lei, P., Wang, Q., Hong, J., Li, Y., *J. Polym. Sci., Part A: Polym. Chem.* **2006**, 44 (22), 6600–6606.
- (16) Turkevich, J., Stevenson, P. C., Hillier, J., *Discuss. Faraday Soc.* **1951**, 11, 55–75.
- (17) Frens, G., *Colloid Polym. Sci.* **1972**, 250 (7), 736–741.
- (18) Zhu, M., Lanni, E., Garg, N., Bier, M. E., Jin, R., *J. Am. Chem. Soc.* **2008**, 130 (4), 1138–1139.
- (19) Brust, M., Fink, J., Bethell, D., Schiffrin, D. J., Kiely, C., *J. Chem. Soc., Chem. Commun.* **1995**, 16, 1655–1656.
- (20) Wu, Z., Suhan, J., Jin, R., *J. Mater. Chem.* **2009**, 19 (5), 622–626.
- (21) Hiramatsu, H., Osterloh, F. E., *Chem. Mater.* **2004**, 16 (13), 2509–2511.
- (22) Karg, M., Schelero, N., Oppel, C., Gradzielski, M., Hellweg, T., von Klitzing, R., *Chem.—Eur. J.* **2011**, 17 (16), 4648–4654.
- (23) Rotzoll, R. *Oberflächengebundene Polymerschlaufen durch kontrollierte radikalische RAFT-Polymerisation*, thesis, Georg-August-Universität Göttingen, **2007**.
- (24) Rotzoll, R., Vana, P., *J. Polym. Sci., Part A: Polym. Chem.* **2008**, 46 (23), 7656–7666.
- (25) Manna, A., Chen, P., Akiyama, H., Wei, T., Tamada, K., Knoll, W., *Chem. Mater.* **2003**, 15 (1), 20–28.
- (26) Zhou, J., Beattie, D. A., Sedev, R., Ralston, J., *Langmuir* **2007**, 23 (18), 9170–9177.
- (27) Li, C., Benicewicz, B. C., *Macromolecules* **2005**, 38 (14), 5929–5936.

Part III

Results

This is the main part of this thesis, where all results are presented and discussed. First, in Chapter 4, general methods to interpret and analyze the images from transmission electron microscopy and atomic force microscopy are described. The next Chapter deals with the design and the analysis of the building blocks which were used for the experiments in the ensuing chapters. In Chapter 6, the cloud-points of aqueous solutions containing the pNIPAm samples are examined with high-pressure experiments. The synthesized anchor RAFT agents are used in polymerizations from silica surfaces in Chapter 7, followed by Chapter 8, where the smart nanohybrids formed by combining the prepared AuNPs and the pNIPAm samples are studied. Future perspectives building on these results are outlined in Chapter 9 and, ultimately, Chapter 10 provides concluding comments.

Chapter 4

Analysis of microscopic images

This chapter is dedicated to two microscopic techniques which work on the nanometer scale: *transmission electron microscopy (TEM)* and *atomic force microscopy (AFM)*. Micrographs obtained with these techniques play a pivotal role for several discussions in this work. In order to gather the information in one place, make it easier to find, and to not interrupt the flow of the further text, the general workflows to acquire and process the images and extract the desired data and information from them will be explained here. Additionally, the explanations for typical features visible in several unrelated micrographs in the rest of the thesis will be given.

4.1 Analysis of transmission electron micrographs

4.1.1 General information obtained by TEM

The resolving power of any wide-field irradiation microscope has a theoretical Abbe diffraction limit of about the half wavelength of the used radiation. That means that light microscopes are restricted to a resolution of about 250 nm. They are well suited to visualize animal cells ($\approx 10\ \mu\text{m}$) or bacteria ($\approx 1\ \mu\text{m}$), but not the nanostructured systems studied in this work. An electron microscope takes advantage of the fact that the wavelength of electrons which are accelerated by a high voltage is by orders of magnitude lower than that of visible light and thus makes the nanoscale accessible. Apart from the type of the used radiation, the setup is very similar to that of a classic transmission light microscope. As a result, the specimen must be transparent to electrons and thus very thin ($< 100\ \text{nm}$). The best transmission electron microscopes have reached resolutions of below 0.05 nm. Even the TEM imaging of double stranded λ -DNA fibers, revealing the double-helix structure, has recently been presented by Gentile *et al.*^[1] (2012). That makes analysis via TEM a standard technique in nanoparticle research, although it is not common in pure

chemistry. (Another type of electron microscopy—scanning electron microscopy, SEM—is used in Section 7.1.3.) In this work, all TEM specimens were prepared by drop-casting: a drop of the nanoparticle sample in colloidal solution was placed on a copper grid coated with a film of amorphous (= structureless) carbon (10–15 nm) as a substrate and it was waited until the solvent had evaporated. The amorphous carbon film is highly transparent to electrons.

For AuNPs, which were the subject of most TEM analyses in the presented work, rough information about their shape and size can also be acquired with different indirect spectroscopic,^[2] chromatographic,^[3] and scattering^[4,5] methods. In particular, optical photospectroscopy exploiting the plasmon resonance effect (see Section 1.2.3.2) was used as fast and easy method for AuNP analysis in this work. It can be seen as complementary to TEM as it does not suffer from the problem that only separated spots of the specimen, which may not be representative, are visualized. It quickly gives information on collective properties such as the degree of aggregation. On the other hand, some samples in this work featured almost identical optical spectra (in the same solvent), but had a completely different appearance under the TE microscope. Only with TEM, true size and shape distributions with assessment of the homogeneity (see Section 4.1.4) are accessible (in addition to the satisfying situation of actually “seeing” the studied samples). Moreover, particles that are smaller than 1 nm or bigger than 200 nm and non-metal impurities are invisible in the optical spectrum, and it is very dependent on the used solvent. The structure of complex nanocomposites can almost exclusively be elucidated with TEM.

The general set-up of a transmission electron microscope and the two major operation modes, which differ in the strength (focal width) of the intermediate lens, are illustrated schematically in Figure 4.1. This work features lots of images taken in *imaging mode*, in which the image plane of the objective lens, where beams with all angles that come from the same point of the specimen meet again, is magnified, leading to a triply magnified image on the screen. A magnified projection of the examined samples is obviously most useful for the analysis of functionalized nanoparticles. But also the *diffraction mode* gives useful information, namely on the crystallinity of the analyzed particles. This shall be demonstrated exemplarily here for AuNPs $\text{Au}^{\text{ci}}\mathbf{v}-3$ from citrate reduction, since the results are generally the same for all examined gold nanocrystals. (More information and images for $\text{Au}^{\text{ci}}\mathbf{v}-3$ can be found in Section 5.1.2.) In diffraction mode (Figure 4.1 right), the back focal plane of the objective lens, where all beams which were scattered from the specimen with the same angle are focused to one point, corresponds to the image plane of the intermediate lens and a doubly magnified diffraction pattern can be observed on the screen. The diffraction pattern for gold nanocrystals $\text{Au}^{\text{ci}}\mathbf{v}-3$ is

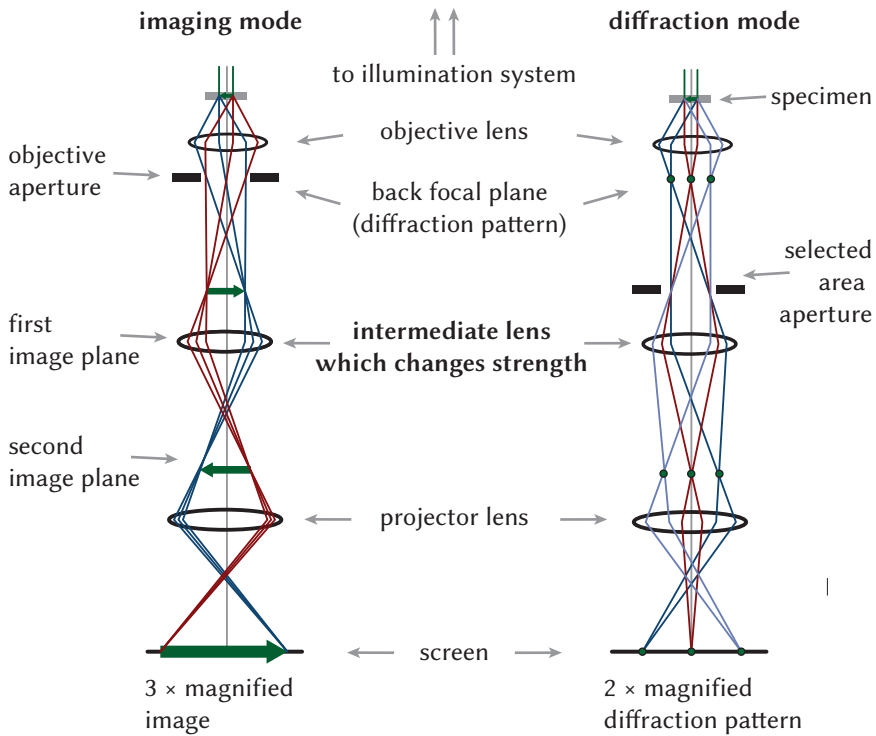


Fig. 4.1: General set-up of a transmission electron microscope, showing the two major operation modes. In imaging mode (same color for beams from same spot), a 3 × magnified image is projected on the screen, in diffraction mode (same color for beams with same angle), a 2 × magnified diffraction pattern is produced.

shown in Figure 4.2. In this image, the central spot is blocked by a beam stopper. The visible diffraction pattern is caused by the scattering of electrons by the gold atoms in the polycrystalline AuNPs.^[6] Because of the large number of different orientations of the crystal planes to the electron beam (polycrystalline particles in random orientations), the Bragg reflexes appear on concentric circles. The radial intensity distribution which was calculated from the whole image, is shown as white overlay. This distribution corresponds clearly to a face-centered cubic (fcc) lattice. On the right of Figure 4.2, the lattice planes—defined by the Miller indices h , k , and l —were assigned to the individual peaks based on their relative positions. (Reciprocal space: Planes with higher distance give reflexes closer to the center.) An

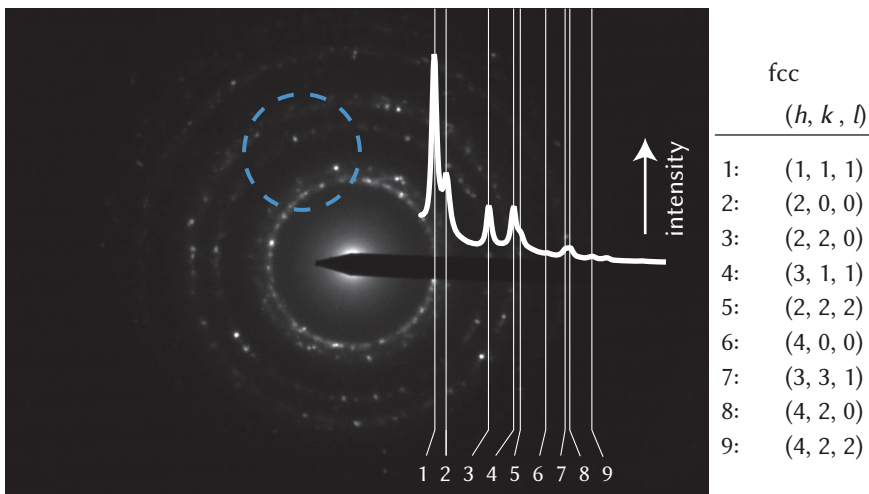


Fig. 4.2: Diffraction pattern of polycrystalline AuNPs $\text{Au}^{\text{ci}}\text{v}-3$ with radial intensity distribution as overlay in white. A beam stopper is visible blocking the central spot. The reflexes are assigned to the Miller indices h, k, l of the corresponding planes of the face-centered cubic (fcc) lattice. The dashed, blue circle indicates the position of the objective aperture for the image in Figure 4.5b.

identical diffraction pattern was observed for all gold nanocrystal samples. All gold nanoclusters such as for example $\text{Au}^{\text{lbs}}\text{v}^{\text{OH}}-5$ (see Section 5.1.3.2) did not exhibit a diffraction pattern different from the empty carbon film. This shows very well that the occurrence of a plasmon resonance signal is correlated to the conduction band of gold atoms being arranged in a (fcc) lattice (see Section 1.2.3.2).

To also calculate the lattice constant from a diffraction pattern as in Figure 4.2, the instrument would have had to be calibrated with a reference substance before, which was not the case. However, that the particles were really composed of gold is not only clear from the context and their high contrast, but could also be evidenced by the emitted characteristic X-rays that can be detected with the *energy-dispersive X-ray (EDX)* detector when particles are in the electron beam. Figure 4.3 shows the EDX spectra of an empty spot in comparison with a spot with AuNPs. The energy of the X-ray signals is characteristic for the atomic structure of the atom from which it was emitted, as it equals the energy difference between particular shells. The electron beam stimulates the emission of characteristic radiation. Here, the signals can be clearly assigned to gold (Cu: carrier grid, Si: grease).

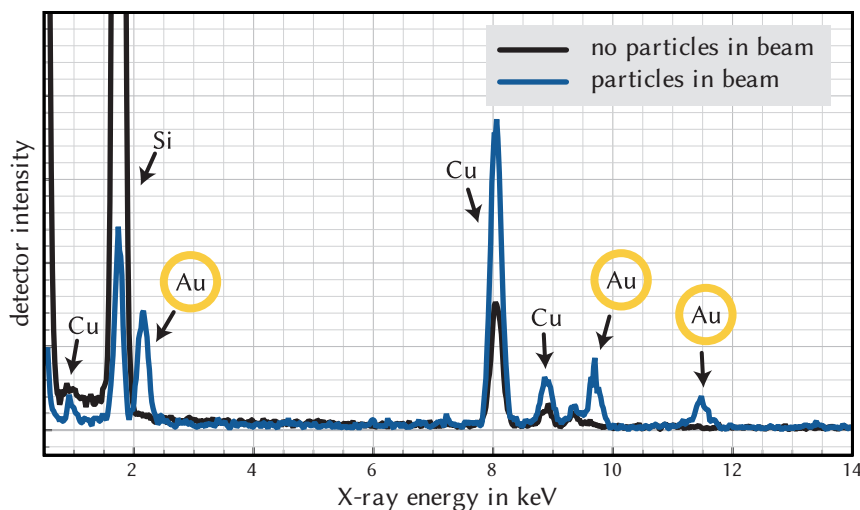


Fig. 4.3: Energy-dispersive X-ray spectra with and without AuNPs in the electron beam. From the emitted characteristic X-rays, it can be deduced that the particles are composed of gold. Here, the actual sample is $\text{Au}^{\text{ci}}\text{V}^{\text{OH}}\text{-13}$ (see Section 8.2.1.2). Three corresponding micrographs can be seen in Figure 8.6.

In imaging mode with only the selected area aperture in the electron beam, the Bragg reflexes appear as bright spots which move over the image when the focus is adjusted. In order to remove the overlying reflexes from the image, an *objective aperture* can be inserted in the back focal plane of the objective lens (see Figure 4.4), so that only the central beam in the diffraction pattern can pass, leading to reflex-free, contrast-enhanced *bright-field images*. If not stated otherwise, all TE micrographs in this work were recorded with this configuration. Such a bright field image of AuNP sample $\text{Au}^{\text{ci}}\text{V-3}$ is shown as micrograph (a) in Figure 4.5. (The circle around the image is the selected-area aperture. It was inserted in the image plane of the objective lens to ensure that all signals come exclusively from the same selected spot.) A characteristic formation of several magnified gold nanocrystals can be seen. The crystal planes of the different homogeneous crystal regions have different orientations to the electron beam and appear darker or brighter, leading to the patterned look, which is typical for polycrystalline particles. Furthermore, regions are darker where the particles overlap. Since their projections are close to circular,

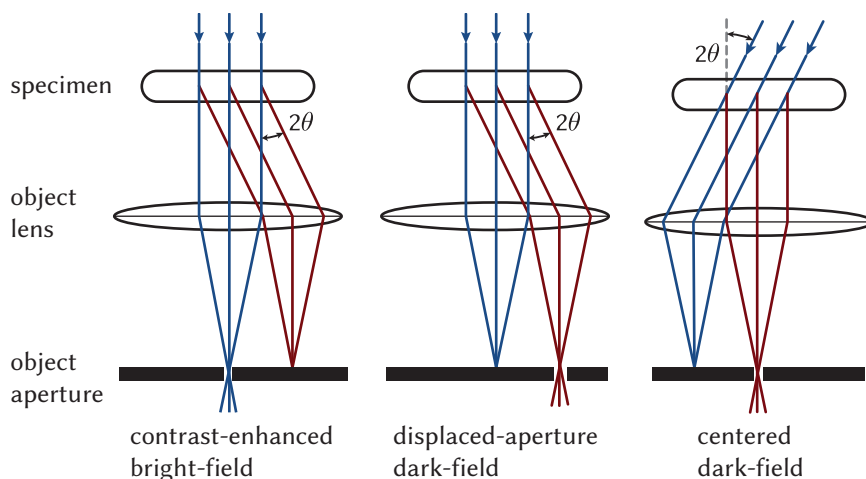


Fig. 4.4: Alignment of electron beam path and objective aperture for different types of TEM imaging modes (compare with Figure 4.1). θ denotes the diffraction angle. The scattered beams are shown in red, the unscattered beams in blue. The recorded images corresponding to these schematics are shown in Figure 4.5.

it can be deduced that the particles have approximately spherical shape.* If the objective aperture is shifted so that now the central beam is blocked in the diffraction pattern and only scattered electrons are let through (position indicated by dashed, blue circle in Figure 4.2), the reflexes form a so-called *displaced-aperture dark-field image* (Figure 4.5b). Due to off-axis aberrations, this micrograph looks somehow distorted. It can be improved by tilting the electron beam over the specimen instead, so that now the scattered electrons go through the center of the objective lens and the centered objective aperture (compare again Figure 4.4). Such a *centered dark-field image* is shown in Figure 4.5c. The characteristic AuNP formation can be recognized again. Dark-field images are for example very helpful to identify crystalline in mixtures with non-crystalline nanoparticles.

4.1.2 Alteration of samples in the microscope

In a TE microscope the sample is inherently heated by the high-energy electron beam. It has to be noted that this effect can change the sample in the observed

*Theoretically, oblate spheroids are projected to circles as well, only the projection of a prolate spheroid is an ellipse.

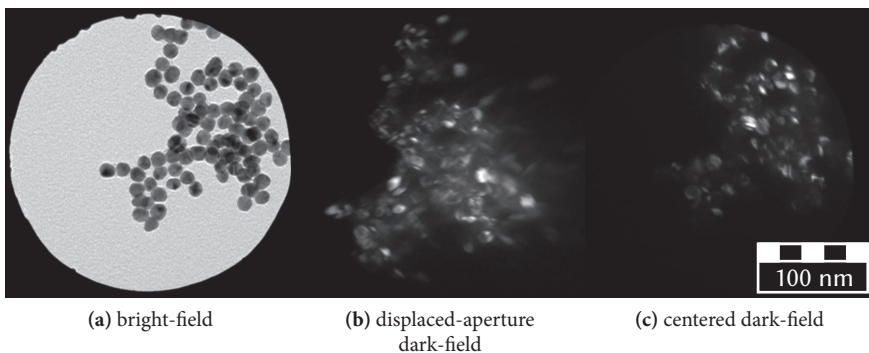
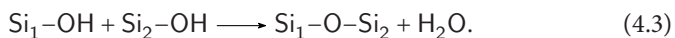
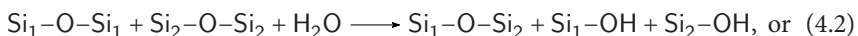
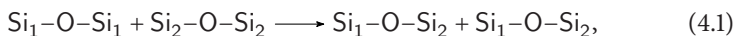


Fig. 4.5: Micrographs of AuNPs (sample $\text{Au}^{\text{ci}}\nu-3$, see Section 5.1.2) in different imaging modes. The electron beam paths in these modes are illustrated schematically in Figure 4.4. The position of the aperture for the second image is indicated as dashed, blue circle in Figure 4.2. For the other two images, the objective aperture was placed around the central beam. In the bright-field micrograph, the selected-area aperture is visible (circle). The spot (and scale) is the same for all three micrographs.

spot. Melting/fusion was observed for silica nanoparticles and small AuNPs. It is demonstrated in Figure 4.6 for silica nanoparticles $\text{SiO}_2^{\text{np}}\nu-2$. They are used for surface polymerizations in Section 7.2. Micrograph (a) was taken immediately after selection of the spot. The particles in this image are larger than the AuNPs in Figure 4.4 but they appear brighter nevertheless. The interaction of matter with the electron beam scales roughly with the atomic number squared and silica produces less contrast than gold. The same effect makes it very hard to visualize organic polymers in the presence of metal particles. The visible particles in the figure appear darker in the center, because here the electrons pass a longer path through the material than on the edges. Notably, there is no spacing between the visible particles. The micrograph in Figure 4.6b shows the same spot after approximately 5 min of irradiation. Fusion of molten particles can be seen.

The coalescence of two silica surfaces (with the silicon atoms Si_1 and Si_2) can occur according to three sintering mechanisms:^[7]



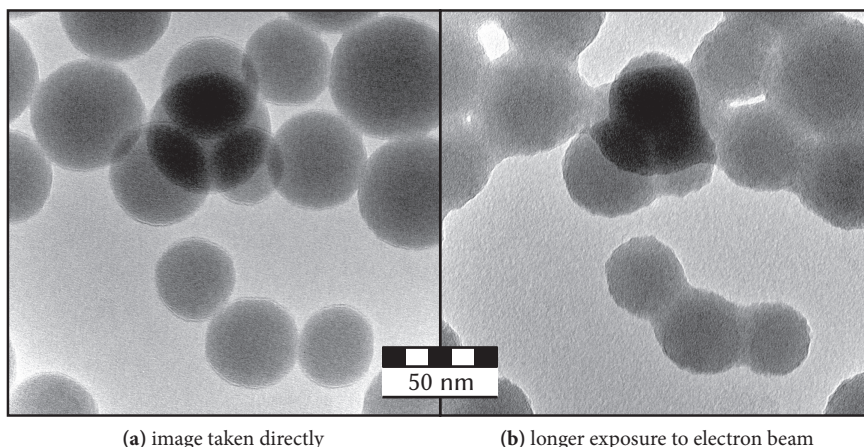


Fig. 4.6: “Melting” and fusion of silica nanoparticles $\text{SiO}_2^{\text{npv-2}}$ under the electron beam. The same spot was irradiated for approximately 5 min.

Considering that the observed fusion takes place in an evacuated TE microscope, reaction (4.1) and reaction (4.3) seem most likely. It is important to be fast at taking the microscopic photographs, when such alterations are observed.

4.1.3 Self-assembly of nanoparticles in TE micrographs

In a typical TEM specimen, the nanoparticles are found in really concentrated regions, lying close to but not on top of each other, while other regions are almost empty. This effect is often called “islanding”.^[8] For very pure samples, homogeneous objects may even self-organize into close-packed hexagonal lattices^[9] on the carbon film, so-called “superlattices”.^[10,11] In several TE micrographs shown in this work, islanding or superlattices are visible: Figures 4.7, 5.3, 5.7, 5.10, 7.5, 8.2, 8.6, 8.9, 8.11, 8.10, and 8.18.

Three different reasonable mechanisms explaining the described behavior can be discussed. All mechanisms assume the structures to be formed in the process of the sample preparation by drop-casting, while the solvent is evaporating:

- The nanoparticles are moving around in the droplets by Brownian motion and repeatedly hit the surface. They need to lose their kinetic energy to come to a rest. This happens by inelastic collisions with already deposited seed particles which grow to increasingly larger aggregates by this mechanism.

- The nanoparticles only settle on the surface after the solvent droplets are completely evaporated. The positions of the nanoparticle islands are reminiscent of the positions of the evaporating droplets, in which the nanoparticles are gradually pushed closer to each other.
- The nanoparticles float on the surface of the solvent droplets where they cluster together because of attractive forces like van-der-Waals interactions^[12] or in particular the so-called “Cheerios effect”,^[13] which is termed after the observation that breakfast cereals form islands on the surface of the milk as a consequence of the irregularity of the meniscus.^[14] When the solvent evaporates, these layers are deposited as a whole.

Independent of the explanation, this effect is very helpful to evaluate the distances in these layers (see Section 8.3.2.1) to gain information on the substances on the particle surface, and also to evaluate single micrographs with many particles to extract size and shape distributions, which is shown in the next section. On the other hand, this phenomenon is also the cause of potential bias since only certain fractions of a sample might selectively self-organize in these assemblies.

4.1.4 Semi-automatic particle size and shape analysis

4.1.4.1 Extraction of characteristic parameters

For functionalization reactions with nanoparticles, it is crucial to have a detailed knowledge of their size and shape parameters, such as the surface area S . For example, if the examined particles turn out to have a diameter of 6 nm instead of expected 3 nm, one already needs 4 times the equivalents of a surface functionalization agent for the same nanoparticle mass, since the surface of a sphere scales with the square of its diameter. A precise diameter distribution is also indispensable to assess the reproducibility of a synthesis procedure or to check if parts of the material are lost when it is purified by centrifugation.

The “selective spot problem” inherent in TEM analysis can only be overcome by examining a large number of particles of a given sample. But this work is so tedious that it is practically impossible to perform by hand. It will be demonstrated in the following, how TE micrographs of nanoparticles—exemplarily for the silica nanoparticles SiO_2^{np} v-2—can be analyzed semi-automatically, allowing the evaluation of large numbers, so that distributions of several size and shape parameters can be obtained.

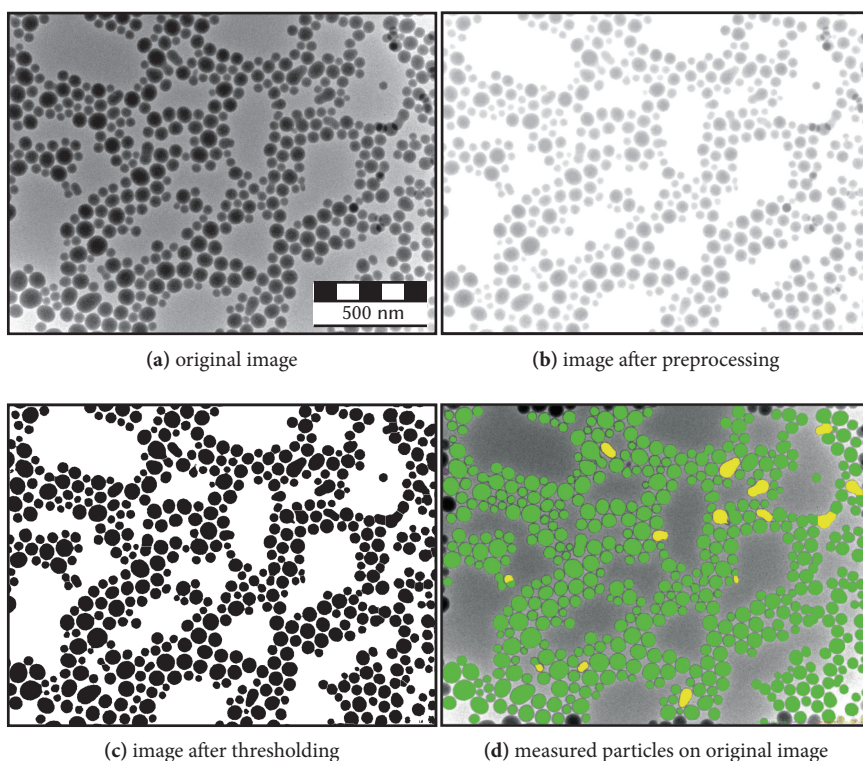


Fig. 4.7: Demonstration of image processing and evaluation for a micrograph of silica nanoparticles $\text{SiO}_2^{\text{np}}\text{v}-2$. Note that the image is not evenly lit. The scale bar was added as an overlay after the processing and applies to all micrographs. The image was preprocessed by background removal (inverted Gaussian) and median smoothing. Micrograph (d) shows the measured particles as green overlay on the original image. Note that particles on the edge are automatically excluded. Touching particles were separated by the watershed filter. In total, 506 particles were counted on this image. The objects colored in yellow were automatically excluded thanks to the circularity criterion (see Section 4.1.4.2).

The first step is just to take several microscopic photographs featuring many nanoparticles. For an image to be suitable for the particle analysis, it should meet the following requirements:

- The image must be representative for the sample. This is especially difficult since particles of comparable sizes tend to agglomerate with each other.^[15]

These homogeneous regions must not be given the preference. The selection of photographed spots is an inevitable human bias, unless the sample is so densely covered (but still without stacking) that random positions can be taken. And even randomly taken micrographs can lead to biased distributions because certain fractions of the sample might preferably be found in larger assemblies, which are very improbable to hit randomly.

- The image must be taken in a magnification at which the smallest present particles are visible.^[16]
- The particles on the image must not be altered by the electron beam (compare Section 4.1.2).
- The objects must not be blurred by a moving image or too high exposure times. Otherwise they appear to be too large.
- The image must be in focus. Underfocused objects appear smaller than they really are, because they feature a bright fringe—a so-called “Fresnel” fringe—around them, which is caused by diffraction on the edge. (The same holds true for visible objective astigmatism.)
- The image should feature the lowest possible degree of particle overlapping or stacking. Overlapping particles can seem to be one larger particle (or two smaller particles when a watershed filter is applied).

An example for a micrograph of silica nanoparticles $\text{SiO}_2^{\text{np}}\nu\text{-2}$, which fulfills the above listed criteria, is image (a) in Figure 4.7. It was taken with a 53 000-fold magnification (referring to the native screen).

In the demonstrated workflow, the processing of the images is done using by the particle analyzer included in IMAGEJ,^{*} a fully-programmable free and open-source image-analysis software with a large worldwide user community, originally developed by Wayne Rasband at the NATIONAL INSTITUTES OF HEALTH in Maryland, US. Being based on Java, it runs on almost any platform and it can be easily extended by additional macros and plugins. This program offers some automated features itself, but they are still quite cumbersome to use, especially since several operations have to be performed by hand for each micrograph. The work is further facilitated by the PARTICLE SIZE ANALYZER MACRO FOR IMAGEJ (“PSA macro”)[†], developed at the Institut Català de Nanotecnologia[‡] in Bellaterra (Barcelona), Spain, by Ralph Sperling.

^{*}<http://rsb.info.nih.gov/ij/>

[†]<https://code.google.com/p/psa-macro/>

[‡]<http://www.nanocat.org>

It gives interactive help with setting the scale, performs automatic preprocessing (background removal and smoothing) and interactive thresholding (division into black and white pixels). It then activates IMAGEJ's built-in nanoparticle analyzer, taking into account different exclusion criteria and optionally applying a watershed-ding (separation of overlapping particles) filter, and processes the acquired data. The process of image preprocessing by inverted Gaussian background removal and median smoothing, thresholding, and automatic particle measurement is shown in images (b), (c), and (d) of Figure 4.7. Eventually, a table is obtained containing several characteristic parameters for each individual nanoparticle. These can be directly related to the particles by the numbers written on the processed image (not shown). This list of parameters is then edited by spreadsheet processing. The process should be repeated with additional micrographs until the average values of the parameters no longer change.

4.1.4.2 Explanation, calculation, and interpretation of parameters

Please refer to the documentation on the homepage for information on how to use the PSA macro. Here, only aspects are explained which are not covered in the documentation, in particular how the different parameters are obtained, how they can be interpreted, and what can be calculated from them.

The area A of the measured nanoparticle is calculated directly by counting the number of black pixels. (The length of the pixels is set in the first step.) From this, the circle-equivalent (area-equivalent) diameter $2r$ can be calculated by

$$2r = 2\sqrt{\frac{A}{\pi}}. \quad (4.4)$$

The circle-equivalent diameter is the diameter of the circle with the same area A as measured for the nanoparticle. In the case of an ellipse, this value would be equivalent to the mean value of the lengths of major and minor axis.

The sphere-equivalent volume is then calculated from the area A in the same way:

$$V = \frac{4}{3\sqrt{\pi}} A^{\frac{3}{2}}. \quad (4.5)$$

Only for perfectly spherical nanoparticles are these functions absolutely accurate. However, when examining large numbers of nanoparticles, deviations from spherical shape will even out, as long as they are not systematic. In this regard, oblate spheroids (although very hard to produce) are especially deceptive shapes, since

they are not distinguishable from spheres in their projection. Oblate spheroids can possibly be identified when they are erected in aggregates.

The perimeter L is calculated automatically by counting the black pixels adjacent to white pixels. This value is mainly useful for the calculation of the circularity C , which is defined as

$$C = \frac{4\pi A}{L^2}. \quad (4.6)$$

In the case of a perfect circle, the value would be $C = 1$. For less circular objects, it decreases down to a theoretical limiting value of $C = 0$ for a straight line of infinite length. The circularity is a powerful exclusion criterion for the automated analysis, since aggregates, most contaminative objects, and scale bars will have a lower circularity than spherical particles. Exploiting this fact, it is often possible to analyze images featuring unwanted particle aggregates and measure exclusively the individual particles. A minimum circularity of $C = 0.8$ is a good value for spherical nanoparticles. Conversely, it might be possible to only analyze the aggregates or other non-spherical objects by setting a maximum circularity. Note that particles with a rough surface tend to have a very high perimeter and thus a very low circularity. For the same reason, low-resolution images often produce higher circularities, because the unevennesses of the surface is not resolved.

Two other shape descriptors are obtained by applying IMAGEJ's ellipse fitting function. The aspect ratio is the length of the major axis divided by the length of the minor axis, both referring to the best elliptical fit. The roundness is its inverse value. Both aspect ratio and roundness can assume values from 1 to 0, 1 being closest to spherical shape. If these values are systematically different from 1, but with a low spread, this is a good indicator for prolate ellipsoidal nanoparticles. The solidity s is the area A divided by the area A_{con} of the convex hull:

$$s = \frac{A}{A_{\text{con}}}. \quad (4.7)$$

The convex hull can be thought of as a rubber band wrapped tightly around the nanoparticle's projection. Its area can only be higher than the actual area of the nanoparticle's projection:

$$A_{\text{con}} \geq A. \quad (4.8)$$

The solidity expresses only the roughness of the surface, as opposed to aspect ratio and roundness, which only describe the general shape. The circularity C is affected by both the surface roughness and the general shape.

All parameters listed above are determined automatically by IMAGEJ and the PSA macro. Further parameters, which are potentially more important for the functionalization reactions, are calculated from these values by spreadsheet processing. As

mentioned above, the surface area S per particle is especially important to know. Assuming spherical shapes, it is obtained from the circle-equivalent diameter $2r$ by

$$S = 4\pi r^2. \quad (4.9)$$

With regard to surface functionalization reactions, the curvature κ of the surface might be an important factor. For surface curvatures, two different definitions—the Gaussian curvature κ_G and the mean curvature κ_m —are in use. They are calculated by

$$\kappa_G = \frac{1}{2r} \quad (4.10)$$

and

$$\kappa_m = \frac{1}{4r^2}, \quad (4.11)$$

assuming spheres.

The masses of the individual nanoparticles are directly obtained from the volumes, when the nanoparticles' density ρ is known:

$$m = \rho \times V. \quad (4.12)$$

If the nanoparticles are large enough to be analyzed by the presented method, their density should almost coincide with the density of the bulk material. For silica nanoparticles, a density of $\rho_{\text{SiO}_2} = 2.65 \text{ g cm}^{-3}$ and for AuNPs a density of $\rho_{\text{Au}} = 19.3 \text{ g cm}^{-3}$ were used. Once the nanoparticle's mass is known, the specific surface S_m is accessible via

$$S_m = \frac{S}{m}. \quad (4.13)$$

The number N_p of atoms or, more generally, molecular units of which each nanoparticle is composed, can be calculated from the particle masses m using the molar mass M :

$$N_p = \frac{m}{M}. \quad (4.14)$$

Finally, the fraction of atoms, or molecular units, situated on the surface of the nanoparticles N_s is a key value, since it corresponds to the number of available binding sites in surface modification reactions. Knowing ρ_p , the “planar density” or number of surface units per area, the formula is

$$N_s = S \times \rho_p. \quad (4.15)$$

The planar density $\rho_{\text{p,SiO}_2}$ of silica, sometimes called “silanol number”, obviously depends on the exact silica modification. Zhuravlev^[17] (1987) measured $\rho_{\text{p,SiO}_2}$

for 100 different silica samples with surface areas ranging from 9.5 to 950 g m⁻² by determining the ratio of the specific concentration of silanol groups (from hydrogen–deuterium exchange) and the specific surface area (from nonspecific adsorption of Kr atoms with the Brunauer-Emmett-Teller (BET)^[18] method). For all 100 examined samples, they obtained values which are very close to the average value of

$$\rho_{\text{p,SiO}_2} = 4.9 \times 10^{18} \text{ m}^{-2}. \quad (4.16)$$

This average value is also assumed for the silica samples in this thesis.*

The number of gold atoms per surface area $\rho_{\text{p,Au}}$ can be calculated assuming a (1, 1, 1) (hexagonal) gold surface with the lattice constant a . If a rectangle is drawn on the hexagonal lattice so that one side connects the centers of two adjacent gold atoms (length: a) and the other side connects these centers with the centers of the gold atoms in the row after the next one (length: $2a$), the area of this rectangle, $a \times 2a = 2a^2$, contains exactly $1 + 4 \times \frac{1}{4} = 2$ gold atoms. The planar density $\rho_{\text{p,Au}}$ is therefore

$$\rho_{\text{p,Au}} = \frac{2}{2a^2} = \frac{1}{a^2} \stackrel{a=2.88 \text{ \AA}^{[20]}}{\approx} 1.21 \times 10^{19} \text{ m}^{-2}. \quad (4.17)$$

After the calculation of all parameters, they can be given in the form of a detailed histogram with suitable binning (combination into groups for histogram bars), as is done in the next chapter for AuNP diameters, surface areas, and masses (see 5.5 and 5.6). Usually, it is sufficient to list the mean values along with the standard deviation σ , the most commonly used measure of spread from the average. It is the square root of the variance of a distribution:

$$\sigma = \sqrt{\frac{\sum_i (x_i - \bar{x})^2}{N - 1}}. \quad (4.18)$$

Here, x_i are the individual values, \bar{x} is their average, and N is the total number of data points. In this work, experimentally determined values are given with a confidence interval of 2σ in the form

$$\text{result} = \bar{x} \pm \sigma.$$

For a normal distribution, 68.27 % of the values lie within this margin. When the range is doubled, it covers 95.45 % of all values.[†]

To complete this section, all parameters for sample $\text{SiO}_2^{\text{np}}\mathbf{v-2}$, extracted from the micrograph shown in Figure 4.7 and 10 others as described, are listed in Table 4.1.

*Note that not all silanol groups are usually accessible in functionalization reactions.^[19]

[†]The standard deviation does not express the margin of error here. The confidence region only covers the spread caused by intrinsically distributed values. The error of measurement is neglected.

Tab. 4.1: Determined size and shape parameters for sample $\text{SiO}_2^{\text{NP}}\text{v-2}$. 11 micrographs, one of them shown in Figure 4.7, featuring a total of 6 257 silica nanoparticles were evaluated.

parameters	values
diameter $2r$	$(50 \pm 12) \text{ nm}$
circularity C	0.87 ± 0.04
surface area	$(8\,500 \pm 4\,500) \text{ nm}^2$
aspect ratio	1.1 ± 0.1
roundness	0.92 ± 0.08
solidity s	0.95 ± 0.02
mean curvature κ_m	$(2.1 \pm 0.7) \times 10^{-2} \text{ nm}^{-1}$
Gaussian curvature κ_G	$(4.9 \pm 5.3) \times 10^{-4} \text{ nm}^{-2}$
volume V	$(8.1 \pm 7.5) \times 10^4 \text{ nm}^3$
particle mass m	$(2.1 \pm 2.0) \times 10^{-16} \text{ g}$
specific surface S_m	$(48 \pm 15) \text{ m}^2 \text{ g}^{-1}$
SiO_2 units per particle N_p	$(2.1 \pm 2.0) \times 10^6$
SiO_2 units on surface	$\approx 2 \%$

4.2 Processing of atomic force micrographs

Atomic force microscopy (AFM) belongs to the group of scanning probe microscopy techniques. The topographical information is gathered by moving an extremely sharp tip mounted on a flexible cantilever very closely over the surface. Forces between the tip and the surface lead to a deflection of the cantilever, which is measured by a laser being reflected from the top of the cantilever to a photodiode. AFM allows for the analysis of non-conductive surfaces with a resolution of below 1 nm. Very recently, de Oteyza *et al.*^[21] (2013) could provide the very first AFM images with atomic scale of an actual chemical reaction taking place with formation of covalent bonds and Zhang *et al.*^[22] (2013) presented the first images of intermolecular hydrogen bonds. In the more related field of AuNP synthesis, Wei *et al.*^[23] (2012) were able to monitor and visualize the growth of gold nanorods on a surface using AFM.

The topographical information is usually represented in the form of a two-dimensional height map. Some programs can also produce three-dimensional projections of the nanosized scene. This representation, with an appropriately scaled z -dimension that does not distort the image, can provide much more meaningful

information when nanoobjects are pictured, since one gets a better impression of their three-dimensional shape and immediately sees if objects are, for instance, really spherical. However, these images have the inherent drawback that the scene can only be viewed from a certain angle and distance. One could show the most information by presenting the AFM scenery in the form of a rotatable and zoomable three-dimensional object, for example in the supporting information of a publication. However, no special software should be required on the receiving side.

In the following, a workflow based exclusively on the use of free software* is presented, which allows the conversion of an AFM image into a three-dimensional model, which can then be embedded in a PDF file. ADOBE READER is probably already installed on the majority of personal computers, independent of the used platform. This program actually includes an integrated and very sophisticated interactive viewer for three-dimensional models.

The workflow starts with GWYDDION,[†] a multi-platform software for the processing, visualization, and analysis of data from scanning probe microscopy techniques. This program has established itself as the standard software for AFM image processing, similar to IMAGEJ for transmission electron microscopy. It can open AFM data recorded with almost any AFM control program. With GWYDDION, the AFM image can be opened, manipulated as desired, and then exported as an ASCII data matrix of z values separated by spaces (export as data type: “.txt”). Within this thesis, a PYTHON script is provided, which was written in collaboration with *Martin Eggers*.[‡] Applying this script, a polygon mesh (a collection of vertices, edges and faces) in the form of a .obj file can be created from the .txt file output from GWYDDION. The complete code of the conversion script can be found in Appendix A of this thesis. The script can also be downloaded as extra material from <http://extras.springer.com/>.

Having navigated to the folder where the script is located and possessing the necessary rights (“chmod +x AFMconvert.py” on UNIX-like systems), the script can be executed with “./AFMconvert.py [file-to-convert].txt --[option]”.

The optional arguments are:

- help, -h – Shows the help message and exits. No positional argument needed.
- scale [s], -s [s] – Scaling factor to be applied to the data in z direction.
- size [z], -z [z] – Size of the broader edge of the AFM scan in m.

*See <https://www.gnu.org/philosophy/free-sw.html>.

[†]<http://gwyddion.net>

[‡]Martin Eggers, Technical University München, eggerts@in.tum.de.

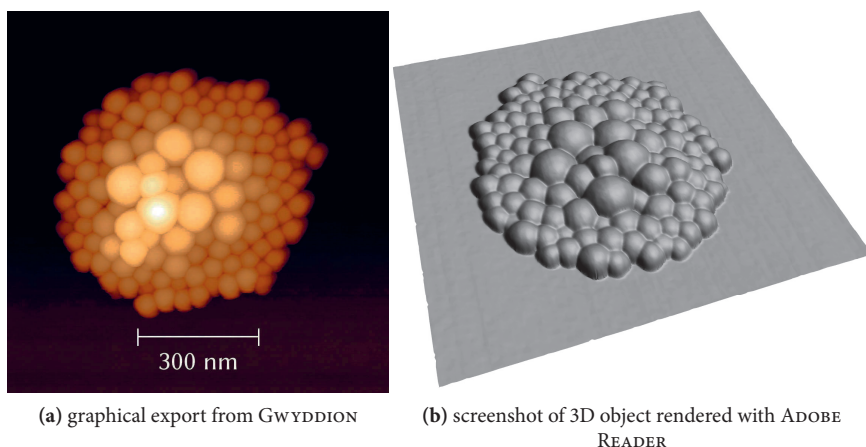


Fig. 4.8: Demonstration of the conversion of AFM images to three-dimensional meshes. (a) is a regular height-map export from GWYDDION. (b) is a screenshot from the same scene, embedded as a three-dimensional object in a PDF file, as rendered by ADOBE READER.

`--recenter, -r` – Adjust origin to match the center of the created mesh.

The only argument that is normally needed is “`--size`”. If it is not provided, a distorted object will be generated. (GWYDDION saves only the z values of the AFM data. The edge length must be noted by hand, for example as part of the file name.)

The produced `.obj` file can then be opened in MESHLAB,* the leading open source mesh processing software, available for all common operating systems. With this program, the mesh can be further modified—typically slightly smoothed or reduced in the number of faces—and then exported as `.U3D` file. Objects of this type can be embedded in PDF files (supporting informations, slides for talks, ...) using L^AT_EX. This way, also the initial view settings or certain camera movements can be defined.

The process is demonstrated for silica nanoparticles SiO_2^{np} v-2, which were also the exemplary objects in Section 4.1.4, in Figure 4.8. They were spin-coated on glass disks from methanol and measured in peak-force tapping mode. Figure 4.8a is a normal graphical height-map export from GWYDDION. Figure 4.8b shows a screenshot from ADOBE READER rendering the three-dimensional object embedded in a PDF file with the standard settings. With ADOBE READER, the object in the

*<http://meshlab.sourceforge.net/>.

original file can be rotated and zoomed, the lighting can be changed, and much more.

Another use of an AFM image converted into a three-dimensional object can be seen on the cover of this thesis. The cover illustration was created by importing a .obj mesh (from an AFM image showing the nanohybrids $\text{AuK}^{\text{TTC}}\text{-14}$, see Section 8.3.2.1) into BLENDER*, a free cross-platform computer graphics program which can be used for the high-quality rendering of 3D scenes and animations, and placing the text and the “hairy nanoparticle” on top of it. Using BLENDER, one could also easily apply textures or materials on the surface or create a video of the rotating object.

*<http://www.blender.org>.

References for Chapter 4

- (1) Gentile, F., Moretti, M., Limongi, T., Falqui, A., Bertoni, G., Scarpellini, A., Santoriello, S., Maragliano, L., Proietti Zaccaria, R., Fabrizio, E. di, *Nano Lett.* **2012**, 12 (12), 6453–6458.
- (2) Yu, L., Andriola, A., *Talanta* **2010**, 82 (3), 869–875.
- (3) Hinterwirth, H., Wiedmer, S. K., Moilanen, M., Lehner, A., Allmaier, G., Waitz, T., Lindner, W., Lämmerhofer, M., *J. Sep. Sci.* **2013**, 36 (17), 2952–2961.
- (4) Khlebtsov, B., Khlebtsov, N., *Colloid J.* **2011**, 73 (1), 118–127.
- (5) Murawska, M., Skrzypczak, A., Kozak, M., *Acta Phys. Pol. A* **2012**, 121 (4), 888–892.
- (6) Zhou, C., Yu, J., Qin, Y., Zheng, J., *Nanoscale* **2012**, 4 (14), 4228–4233.
- (7) Israelachvili, J. N., *Intermolecular and Surface Forces*, 3rd edition; Elsevier: Amsterdam, **2011**.
- (8) Leff, D. V., Brandt, L., Heath, J. R., *Langmuir* **1996**, 12 (20), 4723–4730.
- (9) Korgel, B. A., Fullam, S., Connolly, S., Fitzmaurice, D., *J. Phys. Chem. B* **1998**, 102 (43), 8379–8388.
- (10) Collier, C. P., Vossmeier, T., Heath, J. R., *Annu. Rev. Phys. Chem.* **1998**, 49 (1), 371–404.
- (11) Pileni, M. P., *J. Mater. Chem.* **2011**, 21 (42), 16748–16758.
- (12) Hamaker, H., *Physica* **1937**, 4 (10), 1058–1072.
- (13) Vella, D., Mahadevan, L., *Am. J. Phys.* **2005**, 73 (9), 817–825.
- (14) Stamou, D., Duschl, C., Johannsmann, D., *Phys. Rev. E* **2000**, 62 (4), 5263–5272.
- (15) Ohara, P. C., Leff, D. V., Heath, J. R., Gelbart, W. M., *Phys. Rev. Lett.* **1995**, 75 (19), 3466–3469.
- (16) Weibel, A., Bouchet, R., Boulc' F., Knauth, P., *Chem. Mater.* **2005**, 17 (9), 2378–2385.
- (17) Zhuravlev, L. T., *Langmuir* **1987**, 3 (3), 316–318.
- (18) Brunauer, S., Emmett, P. H., Teller, E., *J. Am. Chem. Soc.* **1938**, 60 (2), 309–319.
- (19) Sindorf, D. W., Maciel, G. E., *J. Phys. Chem.* **1982**, 86 (26), 5208–5219.
- (20) Love, J. C., Estroff, L. A., Kriebel, J. K., Nuzzo, R. G., Whitesides, G. M., *Chem. Rev.* **2005**, 105 (4), 1103–1170.
- (21) Oteyza, D. G. de, Gorman, P., Chen, Y.-C., Wickenburg, S., Riss, A., Mowbray, D. J., Etkin, G., Pedramrazi, Z., Tsai, H.-Z., Rubio, A., Crommie, M. F., Fischer, F. R., *Science* **2013**, 340 (6139), 1434–1437.
- (22) Zhang, J., Chen, P., Yuan, B., Ji, W., Cheng, Z., Qiu, X., *Science* **2013**.
- (23) Wei, Z., Qi, H., Li, M., Tang, B., Zhang, Z., Han, R., Wang, J., Zhao, Y., *Small* **2012**, 8 (9), 1331–1335.

Chapter 5

Building-block design

5.1 Preparation of gold nanoparticles

In order to study AuNPs, they first have to be synthesized. As already described in Section 1.2.3.2, “gold nanoparticles” is just the umbrella term for particles with fundamentally different properties, which in particular depend on their size and the kind of stabilization and thus directly on the synthesis method. Several liquid-chemical synthesis methods were performed and surveyed regarding the suitability of the products for the envisaged functionalization experiments and the experimental ease of implementation with the accessible equipment. In this section, the results from these experiments, the characteristic properties of the produced nanoparticles and feasible analysis methods for them are discussed. In Chapter 8 “Nanohybrids of gold particles”, the functionalization reactions of the synthesized AuNPs using coupling reactions on their surface, the study of their interactions with trithiocarbonate groups, and the employment in grafting-to reactions with different classes of polymers will be presented.

5.1.1 General remarks on AuNP synthesis strategies

Because of the high curvature, the gold atoms on the surface of AuNPs are unsaturated and especially reactive. In order to obtain a stable colloid in a AuNP synthesis, particle aggregation must be prevented. This can be achieved in three fundamentally different ways:^{[1–3] *}

Electrostatic stabilization: The nanoparticles carry a (remaining) charge, so that they (or the oppositely charged ligand layers) repel each other. Gold colloids stabilized in this manner are very sensitive to salts.

*The list only refers to the stability of AuNPs. In order to form a colloidal solution, also a good solubility is required, which is a different matter concerning the interactions with the solvent.

Depletion stabilization: Ligands on the particle surface would lose their configurational entropy when approaching another nanoparticle. This effect creates a repulsion zone with a width coinciding with the ligands' lengths. This type of stabilization may even occur without actual bonds between the ligands and the nanoparticles, as for instance in polymer solutions.^[1]

Steric stabilization: The nanoparticle surface is completely covered with ligands shielding the particle core, so that collisions will not lead to aggregation. The stabilization might be due to strong bonds between ligands and nanoparticles or just between the ligands themselves which do not necessarily need to bind to the surface, for example when they are crosslinked, in a hydrogen-bonded network.

Often, the stabilization is a combination of the last two types. It is important to note that steric stabilization is necessary, but not sufficient, to attain AuNPs that can be precipitated and redispersed.

There are a plethora of different synthesis strategies for stabilized AuNPs. Aside from infrequently used methods like laser ablation^[4–7] of solid gold into liquids or pulsed spark-discharge with gold electrodes,^[8] which follow a top-down approach and are sometimes termed “physical syntheses”, most synthesis strategies are based on a bottom-up approach and are often called “chemical syntheses” in this context. Here, gold(III) ions are reduced in the presence of a stabilizing agent which arrests the growth at a certain point:



The reducing and the stabilizing agent, which is found on the surface of the produced Au(0) particles, may be identical.

In the successful synthesis procedures explored in this thesis (all bottom-up), and in the vast majority of other protocols as well, hydrogen tetrachloroaurate(III) trihydrate is used as gold precursor. This gold salt is the product of dissolving elemental gold in aqua regia and concentration of the solution.^[9–11] It is extremely oxidizing and immediately reacts with most metals on contact. It must therefore be handled using a glass or plastic spatula. With non-selective stabilizing agents, spherical AuNPs are formed. Other shapes can be produced with special stabilizing agents. If an agent is used that preferably binds to certain faces of gold, the symmetry is broken and more advanced structures, such as gold nanorods,^[12,13] are formed.

Almost any imaginable reagent has been demonstrated to be suited to produce AuNPs when added to aqueous solutions of tetrachloroaurate(III) in the above described chemical synthesis. Examples of reduction/stabilizing agents in

recently published “green” synthesis^[14,15] protocols are fruit (banana,^[16] pear,^[17] citrus fruits),^[18] vegetables (cabbage,^[19] horse gram),^[20] flowers (roses^[21], daisies),^[22] plant leaves^[23] (almond,^[24] mahogany,^[25] mango,^[26] olive,^[27] semecarpus,^[28] callistemon,^[29] curry tree,^[30] memecylon),^[31] (culinary) herbs,^[32–35] spices (clove buds,^[36] saffron),^[37] plant roots (ginseng,^[38] ginger),^[39] natural gum^[40,41] and propolis,^[42] bacteria,^[43,44] fungi,^[45–48] algae,^[49] peptides^[50] and proteins and enzymes,^[51,52] gripe water,^[53] butterfly wings,^[54] human skin^[55] and hair.^[56] The reduction of gold ions to AuNPs also works in aerosols^[57] and Leidenfrost drops.^[58] While this truly shows the ease of stopping the gold particle aggregation in any solid matrix to produce a red-stained material, most of the thus produced AuNPs are not suitable to be studied in further reactions, because they possess very ill-defined shapes and sizes and are impossible to isolate from the stabilizing matter.

Well-defined and dispersible AuNPs are obtained by reduction and stabilization with negatively charged ions or individual molecules carrying a functional group that can form a chemical bond with gold, typically thiolates,^[59–62] selenonates,^[63,64] amines,^[65,66] or phosphines.^[67–69] In the following, several AuNP synthesis methods are explored and the properties of the produced nanoparticles and their suitability for functionalization reactions with RAFT agents or polymers are studied. To be able to perform a coupling reaction on the surface of the AuNPs, it is indispensable to prepare AuNPs with ligands carrying additional functional groups on their “free” end, which is a particular challenge in this field, since most standard syntheses employ decorating agents with plain alkyl chains.^[70,71] In this work, it was envisaged to explore synthesis pathways leading to AuNPs decorated with hydroxyl groups. This functional group can potentially be used for many different coupling reactions to introduce further functionalities, especially with the RAFT agents carrying alkoxysilyl anchor groups.

5.1.2 AuNPs via reduction by citrate ions

The synthesis of AuNPs by the reduction of gold ions in a refluxing aqueous solution by sodium citrate was already invented in principle in 1951 by J. Turkevich and his co-workers.^[74–77] Major refinements were added by G. Frens^[78,79] in the 1970s and others later.^[80,81] Because of these inventors, the method is also termed “Turkevich”, “Frens”, or “Turkevich–Frens” method. It is still one of the most widely used methods with hundreds of studies using these AuNPs for a variety of applications. There are, therefore, plenty of data for comparison with the results obtained, when nanoparticles of this type are used.

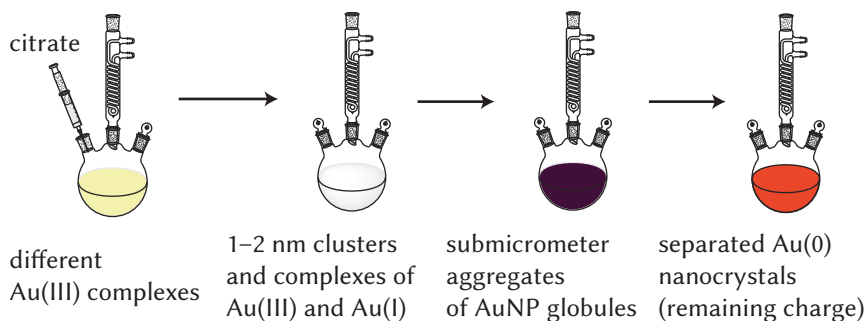


Fig. 5.1: Different steps in the synthesis of AuNPs $\text{Au}^{\text{ci}}\text{v}-3$ by reduction with citrate ions. The characteristic colors reflect the tentatively-formulated transient growth stages.^[72,73]

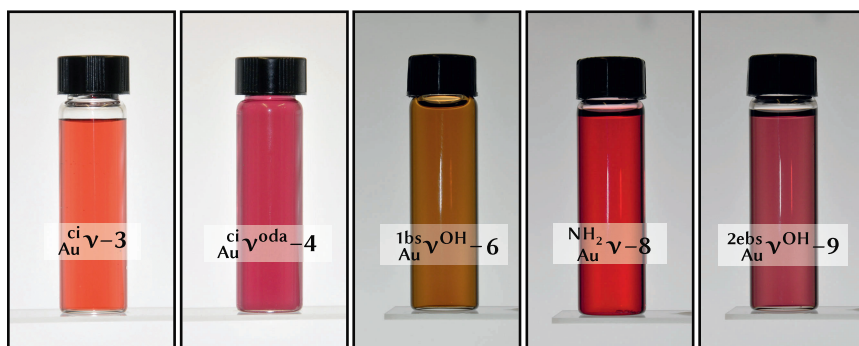


Fig. 5.2: Photographs of colloidal dispersions of selected AuNP samples. The solvents are water for ci-Au v-3 , chloroform for ci-voda-4 , methanol for 1bs-Au vOH-6 , toluene for $\text{NH}_2\text{-Au v-8}$, and DMF for 2ebs-Au vOH-9 . The AuNP concentration in all photos is around 50 mg L^{-1} . See main text for the meaning of the sample identifiers.

5.1.2.1 Mechanism of formation of citrate AuNPs

After addition of the reducing^[82] citrate ions, the AuNP formation proceeds through several growth steps within minutes,^[83] which lead to the solution assuming very characteristic colors. It turns from yellow to colorless, to gray/purple, and eventually to deep orange-red. These steps are illustrated in Figure 5.1. In view of the large number of studies dealing with this method, the underlying formation mechanism is only poorly understood. A reaction path has been tentatively formulated,^[72,84] wherein first, the Au(III) complexes are almost instantaneously reduced to mixed

complexes and clusters of Au(III), Au(I), and Au(0). The citrate ions themselves are oxidized to acetonedicarboxylic acid,^[85] and likely further to acetic and formic acid.^[73] Once a large share of Au(III) has been reduced, domains are formed in the rapidly stirred, supersaturated colorless solution, where these structures are enriched.^[72] Further reduction leads to submicrometer globules containing aggregates of slowly growing AuNPs, arguably by coalescence of small nuclei into larger particles.^[83] This stage corresponds to the purple solution. Earlier postulated networks of gold nanowires^[86] in the purple solution have actually been proven to be drying artifacts formed prior to the *ex-situ* analysis. After the breakdown of the submicrometer aggregates, the sizes of the now separated AuNPs increases rapidly, until all residual gold complexes are consumed. In the final orange-red solution, almost 100 % of the employed gold is found in very homogeneous nanocrystals, which are predominantly stabilized electrostatically by the remaining positive charge on their surface.^[87]

The citrate ions do not form bonds with the AuNPs, but are merely good trivalent counter-ions, forming a dielectric layer.^[88] A photograph of a solution as obtained from the reaction, labelled sample $\text{Au}^{\text{ci}}\mathbf{v-3}$, is shown in Figure 5.2.

5.1.2.2 Experimental details for the citrate method

The size of the AuNPs can in principle be increased by lowering the amount of citrate, but in most cases and also in this work, the lowest obtainable size—around 12–14 nm in diameter—is targeted, since the shapes of this kind of AuNPs become very irregular with lower amounts of sodium citrate. For the production of AuNPs with bigger sizes, the seed-growth reaction starting with seed AuNPs is more advisable.^[89–91]

The citrate method was performed frequently within the work of this thesis and was found to be very delicate and sensitive to seemingly unimportant details. In fact, several attempts were necessary to establish a detailed workflow, with which the product could be obtained reproducibly in the desired quality. It turned out to be necessary to comply with the following practical advice, although not each factor was examined systematically:

- Freshly purified ultrapure (type I) water has to be used for this reaction. Regular demineralized water is not sufficient.
- All glassware was thoroughly cleaned with aqua regia prior to any AuNP synthesis reaction,^[92] but for this method this is especially important. Each piece of glassware (including stirring bar and stoppers) has to be cleaned with freshly-prepared aqua regia for > 60 min and then rinsed with copious amounts of ultrapure water.

- The reaction works better when the same glassware is used repeatedly.
- The gold solution should boil under reflux for about 30 min before adding the sodium citrate and for another 30 min after the solution has turned red.
- It also seemed to be beneficial for the product when the aqueous citrate solution was heated prior to addition to the refluxing gold solution.
- The gold salt must be dissolved in advance, not directly prior to conducting the reaction. (It is sufficient to prepare a more concentrated stock solution which is diluted for the reaction.)

Regarding the last point, it was shown that gold chloride in aqueous solution consists of different species of $[\text{AuCl}_x(\text{OH})_{4-x}]^-$ complexes. It is conceivable that the chloride anions are replaced slowly by hydroxide anions over time.^[93] This is in line with the experimental finding that the pH value of the gold solutions decreased gradually to below pH = 3. The fact that the hydroxyl complexes (low x) are needed for the nanoparticle growth mechanism would indeed explain the necessity to work with pre-dissolved gold chloride. In this regard, it is noteworthy that the citrate ions were found to have the third role of a pH mediator (in addition to reducing agent and capping agent),^[94] shifting the equilibrium of complexes in the desired direction. Attempts to tune the process by manually adjusting the pH value, though, produced no gold colloid at all, neither by thermal nor by ultrasonic initiation.^[95,96]

The extreme sensitivity of the reaction protocol to fine changes also becomes visible by the fact that nanoparticles with significantly smaller sizes are formed when the gold solution is added to the solution of sodium citrate.^[97,98] Also, the addition of very small amounts of sodium chloride has a dramatic effect,^[99] underlining the need for ultrapure water.

The maximum gold concentration in the citrate synthesis is very limited and is apparent simply from the vivid colors of the intermediate species instead of just black. In a series of experiments the gold concentration was systematically increased and the products were analyzed as shown in the next section. The gold concentration of 0.5 mmol L^{-1} , corresponding to 93 mg L^{-1} gold content in the final gold sol in the case of 100 % yield, was found to be the upper limit until the homogeneity (especially the roundness) of the produced AuNPs begins to suffer. Because of this limitation, it was inevitable to prepare a large number of batches in order to obtain the necessary amount for the functionalization reactions. This was possible thanks to the very high reproducibility of successful reactions.

The citrate AuNPs $\text{Au}^{\text{cit}}\mathbf{v-3}$ did not show any sign of alteration, even after months, when they were stored at room temperature in the dark. But due to the electrostatic

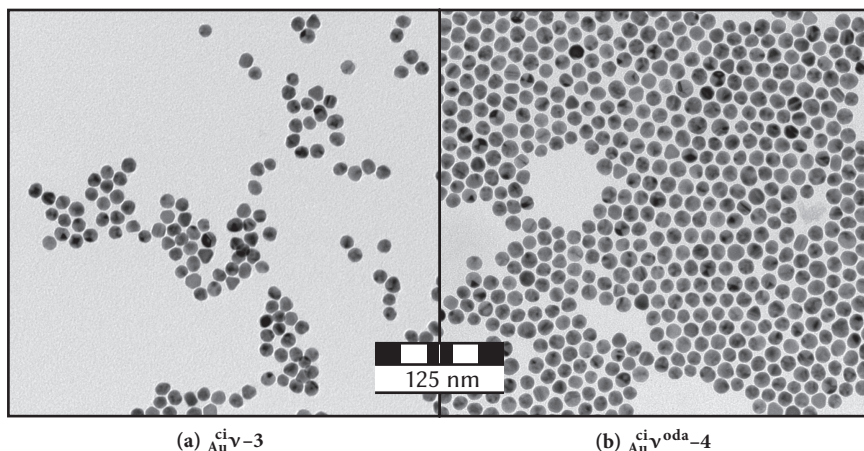


Fig. 5.3: Comparison of TE micrographs of citrate-prepared AuNPs before (AuV-3) and after (AuVoda-4) the functionalization with octadecylamine. The samples were drop-cast from a) water and b) chloroform. The right image is far better suited for particle analysis as it features a significantly larger number of AuNPs with distinct spacings. Also, in the left image, some particles overlap.

stabilization, they immediately aggregate irreversibly when any additive is given to the solution, when it freezes, or when the pH value is adjusted ($\text{pH} \geq 13$). Water is the only solvent with sufficiently large polarity to stabilize these AuNPs. They cannot be transferred to any other solvent, which greatly restricts their field of application. (Thiol-protected AuNPs, as produced in Section 5.1.3, are far more stable.) On the other hand, the highly reactive surface makes this type of AuNPs very suitable for surface-functionalization reactions, since no other bound ligand has to be replaced.

Other advantages are (i) that the particles have high enough masses to be centrifuged down with the accessible equipment,^[100] although it took hours, which enables easy purification in functionalization reactions, and (ii) that except for the sodium citrate no other substances are present in the AuNP dispersion.

5.1.2.3 TEM characterization of citrate AuNPs

Different TE micrographs of the same spot and the diffraction pattern of the citrate AuNPs AuV-3 have already been shown and discussed in Section 4.1.1. Another image can be seen in image (a) of Figure 5.3. The projection of almost all AuNPs

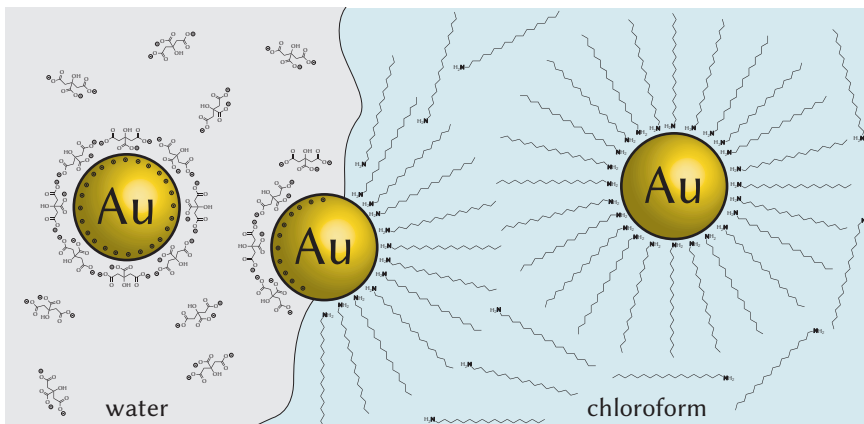


Fig. 5.4: Schematic mechanism of the transfer of citrate AuNPs $\text{Au}^{\text{ci}}\text{v}-3$ from water into chloroform and simultaneous surface functionalization with octadecylamine, giving $\text{Au}^{\text{ci}}\text{v}^{\text{oda}}-4$. The reaction was also performed with toluene in place of chloroform.

was very circular, except for a low number of particles with rounded-triangular shapes, which are always observed within citrate-prepared AuNPs. Since these nanoparticles play a central role in this work, a detailed TEM analysis of their sizes and shapes, as it has been demonstrated in Section 4.1.4, should be performed with a very high number of AuNPs, in order to obtain the very precise values needed for the use in functionalization reactions. At the same time, many batches of this colloid were produced. To be sure of a constant quality, it was necessary to be able to perform a rapid particle analysis after each run. Figure 5.3a shows one of the best taken micrographs for $\text{Au}^{\text{ci}}\text{v}-3$, but it is still not well suited for the semi-automatic particle analysis, because (i) it features only a low number of particles and (ii) some of the disordered particles overlap.

Both problems can be overcome by coating the AuNP surface with a long-chain amine, such as in this case octadecylamine $\text{NH}_2\lambda-11$ (structure in Figure 8.5, Section 8.2).^{*} The functionalization proceeds with a concomitant phase transfer to an organic solvent which is immiscible with water. This approach was originally presented by Karg *et al.*^[101] (2011). The functionalization/transfer mechanism is shown schematically in Figure 5.4. The as-obtained citrate gold sol $\text{Au}^{\text{ci}}\text{v}-3$ is added to a solution of octadecylamine in chloroform or toluene and the mixture is heavily

^{*} Although this is a functionalization reaction, it is discussed here, rather than in Section 8, because its merit for this work is to enable a better nanoparticle analysis.

Tab. 5.1: Size and shape parameters (obtained as described in Section 4.1.4.1) of two different types of explored AuNPs: octadecylamine-coated citrate AuNPs $\text{AuV}^{\text{ci}}\text{oda}-4$ (16 180 particles on 30 micrographs examined), which have identical parameters as the citrate particles $\text{AuV}-3$ themselves, and AuNPs $\text{AuV}^{\text{2ebs}}\text{OH}-9$ (9 688 particles on 15 micrographs) from the two-phase *ex-situ* Brust-Schiffrin synthesis (functionalized with $\text{SH}\lambda^{\text{OH}}-6$, the distribution should be at least similar for the samples from the same synthesis method). These parameters are explained in detail in Section 4.1.4.2.

parameter	$\text{AuV}-3$ ($\text{AuV}^{\text{ci}}\text{oda}-4$)	$\text{AuV}^{\text{2ebs}}\text{OH}-9$
diameter $2r$	$(13.6 \pm 1.4) \text{ nm}$	$(3.4 \pm 0.7) \text{ nm}$
circularity C	0.909 ± 0.02	0.88 ± 0.05
surface area	$(590 \pm 240) \text{ nm}^2$	$(39 \pm 16) \text{ nm}^2$
aspect ratio	1.10 ± 0.07	1.13 ± 0.12
roundness	0.92 ± 0.05	0.89 ± 0.07
solidity s	0.96 ± 0.01	0.92 ± 0.02
mean curvature κ_m	$(7.4 \pm 0.5) \times 10^{-2} \text{ nm}^{-1}$	$(3.0 \pm 0.7) \times 10^{-1} \text{ nm}^{-1}$
Gaussian curvature κ_G	$(5.5 \pm 0.7) \times 10^{-3} \text{ nm}^{-2}$	$(9.7 \pm 5.2) \times 10^{-2} \text{ nm}^{-2}$
volume V	$(1\,400 \pm 2\,200) \text{ nm}^3$	$(24 \pm 15) \text{ nm}^3$
particle mass m	$(2.7 \pm 4.3) \times 10^{-17} \text{ g}$	$(4.7 \pm 2.9) \times 10^{-19} \text{ g}$
specific surface S_m	$(23 \pm 2) \text{ m}^2 \text{ g}^{-1}$	$(94 \pm 21) \text{ m}^2 \text{ g}^{-1}$
Au atoms per particle	$(8.1 \pm 13.2) \times 10^4$	$(1\,400 \pm 900)$
Au atoms on surface	$\approx 9 \%$	$\approx 33 \%$

shaken by hand in a closed container for 1 min. On the interface, the AuNPs are immediately coated by the amphiphilic amine, presumably via a weak associative bond through the neutral amine group's lone electron pair,^[65] and then stabilized by the long hydrocarbon tail. This process proceeds faster than the nanoparticle aggregation by the lower polarity of the organic solvent or charge equilibration and can be directly observed by the red color migrating from the aqueous to the organic phase. The obtained yield of the product (for better distinguishability denoted $\text{AuV}^{\text{ci}}\text{oda}-4$) is almost 100 %, which also demonstrates that no major side-products are formed in the original synthesis with citrate. Using an octadecylamine stock solution, the whole process is conveniently done within a few minutes.

The octadecylamine-coated AuNPs $\text{AuV}^{\text{ci}}\text{oda}-4$ tended to form regions of dense monolayers on the TEM grids, as shown in image (b) of Figure 5.3. This allowed for capturing a large number of particles on one single image. (Read Section 4.1.3 for a

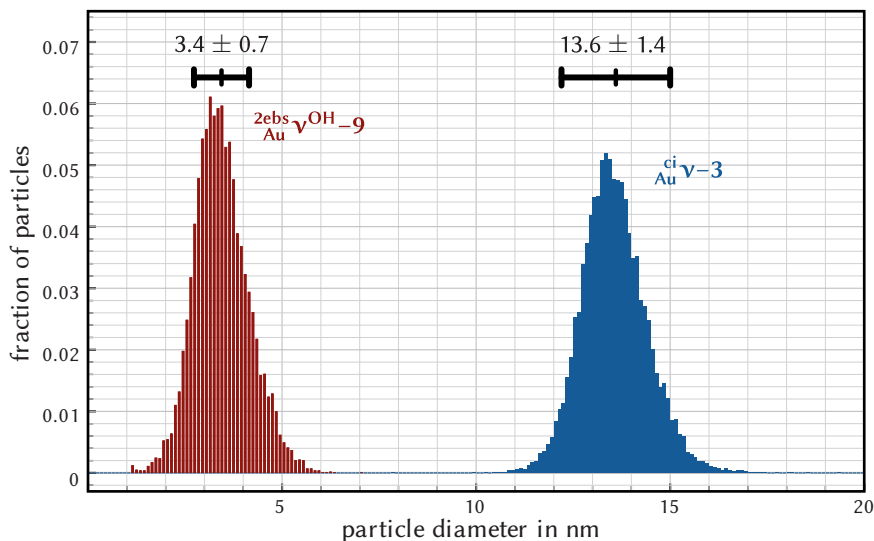


Fig. 5.5: Diameter histograms for citrate AuNPs $\text{Au}^{\text{ci}}\text{v-3}$ (from $\text{Au}^{\text{ci}}\text{v}^{\text{oda}}\text{-4}$, 16 180 particles examined) and *ex-situ* Brust–Schiffrin AuNPs $\text{Au}^{\text{2ebs}}\text{v}^{\text{OH}}\text{-9}$ (9 688 particles examined). The binning step size is 0.1 nm for both samples. See Section 4.1.4 for how the distribution was extracted from the micrographs. (Histogram for $\text{Au}^{\text{ci}}\text{v-3}$ reprinted and adapted with permission from a previous publication.^[102] Copyright 2013 American Chemical Society.)

discussion of the lattice formation.) At the same time, the AuNPs do not overlap. There is even a constant interparticle spacing of approximately 3 nm, caused by the electron-invisible ligand. (Compare the micrograph of silica nanoparticles $\text{SiO}_2^{\text{np}}\text{v-2}$ in Figure 4.7, where the individual particles do touch each other.) Micrographs like that are ideally suited for the semi-automatic extraction of size and shape parameters as presented in Section 4.1.4.1 (left column). The results from the analysis of 16 180 particles on 30 micrographs with a resolution of $2.47 \text{ pixels nm}^{-1}$ (corresponding to a 175 000-fold magnification on the native fluorescent screen) are listed in Table 5.1. It can be directly seen that these particles are very close to perfect spheres and very homogeneous in shape and in size. In Figure 5.5, the diameter histogram is shown in blue. It is close to a normal (Gaussian) distribution with an average value of $2r = (13.6 \pm 1.4) \text{ nm}$ and extremely narrow. Expressing the width of the distribution by the dispersity \mathcal{D} (see Equation (1.15), Section 1.2.1.2) instead of the standard deviation, the value is $\mathcal{D} = 1.010$. Every single measured particle was larger than 10 nm in diameter. In Figure 5.6, histograms of the surface areas and masses,

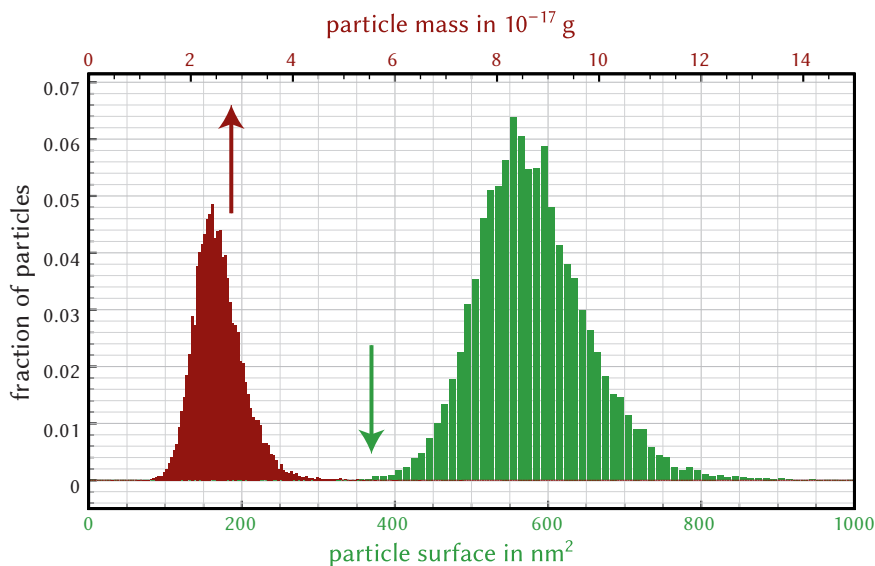
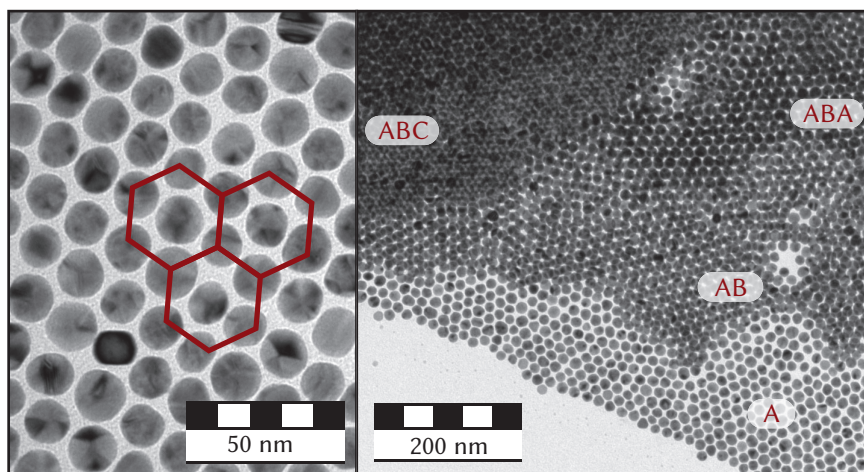


Fig. 5.6: Histograms of the surface areas (green, lower x -axis) and masses (red, upper x -axis) of citrate AuNPs $\text{Au}^{\text{ci}}\text{v-3}$ (total particle count: 16180). The binning step size is 10 nm^2 for the surface histogram and $5 \times 10^{-19} \text{ g}$ for the mass histogram. The x -axes were scaled in a way that the histograms do not overlap. The y -axis applies to both distributions.

calculated assuming spherical shape, are shown. As the surface area and the mass have a squared and cubed correlation with the diameter, these values have higher standard deviations. The dispersity of the masses is already in a typical range for synthetic polymers: $\mathcal{D} = 1.257$. (But that is no fair comparison, since polymers are linear.) The specific surface S_m , which is an especially important value for functionalization reactions, was determined to be $S_m = (23 \pm 2) \text{ m}^2 \text{ g}^{-1}$ of the citrate AuNPs can be determined very precisely. It might be surprising that this value is only half that of silica nanoparticles $\text{SiO}_2^{\text{np}}\text{v-2}$ with significantly higher diameters (compare Table 4.1), but the reason for that is the seven times higher density of gold compared with silica. The information that the citrate AuNPs consist on average of approximately 10 000 gold atoms, of which about 9 % are located on the surface, gives a concrete perception of the structure of $\text{Au}^{\text{ci}}\text{v-3}$.

Micrograph (a) in Figure 5.7 is a close-up of a hexagonal monolayer of $\text{Au}^{\text{ci}}\text{v}^{\text{oda}}\text{-4}$. It shows the ordering, the distinct spacing, and also the patterning of the AuNPs in greater detail. Even regions where these hexagonal layers were stacked to three-



(a) close-up image of hexagonal monolayer

(b) superstacking to close-packed 3-dimensional lattices

Fig. 5.7: Close-packed structures of octadecylamine-coated citrate AuNPs $\text{Au}^{\text{ci}}\text{v}^{\text{oda}}\text{-4}$ drop-cast from toluene. In micrograph (a), three hexagons are exemplarily shown as red overlays. It is well visible that the AuNPs do not touch each other. Micrograph (b) features both principally possible types of close-packed 3-dimensional lattices: hexagonal close-packed (ABA, interstitial gaps visible) and face-centered cubic (ABC, interstitial gaps not visible).

dimensional close-packed *supercrystals* were observed. Micrograph (b) in Figure 5.7 is a special curiosity because here both principally possible ways of stacking can be seen in one single image. In the upper right, the hexagonal sheets are stacked in the sequence ABA, evident by the still visible gaps between the particles of all layers. This corresponds to a hexagonal close-packed lattice which was cut along the $(0, 0, 1)^*$ -plane. In the upper left, the sequence is ABC and all interstitial gaps of the first sheet are covered. This is a fcc lattice cut along the $(1, 1, 1)$ -plane. These findings underline that no directed interparticle forces are influencing the supercrystal growth.

The octadecylamine-coated AuNPs $\text{Au}^{\text{ci}}\text{v}^{\text{oda}}\text{-4}$ were found to aggregate irreversibly within the course of some days, and the TEM samples were therefore prepared immediately. But the nanoparticles were stable enough to be dried and directly redispersed. They could also be centrifuged down and redispersed in fresh

*The planes in a hexagonal close-packed lattice are described by four Miller indices.

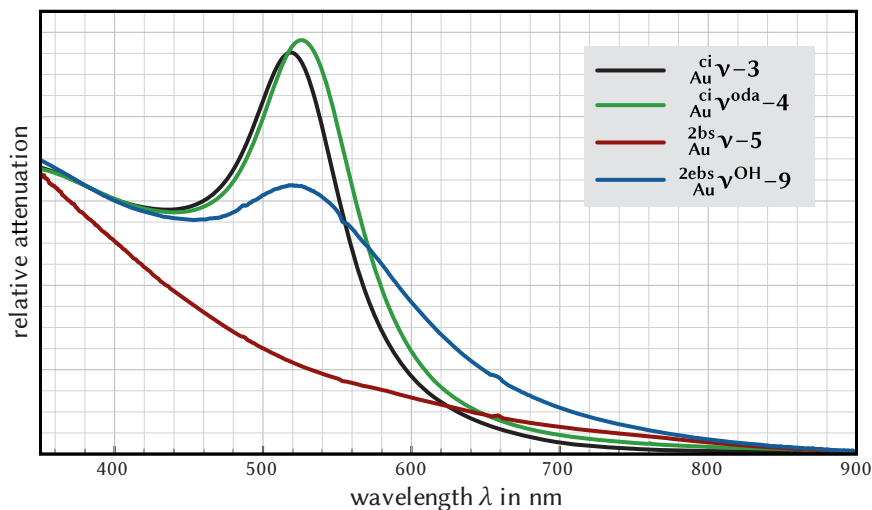


Fig. 5.8: Optical spectra of selected AuNP samples. Gold nanoclusters $\text{Au}^{\text{2bs}}\text{v}-5$ (measured in THF) do not exhibit a plasmon resonance signal. The plasmon peak gets more pronounced with increasing sizes of the AuNPs from $\text{Au}^{\text{2bs}}\text{v}^{\text{OH}}-9$ (measured in DMF) to $\text{Au}^{\text{ci}}\text{v}-3$. The red-shift of the plasmon peak from $\text{Au}^{\text{ci}}\text{v}-3$ to $\text{Au}^{\text{ci}}\text{v}^{\text{oda}}-4$ is caused by the change of the solvent (water to chloroform) and surface composition.

chloroform, thus removing the excess of octadecylamine. After this step, they showed even lower stability and hexagonal patterns were no longer found by TEM. The large excess of the ligand seems to be necessary for the self-assembly process. The lability of the amine–gold bond makes these nanocrystals promising as precursor for other functionalization reactions in which the amine is replaced by other ligands. That will be explored in Section 8.2.1.1.

5.1.2.4 Analysis of citrate AuNPs via optical spectroscopy

The optical properties of gold nanocrystals are especially relevant, since they are not only a very easy means of analysis, but also the critical feature for potential applications (see Section 1.2.3.2). Figure 5.8 shows (among others, which shall be discussed later) the optical spectra of as-prepared AuNPs $\text{Au}^{\text{ci}}\text{v}-3$ in water and those transferred to chloroform with octadecylamine $\text{Au}^{\text{ci}}\text{v}^{\text{oda}}-4$. They feature a very pronounced plasmon resonance signal with a maximum at 518 nm and 526 nm. The slight red shift is caused by the change of the solvent and the surface composition.

Aggregation of the AuNPs can be easily detected by the eye, because the solution turns completely blue. Measuring the gold sol in a spectrophotometer helps to identify more subtle changes in the quality, such as the deviation from spherical shape or the formation of only a small fraction of dimers. In these cases, the maximum of the plasmon resonance peak is shifted to higher wavelengths and it becomes more broad. In this regard, optical spectroscopy is the ideal complementary counterpart to the above-described TEM analysis. While the latter gives very detailed information on selected spots, the first yields information on the solution as a whole. In order to assure the constant quality after the synthesis of a batch of $\text{Au}^{\text{ci}}\mathbf{v-3}$, both an optical spectrum was recorded^[103] and a TEM characterization as outlined in the section before was performed. The AuNPs were only used for further experiments when both methods proved a successful synthesis. In this case, the solution was usually stored in the dark at room temperature for several days before use. This was reported to have a beneficial effect on the AuNP quality,^[104] although it was not found here.

Regarding the plasmon peak's intensity, a high mass attenuation coefficient ε^* ,[†] as defined by the Beer–Lambert law,

$$A = -\log_{10} \left(\frac{I}{I_0} \right) = \varepsilon^* l c^*, \quad (5.2)$$

is desirable for plasmonic applications. A is the absorbance, l the cuvette length, I and I_0 the light intensities of the sample and the reference, and c^* the (mass) concentration.

A concentration-dependent Beer plot, rather than a single optical spectrum, is the proper way to determine ε^* . To this end, optical spectra of solutions of $\text{Au}^{\text{ci}}\mathbf{v-3}$ with different concentrations were recorded and plotted in diagram (a) of Figure 5.9. The more opaque the red color of the curve, the higher was the AuNP concentration in the respective measurement. The highest concentration corresponds to the undiluted gold sol as obtained from the citrate reduction. A higher concentration is therefore only achievable by careful centrifugation and decantation, but in that case it would be hard to find out the exact value for the dissolved mass. From the slope of a plot of the maximum absorbance values against the gold concentration, shown in diagram (b) of Figure 5.9, a value of $\varepsilon^* = 16.6 \text{ L g}^{-1} \text{ cm}^{-1}$ can be calculated according to Equation (5.2). With a particle mass of $2.7 \times 10^{-17} \text{ g}$ from TEM (see previous section), this makes for an attenuation coefficient of $\varepsilon_p = 4.5 \times 10^{-16} \text{ L cm}^{-1}$ per individual particle.

[†]The term “mass attenuation coefficient” is preferable over “mass absorption coefficient” here, because the loss in intensity is not solely due to plasmon absorption and electronic transitions, but also to Rayleigh scattering.

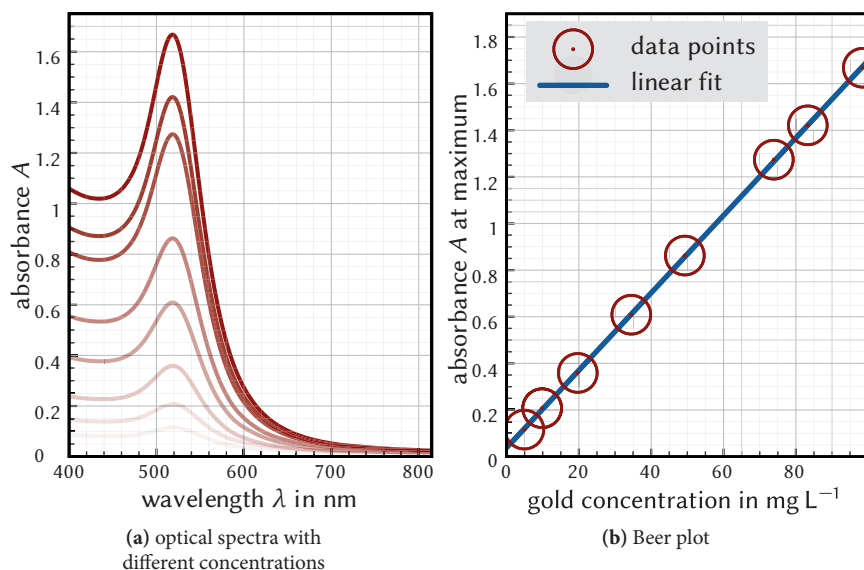


Fig. 5.9: Determination of the optical mass attenuation coefficient ϵ^* for citrate AuNPs $\text{Au}^{\text{cit}}\text{v-3}$ in water. The opacity of the curves in (a) is proportional to the respective gold concentration. From the slope in diagram (b), $\epsilon^* = 16.6 \text{ L g}^{-1} \text{ cm}^{-1}$ can be calculated (Equation (5.2)).

Assuming that ϵ^* does not depend significantly on the surface composition (compare with Figure 5.8), the optical attenuation was used to identify the unknown gold concentrations after the functionalization reactions in Section 8.2.

5.1.3 The Brust–Schiffrin method

The term “Brust–Schiffrin method” or just “Brust method” is widely used to generally tag synthesis procedures leading to AuNPs protected with a thiolate monolayer. M. Brust, D. Schiffrin, and coworkers presented two pioneering, mechanistically different reactions leading to this type of material in the mid-nineties.^[105–108] This was perceived a great breakthrough because for the first time, AuNPs soluble in organic solvents as well as stable in dried form could be conveniently prepared.

5.1.3.1 The two-phase Brust–Schiffrin method

Inspired by a systematic study by Wilcoxon *et al.*^[109] (1993), comparing the utility of different surfactants for the AuNP synthesis, and a publication by Giersig and Mulvaney^[110] (1993), showing the stabilization of AuNPs with alkylthiols, the two-phase Brust–Schiffrin method was historically the first published reaction (1994) producing thiolate-protected AuNPs and might well still be the most commonly used of all AuNP syntheses, along with the citrate reduction.^[91,105] When people speak about the Brust–Schiffrin reaction without further specifying the type, they usually refer to the two-phase reaction, where the gold ions are first transferred from water to toluene with tetraoctylammonium bromide $N^+\lambda-13$ (see Figure 8.5, Section 8.2, for the chemical structure) as phase-transfer catalyst and then reduced to elementary gold in the presence of an alkyl thiol by sodium borohydride. The mechanistic details of this two-phase method depend strongly on the type of employed ligand^[64,111–113] and are still in the process of being completely understood.^[114–116] The reaction is accompanied by the concomitant formation of the corresponding disulfide.

From the concentrations of the reactants, the sizes of the produced AuNPs can be controlled up to diameters of 5–6 nm with this approach—a barrier which is generally difficult to overcome. Recently, several elaborate protocols (often comprising of steps in which the reaction mixture has to be stirred with certain stirrer speeds) have been published which allow the synthesis of thiolate-protected gold nanoclusters of almost one single size. However, these reactions only appear to work for the particular ligand, for which they were optimized. Zhu *et al.*^[117] (2008) presented a low-temperature two-phase Brust–Schiffrin protocol for the production of single-size $Au_{25}(2\text{-phenylethanethiolate})_{18}$ nanoclusters with such a high purity that they were able to crystallize the product and determine the crystal structure by X-ray diffraction. This is the structure which has been shown in Figure 1.5b. The reaction could be reproduced to yield sample $^{2bs}_{Au}v-5$. By optical spectroscopy, however, it could be immediately evidenced that the sample consisted of a mixture of different gold nanoclusters (diameter < 2 nm), though. The spectrum is plotted in Figure 5.8. The absence of gold nanocrystals can be recognized by the lack of a plasmon resonance signal. Because of the mixture of different cluster sizes, no distinct signals belonging to particular electron transitions are visible. The increase of the absorbance with lower wavelengths is due to overlapping electronic interband transitions.^[118–120]

Because of the direct contact with sodium borohydride, sensitive ligands, such as RAFT-active trithiocarbonates, cannot be used in this process. At the same time, the replacement of thiols, once they are on the surface, is very hard, and even in

the presence of a large excess of the competing, different thiol,^[121] the exchange reaction does not go to completion. (50 % is already considered a good value.)^[122] The result is AuNPs with an ill-defined surface composition.

A major advantage of the Brust–Schiffrin method in general (as opposed to the citrate-reduction process outlined above) is the possibility to easily perform it in gram-scale. A serious drawback is the persistent contamination with the residual phase-transfer catalyst, which is very hard to eliminate from the final product.

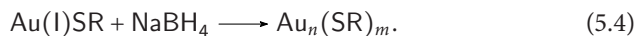
5.1.3.2 The one-phase Brust–Schiffrin method

The one-phase Brust–Schiffrin reaction was in principle a modified version of the corresponding two-phase method.^[106] It avoids the use of a phase-transfer catalyst by performing the reaction in a common solvent for the thiol and the gold ions, and therefore only works for certain combinations of reactants. Typical solvents are methanol and THF.

First, Au(I)SR complexes of unknown structure (rings, networks, or lamellae) and the corresponding disulfide are formed:^[114]



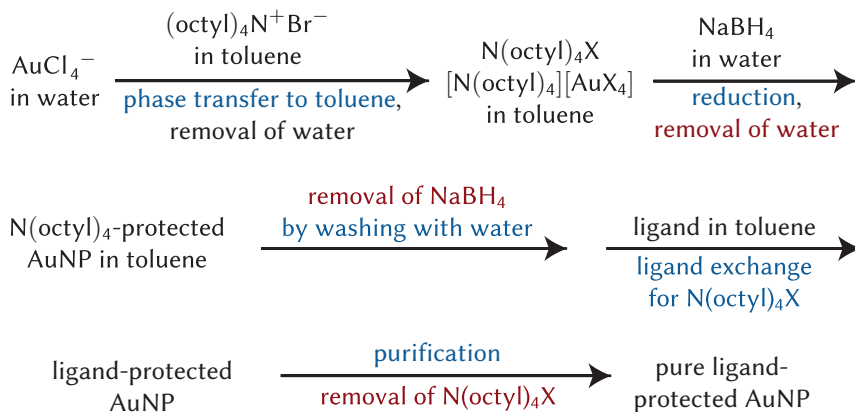
Sodium borohydride is then directly added as reducing agent:



The isolation of the AuNPs from the concomitantly formed disulfide is often very difficult, since both inherently possess very similar solubilities, and only relatively small AuNPs are accessible with the one-phase method, which cannot be separated by centrifugation. The process is not restricted to thiols as protecting ligands.^[123]

The original one-phase synthesis^[106] with the thiol ligand 4-mercaptophenol $\text{SH}\lambda^{\text{OH}}\text{-4}$ was reproduced in this work, because it directly yields the targeted type of hydroxyl-functionalized AuNPs, although in the nanocluster regime. A photograph of the produced brown AuNPs $\text{Au}^{\text{bs}}_{\text{Au}}\text{V}^{\text{OH}}\text{-6}$ can be found in Figure 5.2.

The presence of the protecting ligands on the surface of purified AuNPs could be verified by different methods: While it is not possible to obtain information from ^{197}Au -NMR spectroscopy, the extremely high quadrupole moment of the ground state and the low resonance frequency of the 100 % abundant ^{197}Au nucleus,^[124] one can still detect the ligand signals with classical ^1H - and ^{13}C -NMR methods.^[125–127] Typically, because of the reduced rotatability of the immobilized ligands, the signals are broadened with decreasing surface curvature of the nanoparticles and increasing proximity to the anchor point on the surface.^[128] For $\text{Au}^{\text{bs}}_{\text{Au}}\text{V}^{\text{OH}}\text{-6}$, the characteristic



Scheme 5.1: General reaction scheme of the two-phase *ex-situ* Brust–Schiffrin method. X represents counter-ions like Cl or Br. The actual functionalization reactions with different ligands—thiols and trithiocarbonates—will be discussed in Section 8.1.1.

signals of 4-mercaptophenol $^{1\text{bs}}_{\text{Au}}\mathbf{v}^{\text{OH}}\text{-6}$ were found by ^1H -NMR spectroscopy in deuterated acetone. With elemental analysis, very similar relative elementary compositions are found for the ligands and the coated AuNPs. By the absolute values, the mass fraction of gold and thus the average size of the AuNPs can be estimated. That the easily deprotonatable 4-mercaptophenol $^{\text{SH}}\lambda^{\text{OH}}\text{-4}$ was decorating the surface, was also reflected by the finding that $^{1\text{bs}}_{\text{Au}}\mathbf{v}^{\text{OH}}\text{-6}$ was only soluble in basic (pH > 10), but not in neutral aqueous solutions.

However, gold nanoclusters with other functional ligands could not be successfully synthesized with the one-phase Brust–Schiffrin method. Several attempts were made with 3-mercapto-1-propanol $^{\text{SH}}\lambda^{\text{OH}}\text{-5}$, 6-mercaptohexanol $^{\text{SH}}\lambda^{\text{OH}}\text{-6}$, and 11-mercaptoundecanol $^{\text{SH}}\lambda^{\text{OH}}\text{-7}$ (chemical structures shown in Figure 8.5, Section 8.2) following a procedure by Wu *et al.*^[129] (2009), which should be tolerant to functional groups on the ligands, but only indispersable black powders were formed. The identical reaction could, however, be reproduced with 2-phenylethanethiol $^{\text{SH}}\lambda\text{-1}$, giving $^{1\text{bs}}_{\text{Au}}\mathbf{v}\text{-7}$, indicating a maleficent effect of the hydroxyl group.

5.1.3.3 *Ex-situ* two-phase Brust–Schiffrin method

In both the two-phase and the one-phase Brust–Schiffrin reaction, the protecting thiol makes direct contact with the reducing agent sodium borohydride. A modification of the two-phase process, allowing for the employment of reduction-sensitive

ligands, was first reported by Manna *et al.*^[130] (2003). It was based on the finding by Fink *et al.*^[131] (1998) that the reduction step can be performed in the presence of just the phase-transfer catalyst tetraoctylammonium bromide $N^+\lambda-13$ and protected AuNPs are still formed (by a different mechanism). After the reduction, the ligand is added and immediately replaces the very weakly bound $N^+\lambda-13$. Later, Zhou *et al.*^[132] (2007) demonstrated that the toluene phase, containing the tetraoctylammonium bromide-coated AuNPs, can be thoroughly washed with water prior to the addition of the ligand, thus making sure that absolutely no sodium borohydride remains. The general reaction steps are outlined in Scheme 5.1.

The advantage of the *ex-situ* protocol is not only that it enables the use of ligands which are sensitive to harsh reduction conditions, such as the later discussed trithiocarbonate-type RAFT agents and the azidothiol $SH\lambda^N-9$ (see Section 5.3), but also that the size distribution of the produced AuNPs is independent of the employed protecting agents. That way, a high comparability of the functionalized AuNPs is guaranteed.

As for the in-situ process, a major advantage of the *ex-situ* two-phase Brust-Schiffrin method is the possibility to easily perform it in gram-scale and a likely drawback is the persistent contamination with the residual phase-transfer catalyst. The formed AuNPs have clearly too light masses to be centrifuged down with the accessible equipment. The positive side to this behavior is that it allows for the easy removal of any possibly formed heavier aggregates in the centrifuge.

Nanoparticle characterization The actual coating reactions with different ligands will be discussed in the functionalizations chapter in Section 8.1.1. The current section shall be dedicated only to the general characterization of the AuNPs formed in the tetraoctylammonium bromide micelles under the employed conditions. Since these particles aggregated within hours, when no ligand was added, sample $^{2\text{ebs}}_{\text{Au}}V^{\text{OH}}-9$, functionalized with 11-mercaptoundecanol $SH\lambda^{\text{OH}}-7$ (Section 8.1.1.1), was analyzed as a representative. As stated above, the core particles should be independent of the type of ligand shell here.

Figure 5.10a shows a micrograph of $^{2\text{ebs}}_{\text{Au}}V^{\text{OH}}-9$. The differing contrast of the individual nanosized particles with different orientations to the electron beams can be explained by their crystalline nature. At least the larger particles show patterning and thus comprise several crystal domains. Measuring 9 688 AuNPs on the shown micrograph and 14 other images taken with the same magnification according to the workflow outlined in Section 4.1.4.1, the size and shape parameters listed in Table 5.1 could be obtained. It can be seen that the particles have close-to-spherical shapes and are relatively homogeneous, although to a lower extent than for $^{ci}_{\text{Au}}V-3$. The

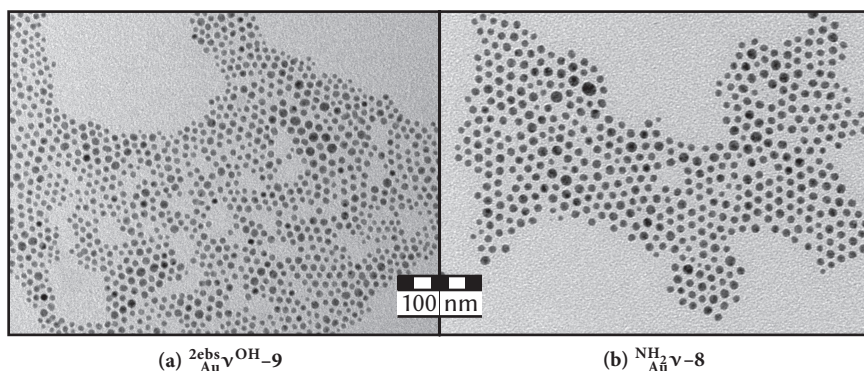


Fig. 5.10: TE micrographs of AuNPs $2^{\text{ebs}}_{\text{Au}}\text{v}^{\text{OH}}-9$ from the *ex-situ* Brust–Schiffrin method (drop-cast from DMF) and of those from reduction with oleylamine $\text{NH}_2_{\text{Au}}\text{v}-8$ (drop-cast from toluene). The latter possess only marginally larger sizes. The interparticle distances make visible that oleylamine $\text{NH}_2\lambda-12$ occupies more space than 11-mercaptoundecanol $\text{SH}\lambda^{\text{OH}}-7$.

diameter histogram, plotted in the diagram in Figure 5.5, is similar to a Gaussian distribution. The particle diameters are with an average of 3.4 nm close to the lower end of the nanocrystal regime. It might be deceptive that the histogram of $2^{\text{ebs}}_{\text{Au}}\text{v}^{\text{OH}}-9$ features higher bars than that of $\text{ci}_{\text{Au}}\text{v}-3$, which shown in the same figure and thus seems to reflect a less broad distribution. This appearance is due to the fact that the same binning step of 0.1 nm was applied for both histograms. Since the absolute diameters are clearly higher for $\text{ci}_{\text{Au}}\text{v}-3$, they are distributed among slightly more bars, although the distribution is narrower. It should also be mentioned that the reproducibility of the sizes in the *ex-situ* two-step Brust–Schiffrin reaction was clearly lower than for the reduction with citrate. For the shown distribution, only one selected sample of those AuNPs was analyzed.

A photograph of $2^{\text{ebs}}_{\text{Au}}\text{v}^{\text{OH}}-9$ is shown in Figure 5.2 and the corresponding optical spectrum in Figure 5.8. The plasmon resonance peak is distinctly present, but less pronounced than for the larger citrate AuNPs $\text{ci}_{\text{Au}}\text{v}-3$. In fact, up to a maximum diameter of about 25 nm, measuring the mass attenuation coefficient ϵ^* at the plasmon resonance peak is an easy method to get an estimate on the size of AuNPs, superior to analyzing position of the maximum of the optical spectrum.^[133–135] With increasing diameter of the AuNPs, ϵ^* becomes higher in this region (see Section 1.2.3.2). For $2^{\text{ebs}}_{\text{Au}}\text{v}^{\text{OH}}-9$, a value of $\epsilon^* = 8.30 \text{ L g}^{-1} \text{ cm}^{-1}$ was determined by a Beer plot in the same way as demonstrated for $\text{ci}_{\text{Au}}\text{v}-3$ in Section 5.1.2.4. Comparing

this value with a calibration curve provided by Rance *et al.*^[136] (2008), gives an approximate average diameter of 2.7 nm. This is roughly in line with the value of 3.4 nm determined via TEM.

5.1.4 Reduction by a long-chain amine

Nanosized gold particles can also be synthesized from gold ions with amines as reduction and stabilization agents. In one-pot approaches, larger particles than formed by the Brust–Schiffrin method are accessible in organic solvents. Amines are only weakly bound to the gold core which makes the produced AuNPs promising for ligand-substitution reactions.^[137]

For this work, the approach was explored with the very low-priced oleylamine, following a procedure by Hiramatsu and Osterloh^[138] (2004), in principle an optimization of a protocol by Jana and Peng^[139] (2003). (Aslam *et al.*^[140] (2004) published a very similar synthesis with oleylamine in water at the same time.) Oleylamine $\text{NH}_2\lambda\text{-12}$ (9-octadecenylamine, structure in Figure 8.5, Section 8.2) is the amine equivalent of oleic acid, a fatty acid which occurs naturally in animal and vegetable fats and oils, and possesses an unsaturated *cis*-unit in the middle of its C_{18} -chain. It has also been used in other published AuNP synthesis protocols.^[141,142] Mechanistically, the oleylamine first forms complexes with the gold ions and subsequently reduces them, being presumably oxidized to the nitrile itself.^[143] The homogeneous particles slowly grow by nucleation and diffusional growth,^[144,145] so that it is in principle possible to target certain particle sizes by quenching the reaction at any point, in addition to adjusting the concentration of the amine. The reaction was performed with an extreme excess of $\text{NH}_2\lambda\text{-12}$ (85 atoms per gold ion) and the produced colloid turned out to stable only when the abundance of the ligand was retained,^[146] so that the as-obtained solution $\text{NH}_2\text{Au}\nu\text{-8}$ in toluene had to be employed in further experiments. It is shown in a photograph in Figure 5.2.

As opposed to the expectations, the decisive issue with the synthesis of $\text{NH}_2\text{Au}\nu\text{-8}$ was the very low reproducibility, arguably due to the fact that oleylamine is generally only available in technical grade with a high content of impurities. It was acquired from two different suppliers (ALDRICH and ACROS ORGANICS) and vastly differing results were obtained, already in the optical appearance of the mixture during the reaction. Since reactions under seemingly identical conditions would lead to different particle size distributions, the detailed TEM analysis was omitted and only one selected micrograph is shown in Figure 5.10. It is notable that the AuNPs are not significantly larger than the *ex-situ* Brust–Schiffrin AuNPs $^{2\text{ebs}}\text{Au}\nu\text{OH-9}$ and that the interparticle distances show that oleylamine $\text{NH}_2\lambda\text{-12}$ occupies more space than 11-mercaptoundecanol $\text{SH}\lambda\text{OH-7}$.

Tab. 5.2: Comparison of the two primarily used methods for the synthesis of AuNPs in this work under different aspects which are important for functionalization reactions with RAFT agents or RAFT polymers. The methodological criteria refer to both the actual synthesis reaction or the produced AuNPs: For the citrate reduction, these are sample $\text{Au}^{\text{ci}}\mathbf{v}-3$, for the *ex-situ* two-phase Brust–Schiffrin reaction, $\text{Au}^{2\text{ebs}}\mathbf{vOH}-9$ is the exemplary representative. For each criterion, the more desirable valuation is colored in green.

criterion	citrate reduction	<i>ex-situ</i> Brust–Schiffrin
solvent	only water	mostly organic
reproducibility	very high	high
maximum mass per batch	very low	high
experimental effort	medium	low
stability	low	high
centrifugation	yes	no
homogeneity of size	very high	medium
regularity of shape	high	medium
purity	very high	medium
plasmon efficiency	high	medium
suitability for microscopy	high	medium

5.1.5 Conclusions on the AuNP syntheses

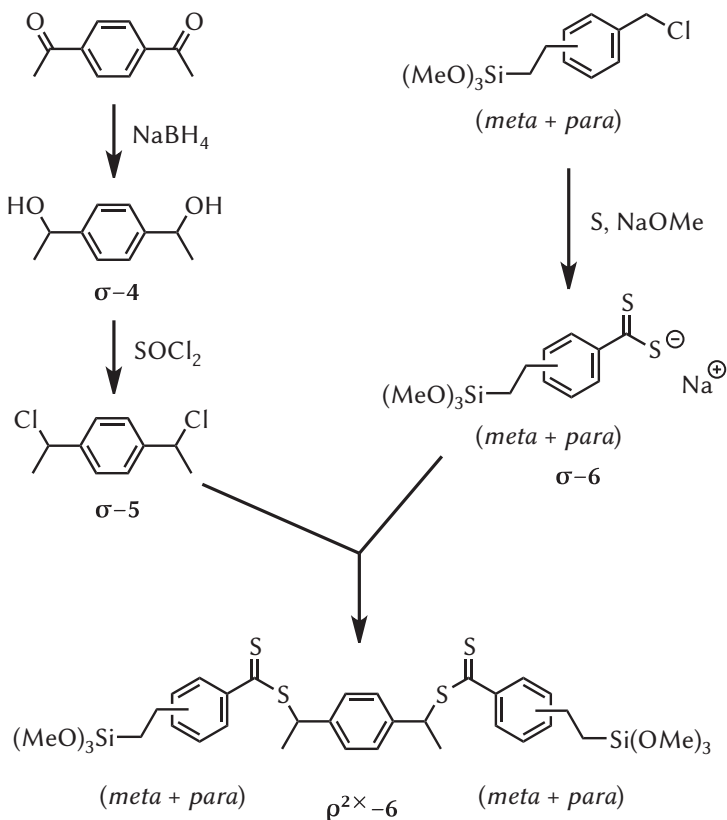
Considering the results from the preceding sections, the two best-established AuNP synthesis routes—the reduction of gold ions by sodium citrate and the two-phase Brust–Schiffrin synthesis—turned out to be also the most suitable ones for the envisaged functionalization reactions in this work, although for the latter, only the special *ex-situ* variant could be used. Only with this method, (i) is the outcome of the particle size independent of the type of employed ligand (a prerequisite for comparability), and (ii) even reduction-sensitive ligands can be employed. In Table 5.2, both methods are contrasted by the assessment under several methodological criteria. The syntheses (or rather the produced particles) can be seen as complementary, as both entail their own advantages and drawbacks.

In view of potential applications based on the plasmon resonance effect (see Section 1.2.3.2), the citrate AuNPs $\text{Au}^{\text{ci}}\mathbf{v}-3$ are arguably better suited than the Brust–Schiffrin particles, since their extremely pronounced plasmon peak even outweighs the approximately $70 \times$ higher masses, so that the mass attenuation coefficient ε^* is still about twice as high. Their much higher masses also make for the possibility

to isolate the (functionalized) particles by centrifugation and for easier analysis by microscopical methods and they are more homogeneous.^[147] On the other hand, the AuNPs from the *ex-situ* Brust–Schiffrin method (as for example $^{2\text{ebs}}_{\text{Au}}\text{V}^{\text{OH}}\text{-9}$), do not suffer from the restriction to water as a solvent, can be produced on a larger scale (although with more impurities), and are more stable, even compared with the citrate AuNPs after potential functionalizations. They can be even stored in dry form. Depending on the targeted application, the higher surface curvature might be advantageous as well. Both methods are reproducible, comparably easy to implement with the accessible equipment, and, despite the fact that the word “gold” gives the impression of very precious materials, they are relatively cheap.

The oleylamine-coated AuNPs $^{\text{NH}_2}\lambda\text{-12}$, on the contrary, were found to be unsuitable candidates with regard to the experiments in the discussed work. Not only was their synthesis very difficult to predict, the AuNPs could also not be isolated from the reaction medium and all attempts to functionalize these AuNPs *in-situ* by direct addition of different ligands to the reaction solution only lead to the immediate precipitation of non-redispersable aggregates. These experiments are therefore not further mentioned. It might be worthwhile to refine the synthesis protocol using an amine ligand, which can be obtained commercially in higher quality.

Although the two methods selected for the AuNP syntheses of this work both produce gold nanocrystals, also routes to gold nanoclusters (see Section 1.2.3.2) were explored. In particular, hydroxyl-functionalized clusters ($^{\text{lbs}}_{\text{Au}}\text{V}^{\text{OH}}\text{-6}$) were readily accessible in a one-pot reaction. Gold nanoclusters have their own inherent advantages over gold nanocrystals: They have a higher specific surface and are more stable, as the bonds to the ligands have generally a higher energy (surface gold atoms less saturated with each other) and collisions have less momentum. In addition, certain catalytic and charging properties are only found in gold nanoclusters. Their lower masses enable the analysis with certain methods which are not suitable for gold nanocrystals, such as mass spectrometry,^[148–151] and, due to the lower gold content, also several spectroscopic methods. Since particular clusters with a “magic number” of gold atoms in the core are more stable than others, samples can be obtained which consist almost exclusively of one single cluster size, either by a very size-selective synthesis method,^[117,152,153] or via purification by selective etching of the less stable clusters,^[154,155] chromatographic methods,^[156,157] electrophoresis,^[158–160] or fractionated precipitation.^[161,162] However, the focus of this work was the production of materials for applications based on the plasmon resonance effect, which is not exhibited by gold nanoclusters. Moreover, as opposed to gold nanocrystals, the surface chemistry of gold clusters is very different from that of planar gold surfaces. It can be expected that possible results are not transferable



Scheme 5.2: Synthesis strategy for Z-RAFT agent $\rho^{2\times}\text{-2}$ with two trimethoxysilyl anchor groups.

to systems with flat gold. Because of these two reasons, gold nanoclusters were excluded from the functionalization experiments.

The thorough characterization of the two types of AuNPs in the focus constitutes a profound groundwork for the subsequent functionalization reactions, which will be discussed in Chapter 8.

5.2 Synthesis of special RAFT agents

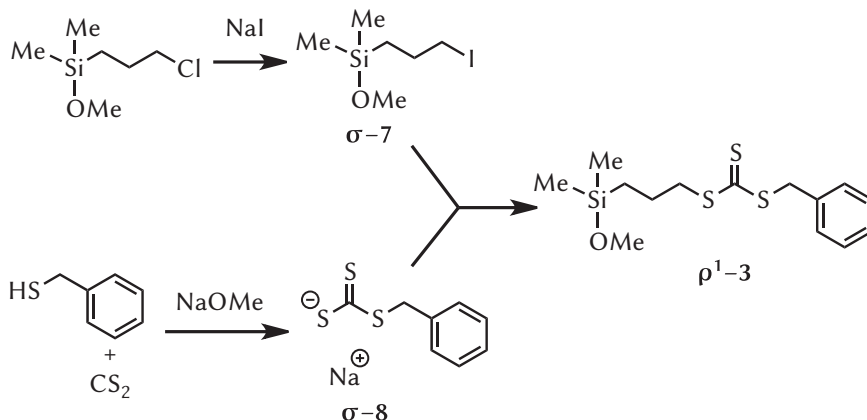
5.2.1 Synthesis of a RAFT agent with two anchor groups

A RAFT agent with two trimethoxysilyl anchor groups can be immobilized on oxide surfaces over two anchor points. It clears the way for the production of especially stable polymer films with doubly-bounded macromolecular loops on the surface (see Figure 1.6). In preceding work, a double-anchor Z-RAFT agent with trithiocarbonate groups had already been used for surface polymerizations.^[163] This principle was expanded to an analogous symmetrical dithiobenzoate compound $\rho^{2x}-2$. The synthesis pathway is outlined in Scheme 5.2. It was devised by Sebastian Primpke and first carried out by him in the framework of a practical laboratory course. According to this convergent synthesis strategy, the R-group fragments $\sigma-5$ and the Z-group fragments $\sigma-6$ are first prepared individually and then coupled under formation of the RAFT groups.

R-group fragment $\sigma-5$: The R-group must interconnect the two RAFT groups and be able to form a good radical upon homolytic cleavage from the RAFT group on both sides. For $\sigma-5$, the phenyl ring fulfills both functions in an ideal way. The methyl groups provide additional radical stabilization. The structural similarity to styrene enables a very high control for this monomer. The compound was obtained by reduction of 1,4-diacetylbenzene to 1,4-bis-(hydroxyethyl)benzene $\sigma-4$, using sodium borohydride, and subsequent chlorination with thionyl chloride.

Z-group fragment $\sigma-6$: The Z-group fragment sodium (1-trimethoxysilyl)ethylthiobenzoate $\sigma-6$ was prepared starting with the commercially available benzyl chloride carrying the trimethoxysilyl anchor group, which had also been used for the synthesis of the mono-anchor Z-RAFT agent ρ^3-1 provided by Robert Rotzoll (chemical structure shown in Figure 5.12). The phenyl group is a good Z-group because the intermediate tertiary RAFT radical is stabilized by mesomeric effects.^[164] Reaction of this compound with elemental sulfur and sodium methoxide yielded the corresponding dithiobenzoate salt.

The coupling of these two fragments to the final RAFT agent is a nucleophilic substitution reaction of the chloride atoms with the dithiobenzoate anions. The final product is a mixture of three constitutional isomers (*meta* + *meta*, *para* + *para*, *meta* + *para*). Impurities or side-products in the target compound do not constitute a real problem as long as they do not possess the silyl anchor group, because all unanchored molecules are removed in the final purification step. However,



Scheme 5.3: Synthesis strategy for Z-RAFT agent ρ^1-3 with a monofunctional anchor group.

although the dithiobenzoate salt $\sigma-6$ had been employed in excess, signals of the monosubstituted product could still be identified in the ^1H -NMR spectrum after the purification. This small fraction of molecules would produce only singly bound polymers rather than loops, since the R-group is not connected to the surface after the immobilization.

A general problem when working with molecules with trimethoxysilyl anchor groups is their tendency to hydrolyse and subsequently to condensate spontaneously.^[165] Dimerization was already detected, when the commercial educt ((chloromethyl)phenylethyl)trimethoxysilane was stored for longer periods of time in the original glass bottle, evidenced by the corresponding signal in the ESI mass spectrum, a second silicon signal in the ^{29}Si -NMR spectrum, and an additional signal of the methoxy groups in the ^1H -NMR spectrum. It is crucial to work under absolutely water-free conditions.

Immobilization of RAFT agent $\rho^{2x}-2$ on the surface of fumed silica $\text{SiO}_2^{\text{fs}}\nu-1$ and subsequent polymerization of styrene will be discussed in Section 7.1.

5.2.2 Synthesis of a RAFT agent with a monofunctional anchor group

Replacement of the most commonly used trimethoxysilyl group with the analogous monosilylether anchor group, which can only form a single covalent bond, prevents

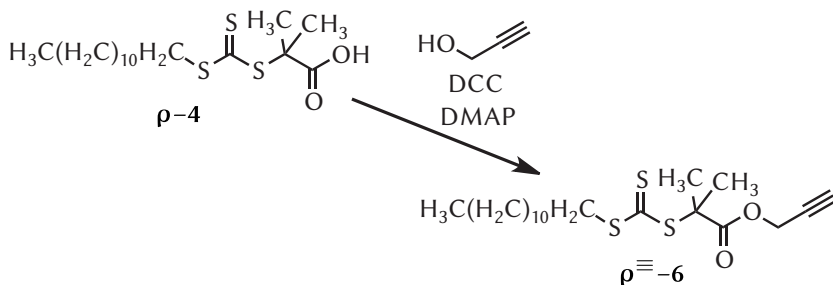
the possibility of RAFT-agent crosslinking in immobilization reactions to oxide surfaces.

In most other synthesis procedures for control agents with monofunctional silyl anchor groups, those are introduced as the last step by the hydrosilylation of an alkene group^[166–168] or by the nucleophilic addition of an amine containing this anchor group to an amide.^[169] Such a strategy cannot be applied for the synthesis of an anchor RAFT agent, since all common RAFT groups do not tolerate these reaction conditions. It is therefore inevitable here to start the synthesis with a compound which already contains the very sensitive and labile silyl ether group, and only reactions under very mild conditions can be utilized. Li and Benicewicz^[170] (2005) implemented this strategy by synthesizing the RAFT group of an R-anchor RAFT agent by a Grignard coupling reaction of dithiobenzoic acid magnesium bromide and the bromide function of the anchor fragment at room temperature. In the case presented here, a convergent synthesis route for the Z-RAFT agent $\rho^1\text{-3}$ with a dimethylmethoxysilyl anchor group was devised, which relies on the nucleophilic substitution reaction taking place at a precursor molecule carrying the desired anchor group, to which a trithiocarbonate salt is coupled. The strategy is depicted in Scheme 5.3.

The advantage in using an organic trithiocarbonate salt for this reaction is that the formed RAFT agent will automatically contain a potent Z-group, regardless of the structure of the substituents. Only the substituent intended to constitute the R-group in the final RAFT agent should form a sufficiently stable radical upon homolytic scission from the trithiocarbonate moiety. The benzyl group fulfills this requirement^[171] and the trithiocarbonate salt $\sigma\text{-8}$ was prepared by the reaction of benzyl mercaptan and carbon disulfide in the presence of sodium methoxide.

3-chloropropyldimethoxysilane is a suitable starting compound for the anchor fragment since it contains both the monofunctional anchor group and on the other side a primary chloride function, which is a good attack point for nucleophilic substitution reactions. All other commercially available molecules with such an anchor group at the time of performing the work did not contain any moieties suitable for converting the molecule to a RAFT agent. The direct nucleophilic substitution reaction with the starting substance 3-chloropropyldimethylmethoxysilane, however, had not been successful. Either no reaction had taken place or the silyl ether group had simultaneously reacted. It was therefore necessary to replace the chloride group with iodide—a better leaving group—in a Finkelstein reaction^[172] with a large excess of sodium iodide at 45 °C, forming compound $\sigma\text{-7}$, prior to the coupling reaction.

The identity of the RAFT agent $\rho^1\text{-3}$ was shown by mass spectrometry and ^1H - and ^{13}C -NMR spectroscopy, although in the ^{13}C -NMR spectrum three individual



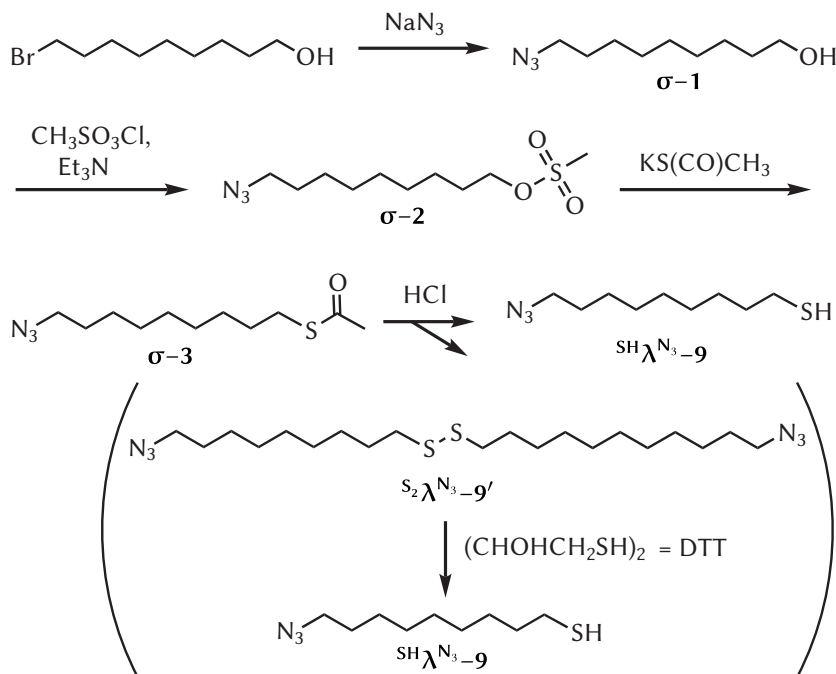
Scheme 5.4: Synthesis of RAFT agent $\rho^{\equiv}-6$ carrying an alkyne group.

signals were found in the region of the quaternary carbon atom of the trithiocarbonate moiety around 224 ppm, evenly spaced by 1 ppm. It was not clear if this was a measurement artifact, if it was caused by complexation to the trithiocarbonate group, or if it was actually indicative of two trithiocarbonate byproducts with otherwise completely identical spectroscopic data. Only a byproduct carrying the anchor group would influence the results in polymerization experiments. No further evidence for the presence of such a byproduct was found in the later study.

Immobilization experiments of ρ^1-3 on the surface of silica nanoparticles $\text{SiO}_2^{\text{NP}}-2$ and subsequent polymerization are covered in Section 7.2. The compound ρ^1-3 was proven to be a good RAFT agent in a preliminary homogeneous polymerization with *n*-butyl acrylate.

5.2.3 Synthesis of a “clickable” RAFT agent

The copper-catalyzed azide-alkyne Huisgen cycloaddition^[173] is arguably the most famous representative of “click” reactions.^[174] Boisselier *et al.*^[122] (2008) have shown that it is possible to perform this reaction on the surface of AuNPs, which are decorated with ligands bearing azide groups.^[175] Using specific conditions (a 1:1-mixture of water and THF as solvent, stoichiometric copper sulfate and sodium ascorbate in an inert atmosphere at 20 °C), the problems caused by the presence of copper in performing this reaction on colloidal gold^[176,177] can be overcome. As a potential coupling partner for azide-decorated surfaces, RAFT agent $\rho^{\equiv}-6$, bearing the complementary alkyne group at its R-group, was designed. The commercially available RAFT agent $\rho-4$ was modified as shown in Scheme 5.4. Propargyl alcohol was coupled to the RAFT agent's carboxylic acid group via a Steglich reaction^[178] with a yield of 86 %. The use of propargyl alcohol greatly facilitates the work-up of



Scheme 5.5: Synthesis of the azidothiol $\text{SH}\lambda\text{N}_3\text{-9}$.

this reaction, since it can be easily removed under vacuum. The identity of $\rho^{\equiv}\text{-6}$ was proven by NMR spectroscopy and elemental analysis.

5.3 Synthesis of the azidothiol

A suitable counterpart of RAFT agent $\rho^{\equiv}\text{-6}$ (see last section) for immobilization on AuNPs should possess a thiol group for anchoring, a relatively long hydrocarbon chain to provide stabilization and solubility of the AuNPs, and an azide group—the complementary unit to the alkyne group—on the other chain end. A synthesis route for a compound that meets these requirements, 1-azidoundecane-11-thiol $\text{SH}\lambda\text{N}_3\text{-9}$, had already been presented in literature.^[179,180] It was followed here, although some modifications had to be made, especially in the last step, and is

depicted in Scheme 5.5. This linear pathway is feasible, since all reactions proceed with relatively high yield.

The synthesis starts with 11-bromo-1-undecanol. As the first step, the azide functionality is introduced by nucleophilic substitution of the bromide with an azide group to 1-azidoundecan-11-ol $\sigma-1$. This is performed first, because the azide group is not very reactive and tolerant to the reaction conditions in the following steps. For the introduction of the thiol group, the hydroxyl group was first converted into a methylsulfonate group (in $\sigma-2$) by reaction with methane sulfonyl chloride. The methylsulfonate moiety constitutes a good leaving group for the following nucleophilic substitution with thioacetate, yielding compound $\sigma-3$.

The thioacetate group can in turn be hydrolyzed under acidic conditions to give the thiol $^{SH}\lambda^{N_3}-9$ and acetic acid. It was found by $^1\text{H-NMR}$ spectroscopy that this saponification reaction already took place during the nucleophilic substitution or its workup, so that the final hydrolysis reaction was only needed to convert the fraction of remaining thioacetate $\sigma-3$.

In contrast to the literature reports, however, the saponification was accompanied by the concomitant oxidation of the thiol to the corresponding disulfide $^{S_2}\lambda^{N_3}-9'$. This coupling reaction could not be prevented, nor could the thiol be isolated from the disulfide by column chromatography, since the retention behavior of both compounds was almost identical for all examined solvent mixtures.

On the one hand, the presence of the disulfide should not pose a problem, since it would equally bind to gold, forming the thiolate.^[181,182] (Both halves of disulfides are found as thiolates at different locations on the AuNPs, not necessarily next to each other.)^[183] On the other hand, the product should be as pure as possible in order to enable a maximum of comparability with literature reports and to exclude any possible influence of the disulfide on the immobilization mechanism. After first experiments with sodium borohydride as reducing agent at different temperatures had either not led to any reaction, or also to the concomitant reduction of the azide group, it was found that by the use of dithiothreitol (Cleland's reagent)^[184] as reducing agent,^[185] it was possible to specifically reduce the disulfide group. After the aqueous work-up, the azidothiol $^{SH}\lambda^{N_3}-9$ was obtained in pure form.

5.4 Preparation of *N*-isopropylacrylamide polymers

RAFT polymers of *N*-isopropylacrylamide (see the structural formula in Figure 5.11) were prepared in order to explore their behavior in aqueous solutions by cloud-

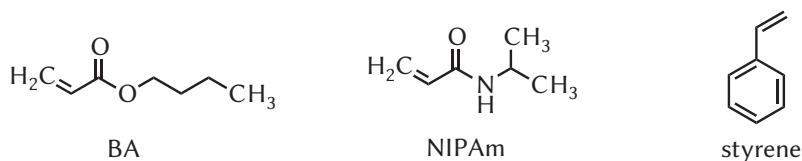


Fig. 5.11: Structural formulas of the monomer molecules used for polymerizations in this work.

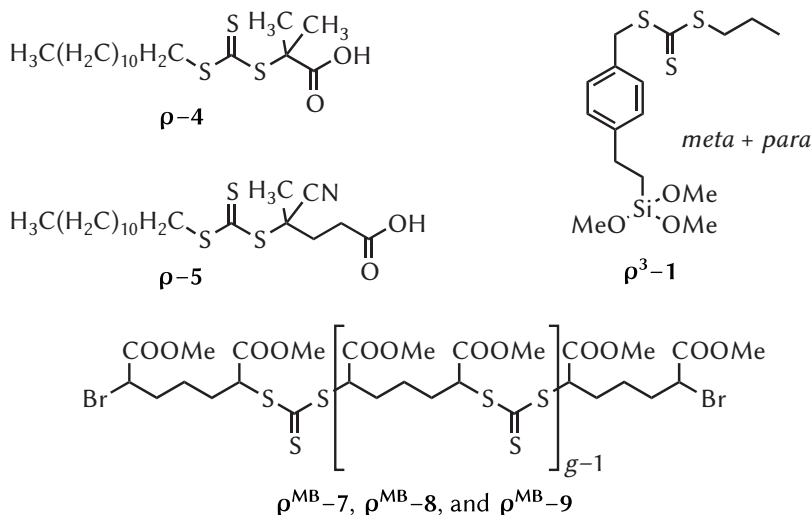


Fig. 5.12: Structural formulas of all RAFT agents used in this work. $g = 1, 2, 3, \dots$

point experiments (see Chapter 6) and to use them in functionalization reactions for AuNPs, exploiting the fact that RAFT groups bind to gold surfaces (see Chapter 8). Because very defined chain lengths are a prerequisite for both applications, special

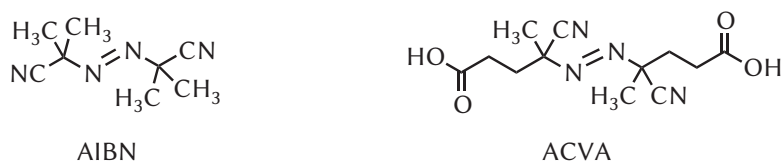


Fig. 5.13: Structural formulas of the initiator compounds used for polymerizations in this work.

effort was directed into finding conditions under which a maximum of control could be exerted over the polymerization. RAFT polymerization is known to be very well suited for this task.^[186,187]

The synthesized pNIPAm samples were of two categorically different types: *conventional polymers* with a single trithiocarbonate group at the chain end and *multiblock polymers* with multiple trithiocarbonate groups along the polymer backbone. (One sample of a third type—the NIPAm star polymer π^* -19—was kindly provided by Nadja Förster.) While most discussed points are relevant to both kinds of polymers, some special characteristics only apply to the multiblock polymers. These will be treated in the standalone Section 5.4.4.

5.4.1 Experimental polymerization conditions

The conventional NIPAm polymers were synthesized in polymerizations π -1 to π -10, using the trithiocarbonate RAFT agents ρ -4^[188] or ρ -5 (structures shown in Figure 5.12). Trithiocarbonates are known to constitute potent control agents for radical polymerizations of NIPAm^[189–192] (as opposed to, for example, dithiocarbamates).^[193] All polymerizations were carried out at atmospheric pressure and 60–70 °C in DMF^[189]. (Other typical solvents are 1,4-dioxane^[194–196] and toluene.)^[197] The structures of the used thermal initiators are depicted in Figure 5.13.

For all polymerizations except π -10, where the highest possible mass of one single sample was sought to be produced, several samples were taken and quenched by exposure to air after defined periods of time. To then isolate the polymer from the solvent and the extant (solid) monomer, it was first precipitated from the polymerization mixture by addition of diethyl ether,^[192,198] which is a solvent for the monomer. The polymer was collected by centrifugation and removal of the supernatant solution. Further purification was achieved by two reprecipitation–centrifugation steps after redissolution in acetone. After this purification, no monomer signal could be detected in the SE chromatogram of the polymer samples.

It can be assumed that in the conducted polymerizations, completely atactic macromolecules were formed,^[199] which is important for comparability.^[200]

All detailed results from the performed polymerizations are documented in Section 3.2.6.1 of the experimental part (Tables 3.1 up to 3.10), along with the individual reaction conditions. In the current part, only those polymer samples are listed in Table 5.3 which were used for further AuNP-coating (Au) or cloud-point experiments (CP).

Tab. 5.3: All pNIPAm samples which were used for further experiments in the overview: the sample identifiers of the polymer and the used RAFT agent, the \overline{M}_n and \mathcal{D} values determined by the RI and the UV detector of the DMAc-SEC set-up. The average number of blocks \overline{b}_{cl} determined by Equation (5.20) after cleavage at the trithiocarbonate groups (1 for conventional polymers), and the indication for which experiments the sample was used in the rest of this work (Au: functionalization of citrate AuNPs $\text{Au}^{\text{cit}}\nu\text{-3}$ in Section 8.2, CP: used for cloud-point experiments in Chapter 6).

sample	RAFT	RI detector		UV detector		\overline{b}_{cl}	used for
		\overline{M}_n in $\frac{\text{g}}{\text{mol}}$	\mathcal{D}	\overline{M}_n in $\frac{\text{g}}{\text{mol}}$	\mathcal{D}		
$\pi\text{-8b}$	$\rho\text{-4}$	1.49×10^4	1.20	1.44×10^4	1.20	1	Au, CP
$\pi\text{-8c}$	$\rho\text{-4}$	2.20×10^4	1.21	2.21×10^4	1.20	1	Au
$\pi\text{-8d}$	$\rho\text{-4}$	2.58×10^4	1.15	2.52×10^4	1.16	1	Au
$\pi\text{-7a}$	$\rho\text{-4}$	3.79×10^4	1.14	3.74×10^4	1.13	1	Au, CP
$\pi\text{-2a}$	$\rho\text{-4}$	4.74×10^4	1.15	4.64×10^4	1.14	1	Au
$\pi\text{-1c}$	$\rho\text{-4}$	5.48×10^4	1.19	5.34×10^4	1.20	1	Au
$\pi^{\times}\text{-1c}'$	$\rho\text{-4}$	5.48×10^4	1.19	–	–	1	Au
$\pi\text{-2b}$	$\rho\text{-4}$	6.77×10^4	1.19	6.48×10^4	1.21	1	Au
$\pi\text{-2d}$	$\rho\text{-4}$	7.44×10^4	1.22	7.03×10^4	1.29	1	Au
$\pi^{\times}\text{-2d}'$	$\rho\text{-4}$	7.44×10^4	1.22	–	–	1	Au
$\pi\text{-4c}$	$\rho\text{-4}$	1.09×10^5	1.38	8.50×10^4	1.57	1	Au
$\pi\text{-10}$	$\rho\text{-5}$	3.17×10^4	1.10	3.21×10^4	1.10	1	Au, CP
$\pi\text{-5d}$	$\rho\text{-4}$	8.04×10^4	1.38	5.23×10^4	1.77	1	CP
$\pi\text{-9}$	$\rho\text{-5}$	2.74×10^4	1.16	2.68×10^4	1.18	1	CP
$\pi^{\text{MB}}\text{-15c}$	$\rho^{\text{MB}}\text{-8}$	4.38×10^4	2.21	4.03×10^4	2.36	4.0	Au
$\pi^{\text{MB}}\text{-17b}$	$\rho^{\text{MB}}\text{-8}$	5.41×10^4	1.78	5.63×10^4	1.75	5.5	Au
$\pi^{\text{MB}}\text{-18a}$	$\rho^{\text{MB}}\text{-9}$	5.95×10^4	1.60	5.66×10^4	1.65	4.2	Au
$\pi^{\text{MB}}\text{-16a}$	$\rho^{\text{MB}}\text{-7}$	7.11×10^4	1.73	6.92×10^4	1.77	2.9	Au
$\pi^{\text{MB}}\text{-11b}$	$\rho^{\text{MB}}\text{-8}$	9.08×10^4	1.68	9.00×10^4	1.71	3.0	Au
$\pi^{\text{MB}}\text{-16b}$	$\rho^{\text{MB}}\text{-7}$	8.87×10^4	1.79	9.17×10^4	1.78	2.4	CP

5.4.2 Determination of monomer conversion

The monomer conversion X_M of a polymerization is by definition:

$$X_{M,g} = \frac{n_{M,0} - n_{M,1}}{n_{M,0}} \stackrel{(1.12)}{=} \frac{m_{M,0} - m_{M,1}}{m_{M,0}} = 1 - \frac{m_{M,1}}{m_{M,0}}, \quad (5.5)$$

$n_{M,0}$ and $m_{M,0}$ being the number and mass of the monomer units in the polymerization solution before the reaction, and $n_{M,1}$ and $m_{M,1}$ the ones after the reaction.

Two different methods turned out to be feasible for the determination of the monomer conversion of the samples after the NIPAm polymerizations: gravimetry and $^1\text{H-NMR}$ spectroscopy. (SEC was found to be very inaccurate in this case.)

For the determination via gravimetry, the mass fractions of the monomer $\omega_{M,0}$ and the solvent ω_S before starting the polymerization are known by their initial masses in the mixture. For a given sample of an arbitrary weight, the corresponding masses can simply be calculated by multiplication of the mass fractions with the total sample mass, which is in turn obtained by subtracting the known mass $m_{C,0}$ of the empty container (here: a centrifuge tube) from the combined mass m_C of container and sample:

$$m_{M,0} = (m_{C,0} - m_C)\omega_{M,0} \quad (5.6)$$

and

$$m_S = (m_{C,0} - m_C)\omega_S. \quad (5.7)$$

The sum of the mass $m_{M,1}$ of the unreacted monomer which has been removed by the purification of the polymer and the mass m_S of the solvent (and any other component which is eliminated during the purification) coincides with the mass difference of the container prior to and after the purification:

$$m_{C,0} - m_{C,1} = m_{M,1} + m_S. \quad (5.8)$$

Insertion of (5.6) and (5.8) in (5.5) yields the equation by which the conversion can finally be calculated:

$$X_{M,g} = 1 - \frac{m_{C,0} - m_{C,1} - m_S}{(m_{C,0} - m_C)\omega_{M,0}} \stackrel{(5.7)}{=} 1 + \frac{\omega_S}{\omega_{M,0}} - \frac{m_{C,0} - m_{C,1}}{(m_{C,0} - m_C)\omega_{M,0}}. \quad (5.9)$$

In the case that the sample had to be split up into several centrifuge tubes (with limited volume) for the purification, the conversion values obtained with Equation (5.9) were averaged.

The determination of the NIPAm conversion by $^1\text{H-NMR}$ spectroscopy can be carried out after measuring $^1\text{H-NMR}$ spectrum of the polymerization mixture. The

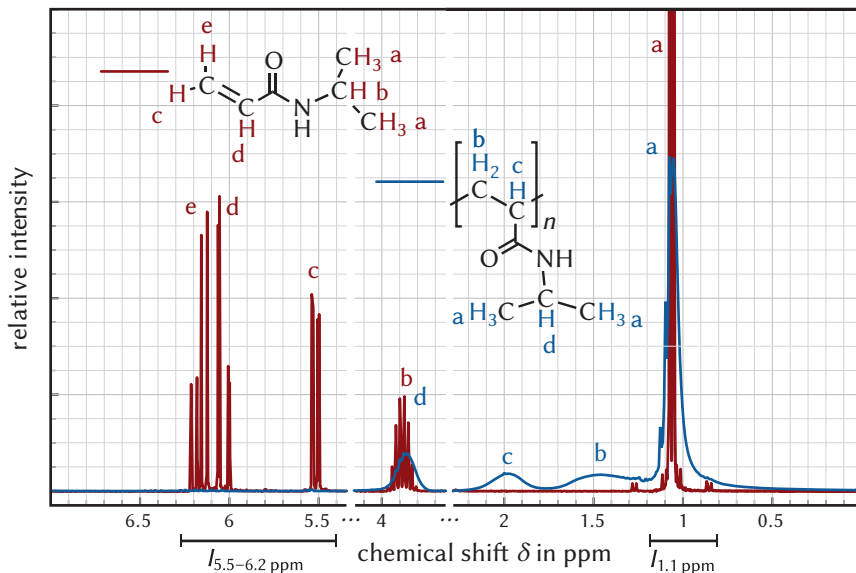


Fig. 5.14: Comparison of the ^1H -NMR spectra of the NIPAm monomer and polymer (measured in perdeuterated DMSO, relative intensities scaled arbitrarily) with assignment of signals. The integrals used in Equation (5.10) are indicated.

spectra of the NIPAm monomer and polymer and the assignments to the corresponding protons are shown in Figure 5.14. Both feature a distinct signal at 1.1 ppm, caused by the six protons of the methyl groups of the isopropyl function. The intensity of this signal is therefore $I_{1.1\text{ ppm}} = 6\text{ H}$ for both polymer and monomer. This signal was set in relation to the three vinyl protons of the monomer which appear in the region of 5.5–6.2 ppm. These protons are not contained in the polymer and its spectrum does not feature any signals in this region. The total intensity of the signals in this region is $I_{5.5-6.2\text{ ppm}} = 3\text{ H}$ for the monomer and $I_{5.5-6.2\text{ ppm}} = 0$ for the polymer. The number of remaining monomer molecules in the polymerization mixture $n_{M,1}$ relative to the number of monomer molecules $n_{M,0}$ before the polymerization (which contribute to the signal at 1 ppm either as monomer or incorporated in a polymer chain) is

$$\frac{n_{M,1}}{n_{M,0}} \stackrel{(1.12)}{=} \frac{m_{M,1}}{m_{M,0}} = \frac{I_{5.5-6.2\text{ ppm}}}{\frac{1}{2} I_{1.1\text{ ppm}}}. \quad (5.10)$$

With (5.5), the conversion is then

$$X_{\text{M,NMR}} = 1 - 2 \frac{I_{5.5-6.2 \text{ ppm}}}{I_{1.1 \text{ ppm}}}. \quad (5.11)$$

It is known that the spin-relaxation times of polymers might be highly retarded by the hindered rotatability.^[201,202] To make sure that the integrals measured by this method are reliable, the spectra were taken with an additional relaxation time of 15 s for three selected pNIPAm samples, guaranteeing a complete spin relaxation. In all cases, no significantly different spectrum was obtained, showing that the method is applicable even when the ¹H-NMR spectra are recorded with usual pulse frequencies. It can be carried out directly with the polymerization solution in DMF without prior concentration, since the DMF signals do not overlap with the respective regions.^[203]

The determination of the NIPAm conversion by ¹H-NMR spectroscopy turned out to be more accurate than the gravimetric method, although it was not performed with all samples. With gravimetry, significantly lower values were obtained for some samples. This is presumably due to the fact that by the purification, always a fraction of the formed polymer remained in solution after the centrifugation and was lost. For some samples with lower polymerization times, no product was obtained at all. In the case that both techniques were applied, only the values obtained by ¹H-NMR spectroscopy are reported in this work.

5.4.3 SEC analysis

SEC (see Section 1.2.1.2) is the standard analysis method for polymers. For the analyses in this work, two SEC systems were accessible, one running with THF as the eluent and the other with DMAc. Although in principle the THF system would be preferable, because only in this solvent, are Mark–Houwink parameters known for pNIPAm,^[204] it just yielded extremely broadened traces—a literature-known issue^[186] caused by the low solubility of pNIPAm in THF, which, however, could not be overcome using the suggested workaround of adding trace amounts of water to the polymer prior to the sample preparation. Nevertheless, the DMAc system was a very good alternative. Excellent analysis results for pNIPAm were also reported for SEC systems running with the structurally related DMF.^[189,205] For the SEC calibration, pMMA standards were preferred over polystyrene standards,^[206] on account of the higher similarity of pNIPAm to pMMA.^[205] Owing to the presence of the trithiocarbonate groups from the RAFT agents, which absorb light at a wavelength of $\lambda \approx 310 \text{ nm}$,^[207] the polymers could also be traced with a UV detector (in addition to the RI detector).

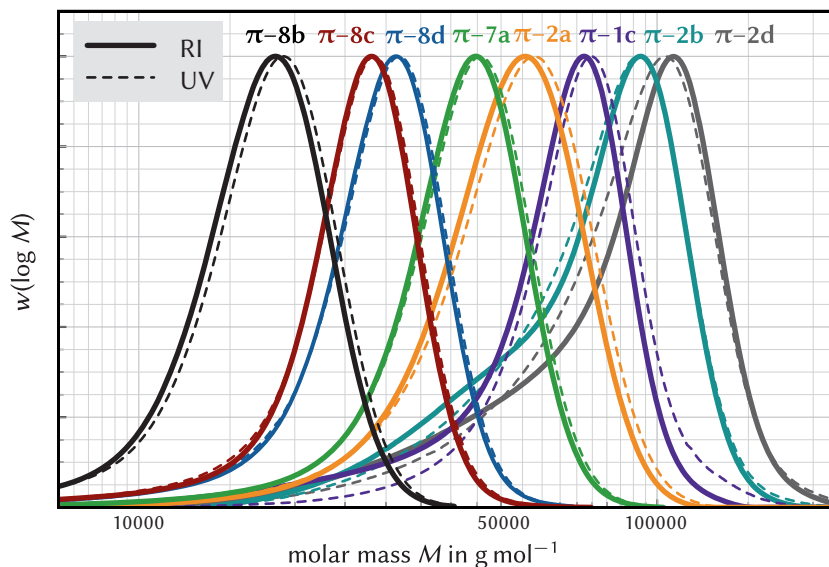
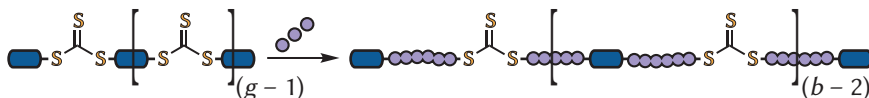


Fig. 5.15: SEC chromatograms (DMAC) of all conventional pNIPAm samples used for AuNP functionalization experiments in this work. See Table 5.3 for the \overline{M}_n and \overline{D} values extracted from these traces. (Reprinted and adapted with permission from a previous publication.^[102] Copyright 2013 American Chemical Society.)

The results from the SEC measurements of the conventional pNIPAm samples can be found in the experimental part (Tables 3.1 up to 3.10), along with the experimental reaction conditions. While for some of the polymerizations, the \overline{M}_n values increased almost linearly with the monomer conversion, as would be expected for a well-controlled RAFT polymerization, this was not true for all cases. As stated above concerning the results by gravimetry, the apparent irregularities are caused by the work-up of the polymerizations. During the precipitation steps in diethyl ether, a fraction of the polymer is lost and the molar mass distribution are “cut off” at lower masses. Because the absolute sample masses differed significantly, the relative amount of diethyl ether, added to precipitate the polymer, was not always the same, which also explains the decreasing molar masses for consecutive samples in some polymerizations. However, since the motivation for conducting the polymerizations was not kinetic analysis, but rather to obtain pure samples with defined molar masses, where all macromolecules carried a trithiocarbonate group, the work-up was ideally suited here. For the experiments in this work, just selected polymer samples were



Scheme 5.6: Employing RAFT agents with g trithiocarbonate groups in a radical polymerization leads to multiblock polymers with $b = g + 1$ blocks. See Figure 5.12 for the structural formula of the used multifunctional RAFT agents.

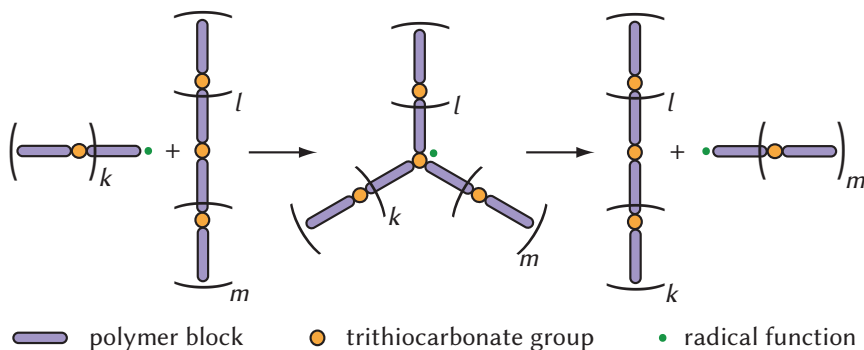
chosen, where the UV signal was superimposed on the RI signal, proving retained trithiocarbonate groups, and where the D value was low. These samples are listed in Table 5.3.

By way of example and because they are the most important, Figure 5.15 shows the SE chromatograms of all conventional pNIPAm samples which were employed in the functionalization of gold nanocrystals (see Section 8.3.2.1).

5.4.4 Multiblock poly(*N*-isopropylacrylamide)

The radical polymerizations $\pi^{\text{MB}}\text{-11}$ to $\pi^{\text{MB}}\text{-18}$ were carried out in the presence of RAFT agents that contain multiple functional trithiocarbonate groups. Apart from the type of employed RAFT agent, the reactions were identical to those for $\pi\text{-1}$ to $\pi\text{-10}$. The polymerization products are macromolecules, in which the g trithiocarbonate groups are incorporated along the polymer backbone,^[208] so-called *multiblock polymers* with $b = g + 1$ blocks.* The spacings between the functional groups increase with the progress of the polymerization.^[213] The reaction is illustrated in Scheme 5.6. On a side note, these polymers could theoretically be employed as macro-RAFT agents in a second radical polymerization with another monomer^[214] to yield *multisegmented copolymers*,^[215–218] polymers with alternating homogeneous segments composed of the two monomers. Such macromolecules, which are otherwise difficult to synthesize,^[219] reveal a unique self-assembly behavior,^[220–222] such as microphase separation,^[223–225] when the individual segments are sufficiently long^[226,227] and have distinctly different properties.^[228] Promising potential applications for multisegmented copolymers are the use as thermoplastic elastomers,^[229–231] compatibilizers for polymer mixtures,^[232–235] or adhesives.^[236,237] Furthermore, they can mimic natural macromolecules^[238–241] with versatile material properties.^[242] A second polymerization step was not explored here, but might be worthwhile in future work.

*One could in principle also prepare those polymers using cyclic trithiocarbonates,^[209–212] but multifunctional RAFT agents have the advantage that the block number of the resulting multiblock polymers can be better controlled.



Scheme 5.7: Redistribution mechanism of the polymer blocks among the macromolecules; $k, l, m = 0, 1, 2, \dots$ Compare the RAFT main equilibrium in Scheme 1.2. (Reprinted and adapted with permission from a previous publication.^[248] Copyright 2010 American Chemical Society.)

The three used multifunctional RAFT agents $\rho^{\text{MB}}\text{-7}$, $\rho^{\text{MB}}\text{-8}$, and $\rho^{\text{MB}}\text{-9}$ had already been prepared in an earlier work^[243,244] by reaction of a suitable dibromide with trithiocarbonate anions on the surface of a ion-exchange resin^[245,246] and fractionation of the product by rinsing the heterogeneous support system with different solvents. Their general structure is depicted in Figure 5.12. Based on SEC analysis,^[244] the RAFT agents possessed $\bar{g} = 4.2$ ($\rho^{\text{MB}}\text{-7}$), 17.3 ($\rho^{\text{MB}}\text{-8}$), and 12.0 ($\rho^{\text{MB}}\text{-9}$) trithiocarbonate groups. Via ^{13}C -NMR spectroscopy, it was made sure that the trithiocarbonate groups were still intact.^[247]

In Tables 3.11 up to 3.18 in Section 3.2.6.1, the individual reaction conditions and the analysis results from the multiblock polymerizations are listed. It can be assumed that the SEC calibration was still applicable here, since the RAFT moieties only constitute a relatively small fraction of the total molar mass. In Figure 5.16 all SE chromatograms of the multiblock polymer samples which were employed in further reactions (see Section 8.3.2.2) and the SE chromatograms of the corresponding cleavage products (see below in Section 5.4.5) are shown.

5.4.4.1 Ideal dispersity of the multiblock polymers

The dispersities of the synthesized multiblock polymers (see Tables 3.11 to 3.18) are considerably higher than for the conventional pNIPAm polymers. This finding can be explained by the fact that the broadness of the distributions of these polymers is mainly caused by the distribution of (possibly very narrow) blocks among the macromolecules. Because of the inherent mechanistic characteristics of RAFT

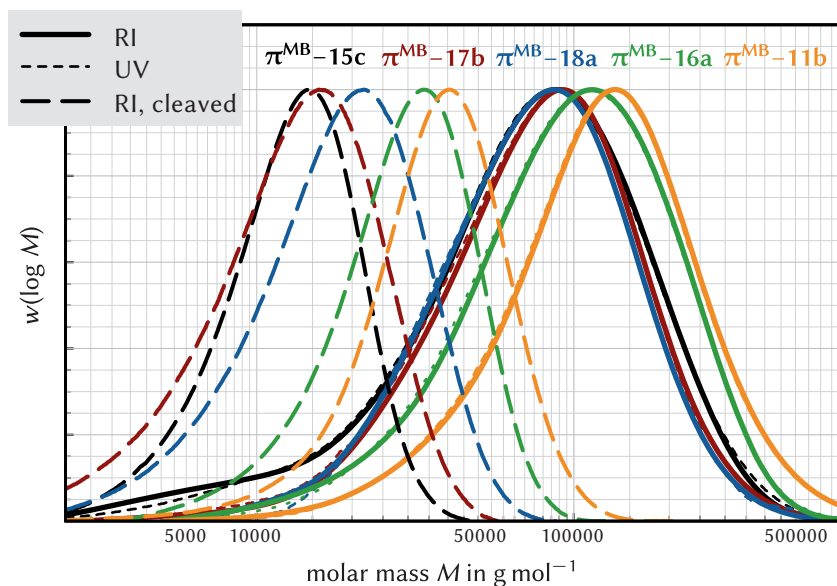


Fig. 5.16: SE chromatograms (DMAC) of the NIPAm multiblock polymer samples used for further AuNP-functionalization experiments in this work and their cleavage products. See Table 5.3 for all details on the polymers. (Reprinted and adapted with permission from a previous publication.^[102] Copyright 2013 American Chemical Society.)

polymerization (see Section 1.2.1.1), the polymer blocks are constantly redistributed between all individual macromolecules in the polymerization system. Thus, regardless of the initial distribution of the multifunctional RAFT agent (presumably a Schultz–Flory distribution),^[249,250] a well predictable block distribution is expected to occur at the end of the polymerization, owing to this reshuffling process.^[248]

The ongoing redistribution mechanism, by which the total number of blocks, trithiocarbonate groups, and macromolecules is not changed, is illustrated in Scheme 5.7. For the final distribution of blocks, it is sufficient to just consider the repeated execution of the depicted step, which must eventually lead to an equilibrium. The only remaining question is with which probability the individual trithiocarbonate groups will be attacked. To this end, two obvious limiting cases can be assumed. *Model A:* Every trithiocarbonate group in the system is attacked with the same probability, regardless of the molecule that it belongs to. *Model B:* Every macromolecule is attacked with equal probability. Within the macromolecules,

every trithiocarbonate group still has an equal chance of being attacked, so that trithiocarbonate groups in macromolecules with fewer blocks are more likely to be attacked. Interpreting these models physically,^[248] the extreme case of model A is rather expected to occur in concentrated systems, where radicals meet potential reaction partners with a faster rate than the actual reaction takes place. The extreme case of model B, in contrast, is rather expected to occur in very dilute solutions with high viscosities, where the reaction rate is mainly governed by diffusion.

In order to be able to assess the quality of the performed multiblock RAFT polymerizations, it is indispensable to know the expected ideal dispersity values which are expected for the arising equilibrium distribution functions A and B.

In previous work,^[248] the block distributions in question could be deduced analytically based on the assumption that, in equilibrium, for macromolecules with any number of blocks, the probabilities of formation and decomposition must coincide. The results were also supported by numerical simulations. The normalized distribution functions \underline{N}_b^A for model A and \underline{N}_b^B for model B in the dependence on the number of blocks b with \bar{b} being the average value are

$$\underline{N}_b^A = \frac{1}{\bar{b}-1} \left(\frac{\bar{b}-2}{\bar{b}-1} \right)^{b-2}, \quad b = 2, 3, \dots \quad (5.12)$$

and

$$\underline{N}_b^B = \frac{4}{\bar{b}^2} \left(\frac{\bar{b}-2}{\bar{b}} \right)^{b-2} (b-1), \quad b = 2, 3, \dots \quad (5.13)$$

For both functions, the corresponding dispersities \mathcal{D}^A and \mathcal{D}^B (see Equation (1.15), Section 1.2.1.2) can be calculated to be

$$\mathcal{D}^A \stackrel{(1.15)}{=} \frac{2\bar{b}^2 - 3\bar{b} + 2}{\bar{b}^2} \quad (5.14)$$

and

$$\mathcal{D}^B = \frac{3}{2} - \frac{1}{\bar{b}}. \quad (5.15)$$

Function B is obviously narrower. These four expressions (5.12) to (5.15) can easily be converted into functions of the number of trithiocarbonate groups g instead of b according to the relations

$$g = b - 1 \quad \text{and} \quad \bar{g} = \bar{b} - 1. \quad (5.16)$$

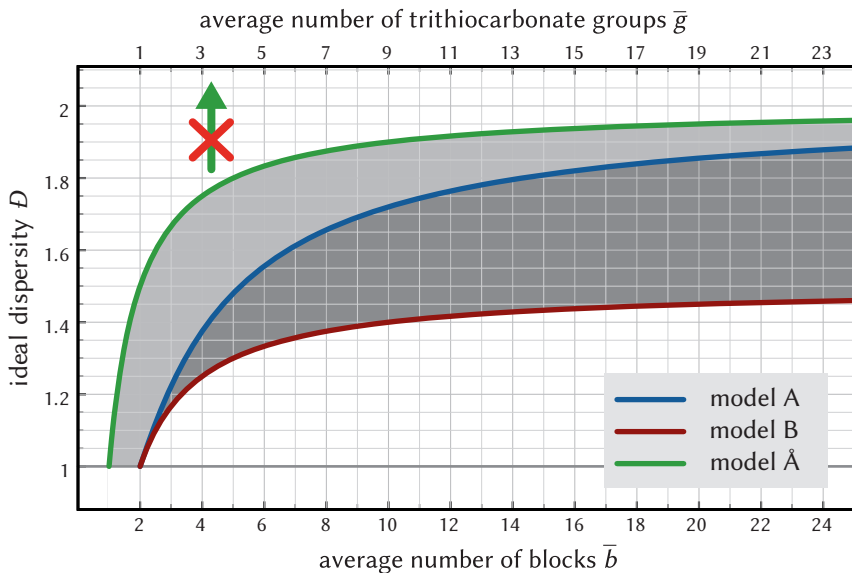


Fig. 5.17: Ideally expected dispersities of multiblock polymers produced by radical polymerization in the presence of multifunctional RAFT agents. In terms of the distribution of trithiocarbonate groups, the ideal dispersities must lie in the darker shaded area. Dispersities as obtained from SEC analysis of molar mass distributions must ideally lie in the total gray-shaded area. Please note that the upper x -axis of \bar{g} does not apply to the curve for model \tilde{A} (green).

The diagram in Figure 5.17 shows the dispersities \bar{D} as a function of the average number of blocks \bar{b} and the average number of trithiocarbonate groups \bar{g} . The dispersity in terms of the distribution of blocks among the molecules must lie within the area shaded in the darker gray. For comparison with measured SEC traces, however, it is more sensible to compare the measured data with the ideal dispersities in terms of molar masses. Those are not identical, because the blocks at the end of the polymer chains (growing on one side) are smaller than the blocks in the middle (growing on both sides). This has been shown experimentally in previous work and can even be exploited as means to get information on the type of block reshuffling.^[244] Depending on the ongoing mechanism, the ratio of middle and end blocks $r_{\ddot{m}/\dot{m}}$ can assume values from 1 (for pure model B) to 2 (for pure model A):

$$1 \leq r_{\ddot{m}/\dot{m}} \leq 2. \quad (5.17)$$

By defining a new effective block number $\overset{\circ}{b}$, for which end blocks only count as half blocks, the distribution function for model A can be corrected. The resulting function $\overset{\circ}{A}$ is a Schultz–Flory distribution for $\overset{\circ}{b}$:

$$\frac{N_{\overset{\circ}{b}}^{\overset{\circ}{A}}}{\overset{\circ}{b}} = \frac{1}{\overset{\circ}{b}} \left(\frac{\overset{\circ}{b} - 1}{\overset{\circ}{b}} \right)^{\overset{\circ}{b}-1}. \quad (5.18)$$

The dispersity of this function is

$$\text{PDI}^{\overset{\circ}{A}} = 2 - \frac{1}{\overset{\circ}{b}}. \quad (5.19)$$

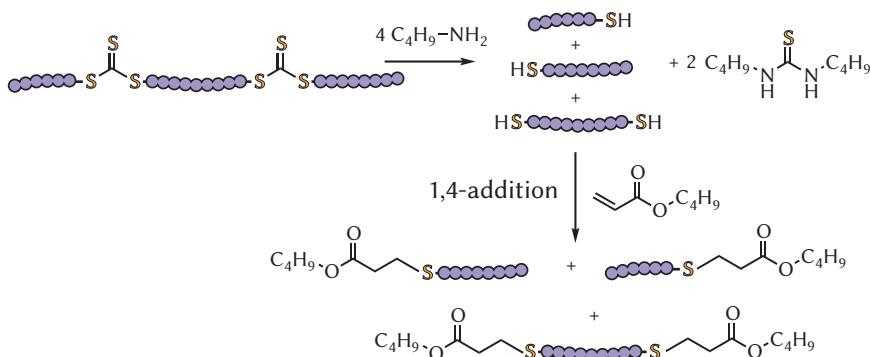
This function is additionally plotted as green line in the diagram in Figure 5.17. Please note that the upper axis does not apply to this curve, since the relation (5.16) holds no longer true here. The dispersities in terms of polymer masses lie somewhere within both shaded areas.*

The actually measured dispersities (see Tables 3.11 to 3.18) are even higher. This cannot be explained by the block distribution and must be caused by a strong broadening of the individual blocks, presumably due to radical combination. This is in line with the observed decrease of the block numbers (see next section).

Regarding the block distribution, the synthesis using multifunctional RAFT agents leads to more homogeneous polymers than with the conventional step-growth approach of polycondensation,^[252] in this case of α - ω -thiol-functionalized prepolymers and carbon disulfide, or of α - ω -halogen-functionalized polymers with trithiocarbonate anions (see Section 1.2.1.1), which would lead to a Schulz–Flory distribution,^[253,254] as has been deduced in literature,^[249,250] even when end-cappers are used to limit the degree of polymerization.^[255] Only with multiple polycondensation steps, can the block distribution become narrower.^[256,257]

The strategy followed here for the synthesis of multiblock polymers is furthermore superior to the coupling of prepolymers, because it can be implemented with less experimental effort, it allows for the production of longer blocks, which are potentially better defined at the same time, and macromolecules with large block numbers can be synthesized. Moreover, the number of blocks can also be better controlled, just by using a mixture of multifunctional RAFT agents with the desired average number of trithiocarbonate groups \bar{b} .^[244]

*The effect of broadening of the distribution by the SEC measurement,^[251] which also raises the dispersities to some extent, is not taken into account here.



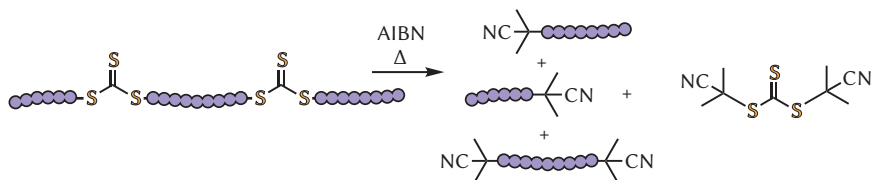
Scheme 5.8: Cleavage of trithiocarbonate groups in polymers by aminolysis with *n*-butyl amine and immediate sealing of the thiol groups with *n*-butyl acrylate.

5.4.5 Cleavage of trithiocarbonate groups

The trithiocarbonate groups of the produced NIPAm polymers can be cleaved in order to i) obtain reference polymers without sulfur-containing groups for AuNP-coating experiments and ii) be able to estimate the number of blocks \bar{b}_{cl} of multiblock polymers by comparison of the average molar mass before $\bar{M}_{n,0}$ and after $\bar{M}_{n,1}$ the reaction according to:

$$\bar{b}_{\text{cl}} = \frac{\bar{M}_{n,0}}{\bar{M}_{n,1}} - 1. \quad (5.20)$$

Trithiocarbonate groups can be split into two thiols and the respective thiourea derivative by nucleophiles, typically amines,^[258,259] or by hydroxide anions.^[260] In Scheme 5.8, a one-pot strategy by Qiu and Winnik^[261] (2006) is depicted, where the thiol groups formed by the aminolysis with *n*-butyl amine are immediately sealed by thiol-Michael addition^[262] of the α,β -unsaturated carbonyl compound *n*-butyl acrylate. The unwanted oxidative coupling reaction to disulfides^[263–265] is thus prevented.^[266] The aminolysis is performed in the presence of tris(2-carboxy-ethyl)phosphine,^[267,268] a common specific reducing agent for disulfides^[269,270] This method had been the preferred method for the cleavage of the multiblock polymers in previous studies.^[244] However here, as opposed to the other work, the pNIPAm samples could not be precipitated by addition of a solvent which at the same time is a good solvent for the other reactants. That is why the polymers had to be recovered by drying for 1 d at 75 °C under high vacuum, making it very work-intensive. In addition, the hereby produced polymers are not ideally suited for



Scheme 5.9: Cleavage of trithiocarbonate groups in polymers by reaction with an excess of radicals, here produced by the decomposition of AIBN.

control experiments on gold surfaces anyway, since their end-groups still contain sulfur.

Because of these reasons, the alternative cleave method of reaction with an excess of radicals,^[271] which produced very similar results in terms of the SEC analysis of the cleavage products, was given preference. It is shown in Scheme 5.9 with AIBN (see Figure 5.13) as radical source. Eventually all polymer chains and trithiocarbonate groups are terminated by a cyanoisopropyl fragment. Reaction was performed at 85 °C to enable the quick decomposition of all initiator molecules. The great excess of AIBN leads to a high content of material with low molecular mass, but the cleaved polymer could be easily isolated by precipitation in diethyl ether as described above. The third cleavage method involving the thermolysis of the trithiocarbonate groups at temperatures between 200 °C and 300 °C^[272–274] was not studied here, because it cannot be excluded that at these temperatures also decomposition of the polymer backbone, altering the outcome of Equation (5.20), takes place.

No signal was observed with the UV detector when the polymers obtained after the cleavage reaction with an excess of AIBN were analyzed by means of SEC, demonstrating the success and the completeness of the reaction. The RI traces of samples $\pi^x\text{-1c}'$ and $\pi^x\text{-2d}'$, yielded by the cleavage of a part of the conventional RAFT polymers $\pi\text{-1c}$ and $\pi\text{-2d}$, were practically unchanged by the cleavage reaction (see Table 5.3), because the polymers carried the trithiocarbonate group at the chain end. In contrast, the SEC traces of the cleaved multiblock polymers (shown in Figure 5.16 for the five further used samples) were shifted to significantly lower molar masses, proving that the trithiocarbonate groups had remained distributed along the polymer backbone during the polymerization. Using Equation (5.20), the number of blocks \bar{b}_{cl} could be calculated by cleaving a small amount of each produced multiblock polymer sample. The individual results are listed in Tables 3.11 up to 3.18 in Section 3.2.6.1 and, for the most relevant samples, in Table 5.3. Although it is known that the numbers obtained by this method are usually too low^[244] and

similar reactions even gave results under the minimum value of 1, the comparably low values for \bar{b}_{cl} and especially the general tendency of decreasing \bar{b}_{cl} with the polymerization times indicate that a certain number of trithiocarbonate groups might have been lost by termination reactions over the course of the polymerizations. Nevertheless, the chosen samples were proven to possess at least a number of trithiocarbonate groups, which is clearly sufficient for obtaining meaningful results in Section 8.3.2.2.

References for Chapter 5

- (1) Lang, N. J., Liu, B., Zhang, X., Liu, J., *Langmuir* **2013**, 29 (20), 6018–6024.
- (2) Zhang, S., Leem, G., Srisombat, L.-o., Lee, T. R., *J. Am. Chem. Soc.* **2008**, 130 (1), 113–120.
- (3) Krumpfer, J. W., Schuster, T., Klapper, M., Müllen, K., *Nano Today* **2013**, 8 (4), 417–438.
- (4) Kalyva, M., Bertoni, G., Milionis, A., Cingolani, R., Athanassiou, A., *Microsc. Res. Technol.* **2010**, 73 (10), 937–943.
- (5) Sobhan, M., Ams, M., Withford, M., Goldys, E., *J. Nanopart. Res.* **2010**, 12 (8), 2831–2842.
- (6) Giorgetti, E., Muniz-Miranda, M., Marsili, P., Scarpellini, D., Giammanco, F., *English J. Nanopart. Res.* **2012**, 14 (1), 1–13.
- (7) Kim, K. K., Kwon, H. J., Shin, S. K., Song, J. K., Park, S. M., *Chem. Phys. Lett.* **2013**, 588, 167–173.
- (8) Tseng, K.-H., Huang, J.-C., *J. Nanopart. Res.* **2011**, 13 (7), 2963–2972.
- (9) Brauer, G., *Handbuch der Präparativen Anorganischen Chemie in drei Bänden*, 3rd edition; Ferdinand Enke Verlag: Stuttgart, **1973**.
- (10) Biltz, W., Wein, W., *Z. Anorg. Allg. Chem.* **1925**, 148 (1), 192–206.
- (11) Thomsen, J., *Chem. Ber.* **1883**, 16 (2), 1585–1587.
- (12) Lohse, S. E., Murphy, C. J., *Chem. Mater.* **2013**, 25 (8), 1250–1261.
- (13) DuChene, J. S., Niu, W., Abendroth, J. M., Sun, Q., Zhao, W., Huo, F., Wei, W. D., *Chem. Mater.* **2013**, 25 (8), 1392–1399.
- (14) Li, X., Xu, H., Chen, Z.-S., Chen, G., *J. Nanomat.* **2011**, 2011, 270974.
- (15) Asmathunisha, N., Kathiresan, K., *Colloids Surf., B* **2013**, 103, 283–287.
- (16) Bankar, A., Joshi, B., Kumar, A. R., Zinjarde, S., *Colloids Surf., B* **2010**, 80 (1), 45–50.
- (17) Ghodake, G., Lee, D., *English Korean J. Chem. Eng.* **2011**, 28 (12), 2329–2335.
- (18) Sujitha, M. V., Kannan, S., *Spectrochim. Acta, Part A* **2013**, 102, 15–23.
- (19) Lekeufack, D. D., Brioude, A., *Dalton Trans.* **2012**, 41 (5), 1461–1464.
- (20) Aromal, S. A., Vidhu, V., Philip, D., *Spectrochim. Acta, Part A* **2012**, 85 (1), 99–104.
- (21) Dubey, S. P., Lahtinen, M., Sillanpää, M., *Colloids Surf., A* **2010**, 364 (1–3), 34–41.
- (22) Mukherjee, S., Sushma, V., Patra, S., Barui, A. K., Bhadra, M. P., Sreedhar, B., Patra, C. R., *Nanotechnology* **2012**, 23 (45), 455103.
- (23) Mittal, A. K., Chisti, Y., Banerjee, U. C., *Biotechnol. Adv.* **2013**, 31 (2), 346–356.
- (24) Ankamwar, B., *E-J. Chem.* **2010**, 7 (4), 1334–1339.
- (25) Mondal, S., Roy, N., Laskar, R. A., Sk, I., Basu, S., Mandal, D., Begum, N. A., *Colloids Surf., B* **2011**, 82 (2), 497–504.
- (26) Philip, D., *Spectrochimica Acta Part A: Molecular and Biomolecular Spectroscopy* **2010**, 77 (4), 807–810.
- (27) Khalil, M. M., Ismail, E. H., El-Magdoub, F., *Arabian J. Chem.* **2012**, 5 (4), 431–437.
- (28) Raju, D., Mehta, U., Hazra, S., *Trees* **2011**, 25 (2), 145–151.

- (29) Kumar, P., Singh, P., Kumari, K., Mozumdar, S., Chandra, R., *Mater. Lett.* **2011**, 65 (4), 595–597.
- (30) Philip, D., Unni, C., Aromal, S. A., Vidhu, V. K., *Spectrochim. Acta, Part A* **2011**, 78 (2), 899–904.
- (31) Elavazhagan, T., Arunachalam, K. D., *Int. J. Nanomed.* **2011**, 6, 1265–1278.
- (32) Dubey, S. P., Lahtinen, M., Sillanpää, M., *Process Biochem.* **2010**, 45 (7), 1065–1071.
- (33) Dwivedi, A. D., Gopal, K., *Colloids Surf., A* **2010**, 369 (1–3), 27–33.
- (34) Narayanan, K. B., Sakthivel, N., *Mater. Charact.* **2010**, 61 (11), 1232–1238.
- (35) Fierascu, R. C., Ion, R. M., Dumitriu, I., *Optoelectron. Adv. Mater. Rapid Commun.* **2010**, 4 (9), 1297–1300.
- (36) Raghunandan, D., Bedre, M. D., Basavaraja, S., Sawle, B., Manjunath, S., Venkataraman, A., *Colloids Surf., B* **2010**, 79 (1), 235–240.
- (37) Vijayakumar, R., Devi, V., Advallan, K., Saranya, D., *Physica E* **2011**, 44 (3), 665–671.
- (38) Leonard, K., Ahmmad, B., Okamura, H., Kurawaki, J., *Colloids Surf., B* **2011**, 82 (2), 391–396.
- (39) Kumar, K. P., Paul, W., Sharma, C. P., *Process Biochem.* **2011**, 46 (10), 2007–2013.
- (40) Wu, C.-C., Chen, D.-H., *Gold Bull.* **2010**, 43 (4), 234–240.
- (41) Vinod, V., Saravanan, P., Sreedhar, B., Devi, D. K., Sashidhar, R., *Colloids Surf., B* **2011**, 83 (2), 291–298.
- (42) Roy, N., Mondal, S., Laskar, R. A., Basu, S., Mandal, D., Begum, N. A., *Colloids Surf., B* **2010**, 76 (1).
- (43) Kalishwaralal, K., Deepak, V., Pandian, S. R. K., Kottaisamy, M., BarathManiKanth, S., Kartikeyan, B., Gurunathan, S., *Colloids Surf., B* **2010**, 77 (2), 257–262.
- (44) Fayaz, A. M., Girilal, M., Rahman, M., Venkatesan, R., Kalaichelvan, P., *Process Biochem.* **2011**, 46 (10), 1958–1962.
- (45) Das, S., Marsili, E., *Rev. Environ. Sci. Biotechnol.* **2010**, 9 (3), 199–204.
- (46) Das, S. K., Das, A. R., Guha, A. K., *Small* **2010**, 6 (9), 1012–1021.
- (47) Du, L., Xian, L., Feng, J.-X., *J. Nanopart. Res.* **2011**, 13 (3), 921–930.
- (48) Dhillon, G. S., Brar, S. K., Kaur, S., Verma, M., *Crit. Rev. Biotechnol.* **2012**, 32 (1), 49–73.
- (49) Shakibaie, M., Forootanfar, H., Mollazadeh-Moghaddam, K., Bagherzadeh, Z., Nafissi-Varcheh, N., Shahverdi, A. R., Faramarzi, M. A., *Biotechnol. Appl. Biochem.* **2010**, 57 (Part 2), 71–75.
- (50) Durán, N., Marcato, P., Durán, M., Yadav, A., Gade, A., Rai, M., *Appl. Microbiol. Biotechnol.* **2011**, 90, 1609–1624.
- (51) Virkutyte, J., Varma, R. S., *Chem. Sci.* **2011**, 2 (5), 837–846.
- (52) Fan, R., Chew, S. W., Cheong, V. V., Orner, B. P., *Small* **2010**, 6 (14), 1483–1487.
- (53) Kirubha, E., Palanisamy, P. K., *J. Nanosci. Nanotechnol.* **2013**, 13 (3), 2289–2294.
- (54) Mu, Z., Zhao, X., Xie, Z., Zhao, Y., Zhong, Q., Bo, L., Gu, Z., *J. Mater. Chem. B* **2013**, 1 (11), 1607–1613.
- (55) Larios-Rodriguez, E., Rangel-Ayon, C., Castillo, S. J., Zavala, G., Herrera-Urbina, R., *Nanotechnology* **2011**, 22 (35), 355601.

- (56) Haveli, S. D., Walter, P., Patriarche, G., Ayache, J., Castaing, J., Van Elslande, E., Tsoucaris, G., Wang, P.-A., Kagan, H. B., *Nano Lett.* **2012**, *12* (12), 6212–6217.
- (57) Thimsen, E., *Chem. Mater.* **2011**, *23* (20), 4612–4617.
- (58) Abdelaziz, R., Disci-Zayed, D., Hedayati, M. K., Pöhls, J.-H., Zillohu, A. U., Erkartal, B., Chakravadhanula, V. S. K., Duppel, V., Kienle, L., Elbahri, M., *Nat. Commun.* **2013**, *4*.
- (59) Ulman, A., *Chem. Rev.* **1996**, *96* (4), 1533–1554.
- (60) Wang, Y., Zeiri, O., Neyman, A., Stellacci, F., Weinstock, I. A., *ACS Nano* **2012**, *6* (1), 629–640.
- (61) Barmparis, G. D., Honkala, K., Remediakis, I. N., *J. Chem. Phys.* **2013**, *138* (6), 064702.
- (62) Cheng, L., Yuan, Y., Zhang, X., Yang, J., *Angew. Chem. Int. Ed.* **2013**, *52* (34), 9035–9039.
- (63) Kurashige, W., Yamaguchi, M., Nobusada, K., Negishi, Y., *J. Phys. Chem. Lett.* **2012**, *3* (18), 2649–2652.
- (64) Zaluzhna, O., Li, Y., Allison, T. C., Tong, Y. J., *J. Am. Chem. Soc.* **2012**, *134* (43), 17991–17996.
- (65) Leff, D. V., Brandt, L., Heath, J. R., *Langmuir* **1996**, *12* (20), 4723–4730.
- (66) Marchetti, B., Joseph, Y., Bertagnolli, H., *J. Nanopart. Res.* **2011**, *13* (8), 3353–3362.
- (67) Warner, M. G., Reed, S. M., Hutchison, J. E., *Chem. Mater.* **2000**, *12* (11), 3316–3320.
- (68) Woehrle, G. H., Warner, M. G., Hutchison, J. E., *J. Phys. Chem. B* **2002**, *106* (39), 9979–9981.
- (69) Guidez, E. B., Hadley, A., Aikens, C. M., *J. Phys. Chem. C* **2011**, *115* (14), 6305–6316.
- (70) Pasquato, L., Pengo, P., Scrimin, P., *J. Mater. Chem.* **2004**, *14* (24), 3481–3487.
- (71) Jadhav, S. A., *J. Mater. Chem.* **2012**, *22* (13), 5894–5899.
- (72) Mikhlin, Y., Karacharov, A., Likhatski, M., Podlipskaya, T., Zubavichus, Y., Veligzhanin, A., Zaikovski, V., *J. Colloid Interface Sci.* **2011**, *362* (2), 330–336.
- (73) Doyen, M., Bartik, K., Bruylants, G., *J. Colloid Interface Sci.* **2013**, *399*, 1–5.
- (74) Turkevich, J., Stevenson, P. C., Hillier, J., *Discuss. Faraday Soc.* **1951**, *11*, 55–75.
- (75) Enüstün, B. V., Turkevich, J., *J. Am. Chem. Soc.* **1963**, *85* (21), 3317–3328.
- (76) Turkevich, J., *Gold Bull.* **1985**, *18* (3).
- (77) Turkevich, J., *Gold Bull.* **1985**, *18* (4).
- (78) Frens, G., *Colloid Polym. Sci.* **1972**, *250* (7), 736–741.
- (79) Frens, G., *Nature Phys. Sci.* **1973**, *241* (105), 20–22.
- (80) Grabar, K. C., Freeman, R. G., Hommer, M. B., Natan, M. J., *Anal. Chem.* **1995**, *67* (4), 735–743.
- (81) Kimling, J., Maier, M., Okenve, B., Kotaidis, V., Ballot, H., Plech, A., *J. Phys. Chem. B* **2006**, *110* (32), 15700–15707.
- (82) Ojea-Jiménez, I., Campanera, J. M., *J. Phys. Chem. C* **2012**, *116* (44), 23682–23691.
- (83) Polte, J., Ahner, T. T., Delissen, F., Sokolov, S., Emmerling, F., Thünemann, A. F., Kraehnert, R., *J. Am. Chem. Soc.* **2010**, *132* (4), 1296–1301.
- (84) Rodríguez-González, B., Mulvaney, P., Liz-Marzán, L. M., *Z. Phys. Chem.* **2007**, *221* (3), 415–426.
- (85) Kumar, S., Gandhi, K. S., Kumar, R., *Ind. Eng. Chem. Res.* **2007**, *46* (10), 3128–3136.

- (86) Pong, B.-K., Elim, H. I., Chong, J.-X., Ji, W., Trout, B. L., Lee, J.-Y., *J. Phys. Chem. C* **2007**, *111* (17), 6281–6287.
- (87) Chow, M., Zukoski, C., *J. Colloid Interface Sci.* **1994**, *165* (1), 97–109.
- (88) Wright, L. B., Rodger, P. M., Walsh, T. R., *RSC Adv.* **2013**, *3* (37), 16399–16409.
- (89) Njoki, P. N., Luo, J., Kamundi, M. M., Lim, S., Zhong, C.-J., *Langmuir* **2010**, *26* (16), 13622–13629.
- (90) Huang, Y., Kim, D.-H., *Langmuir* **2011**, *27* (22), 13861–13867.
- (91) Zhao, P., Li, N., Astruc, D., *Coord. Chem. Rev.* **2013**, *257* (3–4), 638–665.
- (92) Low, A., Bansal, V., *Biomed. Imaging Interv. J.* **2010**, *6* (1), e9.
- (93) Wang, S., Qian, K., Bi, X., Huang, W., *J. Phys. Chem. C* **2009**, *113* (16), 6505–6510.
- (94) Ji, X., Song, X., Li, J., Bai, Y., Yang, W., Peng, X., *J. Am. Chem. Soc.* **2007**, *129* (45), 13939–13948.
- (95) Su, C.-H., Wu, P.-L., Yeh, C.-S., *J. Phys. Chem. B* **2003**, *107* (51), 14240–14243.
- (96) Uppal, M. A., Kafizas, A., Ewing, M. B., Parkin, I. P., *New J. Chem.* **2010**, *34* (12), 2906–2914.
- (97) Sivaraman, S. K., Kumar, S., Santhanam, V., *J. Colloid Interface Sci.* **2011**, *361* (2), 543–547.
- (98) Ojea-Jiménez, I., Bastús, N. G., Puentes, V., *J. Phys. Chem. C* **2011**, *115* (32), 15752–15757.
- (99) Zhao, L., Jiang, D., Cai, Y., Ji, X., Xie, R., Yang, W., *Nanoscale* **2012**, *4* (16), 5071–5076.
- (100) Balasubramanian, S. K., Yang, L., Yung, L.-Y. L., Ong, C.-N., Ong, W.-Y., Yu, L. E., *Biomaterials* **2010**, *31* (34), 9023–9030.
- (101) Karg, M., Schelero, N., Oppel, C., Gradzielski, M., Hellweg, T., von Klitzing, R., *Chem.—Eur. J.* **2011**, *17* (16), 4648–4654.
- (102) Ebeling, B., Vana, P., *Macromolecules* **2013**, *46* (12), 4862–4871.
- (103) Watanabe-Tamaki, R., Ishikawa, A., Tanaka, T., *Appl. Phys. Lett.* **2013**, *102* (4), 043110.
- (104) Uppal, M. A., Kafizas, A., Lim, T. H., Parkin, I. P., *New J. Chem.* **2010**, *34* (7), 1401–1407.
- (105) Brust, M., Walker, M., Bethell, D., Schiffrin, D. J., Whyman, R., *J. Chem. Soc., Chem. Commun.* **1994**, (7), 801–802.
- (106) Brust, M., Fink, J., Bethell, D., Schiffrin, D. J., Kiely, C., *J. Chem. Soc., Chem. Commun.* **1995**, *16*, 1655–1656.
- (107) Bethell, D., Brust, M., Schiffrin, D., Kiely, C., *J. Electroanal. Chem.* **1996**, *409* (1–2), 137–143.
- (108) Brust, M., Bethell, D., Kiely, C. J., Schiffrin, D. J., *Langmuir* **1998**, *14* (19), 5425–5429.
- (109) Wilcoxon, J. P., Williamson, R. L., Baughman, R., *J. Chem. Phys.* **1993**, *98* (12), 9933–9950.
- (110) Giersig, M., Mulvaney, P., *Langmuir* **1993**, *9* (12), 3408–3413.
- (111) Li, Y., Zaluzhna, O., Tong, Y. J., *Chem. Commun.* **2011**, *47* (21), 6033–6035.
- (112) Huang, X., Li, B., Zhang, H., Hussain, I., Liang, L., Tan, B., *Nanoscale* **2011**, *3* (4), 1600–1607.
- (113) Li, Y., Zaluzhna, O., Zangmeister, C. D., Allison, T. C., Tong, Y. J., *J. Am. Chem. Soc.* **2012**, *134* (4), 1990–1992.
- (114) Goulet, P. J. G., Lennox, R. B., *J. Am. Chem. Soc.* **2010**, *132* (28), 9582–9584.
- (115) Perala, S. R. K., Kumar, S., *Langmuir* **2013**, *29* (31), 9863–9873.

- (116) Zhu, L., Zhang, C., Guo, C., Wang, X., Sun, P., Zhou, D., Chen, W., Xue, G., *J. Phys. Chem. C* **2013**, *117* (21), 11399–11404.
- (117) Zhu, M., Lanni, E., Garg, N., Bier, M. E., Jin, R., *J. Am. Chem. Soc.* **2008**, *130* (4), 1138–1139.
- (118) Sendroiu, I. E., Mertens, S. F. L., Schiffrin, D. J., *Phys. Chem. Chem. Phys.* **2006**, *8* (12), 1430–1436.
- (119) Garcia, M. A., *J. Phys. D: Appl. Phys.* **2011**, *44* (28), 283001.
- (120) Zhu, S., Chen, T., Liu, Y., Liu, Y., Fung, S., English, *J. Nanopart. Res.* **2012**, *14* (5), 1–6.
- (121) Kassam, A., Bremner, G., Clark, B., Ulibarri, G., Lennox, R. B., *J. Am. Chem. Soc.* **2006**, *128* (11), 3476–3477.
- (122) Boisselier, E., Salmon, L., Ruiz, J., Astruc, D., *Chem. Commun.* **2008**, (44), 5788–5790.
- (123) Zaluzhna, O., Li, Y., Zangmeister, C., Allison, T. C., Tong, Y. J., *Chem. Commun.* **2012**, *48* (3), 362–364.
- (124) Shaw, C. F., *Chem. Rev.* **1999**, *99* (9), 2589–2600.
- (125) Hostetler, M. J., Templeton, A. C., Murray, R. W., *Langmuir* **1999**, *15* (11), 3782–3789.
- (126) Wu, Z., Gayathri, C., Gil, R. R., Jin, R., *J. Am. Chem. Soc.* **2009**, *131* (18), 6535–6542.
- (127) Canzi, G., Mrse, A. A., Kubiak, C. P., *J. Phys. Chem. C* **2011**, *115* (16), 7972–7978.
- (128) Hostetler, M. J., Wingate, J. E., Zhong, C.-J., Harris, J. E., Vachet, R. W., Clark, M. R., Londono, J. D., Green, S. J., Stokes, J. J., Wignall, G. D., Glish, G. L., Porter, M. D., Evans, N. D., Murray, R. W., *Langmuir* **1998**, *14* (1), 17–30.
- (129) Wu, Z., Suhan, J., Jin, R., *J. Mater. Chem.* **2009**, *19* (5), 622–626.
- (130) Manna, A., Chen, P., Akiyama, H., Wei, T., Tamada, K., Knoll, W., *Chem. Mater.* **2003**, *15* (1), 20–28.
- (131) Fink, J., Kiely, C. J., Bethell, D., Schiffrin, D. J., *Chem. Mater.* **1998**, *10* (3), 922–926.
- (132) Zhou, J., Beattie, D. A., Sedev, R., Ralston, J., *Langmuir* **2007**, *23* (18), 9170–9177.
- (133) Scaffardi, L. B., Pellegrini, N., Sanctis, O. de, Tocho, J. O., *Nanotechnol.* **2005**, *16* (1), 158.
- (134) Jain, P. K., Lee, K. S., El-Sayed, I. H., El-Sayed, M. A., *J. Phys. Chem. B* **2006**, *110* (14), 7238–7248.
- (135) Liu, X., Atwater, M., Wang, J., Huo, Q., *Colloids Surf., B* **2007**, *58* (1), 3–7.
- (136) Rance, G. A., Marsh, D. H., Khlobystov, A. N., *Chem. Phys. Lett.* **2008**, *460* (1-3), 230–236.
- (137) Rucareanu, S., Gandubert, V. J., Lennox, R. B., *Chem. Mater.* **2006**, *18* (19), 4674–4680.
- (138) Hiramatsu, H., Osterloh, F. E., *Chem. Mater.* **2004**, *16* (13), 2509–2511.
- (139) Jana, N. R., Peng, X., *J. Am. Chem. Soc.* **2003**, *125* (47), 14280–14281.
- (140) Aslam, M., Fu, L., Su, M., Vijayamohanan, K., Dravid, V. P., *J. Mater. Chem.* **2004**, *14* (12), 1795–1797.
- (141) Shen, C., Hui, C., Yang, T., Xiao, C., Tian, J., Bao, L., Chen, S., Ding, H., Gao, H., *Chem. Mater.* **2008**, *20* (22), 6939–6944.
- (142) Polavarapu, L., Xu, Q.-H., *Nanotechnology* **2009**, *20* (18), 185606.
- (143) Capdevielle, P., Lavigne, A., Sparfel, D., Baranne-Lafont, J., Nguyen, K. C., Maumy, M., *Tetrahedron Lett.* **1990**, *31* (23), 3305–3308.

- (144) LaMer, V. K., Dinegar, R. H., *J. Am. Chem. Soc.* **1950**, 72 (11), 4847–4854.
- (145) Privman, V., Goia, D. V., Park, J., Matijevic, E., *J. Colloid Interface Sci.* **1999**, 213 (1), 36–45.
- (146) Compton, O. C., Osterloh, F. E., *J. Am. Chem. Soc.* **2007**, 129 (25), 7793–7798.
- (147) Jones, M. R., Macfarlane, R. J., Prigodich, A. E., Patel, P. C., Mirkin, C. A., *J. Am. Chem. Soc.* **2011**, 133 (46), 18865–18869.
- (148) Harkness, K. M., Cliffel, D. E., McLean, J. A., *Analyst* **2010**, 135 (5), 868–874.
- (149) Tsunoyama, H., Negishi, Y., Tsukuda, T., *J. Am. Chem. Soc.* **2006**, 128 (18), 6036–6037.
- (150) Tracy, J. B., Crowe, M. C., Parker, J. F., Hampe, O., Fields-Zinna, C. A., Dass, A., Murray, R. W., *J. Am. Chem. Soc.* **2007**, 129 (51), 16209–16215.
- (151) Qian, H., Zhu, Y., Jin, R., *Proc. Natl. Acad. Sci. U.S.A.* **2012**, 109 (3), 696–700.
- (152) Qian, H., Jin, R., *Chem. Mater.* **2011**, 23 (8), 2209–2217.
- (153) Zhu, Y., Qian, H., Jin, R., *J. Mater. Chem.* **2011**, 21 (19), 6793–6799.
- (154) Wilcoxon, J. P., Provencio, P., *J. Phys. Chem. B* **2003**, 107 (47), 12949–12957.
- (155) Shichibu, Y., Negishi, Y., Tsunoyama, H., Kanehara, M., Teranishi, T., Tsukuda, T., *Small* **2007**, 3 (5), 835–839.
- (156) Sperling, R. A., Liedl, T., Duhr, S., Kudera, S., Zanella, M., Lin, C.-A. J., Chang, W. H., Braun, D., Parak, W. J., *J. Phys. Chem. C* **2007**, 111 (31), 11552–11559.
- (157) Knoppe, S., Boudon, J., Dolamic, I., Dass, A., Bürgi, T., *Anal. Chem.* **2011**, 83 (13), 5056–5061.
- (158) Schaaff, T. G., Knight, G., Shafigullin, M. N., Borkman, R. F., Whetten, R. L., *J. Phys. Chem. B* **1998**, 102 (52), 10643–10646.
- (159) Negishi, Y., Nobusada, K., Tsukuda, T., *J. Am. Chem. Soc.* **2005**, 127 (14), 5261–5270.
- (160) Bass, J. D., Ai, X., Bagabas, A., Rice, P. M., Topuria, T., Scott, J. C., Alharbi, F. H., Kim, H.-C., Song, Q., Miller, R. D., *Angew. Chem., Int. Ed.* **2011**, 123 (29), 6668–6672.
- (161) Jiang, P., Xie, S.-s., Yao, J.-n., Pang, S.-j., Gao, H.-j., *J. Phys. D: Appl. Phys.* **2001**, 34, 2255–2259.
- (162) Wu, Z., Chen, J., Jin, R., *Adv. Funct. Mater.* **2011**, 21 (1), 177–183.
- (163) Rotzoll, R., Vana, P., *J. Polym. Sci., Part A: Polym. Chem.* **2008**, 46 (23), 7656–7666.
- (164) Chiefari, J., Mayadunne, R. T. A., Moad, C. L., Moad, G., Rizzardo, E., Postma, A., Thang, S. H., *Macromolecules* **2003**, 36 (7), 2273–2283.
- (165) Osterholtz, F., Pohl, E., *J. Adhes. Sci. Tech.* **1992**, 6 (1), 127–149.
- (166) Carrot, G., Diamanti, S., Manuszak, M., Charleux, B., Vairon, J.-P., *J. Polym. Sci., Part A: Polym. Chem.* **2001**, 39 (24), 4294–4301.
- (167) Tsujii, Y., Ejaz, M., Sato, K., Goto, A., Fukuda, T., *Macromolecules* **2001**, 34 (26), 8872–8878.
- (168) Audouin, F., Blas, H., Pasetto, P., Beaunier, P., Boissière, C., Sanchez, C., Save, M., Charleux, B., *Macromol. Rapid Commun.* **2008**, 29 (11), 914–921.
- (169) Blas, H., Save, M., Boissière, C., Sanchez, C., Charleux, B., *Macromolecules* **2011**, 44 (8), 2577–2588.
- (170) Li, C., Benicewicz, B. C., *Macromolecules* **2005**, 38 (14), 5929–5936.

- (171) Coote, M. L., Lin, C. Y., Beckwith, A. L. J., Zavitsas, A. A., *Phys. Chem. Chem. Phys.* **2010**, *12* (33), 9597–9610.
- (172) Finkelstein, H., *Ber. Dtsch. Chem. Ges.* **1910**, *43* (2), 1528–1532.
- (173) Spiteri, C., Moses, J. E., *Angew. Chem. Int. Ed.* **2010**, *49* (1), 31–33.
- (174) Kolb, H. C., Finn, M. G., Sharpless, K. B., *Angew. Chem. Int. Ed.* **2001**, *40* (11), 2004–2021.
- (175) Li, N., Binder, W. H., *J. Mater. Chem.* **2011**, *21* (42), 16717–16734.
- (176) Fleming, D. A., Thode, C. J., Williams, M. E., *Chem. Mater.* **2006**, *18* (9), 2327–2334.
- (177) Thode, C. J., Williams, M. E., *J. Colloid Interface Sci.* **2008**, *320* (1), 346–352.
- (178) Neises, B., Steglich, W., *Angew. Chem., Int. Ed.* **1978**, *17* (7), 522–524.
- (179) Shon, Y.-S., Kelly, K. F., Halas, N. J., Lee, T. R., *Langmuir* **1999**, *15* (16), 5329–5332.
- (180) Collman, J. P., Devaraj, N. K., Chidsey, C. E. D., *Langmuir* **2004**, *20* (4), 1051–1053.
- (181) Hasan, M., Bethell, D., Brust, M., *J. Am. Chem. Soc.* **2002**, *124* (7), 1132–1133.
- (182) Navarro, J. R. G., Plugge, M., Loumagne, M., Sanchez-Gonzalez, A., Mennucci, B., Debarre, A., Brouwer, A. M., Werts, M. H. V., *Photochem. Photobiol. Sci.* **2010**, *9* (7), 1042–1054.
- (183) Ionita, P., Caragheorgheopol, A., Gilbert, B. C., Chechik, V., *J. Am. Chem. Soc.* **2002**, *124* (31), 9048–9049.
- (184) Cleland, W. W., *Biochemistry* **1964**, *3* (4), 480–482.
- (185) Canaria, C. A., Smith, J. O., Yu, C., Fraser, S. E., Lansford, R., *Tetrahedron Lett.* **2005**, *46* (28), 4813–4816.
- (186) Ganachaud, F., Monteiro, M. J., Gilbert, R. G., Dourges, M.-A., Thang, S. H., Rizzardo, E., *Macromolecules* **2000**, *33* (18), 6738–6745.
- (187) Ganachaud, F., Monteiro, M. J., Gilbert, R. G., *Macromol. Symp.* **2000**, *150* (1), 275–281.
- (188) Keddie, D. J., Moad, G., Rizzardo, E., Thang, S. H., *Macromolecules* **2012**, *45* (13), 5321–5342.
- (189) Convertine, A. J., Ayres, N., Scales, C. W., Lowe, A. B., McCormick, C. L., *Biomacromolecules* **2004**, *5* (4), 1177–1180.
- (190) Bouchékif, H., Narain, R., *J. Phys. Chem. B* **2007**, *111* (38), 11120–11126.
- (191) Nuopponen, M., Kalliomäki, K., Laukkanen, A., Hietala, S., Tenhu, H., *J. Polym. Sci., Part A: Polym. Chem.* **2008**, *46* (1), 38–46.
- (192) Vogt, A. P., Sumerlin, B. S., *Macromolecules* **2008**, *41* (20), 7368–7373.
- (193) Schilli, C., Lanzendorfer, M. G., Muller, A. H. E., *Macromolecules* **2002**, *35* (18), 6819–6827.
- (194) Shan, J., Zhao, Y., Granqvist, N., Tenhu, H., *Macromolecules* **2009**, *42* (7), 2696–2701.
- (195) Liu, Q., Zhang, P., Lu, M., *J. Polym. Sci., Part A: Polym. Chem.* **2005**, *43* (12), 2615–2624.
- (196) Said-Mohamed, C., Niskanen, J., Karesoja, M., Pulkkinen, P., Tenhu, H., Daoud, M., Lee, L.-T., *Soft Matter* **2011**, *7* (15), 7112–7122.
- (197) Jeon, H. J., Go, D. H., Choi, S.-y., Kim, K. M., Lee, J. Y., Choo, D. J., Yoo, H.-O., Kim, J. M., Kim, J., *Colloids Surf., A* **2008**, *317* (1–3), 496–503.
- (198) Liu, Y., Tu, W., Cao, D., *Ind. Eng. Chem. Res.* **2010**, *49* (6), 2707–2715.

- (199) Ray, B., Isobe, Y., Matsumoto, K., Habaue, S., Okamoto, Y., Kamigaito, M., Sawamoto, M., *Macromolecules* **2004**, 37 (5), 1702–1710.
- (200) Ray, B., Okamoto, Y., Kamigaito, M., Sawamoto, M., Seno, K.-i., Kanaoka, S., Aoshima, S., *Polym. J.* **2005**, 37 (3), 234–237.
- (201) Barner-Kowollik, C., Heuts, J. P. A., Davis, T. P., *J. Polym. Sci., Part A: Polym. Chem.* **2001**, 39 (5), 656–664.
- (202) Boschmann, D., Mänz, M., Pöppler, A.-C., Sörensen, N., Vana, P., *J. Polym. Sci., Part A: Polym. Chem.* **2008**, 46 (21), 7280–7286.
- (203) Gottlieb, H., Kotlyar, V., Nudelman, A., *J. Org. Chem.* **1997**, 62 (21), 7512–7515.
- (204) Fujishige, S., *Polymer J.* **1987**, 19 (3), 297–300.
- (205) McKee, J. R., Ladmiral, V., Niskanen, J., Tenhu, H., Armes, S. P., *Macromolecules* **2011**, 44 (19), 7692–7703.
- (206) Jeong, N. S., Hasan, M., Phillips, D. J., Saaka, Y., O'Reilly, R. K., Gibson, M. I., *Polym. Chem.* **2012**, 3 (3), 794–799.
- (207) Müller, A., Krebs, B., *Monatsh. Chem.* **1967**, 98 (4), 1540–1544.
- (208) You, Y.-Z., Hong, C.-Y., Pan, C.-Y., *Chem. Commun.* **2002**, 25, 2800–2801.
- (209) Hong, J., Wang, Q., Lin, Y., Fan, Z., *Macromolecules* **2005**, 38 (7), 2691–2695.
- (210) Wang, Q., Li, Y.-X., Hong, J., Fan, Z.-Q., *Chin. J. Polym. Sci.* **2006**, 24 (6), 593–597.
- (211) Lei, P., Wang, Q., Hong, J., Li, Y., *J. Polym. Sci., Part A: Polym. Chem.* **2006**, 44 (22), 6600–6606.
- (212) Zhang, L., Wang, Q., Lei, P., Wang, X., Wang, C., Cai, L., *J. Polym. Sci., Part A: Polym. Chem.* **2007**, 45 (13), 2617–2623.
- (213) Roy, A.-L., Bui, C., Rau, I., Kajzar, F., Charleux, B., Save, M., Kreher, D., Attias, A.-J., *Polymer* **2014**, 55 (3), 782–787.
- (214) Motokucho, S., Sudo, A., Endo, T., *J. Polym. Sci., Part A: Polym. Chem.* **2006**, 44 (21), 6324–6331.
- (215) Nagata, M., Sato, Y., *J. Polym. Sci., Part A: Polym. Chem.* **2005**, 43 (11), 2426–2439.
- (216) Sommerdijk, N. A. J. M., Holder, S. J., Hiorns, R. C., Jones, R. G., Nolte, R. J. M., *Macromolecules* **2000**, 33 (22), 8289–8294.
- (217) Zhang, Q., Ye, J., Lu, Y., Nie, T., Xie, D., Song, Q., Chen, H., Zhang, G., Tang, Y., Wu, C., Xie, Z., *Macromolecules* **2008**, 41 (6), 2228–2234.
- (218) Hadjantoniou, N. A., Triftaridou, A. I., Kafouris, D., Gradzielski, M., Patrickios, C. S., *Macromolecules* **2009**, 42 (15), 5492–5498.
- (219) Vandenbergh, J., Junkers, T., *Macromolecules* **2014**, 47 (15), 5051–5059.
- (220) Termonia, Y., *Biomacromolecules* **2004**, 5 (6), 2404–2407.
- (221) Lee, J., Bae, Y. H., Sohn, Y. S., Jeong, B., *Biomacromolecules* **2006**, 7 (6), 1729–1734.
- (222) Jia, Z., Xu, X., Fu, Q., Huang, J., *J. Polym. Sci., Part A: Polym. Chem.* **2006**, 44 (20), 6071–6082.
- (223) Panyukov, S., Potemkin, I., *J. Exp. Theor. Phys.* **1997**, 85 (1), 183–188.
- (224) Pospiech, D., Haussler, L., Eckstein, K., Voigt, D., Jehnichen, D., Gottwald, A., Kollig, W., Janke, A., Grundke, K., Werner, C., Kricheldorf, H. R., *Macromol. Symp.* **2001**, 163 (1), 113–126.

- (225) Lee, D., Lee, S.-H., Kim, S., Char, K., Park, J. H., Bae, Y. H., *J. Polym. Sci., Part B: Polym. Phys.* **2003**, *41* (20), 2365–2374.
- (226) Huh, K. M., Bae, Y. H., *Polymer* **1999**, *40* (22), 6147–6155.
- (227) Wu, C., Xie, Z. W., Zhang, G. Z., Zi, G. F., Tu, Y. F., Yang, Y. L., Cai, P., Nie, T., *Chem. Commun.* **2002**, *23*, 2898–2899.
- (228) Fakirov, S., Gogeva, T., *Macromol. Chem. Phys.* **1990**, *191* (3), 603–614.
- (229) Hoeschele, G. K. von, Witsiepe, W. K., *Macromol. Mater. Eng.* **1973**, *29* (1), 267–289.
- (230) Seefried, C. G., Koleske, J. V., Critchfield, F. E., *J. Appl. Polym. Sci.* **1975**, *19* (9), 2493–2502.
- (231) Bonart, R., *Polymer* **1979**, *20* (11), 1389–1403.
- (232) Leclerc, E., Daoud, M., *Macromolecules* **1997**, *30* (2), 293–300.
- (233) Gersappe, D., Harm, P. K., Irvine, D., Balazs, A. C., *Macromolecules* **1994**, *27* (3), 720–724.
- (234) Eastwood, E. A., Dadmun, M. D., *Macromolecules* **2002**, *35* (13), 5069–5077.
- (235) Eastwood, E., Viswanathan, S., O'Brien, C. P., Kumar, D., Dadmun, M. D., *Polymer* **2005**, *46* (12), 3957–3970.
- (236) Creton, C., *MRS Bulletin* **2003**, *28* (6), 434–439.
- (237) Bussels, R. *(Multi)block copolymer synthesis via controlled radical polymerization in aqueous dispersions*, Ph.D. thesis, University of Eindhoven, **2004**.
- (238) Guan, Z. B., Roland, J. T., Bai, J. Z., Ma, S. X., McIntire, T. M., Nguyen, M., *J. Am. Chem. Soc.* **2004**, *126* (7), 2058–2065.
- (239) Ayres, L., Adams, P. H. H. M., Löwik, D. W. P. M., Hest, J. C. M. van, *Biomacromolecules* **2005**, *6* (2), 825–831.
- (240) Vandermeulen, G. W. M., Klok, H. A., *Macromol. Biosci.* **2004**, *4* (4), 383–398.
- (241) Rösler, A., Klok, H.-A., Hamley, I. W., Castelletto, V., Mykhaylyk, O. O., *Biomacromolecules* **2003**, *4* (4), 859–863.
- (242) Biemond, G. J. E., Feijen, J., Gaymans, R. J., *Macromol. Mater. Eng.* **2009**, *294* (8), 492–501.
- (243) Ebeling, B. *Multiblock-Copolymere durch RAFT-Polymerisation*, thesis, Georg-August-Universität Göttingen, **2009**.
- (244) Ebeling, B., Vana, P., *Polymers* **2011**, *3* (2), 719–739.
- (245) Tamami, B., Kiasat, A. R., *J. Chem. Res.* **1998**, *8*, 454–455.
- (246) Tamami, B., Kiasat, A. R., *Iran. Polym. J.* **1999**, *8* (1), 17–23.
- (247) Copeland, C., Conway, R. J., Patroni, J. J., Stick, R. V., *Aust. J. Chem.* **1981**, *34* (3), 555–557.
- (248) Ebeling, B., Eggers, M., Vana, P., *Macromolecules* **2010**, *43* (24), 10283–10290.
- (249) Stockmayer, W. H., *J. Polym. Sci., Part A: Polym. Chem.* **1952**, *9* (1), 69–71.
- (250) Sippel, A., Heim, E., *J. Polym. Sci., Part A: Polym. Chem.* **1961**, *54* (159), 83–100.
- (251) Wolpers, A., Russell, G. T., Vana, P., *Macromol. Theory Simul.* **2011**, *20* (8), 667–674.
- (252) Hadjichristidis, N., Pitsikalis, M., Iatrou, H. In *Block Copolymers I*; Advances in Polymer Science, Vol. 189; Springer: Berlin, 2005, 1–124.

- (253) Schulz, G. V., *Z. Phys. Chem.* **1935**, B30, 379.
- (254) Flory, P. J., *J. Am. Chem. Soc.* **1936**, 58 (10), 1877–1885.
- (255) Knoester, H., *Macromol. Theory Simul.* **2009**, 18 (1), 61–69.
- (256) Case, L. C., *J. Polym. Sci.* **1959**, 37 (131), 147–154.
- (257) Case, L. C., *J. Polym. Sci.* **1959**, 39 (135), 175–182.
- (258) Johnston, T. P., Stringfellow, C. R., Gallagher, A., *J. Org. Chem.* **1962**, 27 (11), 4068–4070.
- (259) Strube, O. I., Schmidt-Naake, G., *Macromol. Symp.* **2009**, 275–276 (1), 13–23.
- (260) Llauro, M. F., Loiseau, J., Boisson, F., Delolme, F., Ladaviere, C., Clavierie, J., *J. Polym. Sci., Part A: Polym. Chem.* **2004**, 42 (21), 5439–5462.
- (261) Qiu, X.-P., Winnik, F. M., *Macromol. Rapid Commun.* **2006**, 27 (19), 1648–1653.
- (262) Nair, D. P., Podgórski, M., Chatani, S., Gong, T., Xi, W., Fenoli, C. R., Bowman, C. N., *Chem. Mater.* **2013**, 26 (1), 724–744.
- (263) Whittaker, M. R., Goh, Y.-K., Gemici, H., Legge, T. M., Perrier, S., Monteiro, M. J., *Macromolecules* **2006**, 39 (26), 9028–9034.
- (264) Gemici, H., Legge, T. M., Whittaker, M., Monteiro, M. J., Perrier, S., *J. Polym. Sci., Part A: Polym. Chem.* **2007**, 45 (11), 2334–2340.
- (265) You, Y.-Z., Zhou, Q.-H., Manickam, D. S., Wan, L., Mao, G.-Z., Oupicky, D., *Macromolecules* **2007**, 40 (24), 8617–8624.
- (266) Lima, V., Jiang, X., Brokken-Zijp, J., Schoenmakers, P. J., Klumperman, B., Linde, R. V. D., *J. Polym. Sci., Part A: Polym. Chem.* **2005**, 43 (9), 959–973.
- (267) Burns, J. A., Butler, J. C., Moran, J., Whitesides, G. M., *J. Org. Chem.* **1991**, 56 (8), 2648–2650.
- (268) Han, J. C., Han, G. Y., *Anal. Biochem.* **1994**, 220 (1), 5–10.
- (269) Kirley, T. L., *Anal. Biochem.* **1989**, 180 (2), 231–236.
- (270) Ganesh, K., Kishore, K., *Macromolecules* **2002**, 35 (7), 2483–2490.
- (271) Perrier, S., Takolpuckdee, P., Mars, C. A., *Macromolecules* **2005**, 38 (6), 2033–2036.
- (272) Chong, B., Moad, G., Rizzardo, E., Skidmore, M., Thang, S. H., *Aust. J. Chem.* **2006**, 59 (10), 755–762.
- (273) Postma, A., Davis, T. P., Moad, G., O'Shea, M. S., *Macromolecules* **2005**, 38 (13), 5371–5374.
- (274) Postma, A., Davis, T. P., Evans, R. A., Li, G., Moad, G., O'Shea, M. S., *Macromolecules* **2006**, 39 (16), 5293–5306.

Chapter 6

High-pressure phase behavior of aqueous pNIPAm solutions

The underlying theory for the following experiments, namely the special properties of pNIPAm in aqueous systems, was outlined in Section 1.2.2. This chapter is dedicated to the study of the special responsive behavior of this polymer upon exertion of high pressures. In this sense, it is first dealt with using the polymeric building block alone. By the later combination with nanoparticles, the polymer's special responsive features can then be passed on to the resulting smart nanohybrids.

The synthesis of the pNIPAm samples was presented in Section 5.4. An overview of the very defined samples that were studied in the current chapter can be found in Table 5.1.

6.1 Current state of research regarding the high-pressure experiments

Within the large number of studies on aqueous pNIPAm solutions (see Figure 1.2), the influence of the pressure on the responsive behavior is treated comparably sparsely. Although these experiments greatly widen the scope of attained information and contribute to the understanding of the systems, the vast majority of measurements are carried out at atmospheric pressure. This is arguably due to the fact that these experiments involve a high experimental effort and require specially designed high-pressure installations.^[1] However, there are a couple of reports. In order to be able to view the performed experiments in the right context, the state of the art of high-pressure experiments with aqueous pNIPAm solutions is outlined in a chronological approach, prior to the presentation of the actual experiments. It will probably be helpful for following along the rest of this section to already have a

look at the general shape of an actual cloud-point curve, for example in the diagram in Figure 6.6.

The first article treating pNIPAm at substantially increased^[2–6] pressures in any form was published by Lee *et al.*^[7] (1990). They analyzed the volume of highly crosslinked pNIPAm hydrogel particles at pressures up to 170 bar and stated that the swelling behavior was relatively insensitive to pressure changes. Ohta *et al.*^[8] (1991) then studied aqueous solutions of linear pNIPAm using a simple high-pressure apparatus^[9] that allowed to increase the pressure up to 400 bar and to study the solution by ¹H-NMR spectroscopy, but not optically. From the measured transverse relaxation times (T_2), they concluded that the application of pressure generally prevents the clouding of the solution.

Otake *et al.*^[10] (1993) were the first to detect the actual cloudiness of aqueous pNIPAm solutions at pressures up to 2500 bar by light scattering and could present a phase diagram, showing the general features, although the pNIPAm sample had been prepared by conventional radical polymerization (see Section 1.2.1.1) and was quite ill-defined ($\bar{D} = 3.0$). Their phase diagram showed that the cloud temperature first increases by approximately 2°C, when the pressure is raised, and then re-decreases at pressures of over about 500 bar. Conversely, the described curve shape indicates that raising the pressure at a constant temperature slightly over the cloud temperature at atmospheric pressure will lead to the solution first becoming turbid and then clearing up again. At these high temperatures, the phase-separation curve is very sensitive to temperature changes, but very insensitive to pressure changes (*temperature-induced clouding*). Following the curve beyond the turning point to lower temperatures, the cloud pressures become increasingly higher up to values of over 2000 bar. Below the atmospheric-pressure cloud temperature, increasing the pressure always leads to a phase change from clear to turbid. Otake *et al.* already postulated that different factors govern the clouding process in the low-pressure and the high-pressure region. Kunugi *et al.*^[11] (1997) confirmed that the cloud-point curve features a turning point, when comparing the high-pressure behavior of pNIPAm ($\bar{D} = 3.3$) in water with that of a similar polymer, poly(*N*-vinylisobutyramide).

In a follow-up publication,^[12] they studied the influence of added salts on the high-pressure behavior of aqueous solutions of these two polymers. Depending on the type of salt used (and in particular on the type of anions), they reported a shift of the cloud curves to lower pressures, approximately linear with the concentration. Some ions led to a shift of the cloud-point curves to higher pressures, but only when the salt was added in very low concentrations.^[12] In a second follow-up publication,^[13] fractionated, and thus more defined, pNIPAm samples ($\bar{M}_n = 1.2 \times 10^4$ g mol⁻¹, 4.9×10^4 g mol⁻¹, 60×10^4 g mol⁻¹, and $\bar{D} = 1.5, 1.8, 2.5$) were examined for the first

time. It was found that the cloud-point curves are shifted to slightly lower cloud pressures with increasing molar mass. Hereby, the authors could also show that the dependence of the phase-separation curve on the temperature becomes very weak at temperatures below 0 °C (*pressure-induced clouding*). Later, it was reported that incorporation of acrylic acid into the pNIPAm chains increases the sensitivity towards changes of the pH value in high-pressure experiments.^[14] Rebelo *et al.*^[15] (2002) confirmed the postulated dependence of the polymers' \overline{M}_n values on their high-pressure behavior in aqueous solutions and also stated that the curves are almost independent of the pNIPAm concentration. It seems, however, that the critical composition is shifted to slightly lower values (from 6.5 %) when pressure is applied.^[16]

In a series of publications, E. Kato^[17–25] studied the thermodynamic and material properties of highly crosslinked pNIPAm hydrogels in a high-pressure cell. Compressing a gel is, nevertheless, experimentally totally different from examining true solutions and gives insight into other aspects of the phase transition,^[26] although hydrogels are arguably one of the major high-pressure applications for pNIPAm. Kitada^[27] (2001) directly prepared a pNIPAm hydrogel with possibly advantageous structural properties by crosslinking at pressures of 2 000 bar. Shibayama *et al.*^[28] (2004) investigated aqueous solutions of both non-crosslinked pNIPAm and pNIPAm networks (and later as well copolymers with acrylic acid)^[29,30] using the same set-up by small-angle neutron scattering, going up to pressures of about 2 000 bar, and showed that both systems are indeed comparable and that the non-interconnected polymer can therefore be regarded as a model system for the hydrogels, the curve of the latter only being systematically shifted to slightly higher cloud pressures, presumably due to the chemical nature of the crosslinker. The same group also compared the cloud curves of solutions in H₂O with those in D₂O. The finding that the cloud temperatures were systematically higher in D₂O was explained by the molar volume isotope effect.^[31] A downside of the study of Shibayama *et al.*^[28] (2004), in addition to the fact that they conceal the molar mass of the examined polymers, is the limitation that they could only perform measurements at temperatures higher than room temperature and therefore unrealistically extrapolated elliptical curves into the low-temperature regime.

Meersman *et al.*^[32] (2005) investigated the hydration properties of pNIPAm chains in aqueous solution by Fourier transform infrared spectroscopy at the temperature-induced phase transition at low pressures and the pressure-induced phase transition at very high pressures of 10 000 bar. Their results showed that the underlying mechanisms of the phase transition at high and low pressures (temperature-induced and pressure-induced clouding) are fundamentally different on a microscopic level, although the macroscopic effect of clouding is visually iden-

tical. (See Section 1.2.2.1 for the theoretical coverage of the temperature-induced clouding—the coil-to-globule transition.) Higher pressures lead to a strengthening of both the hydration of the polymer's amide groups and of the C–H...O hydrogen bonds of water molecules to the hydrophobic alkyl groups, and thus to an increasing temperature of the phase transition. However, the temperature increase is only very low and hard to observe because of the steepness of the cloud curve. After the pressure-induced increase of the polymer's solubility, another effect takes over, which leads to a decrease of the cloud temperature at higher pressures. The curve proceeds through the low-temperature region and the cloud-point curve becomes increasingly temperature-independent. Meersman *et al.* attribute the phase transition at low temperatures to water–water interactions, by which the interactions between water and pNIPAm are destabilized.^[32] In a later study,^[33,34] they proved the reversibility of the phase-separation process by hybrid two-dimensional correlation infrared spectroscopy.^[35,36] Pühse *et al.*^[37] (2010) extended the Fourier transform infrared measurements of aqueous pNIPAm solutions to low temperatures over a wide range up to 10 000 bar and confirmed the postulation by Meersman *et al.* that the hydration of pNIPAm increases at high pressures. They attributed—at least in part—the weakening of the hydrophobic interactions as being responsible for the occurring phase separation.

Recently, the structure of pNIPAm microgels^[38] (gels in the colloidal-size domain)^[39] under high pressure was examined.^[1,40] The main difference of microgels is that the transition is only characterized by shrinking of the gels, which usually still stay colloidally stable, so that no macroscopic effect results.

It is generally thought that the mechanism at low temperatures/high pressures resembles that of “cold” denaturation of proteins^[41] and other natural macromolecules, that means, the phenomenon that proteins can also be denatured by applying high pressures.^[42,43] Aqueous solutions of pNIPAm are regarded as a model system^[44] to study this phenomenon,^[45,46] being the main motivation behind several of the previously referenced studies. It was shown that indeed thermodynamic parameters in the same order of magnitude were found for both clouding processes.^[37,47] Using a polymer model system has the advantage that it is easy to handle, the process is reversible and can be isolated from other factors like secondary-structure changes and the spectroscopic data are free from signals caused by irrelevant functional groups.

Very recently, Osaka *et al.*^[48] (2012), following up another study, where they performed quasi-elastic neutron scattering with aqueous pNIPAm solutions under high pressures,^[49] studied the ternary system of pNIPAm in mixtures of water and another solvent, DMSO, which exhibits cononsolvency behavior with a UCST-like curve (see Figure 1.3) at the side of higher DMSO content, under high pres-

tures. (Cononsolvency of aqueous pNIPAm solutions was described theoretically in Section 1.2.2.2.) They found inverted convexities of the pressure–temperature phase-separation curves at very low and very high concentrations of DMSO as cononsolvent,^[48] but did not provide data in between these two concentration regimes, because they were not able to cool their apparatus.

In the work presented in the following, a remaining informational gap is closed and the understanding of aqueous pNIPAm systems is pushed forward by mapping out the pressure–temperature phase behavior of solutions of pNIPAm in mixed solutions of water and several other organic solvents which provoke cononsolvency, up to low temperatures and high pressures in a discontinuously operated high-pressure cell. In addition, a series of cloud curves with ethanol as the additive over the whole cononsolvency region will be presented, in which a gradual complete inversion of the phase behavior is observed.

6.2 Experimental acquisition of cloud-point curves

6.2.1 Acquisition of cloud points at elevated pressures

The pressure–temperature curves of the aqueous pNIPAm solutions were obtained with a set-up shown schematically in Figure 6.1. It featured a temperature-controlled stainless-steel high-pressure cell with a sapphire window of 21.2 mm aperture on one side, through which the cell's constantly stirred internal volume could be monitored and recorded with a borescope camera, which was fitted into the cell body. It is especially noteworthy that, as opposed to set-ups used in most of the above listed studies, the optical cell could not only be heated, but also cooled to very low temperatures, thus expanding the accessible range. The temperatures were determined with a thermocouple going directly into the solution. The whole set-up had originally been assembled by members of the group of Professor Dr. M. Buback in Göttingen.^[51–54] A more technical close-up of the high-pressure cell was already shown in Figure 2.1 in the instrumental part. The high pressures were generated and regulated by pressing *n*-heptane as pressurizing medium into the cell with a syringe pump.

Homogeneity of the reacting system was monitored by visual inspection. A turbid solution appeared dark. Figure 6.2 displays stills of a clear and a turbid solution in the high-pressure cell, extracted from the borescope camera's video. The individual cloud points were obtained by variation of pressure at given temperatures. (But identical values are in principle obtained by temperature variation.)^[11] While the

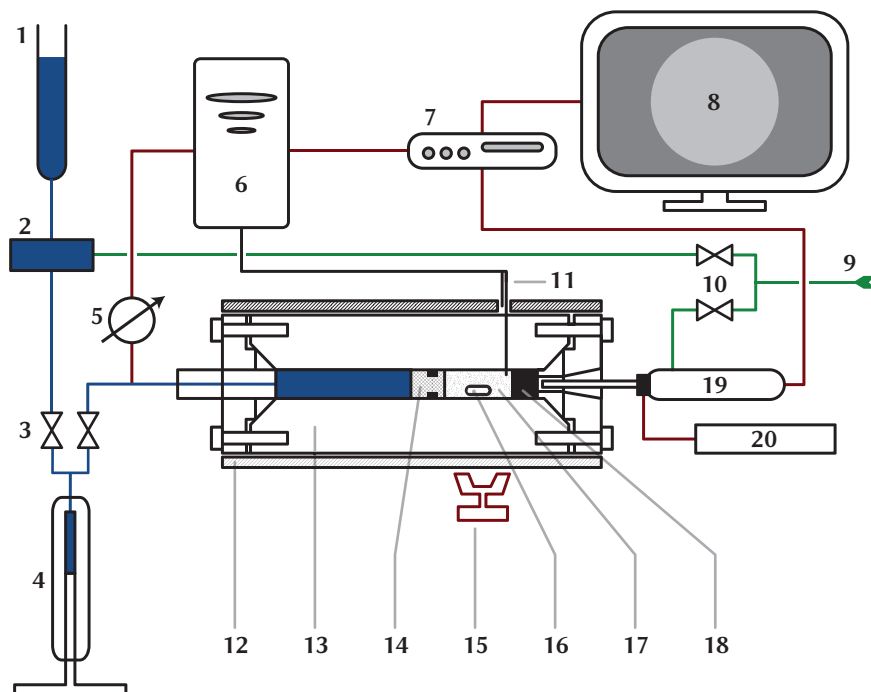


Fig. 6.1: Set-up for the high-pressure cloud-point measurements. 1) pressurizing fluid *n*-heptane, 2) HPLC pump, 3) double spindle valve, 4) syringe pump, 5) strain gauge as pressure transducer, 6) computer, 7) hard-disc recorder, 8) screen, 9) dehydrated compressed air, 10) valves, 11) sheathed thermocouples, 12) temperature control shell, 13) stainless-steel cell body, 14) movable piston with O-ring, 15) magnetic drive, 16) stirring bar, 17) internal volume with sample solution, 18) sapphire window, 19) video borescope camera, 20) halogen light source. See Figure 2.1 for a close-up technical sketch of the cell. (Reprinted and adapted with permission from a previous publication.^[50] Copyright 2014 American Chemical Society.)

temperature was constant, the reproducibility of the cloud-point pressures was usually better than ± 20 bar.

6.2.1.1 Range of operation

The cell had been laid out to be tight during operation up to 3 000 bar, marking the maximum pressure for the measurements. The lowest possible pressure was the atmospheric pressure of around 1 bar. The highest temperature was about 300 °C,

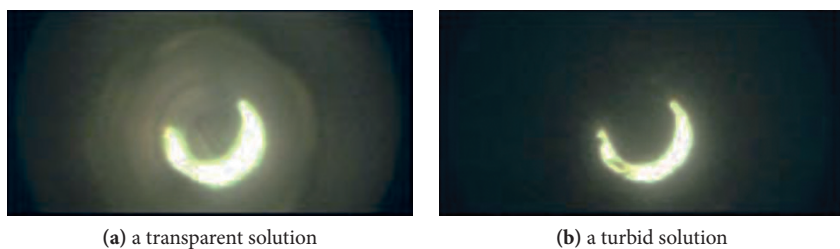


Fig. 6.2: Stills of the inside of the high-pressure cell for cloud-point determination, extracted from the borescope camera's video. The difference can be clearly distinguished. For (a), the screw on the movable piston (see Figure 2.1), the movement of the stirring bar and possibly moving air bubbles can be seen. The bright crescent is the reflection of the light source on the sapphire window. The polymer concentration of the photographed solution is 5 g L^{-1} . (Reprinted and adapted with permission from a previous publication.^[50] Copyright 2014 American Chemical Society.)

but this limit was practically irrelevant, as the cloud points at increased pressures were generally found at low temperatures.

The lower barrier for the measurements was the freezing of the water. Since water exhibits the anomaly that the molar volume of the frozen state ice is higher than that of the liquid state, the freezing point can be depressed by applying increased pressures, making it possible to measure the phase behavior of aqueous solutions down to temperatures below 0°C in high-pressure experiments. In order to quantify this statement, an expression for the mathematical description of the fusion curve of pure water—exceeding the mere statement of it having a negative steepness—shall be formulated. Based on the Clausius–Clapeyron equation, which describes the slope of the phase-separation line, a formula can be found relatively easily:

$$\frac{dp}{dT} = \frac{\Delta H_{\text{m,fus}}}{T \Delta V_{\text{m,fus}}}. \quad (6.1)$$

Here, T is the temperature, p the pressure, $\Delta H_{\text{m,fus}}$ the molar latent heat of fusion, and $V_{\text{m,fus}}$ the molar volume change at the transition.

$\Delta V_{\text{m,fus}}$ can be calculated from the different densities ρ_l of water and ρ_s of ice:

$$\Delta V_{\text{m,fus}} = \frac{M_{\text{H}_2\text{O}}}{\rho_l} - \frac{M_{\text{H}_2\text{O}}}{\rho_s}. \quad (6.2)$$

The molar mass of water is $M_{\text{H}_2\text{O}} = 18.02 \text{ g mol}^{-1}$. It can be assumed that the density of ice remains constant at $\rho_s = 0.917 \text{ g cm}^{-3}$ over the whole range of interest. (The

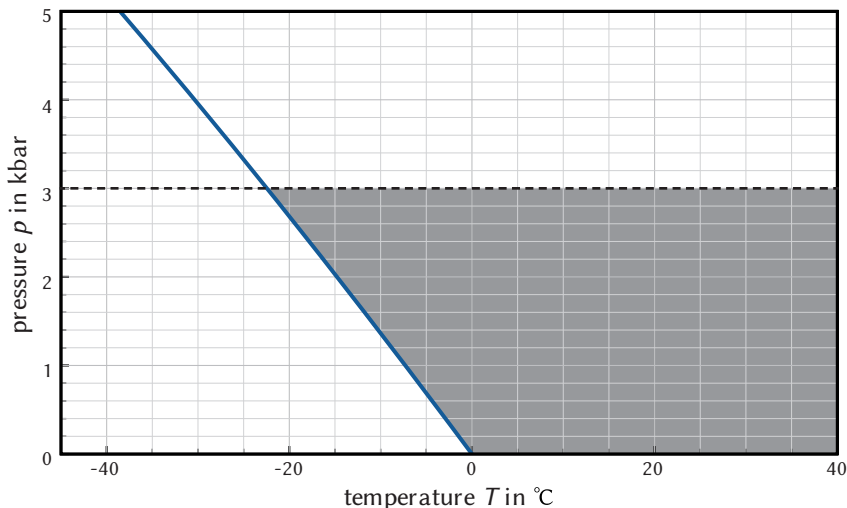


Fig. 6.3: Range of operation (shaded area) of the high-pressure apparatus for water. It is limited by the maximum pressure for which the cell was designed (dashed line) and the freezing curve of water (blue line), which was calculated via (6.6). (Reprinted and adapted with permission from a previous publication.^[50] Copyright 2014 American Chemical Society.)

solid phase is the hexagonal ice phase I_h all along the melting curve.) Liquid water, however, is compressed to a small extent under high pressures. For -15°C , a value of $\rho_l(15^\circ\text{C}) \approx 0.997 \text{ g cm}^{-3}$ was found,^[55–57] as opposed to the maximum value of $\rho_l(4^\circ\text{C}) = 1.00 \text{ g cm}^{-3}$. Assuming a linear correlation^[58] for values below the maximum of 4°C , one obtains:

$$\Delta V_{m,\text{fus}}(T) = \frac{18.02 \text{ g mol}^{-1}}{1.00 \text{ g cm}^{-3} - (269.15 \text{ K} - T) \times 3 \times 10^{-4} \text{ g cm}^{-3} \text{ K}^{-1}} - \frac{18.02 \text{ g mol}^{-1}}{0.917 \text{ g cm}^{-3}}. \quad (6.3)$$

In view of the higher and more uncertain temperature dependency of the latent heat of fusion, however, the temperature dependency of $\Delta V_{m,\text{fus}}$ is neglected here and an average value of $\rho_l = 0.998 \text{ g cm}^{-3}$ is assumed for the density of liquid water, so that the expression reduces to

$$\Delta V_{m,\text{fus}}(T) = \frac{18.02 \text{ g mol}^{-1}}{0.998 \text{ g cm}^{-3}} - \frac{18.02 \text{ g mol}^{-1}}{0.917 \text{ g cm}^{-3}} = -1.59 \text{ cm}^3 \text{ mol}^{-1}. \quad (6.4)$$

The latent heat of fusion $\Delta H_{m,\text{fus}}$ of water is $\Delta H_{m,\text{fus}}(0^\circ\text{C}) = 6.01 \text{ kJ mol}^{-1}$.^[59] For -15°C , a value of $\Delta H_{m,\text{fus}}(-15^\circ\text{C}) = 5.4 \text{ kJ mol}^{-1}$ was found by Bertolini *et al.*^[60] (1985), who also reported a very linear correlation with the temperature, so that it can be formulated that

$$\begin{aligned}\Delta H_{m,\text{fus}} &= 6.01 \text{ kJ mol}^{-1} + 0.04 \text{ kJ mol}^{-1} \text{ K}^{-1} (T - 273 \text{ K}) \\ &= 0.04 \text{ kJ mol}^{-1} \text{ K}^{-1} \times T - 4.91 \text{ kJ mol}^{-1}.\end{aligned}\quad (6.5)$$

Insertion of (6.4) and (6.5) in (6.2), integration from $T_1 = 273.16 \text{ K}$ and $p_1 = 6.1173 \times 10^{-3} \text{ bar}$ (triple point) to T_2 and p_2 , and separation of p_2 finally yields:

$$p_2 = -1.04546 \times 10^5 \text{ bar} - 251.57 \text{ bar} \times T_2 \text{ K}^{-1} + 3.0885 \text{ bar} \times \ln(T_2 \text{ K}^{-1}). \quad (6.6)$$

The digits of the parameters do not reflect the significance, but are needed for the curve to not miss the triple point, given the mathematical form of the function. The eventually found Formula (6.6) renders very well the experimental data for the freezing curve.^[61]

Figure 6.3 shows a plot of (6.6). The dashed line is the maximum pressure for which the cell design was laid out. The lowest temperature of operation was therefore about -20°C . The total shaded area of the diagram indicates the range, in which phase-behavior measurements could in principle be performed. It can be seen that the freezing curve is so steep that one would gain only a small decrease of the minimum temperature in the case that the cell was replaced with another, more sturdy one. In practice, no pure water was used, but mixtures with pNIPAm and possibly other additives. This leads to further freezing-point depression. Hence, the curve for pure water in Figure 6.3 can be seen as the upper limiting level.

6.2.2 Acquisition of cloud points at atmospheric pressure

The cloud points at atmospheric pressure were measured in a spectrophotometer, equipped with a heating function, and not in the high-pressure apparatus, because the latter did not allow the pressures to be set precisely in the region of very low pressures, and the spectrophotometer also enabled a more detailed view on the optical effect of the clouding.

For a 1 g L^{-1} aqueous solution of $\pi\text{-5}$, the complete optical spectrum was measured exemplarily every 5 s while heating up the sample over the cloud temperature of $T_c = 32.9^\circ\text{C}$, at a rate of approximately 2°C min^{-1} . All taken spectra are shown in Figure 6.4. The color of the curves in the diagram turns gradually from blue to red for higher temperatures. (The difference between the first and the last curve is only about 1°C . But even this delay is expected to be only a kinetic effect. The

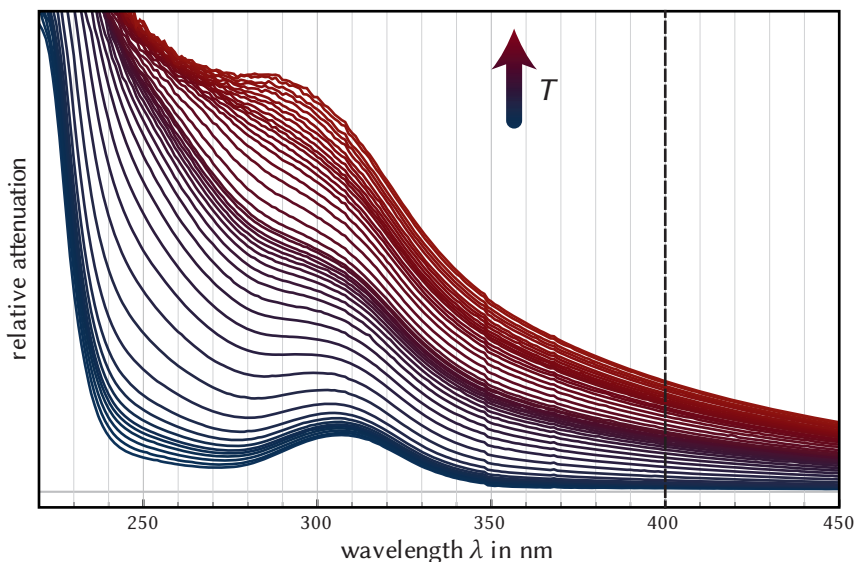


Fig. 6.4: Optical spectra taken continuously (5 s per run) while heating (blue to red) an aqueous solution of RAFT-prepared pNIPAm (sample π -5d with 1 g L^{-1}) over the cloud temperature. The peak at $\lambda = 307 \text{ nm}$ is caused by the absorption of the trithiocarbonate end-group. For the actual cloud-temperature measurements, only the attenuation at the wavelength of $\lambda = 400 \text{ nm}$, marked with a dashed line, was scanned, allowing for a higher signal-to-noise ratio. (Reprinted and adapted with permission from a previous publication.^[50] Copyright 2014 American Chemical Society.)

clouding is remarkably abrupt.) The peak at around 320 nm is caused by absorption of the trithiocarbonate group,^[62] which is incorporated as polymer end group (see Section 5.4.1). It can be seen that along with the clouding, the whole optical spectrum is increased, due to scattering and absorption at the formed agglomerates of polymer globules. It was decided to only monitor the attenuation at the wavelength of $\lambda = 400 \text{ nm}$, marked in Figure 6.4 with a dashed line, in subsequent cloud-temperature measurements. This allowed for both a higher repetition rate and a lower measuring time, giving a higher time-resolution (12 min^{-1}) and an increased signal-to-noise ratio at the same time. At the wavelength of $\lambda = 400 \text{ nm}$, the attenuation was almost zero at lower temperatures, but the clouding still provoked a very distinct change in the spectrum. Other groups chose the wavelength of $\lambda = 500 \text{ nm}$ in similar measurements.^[11,12]

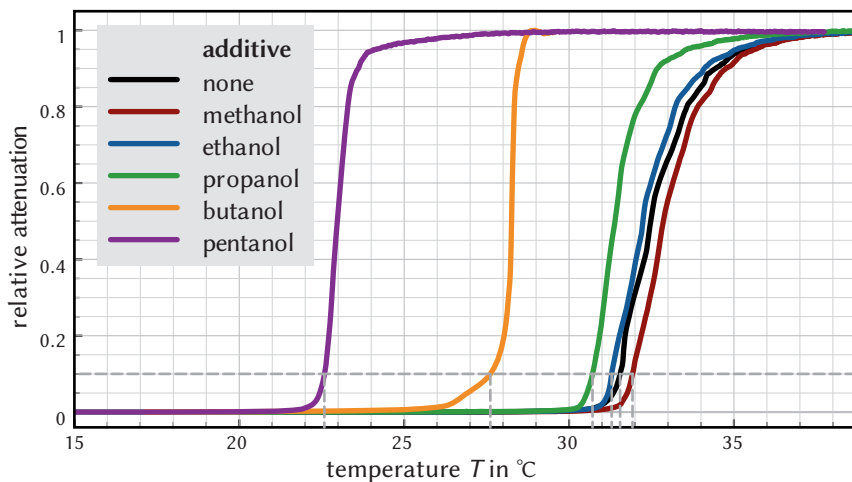


Fig. 6.5: Determination of the cloud-point at atmospheric pressure ($\lambda = 400$ nm), demonstrated for different aqueous pNIPAm solutions (sample π -10) with equal amounts (75 mmol L^{-1}) of terminal n -alcohols as additives. The horizontal dashed line indicates the relative attenuation (10 % of the maximum) which had to be exceeded for the solution to be considered turbid. (Reprinted and adapted with permission from a previous publication.^[50] Copyright 2014 American Chemical Society.)

In Figure 6.5, the analysis procedure at atmospheric pressure is demonstrated exemplarily for aqueous solutions of pNIPAm (sample π -10, 5 g L^{-1}) with equal amounts of different n -alcohols (75 mmol L^{-1}). The measured values can be found again in Figure 6.9 below. The attenuation which had to be exceeded for the solution to be considered turbid, 10 % of the maximum value, is marked with a dashed line. For all cloud-point curves shown in this chapter, the values at atmospheric pressure were obtained this way.

6.3 Finding reference conditions

6.3.1 Polymer concentration for the measurements

At first, in order to find a reference concentration for all subsequent measurements, the same pNIPAm sample π -5d ($\bar{M}_n = 8.04 \times 10^4 \text{ g mol}^{-1}$, $D = 1.38$) was measured in the three different concentrations of $c = 0.2 \text{ g L}^{-1}$, 1.0 g L^{-1} , and 5.0 g L^{-1} . These are typical concentrations used in the literature.^[63] A higher concentration than

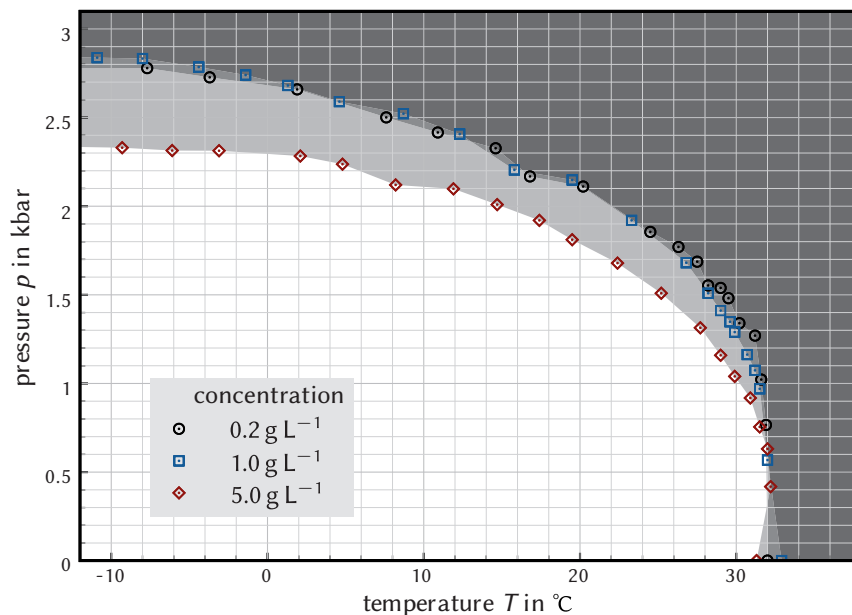


Fig. 6.6: Effect of the polymer concentration on the cloud points: cloud-point curves of an aqueous solution with different concentrations of pNIPAm (sample π -5d).

5.0 g L^{-1} would not be practical because the polymer already needed several hours to dissolve during the sample preparation and with the required minimum sample volume of 50 mL per measurement this concentration already means using up 250 mg of polymer in one single run. The obtained cloud-point curves are shown in the diagram in Figure 6.6. They are plotted as a function of the temperature, since the points were obtained by variation of pressure at given temperatures. The areas where the solutions were cloudy are shaded in gray in all diagrams in this Section. Kunugi *et al.* interpreted the cloud-point curves as quarter ellipses and fitted their data accordingly.^[13] Elliptical curve shape is also expected for the cold denaturation of proteins.^[64] In the experiments presented here, however, not all recorded cloud-point curves exhibited re-decreasing values in the observed range, and this finding was in no case very pronounced. For want of a known physically justified mathematical function to describe the cloud-point curves, the data points were just connected linearly for the shading.

The general shape of the cloud-point curves is the same for all measurements with pNIPAm samples and relatively low concentrations of additives. It is therefore discussed first in general at this point, before the details will be highlighted for the individual measurements. As already mentioned when outlining the state of the art, the curves feature a (barely visible) turning point at some degrees above the atmospheric-pressure cloud temperature and around 500 bar, before proceeding to lower values with constantly decreasing influence of the temperature. There, the curve is very flat and the clouding becomes an almost solely pressure-induced phenomenon. For the temperatures above the cloud temperature at atmospheric pressure, the slope of the curves is very high and it was thus not possible to obtain reliable values in that region. Nevertheless, the shape of this region has been examined in the literature with other methods and it is absolutely undisputed that a maximum in the curves does indeed occur with a pressure of about 500–1 000 bar at the highest temperature.^[10,11,13–15]

Getting back to the actual cloud-point curves in Figure 6.6, the curve measured for a polymer concentration of 0.2 g L^{-1} and the one with 1.0 g L^{-1} are almost superimposed. The curve with a concentration of 5.0 g L^{-1} starts in the same region for higher temperatures, but lies clearly under the other curves in the region of lower temperatures. This might in part be due to the optical effect that the clouding is earlier visible, but the abruptness of the transition makes this unlikely (compare with Figure 6.5). At 2 300 bar, the difference to the other two cloud-point curves is approximately 15°C . This immense discrepancy proves a concentration dependence in aqueous pNIPAm systems at high pressures, unlike stated elsewhere.^[10] All following curves in this chapter were measured with the same polymer concentration of 5 g L^{-1} , because this concentration is close to the critical concentration at atmospheric pressure^[16,65] and allowed for a more unambiguous optical detection of the clouding at all temperatures (compare with Figure 6.2). A cloud curve found at lower pressures is also preferable in view of the maximum pressure of 3 000 bar in the cell (see Figure 6.3), given the finding presented below (Section 6.4.1.2) that some additives shift the low-temperature region to higher pressures. Nevertheless, it is important to be aware of the concentration effect, especially when comparing obtained results with literature data.

6.3.2 Influence of the polymer chain-length

Even regarding the cloud point of pure aqueous pNIPAm solutions at atmospheric pressure, there is a controversy in literature on whether it is increased,^[66,67] decreased,^[68,69] or not affected^[70–72] by the molar mass of the pNIPAm chains. In the most recent publication on this issue, Furyk *et al.*^[73] (2006) examined fractionated

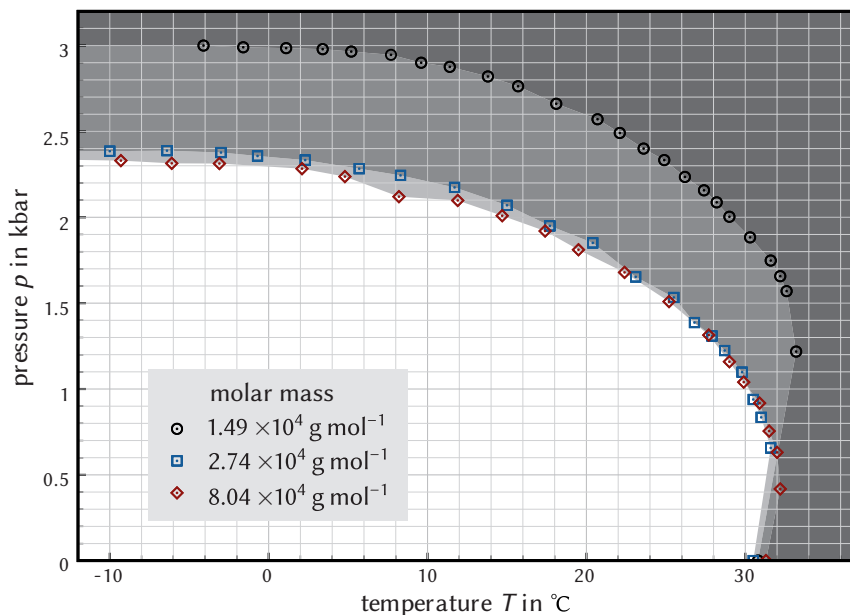


Fig. 6.7: Effect of the molar mass on the cloud points: cloud-point curves of aqueous solutions of pNIPAm samples π -8b, π -9, and π -5d ($c = 5 \text{ g L}^{-1}$), samples listed with increasing \bar{M}_n values). (Reprinted and adapted with permission from a previous publication.^[50] Copyright 2014 American Chemical Society.)

pNIPAm samples with very defined molar masses with regard to their cloud points in aqueous solutions and came to the convincing conclusion that there is no effect of the molar masses and that small changes in the cloud temperature are solely caused by different end-group concentrations.

Figure 6.7 shows the cloud-point curves of equally concentrated aqueous solutions of the polymer samples π -8b ($\bar{M}_n = 1.49 \times 10^4 \text{ g mol}^{-1}$, $\bar{D} = 1.20$), π -9 ($\bar{M}_n = 2.74 \times 10^4 \text{ g mol}^{-1}$, $\bar{D} = 1.16$), and π -5d ($\bar{M}_n = 8.04 \times 10^4 \text{ g mol}^{-1}$, $\bar{D} = 1.38$), that possess distinctly different molar masses. While all three systems exhibit the atmospheric-pressure cloud point at approximately the same temperature, it is evident, that for the system with the shortest polymer chains, the cloud points at lower temperatures are found at significantly increased pressures. Or, speaking in terms of temperature variation, at a pressure of 2000 bar, the cloud point of the solution of π -8b is found at a 12.4°C lower temperature than that of the solution of π -9. Between the other two systems, the effect is much less pronounced. The finding of

lowered cloud-point curves for NIPAm polymers with higher molar masses is in line with literature reports,^[13,15] but it is more pronounced here, presumably due to the lower dispersity of the examined samples. At first, the higher end-group concentration seems unlikely as the reason for the systematic shift, because the RAFT agent **p-4** itself is only very poorly soluble in water. But the effect is comparable to the finding presented below (Section 6.4.1.2) that *n*-alcohols increase the solubility at low temperatures with increasing length of the hydrophobic alkyl chain. In this sense, the hydrophobic end groups would then act as a compatibilizer for the solution. However, other factors, such as a kinetically strongly retarded agglomeration of smaller globules under high pressures, cannot be ruled out.

As seen above for the concentration dependence, also the curves for different molar masses of the NIPAm polymer illustrate very well that from coinciding cloud temperatures at atmospheric pressure, it cannot be concluded that the cloud points are identical over the whole pressure/temperature range, which should be taken into account for any considerations. Moreover, the necessity of using samples with very low dispersities is highlighted, ideally with not too low \overline{M}_n values.

All curves discussed in the rest of this chapter are from solutions of the very defined sample **π -9** ($\overline{M}_n = 2.74 \times 10^4 \text{ g mol}^{-1}$, $\mathcal{D} = 1.16$) or sample **π -10** ($\overline{M}_n = 3.17 \times 10^4 \text{ g mol}^{-1}$, $\mathcal{D} = 1.10$), which was purposely prepared in a particularly high amount to enable experiments with a maximum of comparability. Both samples are comparable in their chain-length characteristics.

6.4 Effect of additives

6.4.1 Effect of additives at low concentrations

6.4.1.1 Ionic additives

As outlined in Section 6.1, the effect of added inorganic salts on the pressure-temperature cloud-point behavior of aqueous pNIPAm solutions has already been studied.^[12,13]

Here, only one cloud-point curve with added NaCl is presented as an example to be able to compare the measurements with organic additives to the aqueous pNIPAm solution with this curve. In Figure 6.8, the cloud-point curve of an aqueous solution of **π -9** is reproduced from Figure 6.7 and in addition the curve is plotted where 0.2 mol L^{-1} of NaCl were added to the same solution, which is still clear at room temperature.* The decrease of the cloud pressures is in line with the results

* An isotonic saline contains 0.154 mol L^{-1} of NaCl and sea water on average 0.6 mol L^{-1} , so that the examined solution has a concentration between these values.

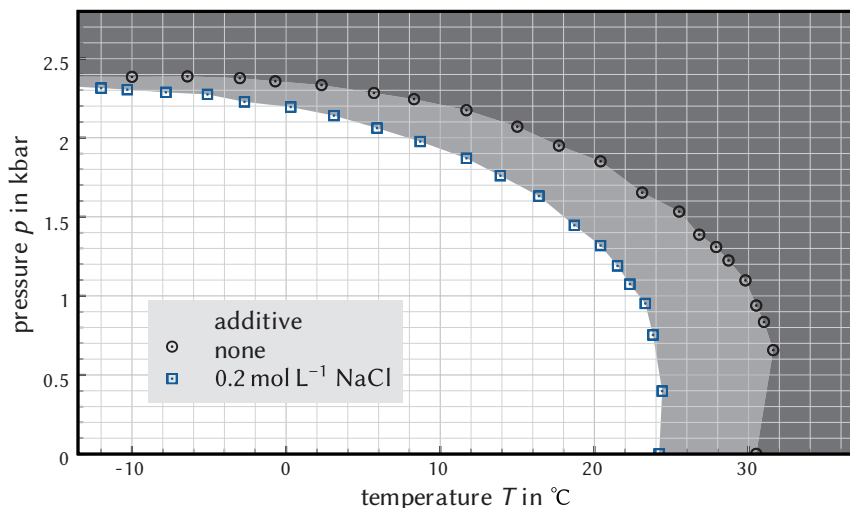


Fig. 6.8: Effect of added salt on the cloud-points: cloud-point curves of a pure aqueous pNIPAm solution (π -9, 5 g L⁻¹) and of a solution with an additional amount of NaCl (0.2 mol L⁻¹). The regions where the solution was turbid are shaded in gray. (Reprinted and adapted with permission from a previous publication.^[50] Copyright 2014 American Chemical Society.)

from literature.^[12,13] Notably and in total contrast to the curve from a sample with lower molar polymer masses (Figure 6.7), the curve with NaCl starts at atmospheric pressure very far from the solution without additives and then approaches it with decreasing temperatures. At 25 °C, the solution containing NaCl is already turbid at atmospheric pressure, while the solution without NaCl remains clear up to pressures of over 1500 bar. At -10 °C, both solutions turn turbid at approximately the same pressure. It seems that added salts mainly influence the temperature-induced clouding, while the chain lengths primarily affect the pressure-induced clouding at low temperatures. This totally different tendency again shows the necessity to have a detailed look on the whole cloud-point curve for any considerations.

As stated above, the pressure-induced phase transition in the low-temperature range seems to be fundamentally different from the well-known coil-to-globule transition at atmospheric pressure,^[32] which is also supported by the fact that the turbid solutions at low temperatures differed from the turbid solutions at higher temperatures in their appearance being less opaque. The clouding at low temperatures is probably not caused by dehydration of the polymer chains, but rather by the completely different properties and formed structures of supercooled water

in this high-pressure region,^[74–87] but a liquid–liquid transition^[88,89] with a categorically different cooperative medium-range ordering can be excluded.^[90,91] For example, a strengthening of the intermolecular water–water hydrogen bonds at high pressures has been reported^[92] in addition to the increase in density, which could overcompensate the strengthening of the water–polymer interactions. The shape of the cloud-point curve makes clear that this effect must be mainly dependent on the pressure, rather than the temperature, or that two opposite effects compensate each other.

6.4.1.2 Organic solvents as additives

The studies were now expanded to different organic solvents as additives to aqueous pNIPAm solutions. Preliminary experiments with *n*-propanol had shown that 0.075 mol L^{−1} (\approx 1 additive molecule per 1000 water molecules) was well suited as a constant additive concentration, provoking significant changes in the cloud-point curve, while these effects are still small enough to leave the curves within the observable region. All examined solvents are completely miscible with water in this concentration.

In Figure 6.9, the cloud-point curves of an aqueous solution of pNIPAm sample π -10 ($\overline{M}_n = 3.17 \times 10^4$ g mol^{−1}, $\overline{D} = 1.10$) are shown, contrasting the solution in pure water with the solutions containing the homologous row of *n*-alcohols up to *n*-pentanol. At atmospheric pressure, the cloud temperatures are increasingly lowered with higher hydrophobicity of the added alcohol (also see Figure 6.5), from 31.5 °C for the pure solution to 22.6 °C for the system with *n*-pentanol, an exception being the small rise to a cloud temperature of 31.9 °C which occurs for methanol at this low concentration. The measured values are in line with the expectations based on the literature^[63] and nicely illustrate the classic effect of cononsolvency, since all alcohols are good solvents for the polymer.

Following the cloud-point curves to low temperatures, however, this effect is completely reversed. In the low-temperature region, the added alcohols lead to a considerable increase of the cloud pressures. For temperatures lower than 0 °C, all curves with added cononsolvents lie more than 300 bar above the curve without additives. With respect to the maximum pressures, found for all curves in the region around −10 °C, the effect is higher for more hydrophobic alcohols. However, the influence of the chemical nature of the cononsolvent is clearly less pronounced in the low-temperature than in the high-temperature range. For example, the maximum of the curve for the system with *n*-pentanol lies only 130 bar higher than the maximum of the curve for the solution with added methanol. This again indicates that the temperature-induced and the pressure-induced clouding are indeed caused by

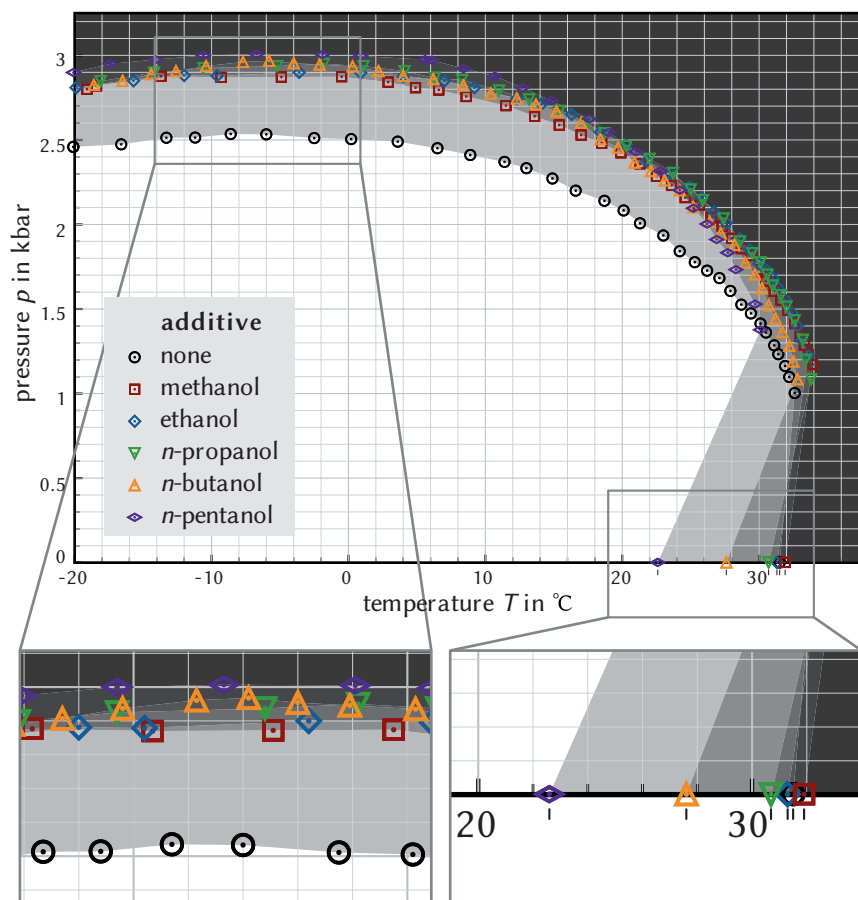


Fig. 6.9: Effect of different alcohols on the cloud-points: cloud-point curves of aqueous solutions of pNIPAm solutions (sample π -10, $c = 5 \text{ g L}^{-1}$) with no additive and different n -alcohols as additives ($c = 0.075 \text{ mol L}^{-1}$). The areas where the solution was turbid are shaded in gray. The two frames below the diagram are 200 % magnifications of the low-temperature and the high-temperature region for better visibility. Figure 6.5 shows the determination of the cloud-points at atmospheric pressure for the six systems examined in this diagram. (Reprinted and adapted with permission from a previous publication.^[50] Copyright 2014 American Chemical Society.)

substantially different processes. The converse effect of the cononsolvents in the two temperature regimes necessarily entails that all curves must cross each other at some point in between.

While the addition of salt simply had an increasingly smaller pressure-reducing effect in the low-temperature regime (Figure 6.8), the organic additives even increase the cloud pressures in this region. This diversity in their behavior indicates different cloud-point lowering mechanisms for alcohols and salts. An analogous effect to the one of the alcohols was found for the additives acetone, 2-propanol, and DMF, measured at the same concentration of 0.075 mol L^{-1} (data not shown).

The observed opposite effect in the two temperature regions can be interpreted in terms of solvent–solvent interactions (see Section 1.2.2.2): If, at atmospheric pressure, the solubility of pNIPAm is reduced by the energetically favorable structures formed between water and the additive, it can be assumed that these structures are just destroyed at high pressures, making the polymer even more soluble in the therefore more hydrophobic solvent mixture. One could also argue that an opposite finding could be considered as an argument refuting this model, since it is very unlikely that solvent–solvent structures are preserved at such high pressures. For an interpretation in terms of solvent–polymer interactions, one would have to assume that the structures formed by competitive binding of the additive molecules to the polymer chains require more space than the associates with water and are thus pushed back at high pressures. The explanation for the increased solubility would then again be the higher hydrophobicity of the solvent mixture as in the former argument. To be able to shed more light on this aspect, it would first be necessary to thoroughly understand the mechanism behind the clouding at low temperatures. However, given the results presented here alone, it can be clearly stated that, regardless of the preferable explanation for the cononsolvency effect found for aqueous pNIPAm solutions, it only occurs at low pressures.

6.4.2 The cononsolvency region

Finally, the effect of one of the additives was studied over the whole cononsolvency range (see Section 1.2.2.2), systematically varying the concentration of added alcohol. Ethanol was designated for this task, since it is miscible with water at all concentrations and is the most ubiquitous and least poisonous of all examined solvents. The system water/pNIPAm/ethanol shows UCST-behavior (see Figure 1.3) at the branch of higher ethanol content of the cononsolvency miscibility gap at atmospheric pressure.^[93]

The mole fractions x of added ethanol were chosen in a preliminary experiment, in which ethanol was added in small portions to an aqueous pNIPAm solution

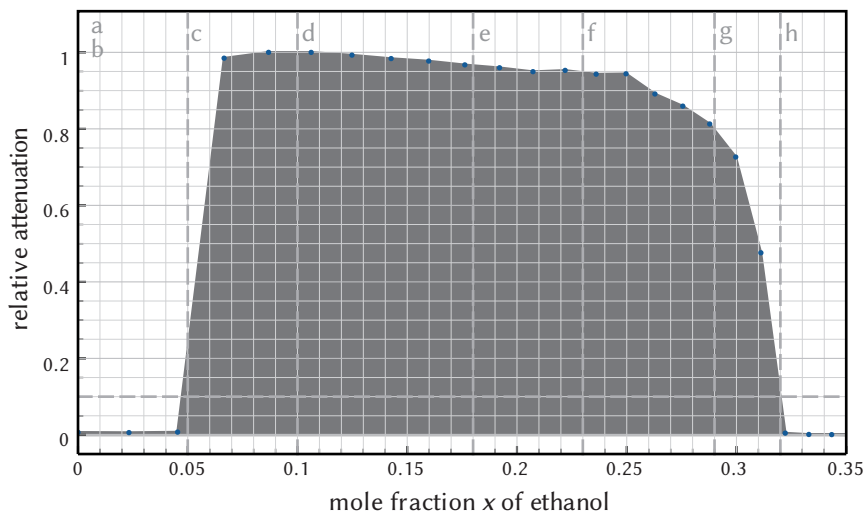


Fig. 6.10: Relative attenuation ($\lambda = 400$ nm) of an aqueous pNIPAm (sample π -10, 5 g L^{-1}) solution at 20°C and atmospheric pressure with increasing mole fraction of added ethanol. The region where the solution was turbid is shaded in gray. (Hereby, the points are interpolated linearly.) The vertical dashed gray lines, labeled with letters, mark the concentrations which were used for the corresponding cloud-point measurements shown in Figure 6.11. (Reprinted and adapted with permission from a previous publication.^[50] Copyright 2014 American Chemical Society.)

(still sample π -10 with $c = 5 \text{ g L}^{-1}$) at 20°C , while constantly monitoring the attenuation at $\lambda = 400$ nm in a spectrophotometer. In the acquired diagram, shown in Figure 6.10, the miscibility gap is well visible, approximately extending from $x = 0.05$ to $x = 0.32$, which corresponds well to the expectations based on the literature.^[93] Notably, the clouding process is more abrupt than the solution clearing up again, when more ethanol is added. The compositions of the samples, for which the cloud-point curves were then acquired, are marked with vertical dashed lines:

- a) pure aqueous pNIPAm solution,
- b) very little amount of ethanol added (sample identical to the one examined in Figure 6.9),
- c) lower boundary of the miscibility gap,
- d) lower half of the miscibility gap,

- e) approximate middle of the miscibility gap,
- f) upper half of the miscibility gap,
- g) solution beginning to clear up,
- h) upper boundary of the miscibility gap.

Figure 6.11 shows all cloud-point curves obtained for these systems. The labels in this diagram correspond to the marked compositions in Figure 6.10. The trend from diagram 6.11a to diagram 6.11b was already discussed above.* Both effects at low and high temperatures then increase with higher concentrations of ethanol. In diagram 6.11c, the curve is even further rotated and clouding is no longer observed at all at low temperatures. At the same time, the turbid region extends to lower temperatures in the atmospheric-pressure regime—the classic cononsolvency effect. The apparent clockwise rotation of the phase diagram proceeds with increasing mole fraction of ethanol via diagrams 6.11d and 6.11e, through to diagram 6.11f, where a certain composition in the middle of the atmospheric cononsolvency miscibility gap is reached. For this very specific mixture, the solution is turbid over the whole temperature range at lower pressures and becomes clear by increasing the pressure to values of over approximately 1 000 bar, almost completely independent of the system's temperature. The very low slope of this curve is remarkable and makes the system work as a temperature-independent pressure switch.

When further increasing the concentration of ethanol (diagrams g and h of Figure 6.11), the solution becomes turbid only for very low temperatures and pressures and the phase-transition curve is eventually shifted out of the experimentally accessible region so that the system appears as completely miscible. It can be envisaged that this behavior is representative for all cononsolvency systems which exhibit a UCST behavior for high cononsolvent concentrations at atmospheric pressure, such as systems containing the other alcohols with longer hydrocarbon chains or DMSO (see Section 1.2.2.2).^[93] Notably, the phase-behavior becomes completely converse to the situation without additive, when adding ethanol:

- At an arbitrary constant pressure, the aqueous system turns turbid when increasing the temperature (LCST behavior), whereas it clears up with raising temperature when the ethanol content is higher than approximately $x = 0.23$.
- At a constant temperature, the aqueous system turns turbid when increasing the pressure, whereas it clears up in the mixture with ethanol.

*The mole fraction $x = 0.001$ is identical to a concentration of $c = 0.075 \text{ mol L}^{-1}$ in water.

Given the above findings, the expressions “temperature-induced clouding” and “pressure-induced clouding” can no longer be reasonably applied for such high ethanol concentrations, although still two different phase-transition mechanisms are expected to exist. Once again, solvent–solvent interactions and solvent–polymer interactions (see Section 1.2.2.2) can be attributed for this behavior, in an analogous way as described above, only that both effects become more pronounced. A conceivable, but yet speculative explanation based on solvent–solvent interactions, namely the formation of network or cluster structures of water and ethanol, could be as follows: The higher the concentration of ethanol in the system, the lower the degree of ethanol which is incorporated in structures with water molecules.^[93] This would presumably lead to a more readily occurring and stronger release of ethanol molecules when the hydration structures break by exertion of pressure, enabling the ethanol to interact with the NIPAm polymer. Ethanol is less polar than water and it is reasonable to expect that it interacts in a manner which is more van-der-Waals-force based and therefore less pressure dependent than the very directed interactions between water and pNIPAm. This fact would shift the cloud curve to higher pressures in the low-temperature region, while the cononsolvency lowers the cloud temperature at ambient pressure. The combination of both effects would then lead to the apparent clockwise rotation of the cloud curves. At higher ethanol contents, undirected interactions then seem to govern the solvency over the whole temperature range.

6.5 Conclusions from the cloud-point experiments

In this chapter, by capitalizing on the option of applying elevated pressures, a completely new aspect of phase behavior was found for the already very well studied systems of aqueous pNIPAm solutions.

Conversely to their effect at atmospheric pressure, all common organic cononsolvents lead to an increasing solubility of the polymer in the low-temperature/high-pressure region, when added in low concentrations. A gradual and complete inversion of the phase-separation behavior regarding both the effects of pressure and temperature was found by increasing the mole fraction of added ethanol over the whole cononsolvency range. As a very special case, at a mole fraction of $x = 0.23$, the system clears up independent of temperature at a constant pressure of about 1 000 bar. By the mere addition of some drops of ethanol to the solution, the effect of high pressures on the phase behavior can thus be turned upside down.

The presented findings support the assumption of substantially different clouding mechanisms for the high-temperature and the low-temperature regions. Assuming solvent–solvent interactions as the main reason for the observations, the pNIPAm in the presented systems can be very useful as a probe^[94] for indirectly exploring the structures formed in mixtures of water and other solvents. Moreover, these results will prove useful for theorists modeling the interplay between hydrophilic and hydrophobic interactions or working on descriptions of the cononsolvency effect, for example with respect to the behavior of proteins and other natural macromolecules in the presence of organic solvents. For a theoretical model to be accepted by the scientific community, it should be able to account for the presented findings at high pressures.

In addition to the obvious sensory applications, the results might also be useful in the fields of food processing and medicine—the treatment in an autoclave is a standard method for sterilization. The pressure range examined here of up to 3 000 bar can be realistically realized in industrial processes. After all, the record for the pressure achieved with the most modern technologies is already over 2 000 times higher.^[95] One can also envision the use of crosslinked pNIPAm hydrogels which expel their loadings induced by high pressures and could, hence, be used for the study of high-pressure catalysis, potentially in deep-sea science.^[24] On the deepest grounds of the oceans, the hydrostatic pressure is around 1 000 bar.

In a modular approach, outlined in Section 8.3.2.1, the pNIPAm samples examined in this chapter will be used to assemble advanced nanohybrids, in which the special properties presented here are combined with the extraordinary optical features of gold nanocrystals.

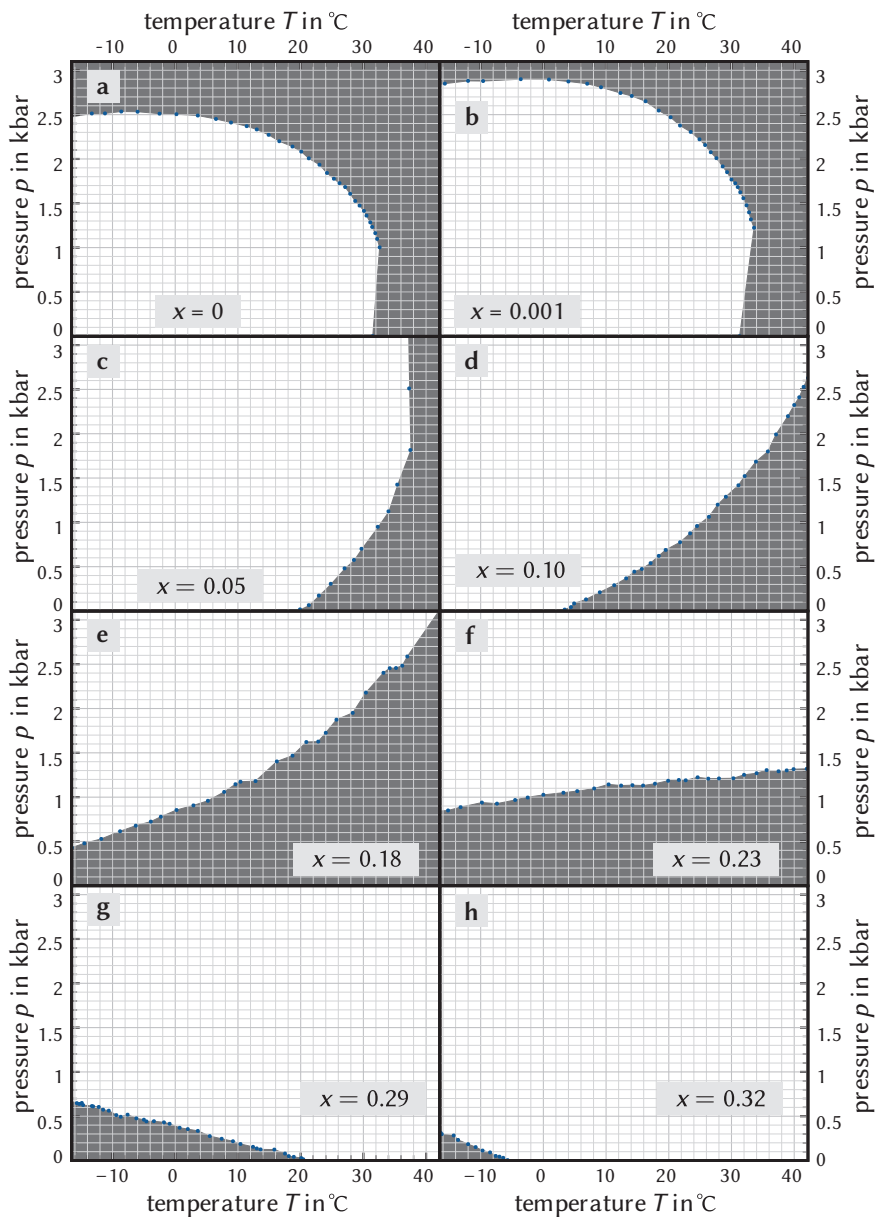


Fig. 6.11: Cloud-point curves of aqueous solutions of pNIPAm (sample π -10, $c = 5 \text{ g L}^{-1}$) with increasing mole fractions x of ethanol as additive. The areas where the solution was turbid are shaded in gray. (Hereby, the points are interpolated linearly.) The compositions of the samples are also shown as vertical dashed lines in Figure 6.10. (Reprinted and adapted with permission from a previous publication.^[50] Copyright 2014 American Chemical Society.)

References for Chapter 6

- (1) Grobelny, S., Hofmann, C. H., Erlikamp, M., Plamper, F. A., Richtering, W., Winter, R., *Soft Matter* **2013**, 9 (25), 5862–5866.
- (2) Hirotsu, S., *J. Chem. Phys.* **1988**, 88 (1), 427–431.
- (3) Hirotsu, S., Onuki, A., *J. Phys. Soc. Jap.* **1989**, 58 (5), 1508–1511.
- (4) Li, Y., Tanaka, T., *J. Chem. Phys.* **1989**, 90 (9), 5161–5166.
- (5) Hirotsu, S., *Macromolecules* **1990**, 23 (3), 903–905.
- (6) Hirotsu, S., *J. Chem. Phys.* **1991**, 94 (5), 3949–3957.
- (7) Lee, K., Cussler, E., Marchetti, M., McHugh, M., *Chem. Eng. Sci.* **1990**, 45 (3), 766–767.
- (8) Ohta, H., Ando, I., Fujishige, S., Kubota, K., *J. Polym. Sci., Part B: Polym. Phys.* **1991**, 29 (8), 963–968.
- (9) Sanefuji, T., Ando, I., Inoue, Y., Uematsu, I., Shoji, A., *Macromolecules* **1985**, 18 (3), 583–585.
- (10) Otake, K., Karaki, R., Ebina, T., Yokoyama, C., Takahashi, S., *Macromolecules* **1993**, 26 (9), 2194–2197.
- (11) Kunugi, S., Takano, K., Tanaka, N., Suwa, K., Akashi, M., *Macromolecules* **1997**, 30 (15), 4499–4501.
- (12) Suwa, K., Yamamoto, K., Akashi, M., Takano, K., Tanaka, N., Kunugi, S., *Colloid Polym. Sci.* **1998**, 276 (6), 529–533.
- (13) Kunugi, S., Yamazaki, Y., Takano, K., Tanaka, N., Akashi, M., *Langmuir* **1999**, 15 (12), 4056–4061.
- (14) Yamazaki, Y., Tada, T., Kunugi, S., *English Colloid Polym. Sci.* **2000**, 278 (1), 80–83.
- (15) Rebelo, L. P. N., Visak, Z. P., Sousa, H. C. de, Szydlowski, J., Gomes de Azevedo, R., Ramos, A. M., Najdanovic-Visak, V., Nunes da Ponte, M., Klein, J., *Macromolecules* **2002**, 35 (5), 1887–1895.
- (16) Gomez de Azevedo, R., Rebelo, L. P. N., Ramos, A. M., Szydlowski, J., Sousa, H. C. de, Klein, J., *Fluid Phase Equilib.* **2001**, 185 (1–2), 189–198.
- (17) Kato, E., Kitada, T., Nakamoto, C., *Macromolecules* **1993**, 26 (7), 1758–1760.
- (18) Kato, E., Kitada, T., *J. Phys. Soc. Jap.* **1994**, 63 (7), 2831–2832.
- (19) Kato, E., *J. Chem. Phys.* **1994**, 101 (1), 468–472.
- (20) Kato, E., Murakami, T., *J. Phys. Soc. Jap.* **1995**, 64 (5), 1449–1452.
- (21) Nakamoto, C., Kitada, T., Kato, E., *Polym. Gels Networks* **1996**, 4 (1), 17–31.
- (22) Kato, E., *J. Chem. Phys.* **1997**, 106 (9), 3792–3797.
- (23) Kato, E., *J. Chem. Phys.* **2000**, 113 (3), 1310–1314.
- (24) Kato, E., *J. Appl. Polym. Sci.* **2005**, 95 (5), 1069–1072.
- (25) Kato, E., *J. Appl. Polym. Sci.* **2005**, 97 (1), 405–412.
- (26) Zhong, X., Wang, Y.-X., Wang, S.-C., *Chem. Eng. Sci.* **1996**, 51 (12), 3235–3239.
- (27) Kitada, T., *J. Polym. Sci., Part A: Polym. Chem.* **2001**, 39 (13), 2315–2325.
- (28) Shibayama, M., Isono, K., Okabe, S., Karino, T., Nagao, M., *Macromolecules* **2004**, 37 (8), 2909–2918.

- (29) Nasimova, I., Karino, T., Okabe, S., Nagao, M., Shibayama, M., *Macromolecules* **2004**, 37 (23), 8721–8729.
- (30) Nasimova, I., Karino, T., Okabe, S., Nagao, M., Shibayama, M., *J. Chem. Phys.* **2004**, 121 (19), 9708–9715.
- (31) Buckingham, A. D., Hentschel, H. G. E., *J. Polym. Sci., Polym. Phys. Ed.* **1980**, 18 (4), 853–861.
- (32) Meersman, F., Wang, J., Wu, Y., Heremans, K., *Macromolecules* **2005**, 38 (21), 8923–8928.
- (33) Wu, Y., Meersman, F., Ozaki, Y., *Macromolecules* **2006**, 39 (3), 1182–1188.
- (34) Wu, Y., Meersman, F., Heremans, K., Ozaki, Y., *J. Mol. Struct.* **2006**, 799 (1–3), 134–140.
- (35) Wu, Y., Jiang, J.-H., Ozaki, Y., *J. Phys. Chem. A* **2002**, 106 (11), 2422–2429.
- (36) Wu, Y., Yuan, B., Zhao, J.-G., Ozaki, Y., *J. Phys. Chem. B* **2003**, 107 (31), 7706–7715.
- (37) Puehse, M., Keerl, M., Scherzinger, C., Richtering, W., Winter, R., *Polymer* **2010**, 51 (16), 3653–3659.
- (38) Pelton, R., *Adv. Colloid Interface Sci.* **2000**, 85 (1), 1–33.
- (39) Saunders, B. R., Vincent, B., *Adv. Colloid Interface Sci.* **1999**, 80 (1), 1–25.
- (40) Lietor-Santos, J. J., Sierra-Martin, B., Gasser, U., Fernandez-Nieves, A., *Soft Matter* **2011**, 7 (14), 6370–6374.
- (41) Kunugi, S., Tanaka, N., *Biochim. Biophys. Acta* **2002**, 1595 (1–2), 329–344.
- (42) Winter, R., Lopes, D., Grudzielanek, S., Vogtt, K., *J. Non-Equilib. Thermodyn.* **2007**, 32 (1), 41–97.
- (43) Mishra, R., Winter, R., *Angew. Chem. Int. Ed.* **2008**, 47 (35), 6518–6521.
- (44) Tamura, T., Yamaoka, T., Kunugi, S., Panitch, A., Tirrell, D. A., *Biomacromolecules* **2000**, 1 (4), 552–555.
- (45) Hummer, G., Garde, S., García, A. E., Paulaitis, M. E., Pratt, L. R., *Proc. Natl. Acad. Sci. U.S.A.* **1998**, 95 (4), 1552–1555.
- (46) Kunugi, S., Kameyama, K., Tada, T., Tanaka, N., Shibayama, M., Akashi, M., *Braz. J. Med. Biol. Res.* **2005**, 38, 1233–1238.
- (47) Paschek, D., Nonn, S., Geiger, A., *Phys. Chem. Chem. Phys.* **2005**, 7 (14), 2780–2786.
- (48) Osaka, N., Shibayama, M., *Macromolecules* **2012**, 45 (4), 2171–2174.
- (49) Osaka, N., Shibayama, M., Kikuchi, T., Yamamuro, O., *J. Phys. Chem. B* **2009**, 113 (39), 12870–12876.
- (50) Ebeling, B., Eggers, S., Hendrich, M., Nitschke, A., Vana, P., *Macromolecules* **2014**, 47 (4), 1462–1469.
- (51) Buback, M., Latz, H., *Macromol. Chem. Phys.* **2003**, 204 (4), 638–645.
- (52) Becker, F., Buback, M., Latz, H., Sadowski, G., Tumakaka, F., *Fluid Phase Equilib.* **2004**, 215 (2), 263–282.
- (53) Latz, H. *Kinetische und thermodynamische Untersuchungen der Hochdruck-Copolymerisation von Ethen mit (Meth)Acrylsäureestern*, Ph.D. thesis, Georg-August-Universität Göttingen, **2004**.
- (54) Tumakaka, F., Sadowski, G., Latz, H., Buback, M., *J. Supercrit. Fluids* **2007**, 41 (3), 461–471.
- (55) Hare, D. E., Sorensen, C. M., *J. Chem. Phys.* **1987**, 87 (8), 4840–4845.

- (56) Sotani, T., Arabas, J., Kubota, H., Kijima, M., Asada, S., *High Temp. High Press.* **2000**, 32 (4), 433–440.
- (57) Asada, S., Sotani, T., Arabas, J., Kubota, H., Matsuo, S., Tanaka, Y., *J. Phys.: Condens. Matter* **2002**, 14 (44), 11447.
- (58) Saul, A., Wagner, W., *J. Phys. Chem. Ref. Data* **1989**, 18 (4), 1537–1564.
- (59) *Handbook of Chemistry and Physics*; Lide, D. R., Ed.; CRC PRESS: **2003–2004**; Vol. 84th.
- (60) Bertolini, D., Cassettari, M., Salvetti, G., *Chem. Phys. Lett.* **1985**, 119 (6), 553–555.
- (61) Verma, M. P., *Computers Geosci.* **2003**, 29 (9), 1155–1163.
- (62) Müller, A., Krebs, B., *Monatsh. Chem.* **1967**, 98 (4), 1540–1544.
- (63) Patel, T., Ghosh, G., Yusa, S.-i., Bahadur, P., *J. Dispersion Sci. Technol.* **2011**, 32 (8), 1111–1118.
- (64) Smeller, L., *Biochim. Biophys. Acta* **2002**, 1595 (1–2), 11–29.
- (65) Okada, Y., Tanaka, F., *Macromolecules* **2005**, 38 (10), 4465–4471.
- (66) Zheng, X., Tong, Z., Xie, X., Zeng, F., *Polym. J.* **1998**, 30 (4), 284–288.
- (67) Tong, Z., Zeng, F., Zheng, X., Sato, T., *Macromolecules* **1999**, 32 (13), 4488–4490.
- (68) Schild, H. G., Tirrell, D. A., *J. Phys. Chem.* **1990**, 94 (10), 4352–4356.
- (69) Baltes, T., Garret-Flaudy, F., Freitag, R., *J. Polym. Sci., Part A: Polym. Chem.* **1999**, 37 (15), 2977–2989.
- (70) Fujishige, S., Kubota, K., Ando, I., *J. Phys. Chem.* **1989**, 93 (8), 3311–3313.
- (71) Tiktupulo, E. I., Uversky, V. N., Lushchik, V. B., Klenin, S. I., Bychkova, V. E., Ptitsyn, O. B., *Macromolecules* **1995**, 28 (22), 7519–7524.
- (72) Ding, Z., Chen, G., Hoffman, A. S., *Bioconjugate Chem.* **1996**, 7 (1), 121–125.
- (73) Furyk, S., Zhang, Y., Ortiz-Acosta, D., Cremer, P. S., Bergbreiter, D. E., *J. Polym. Sci., Part A: Polym. Chem.* **2006**, 44 (4), 1492–1501.
- (74) Poole, P. H., Sciortino, F., Essmann, U., Stanley, H. E., *Nature* **1992**, 360 (6402), 324–328.
- (75) Poole, P. H., Sciortino, F., Grande, T., Stanley, H. E., Angell, C. A., *Phys. Rev. Lett.* **1994**, 73 (12), 1632–1635.
- (76) Tanaka, H., *Nature* **1996**, 380 (6572), 328–330.
- (77) Mishima, O., Stanley, H. E., *Nature* **1998**, 392 (6672), 164–168.
- (78) Mishima, O., Stanley, H. E., *Nature* **1998**, 396 (6709), 329–335.
- (79) Rønne, C., Åstrand, P.-O., Keiding, S. R., *Phys. Rev. Lett.* **1999**, 82 (14), 2888–2891.
- (80) Starr, F. W., Sciortino, F., Stanley, H. E., *Phys. Rev. E* **1999**, 60 (6), 6757–6768.
- (81) Errington, J. R., Debenedetti, P. G., Torquato, S., *Phys. Rev. Lett.* **2002**, 89 (21), 215503.
- (82) Giovambattista, N., Buldyrev, S. V., Starr, F. W., Stanley, H. E., *Phys. Rev. Lett.* **2003**, 90 (8), 085506.
- (83) Paschek, D., *J. Chem. Phys.* **2004**, 120 (14), 6674–6690.
- (84) Scala, A., Starr, F. W., La Nave, E., Sciortino, F., Stanley, H. E., *Nature* **2000**, 406 (6792), 166–169.
- (85) Soper, A. K., Ricci, M. A., *Phys. Rev. Lett.* **2000**, 84 (13), 2881–2884.

- (86) Okhulkov, A. V., Demianets, Y. N., Gorbaty, Y. E., *J. Chem. Phys.* **1994**, *100* (2), 1578–1588.
- (87) Brovchenko, I., Geiger, A., Oleinikova, A., *J. Chem. Phys.* **2003**, *118* (21), 9473–9476.
- (88) Tanaka, H., *Phys. Rev. E* **2000**, *62* (5), 6968–6976.
- (89) Bellissent-Funel, M.-C., *Europhys. Lett.* **1998**, *42* (2), 161.
- (90) Mishima, O., *Phys. Rev. Lett.* **2000**, *85* (2), 334–336.
- (91) Paschek, D., *Phys. Rev. Lett.* **2005**, *94* (21), 217802.
- (92) Cavaille, D., Combes, D., Zwick, A., *J. Raman Spectrosc.* **1996**, *27* (11), 853–857.
- (93) Costa, R. O., Freitas, R. F., *Polymer* **2002**, *43* (22), 5879–5885.
- (94) Yang, C., Li, W., Wu, C., *J. Phys. Chem. B* **2004**, *108* (31), 11866–11870.
- (95) Dubrovinsky, L., Dubrovinskaia, N., Prakapenka, V. B., Abakumov, A. M., *Nat. Commun.* **2012**, *3*, 1163.

Chapter 7

Nanocomposites via polymerization from silica

In Sections 5.2.1 and 5.2.2, it was shown how the two special RAFT agents $\rho^{2x}-2$ and ρ^1-3 , equipped with methoxysilyl anchor groups at their stabilizing Z-groups could be synthesized. Methoxysilyl groups can be irreversibly fastened on silica substrates via the formation of siloxy bonds. In the following, it will be shown how these RAFT agents can play to their special strengths by immobilizing them on different types of silica substrates and employing the products in radical surface polymerizations. In both systems, for each of which one exemplary polymerization is discussed, the approach of exploiting the unique mechanistic feature of the RAFT process—the surface-tethering of the controlling RAFT moiety—is pursued (see Section 1.2.4.1). The resulting silica–polystyrene and silica–poly(*n*-butyl acrylate) nanocomposites cannot be called “smart” in the sense that they react to outer stimuli in a dramatic way as the nanohybrids at the center of the next chapter. However, the systems presented here are fitting to demonstrate the power of rationally employed RAFT polymerization, giving rise to extraordinary nanostructured materials, which one could on no account obtain by just adding the silica particles to a bulk polymer.

Silica nanoparticles were chosen as carrier substrates here, because they are cheap, very stable, and resistant, and they possess a surface with silanol groups, which is easy to functionalize. They can be produced or obtained commercially in different shapes and sizes.^[1] These characteristics make them the most commonly used systems for the study of surface polymerizations and the production and analysis of nanocomposites with organic polymers.^[2,3] One of the main industrial applications of silica nanoparticles is the use as fillers in polymeric materials. Coating of the silica surface with the corresponding polymer is thought to enhance the interactions at the interfaces between the silica and the polymer matrix, thus preventing particle separation, which leads to far superior material properties.^[4]

7.1 Polymer nanoloops on fumed silica

7.1.1 The substrate fumed silica

Fumed silica consists of nanodroplets of amorphous silica, which are fused into branched and chainlike secondary particles. Those are in turn agglomerated into tertiary structures, resulting in a powder with a very high specific surface, typically over $200 \text{ m}^2 \text{ g}^{-1}$.^[5] Fumed silica is also known as “pyrogenic silica”, because it is made by flame pyrolysis of silicon tetrachloride or quartz sand in an electrical arc.^[6] Due to the extremely high surface, this mesoporous material is ideally suited as solid carrier material to study polymerization kinetics on solid surfaces. The low price allows for the design of nanocomposite materials for scaled-up commercial applications. In fact, the employment of fumed silica as filler in polymeric materials, paints, coatings, and adhesives is a common industrial routine.^[3]

Fumed silica consists of visible micrograins, which slowly settle from their coarse dispersions without continuous stirring. This comes with the benefit that they can just be filtered off for separation after heterogeneous reactions. Z-RAFT-functionalized fumed silica can thus potentially be employed as a recyclable heterogeneous polymerization control system, which can be easily collected in technical processes.

7.1.2 Immobilization of the RAFT agent

RAFT agent $\text{P}^{2\text{x}}\text{-2}$ was immobilized irreversibly on the commercially acquired fumed silica $\text{SiO}_2^{\text{fs}}\text{-1}$ with catalytic amounts of maleic anhydride and water. According to the supplier, $\text{SiO}_2^{\text{fs}}\text{-1}$ had a specific surface of $(390 \pm 40) \text{ m}^2 \text{ g}^{-1}$ and a surface density of silanol groups of approximately 2.5 nm^{-2} . Sample $\text{SiP}^{2\text{x}}\text{-1}$, obtained by the immobilization procedure, possessed a loading of $0.066 \text{ mmol g}^{-1}$ (based on sulfur content by elemental analysis, see Equation (7.2) below), corresponding to 0.11 molecules per nm^2 (or $0.2 \text{ } \mu\text{mol m}^{-2}$). A relatively low value was targeted, since not all silanol groups of the mesoporous silica are accessible and the formation of crosslinked RAFT-molecule aggregates should be minimized. Mechanistically, the immobilization proceeds by hydrolyzation of the trimethoxysilyl groups which may first condensate with each other.^[7] This network can then bind to the silanol groups on the surface^[8,9] by condensation.^[10] The whole process, and the fact that some silanol groups are more exposed than others, presumably lead to an irregular distribution of the surface-immobilized RAFT agents in $\text{SiP}^{2\text{x}}\text{-1}$. Figure 7.1 shows three images of the same spot on $\text{SiP}^{2\text{x}}\text{-1}$, taken with scanning electron microscopy (SEM) in different magnifications. A characteristic and very fine mesoporous struc-

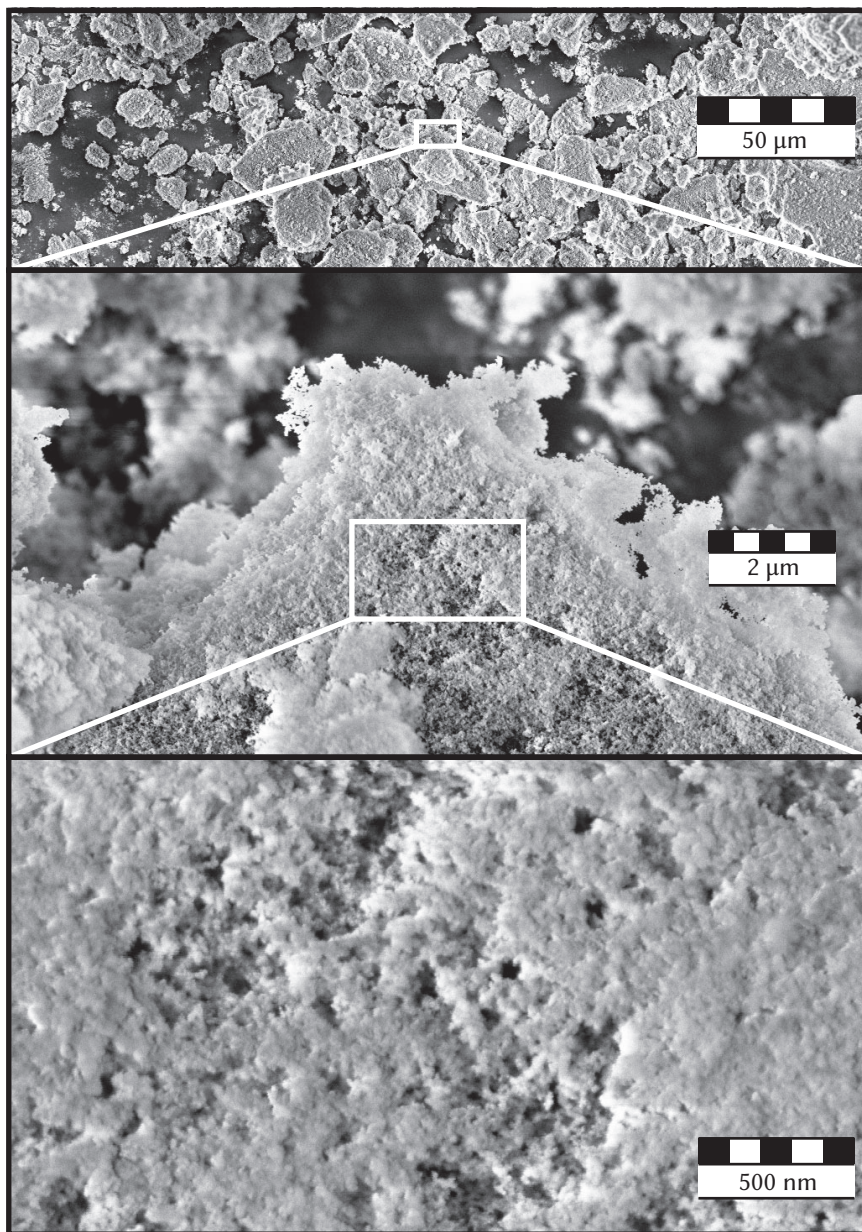


Fig. 7.1: SE micrographs of the RAFT-functionalized fumed silica $\text{fs}_{\text{si}}\text{P}^{2\times}-1$ with different magnifications of the same spot. The sample was coated with a gold film ($\approx 8\text{ nm}$) prior to the measurement.

Tab. 7.1: Polymerization data for $\text{fs}_{\text{si}}\text{K}^{2\times}-1$. The conversions $X_{\text{M,g}}$ were determined by gravimetry (Equation (5.9)) and the mass fractions of polymer ω_{p} in the produced nanohybrids by thermogravimetric analysis. The \overline{M}_{n} and \overline{D} values were obtained by SEC analysis (THF, RI detector).

	number	$\text{fs}_{\text{si}}\text{K}^{2\times}\text{-1}$	T	60 °C			
	monomer	styrene	c_{M}	8.7 mol L ⁻¹			
	RAFT agent	$\text{fs}_{\text{si}}\text{P}^{2\times}\text{-1}$	c_{RAFT}	104 mg L ⁻¹			
	initiator	AIBN	c_{ini}	5.0×10^{-3} mol L ⁻¹			
$\text{fs}_{\text{si}}\text{K}^{2\times}\text{-1}$			in solution		on surface		
	t in h	$X_{\text{M,g}}$	ω_{p}	\overline{M}_{n} in $\frac{\text{g}}{\text{mol}}$	\mathcal{D}	\overline{M}_{n} in $\frac{\text{g}}{\text{mol}}$	\mathcal{D}
a	2	0.056	0.101	8.46×10^4	2.27	2.13×10^4	3.27
b	5	0.11	0.139	11.20×10^4	2.06	2.65×10^4	3.69
c	7	0.21	0.199	10.90×10^4	1.88	2.74×10^4	3.87
d	9	0.26	0.220	11.10×10^4	1.88	3.13×10^4	3.83
e	15	0.28	0.403	12.50×10^4	1.89	5.05×10^4	3.54
f	28	0.50	0.264	14.20×10^4	2.09	2.88×10^4	4.42

ture is visible. The primary particles (and, of course, the RAFT agent), however, are not resolved.

7.1.3 Surface polymerization

The exemplary surface-confined RAFT polymerization $\text{fs}_{\text{si}}\text{K}^{2\times}-1$ of styrene (see the structural formula in Figure 5.11, Section 5.4) performed with the RAFT-functionalized fumed silica $\text{fs}_{\text{si}}\text{P}^{2\times}-1$ shall be discussed here. It was carried out in bulk at $60\text{ }^{\circ}\text{C}$ under constant stirring with AIBN (see Figure 5.13, Section 5.4) as initiator. No sacrificial RAFT agent was added. The conversion of the six samples, which were obtained after defined polymerization times, were determined gravimetrically (Equation (5.9), Section 5.4.2, mathematically treating the fumed silica as part of the container). All data concerning this polymerization are listed in Table 7.1.

Figure 7.2 shows a schematic illustration of the ongoing graft-polymerization mechanism. The dual anchoring of both ends of the RAFT agent eliminates the major drawback entailed by the RAFT Z-approach, that the growing radicals depart from the surface and have to come back for the control to be maintained (see Section 1.2.4.1). With a doubly-bound RAFT agent, the growing polymer chains

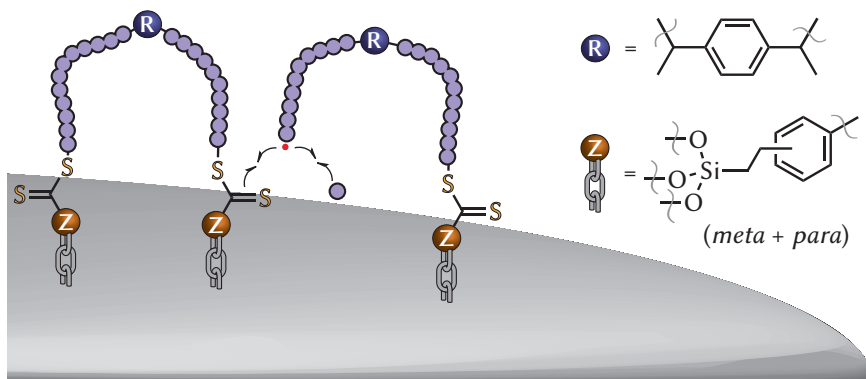


Fig. 7.2: Schematic illustration of the formation of polystyrene loops on the surface of fumed silica by Z-RAFT polymerization $tsk^{2x}-1$. The structure of the unbound RAFT agent $\rho^{2x}-2$ is shown in Scheme 5.2.

remain still attached to the surface via the link on their other end, allowing for surface polymerizations with low RAFT-agent concentrations. By employing a bipedal RAFT agent, the advantages of Z-group- and R-group-immobilized RAFT agents are thus combined. Moreover, in the case of single termination events other than surface radical combination, the polymer chain only becomes singly-bound and is not lost. The remaining anchor point on the surface can potentially be reactivated by initiator-terminated macromolecules from the solution. These characteristics render the double Z-approach far superior in contrast to the Z-variant with only singly bound RAFT agents. As long as termination events are kept low during the polymerization, polymer loops of controlled chain length are inherently obtained on the surface—a new and promising class of polymer brushes without chain ends, which is very difficult to produce using alternative strategies.

The solution polymer was analyzed by means of SEC analysis in THF after separation from the polymerization mixture, first by filtration and rinsing with THF and toluene, then by Soxhlet extraction with dichloromethane. Solution polymer, which is only physisorbed on the fumed silica, is completely washed off in this process.^[11] The formation of polymeric material in solution is an inherent phenomenon caused by the use of a homogeneous initiator. As it can be seen from the values in Table 7.1, the confinement of the RAFT molecules to the surface leads to a practically uncontrolled polymerization in solution, giving rise to polymers with broadly distributed and comparably high molar masses.

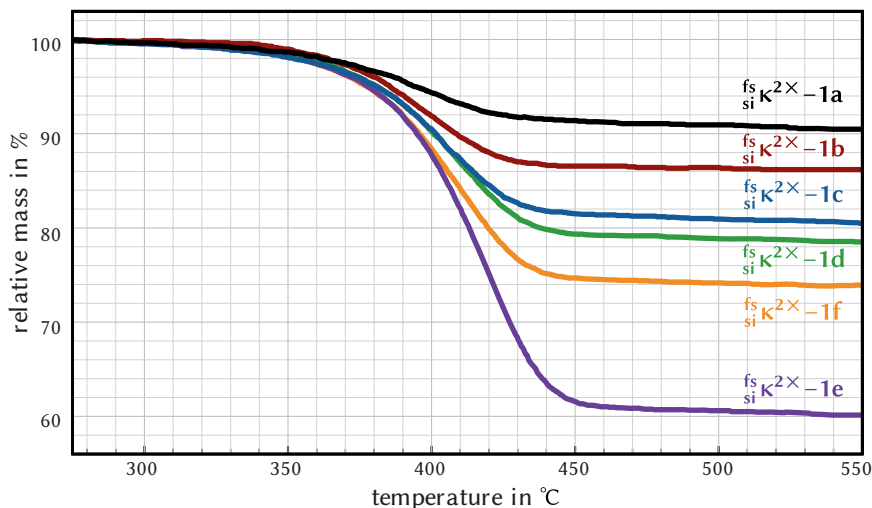
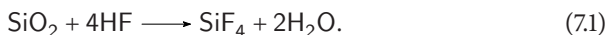


Fig. 7.3: Thermogravimetric analysis of all samples of the styrene-silica nanocomposite $f_{\text{si}}^{\text{fs}}\text{K}^{2\times}-1$. The step around 400 °C is caused by the evaporation of decomposed polystyrene, while the fumed silica is retained. The curves were set to 100 % relative mass at 250 °C.

7.1.4 Analysis of the produced nanocomposites

In order to isolate and analyze the formed macromolecules, which were covalently bound on the surface of the fumed silica, a fraction of each sample was treated with hydrofluoric acid. The silica part of the composites is thus dissolved according to the reaction



While potential siloxy linkages between the polymers are also split up in the process, the polymer itself is not disintegrated by hydrofluoric acid. The SEC results for the cleaved-off polymers can also be found in Table 7.1. For the calculation of the \overline{M}_n and \overline{D} values, the signals at low molar masses—presumably caused by silica disintegration products—were ignored.

The relatively high dispersities of the surface-bound polymer chains is due to the fact that certain positions on the surface of the fumed silica are more exposed than others (see Figure 7.1) and the RAFT polymers at these spots have a higher chance of being attacked from solution radicals. In contrast to the polymers from the solution, the molar masses of the surface polymers are very low. This gives the impression that they grow in a controlled fashion in an isolated domain, and no

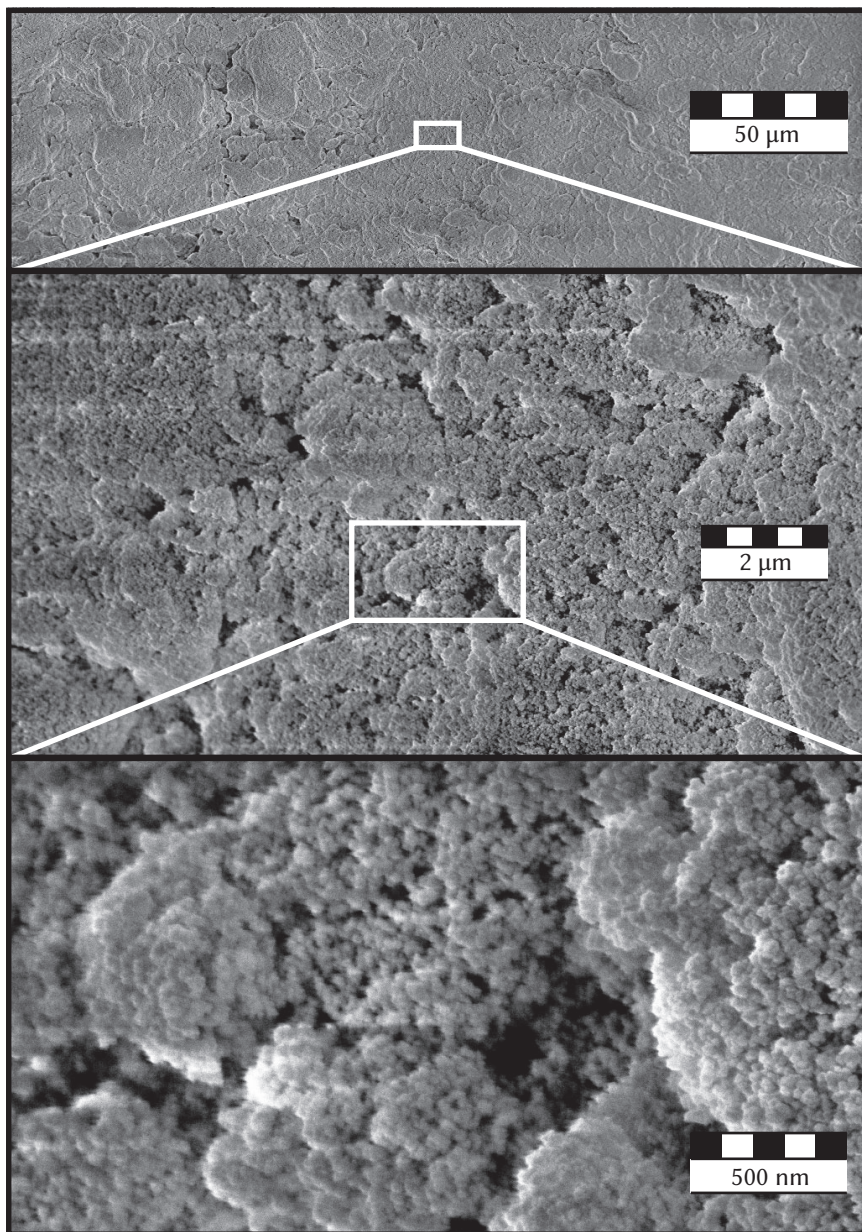


Fig. 7.4: SE micrographs of the polystyrene-coated fumed silica sample $f_{si}^{2x}-1c$ magnifications of the same spot. Although this sample consists of about 20 % polystyrene, the visible characteristic surface mesostructures are retained (compare with Figure 7.1). The sample was coated with a gold film (≈ 8 nm) prior to the measurement.

initiator-terminated chains replace the RAFT polymer on the surface, which should lead to the equilibration of the molar masses of surface and solution polymers. The average molar masses first increase with the conversion, indicative of a controlled loop expansion, until they abruptly drop to an almost halved value from sample $\text{f}_{\text{si}}^{\text{f}}\text{K}^{2\times}-1\text{e}$ to sample $\text{f}_{\text{si}}^{\text{f}}\text{K}^{2\times}-1\text{f}$. This decrease of the molar masses could be reproduced in other polymerizations with $\text{f}_{\text{si}}^{\text{f}}\text{P}^{2\times}-1$ and is as a matter of principle only possible for Z-RAFT-, rather than R-RAFT polymerizations. With the latter, once formed, polymer chains cannot be split off from the surface, even in the case of termination reactions. Here, the drop in the molar masses of the surface polymers, must be explained by the substitution of “living” macromolecular chains with initiator-terminated shorter ones. It might seem surprising that this replacement would only take place with exceptionally short radicals, giving the very high \overline{M}_n values of the corresponding solution polymers, but (i) small radicals are more mobile and less shielded than larger ones and (ii) the majority of the polymer chains in solution is already “dead” and not available for a radical substitution reaction. That the drop in the \overline{M}_n values occurs not before a monomer conversion of $X_M \approx 0.5$ shows that the polymerization is well controlled up to this high value. As stated above, when one end is disconnected, the polymer chains still remain bound to the surface with the other end, making the double-anchoring approach much more robust towards this kind of event.

The observed trend in the \overline{M}_n values was consistent with the results from thermogravimetric analysis (TGA) (also listed in Table 7.1). Using this technique, the mass fraction of surface polymer ω_p can be obtained by monitoring the mass of the sample while heating it up, as demonstrated for all samples of $\text{f}_{\text{si}}^{\text{f}}\text{K}^{2\times}-1$ in Figure 7.3. (The masses at 250 °C were set to 100 %.) The drop beginning at around 300 °C is caused by the decomposition and evaporation of the polystyrene. Because the silica remains on the microbalance, the relative size of the visible step is the reciprocal value of ω_p . The high consistency of the \overline{M}_n and the ω_p values shows that the total number of polymer chains on the silica surface remains constant, which validates the arguments above. Notably, for sample $\text{f}_{\text{si}}^{\text{f}}\text{K}^{2\times}-1\text{e}$ a remarkable value of $\omega_p = 0.4$ is reached. Almost half of this nanocomposite consists of polymer.

Figure 7.4 shows three SEM images of a spot on sample $\text{f}_{\text{si}}^{\text{f}}\text{K}^{2\times}-1\text{c}$. Although it contains $\approx 20\%$ polymer, the mesostructure is completely retained as before the polymerization (compare with Figure 7.1). The precise formation of a thin polymer film on a mesostructured material would be impossible to achieve by mere physisorption of the polymer—another illustration of the power of surface-initiated polymerizations.

Since the polymers are bound to the silica surface through the still active RAFT groups, the synthesized nanocomposites could in principle be employed in subsequent polymerizations with another monomer, in order to produce block-copolymer loops. One could then harvest the block copolymers by the reaction with excess radicals (see Section 5.4.5) and the recycled and recovered RAFT-functionalized fumed silica could be used repeatedly in a technical process, in this sense acting like a heterogeneous solid-supported polymerization control system.

7.2 Polymers with single covalent bonds to silica nanoparticles

7.2.1 The substrate silica nanoparticles

The second presented type of silica–polymer nanocomposites was synthesized via surface polymerizations from spherical silica nanoparticles $\text{siO}_2^{\text{np}}\mathbf{v-2}$ —the particles, which were examined exemplarily by TEM and AFM in Sections 4.1 and 4.2. As opposed to the primary particles of the fumed silica $\text{siO}_2^{\text{fs}}\mathbf{v-1}$ from the preceding section, these particles are not agglomerated into higher structures. They form stable colloids in polar solvents and were acquired commercially in the form of a dispersion in methanol, but very similar silica nanoparticles can also be synthesized in house by the Stöber process^[12–15] with relative ease. It was found that the silica nanoparticles $\text{siO}_2^{\text{np}}\mathbf{v-2}$ ($2r = 50 \text{ nm} \pm 12 \text{ nm}$) could be dried and stored without irreversible aggregation for approximately 1 d and thus be transferred to other solvents. (See Section 4.1 for the fusion mechanisms of silica nanoparticles.)

With regard to their surface chemistry, $\text{siO}_2^{\text{np}}\mathbf{v-2}$ was practically equivalent to $\text{siO}_2^{\text{fs}}\mathbf{v-1}$, but their distinct nanostructure requires a totally different handling. They cannot be subjected to filtration or Soxhlet extraction. Moreover, the particle aggregation, leading to the adulteration of the material, is an imminent threat which must be prevented.

7.2.2 Immobilization of the RAFT agent

For immobilization reactions on the surface of the silica nanoparticles $\text{siO}_2^{\text{np}}\mathbf{v-2}$, it is crucial that they be completely dispersed. In the case of the formation of aggregates, the accessible surface area is drastically reduced. Dry nanoparticles obtained by centrifugation were redissolved in different solvents, in order to find the best suited one. Analysis via TEM revealed that in solvents with a low polarity, huge aggregates with almost no detectable individual particles had formed, while in very polar

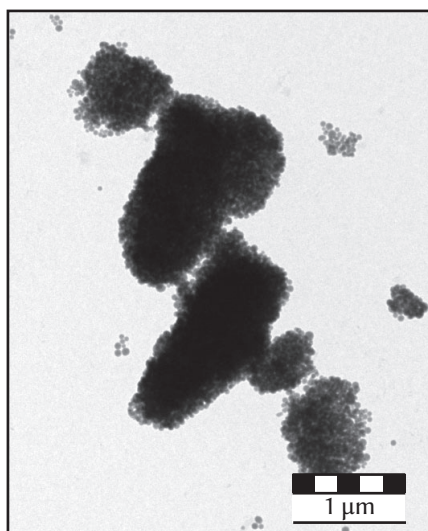
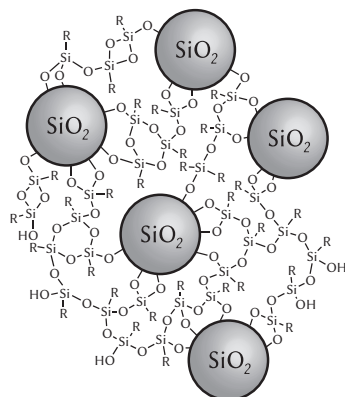
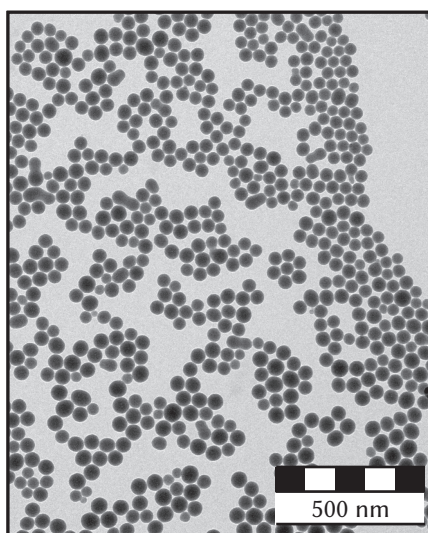
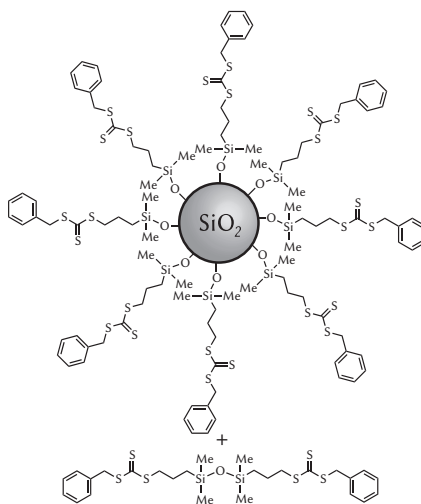
(a) TE micrograph of nPP^3-2 (b) schematic structure of nPP^3-2 (c) TE micrograph of nPP^1-3 (d) schematic structure of nPP^1-3

Fig. 7.5: Functionalization of silica nanoparticles SiO_2 with RAFT agents carrying different anchor groups; nPP^3-2 : functionalized with RAFT agent ρ^3-1 agent with a trimethoxysilyl anchor group (exact structure in 5.12, Section 5.2); nPP^1-3 : functionalized with RAFT agent ρ^1-3 with a monomethoxysilyl anchor group.

solvents, the silica particles were individually distributed on the TEM grids. The order found for the suitability of the examined solvents was: water > methanol > 1,2-dimethoxyethane > acetone > THF > dichloromethane > toluene. Since water and methanol are not suited as solvents for the immobilization reaction, because they react with the anchor group themselves, the next best solvent 1,2-dimethoxyethane was chosen. 1,2-Dimethoxyethane had already been successfully used in a similar study with a RAFT agent bearing a triethoxysilane anchor group.^[16] Apart from the different solvent, the immobilization could be carried as for the RAFT agent $\rho^{2x}-2$ in Section 7.1.2. The work-up must then be performed by repeated centrifugation and redispersion, since the isolated silica nanoparticles $\rho^{2x}-2$ are too small to be subjected to Soxhlet extraction or filtration.

Also the requirements for a suitable RAFT agent are different. While for the fumed silica the brute approach of just forming as many bonds as possible was apt, the nanoparticles $\text{SiO}_2^{\text{np}}\nu-2$ need to be treated with more tact and sensitivity. It must be made sure that they remain individually dispersed in the colloid and crosslinking processes must be prevented, which are not only caused by grafting of a RAFT agent with two anchor groups (for example $\rho^{2x}-2$) to two different particles. Crosslinking already occurs through the trifunctional nature of the common trimethoxysilyl anchor group. These anchor groups also undergo self-condensation to possibly three-dimensional aggregates, which then interconnect the nanoparticles.^[17] To discover whether this effect posed a problem for the functionalization of $\text{SiO}_2^{\text{np}}\nu-2$, the trimethoxysilyl RAFT agent ρ^3-1 (see Figure 5.12, Section 5.2 for the structural formula) was first used for the functionalization.

The TEM analysis of the resulting material $\text{SiO}_2^{\text{np}}\rho^3-2$ revealed large aggregates of nanoparticles. One representative micrograph is shown in Figure 7.5a. Figure 7.5b shows the hypothetical crosslinking structures in these aggregates. It can be noted at this point that the analogous effect was also found when it was attempted to immobilize the RAFT agent ρ^3-1 on the surface of the 4-mercaptophenol-protected gold nanoclusters $\text{Au}^{\text{lbs}}\nu^{\text{OH}}-6$ and the 11-mercaptopundecanol-coated AuNPs $\text{Au}^{\text{2ebs}}\nu^{\text{OH}}-9$. As a matter of fact, a solution of ρ^3-1 readily flocculated upon contact with water, indicative of the formation of large crosslinked aggregates with visible dimensions.

This crosslinking reaction can be avoided by using a RAFT agent carrying a monomethoxysilyl group, which is only able to form a single covalent bond by condensation. Of course, self-condensation can still occur, but the formed dimers cannot form any more bonds to the silica surface and are easily removed during the work-up of the immobilization. In principle, one could also first immobilize molecules with a monofunctional silylether moiety and another functional group on the surface, to which the RAFT agent is coupled in a second step.^[18,19] But carrying out two surface-immobilization reactions in a row entails more experimental effort

and inherently reduces the final loading. It is advantageous to directly start with a RAFT agent containing the monofunctional anchor group—an approach, which had been already done with ATRP,^[20–22] NMP,^[23] and the RAFT R-approach,^[24] but, to the best of the author's knowledge, not with the RAFT Z-approach.

In Section 5.2.2, the synthesis of RAFT agent ρ^1-3 with a monomethoxysilyl anchor group (see Scheme 5.3) was already presented. This RAFT agent was now immobilized on the surface of SiO_2 $\nu-2$ as described above. A large excess of ρ^1-3 could be used without any problems and is even advisable. After complete coverage of the surface, just more dimers are formed, which are then removed.

Figure 7.5c shows a TE micrograph of the silica particles SiP^1-3 functionalized with ρ^1-3 . It was seen that this time, the nanoparticles were well separated from each other and no crosslinking had occurred. The modification of the anchor group had been a success. The adjacent image in Figure 7.5d shows the schematic structure of SiP^1-3 and the corresponding dimer.

In order to determine the grafting density of the RAFT agent, sample SiP^1-3 was analyzed by elemental analysis. A sulfur mass fraction of $\omega_S = 0.2 \times 10^{-2}$ was detected. From this, the molecule density β_S on the surface can be calculated from the mass of sulfur per molecule M_S and the specific surface S_m from TEM (see Equation (4.13) and Table 4.1) by

$$\beta_S = \frac{\omega_S}{M_S S_m} \stackrel{\text{here}}{=} 0.4 \mu\text{mol m}^{-2}. \quad (7.2)$$

This value was significantly lower than when the same RAFT agent was immobilized on silica nanoparticles of lower sizes (not shown). A reason might be the steric hindrance accompanying the lower surface curvature or just the increasing inaccuracy of the elemental analysis. The density of silanol groups—the theoretical upper limit—is about $\rho_{\text{SiO}_2} = 8 \mu\text{mol m}^{-2}$.^[25,26]

7.2.3 Surface polymerization

The functionalized silica particles ρ^1-3 were employed in the radical RAFT polymerization SiP^1-2 of *n*-butyl acrylate (BA, see the structural formula in Figure 5.11, Section 5.4) with AIBN as the initiator. In preliminary polymerizations of BA in the presence of the free RAFT agent ρ^1-3 , a good control had been achieved. The polymerization was performed in solution of 1,2-dimethoxyethane to keep the particles finely dispersed. Thanks to its monofunctional anchor group, ρ^1-3 could be added as sacrificial RAFT agent without the risk that it could crosslink the nanoparticles through previously unreacted silanol groups.

Tab. 7.2: Polymerization data for $\text{np}_{\text{si}}\mathbf{k}^1\text{-2}$. The conversions $X_{\text{M,g}}$ were determined by gravimetry (Equation (5.9)) and the mass fractions of polymer ω_{p} by thermogravimetric analysis. The \overline{M}_{n} and \mathcal{D} values were obtained by SEC analysis (THF, RI detector).

number	$\text{np}_{\text{si}}\mathbf{k}^1\text{-2}$	T	60 °C
solvent	DMF	$n_{\text{M}}/n_{\text{S}}$	1/3
monomer	BA	c_{M}	1.74 mol L ⁻¹
RAFT agent	$\text{np}_{\text{si}}\mathbf{P}^1\text{-3}$ (+ $\mathbf{p}^1\text{-3}$)	c_{RAFT}	225 mg L ⁻¹ (+ 10 mmol L ⁻¹)
initiator	AIBN	c_{ini}	5.0×10^{-3} mol L ⁻¹

$\text{np}_{\text{si}}\mathbf{k}^1\text{-2}$	t in h	$X_{\text{M,g}}$	ω_{p}	in solution		on surface	
				\overline{M}_{n} in $\frac{\text{g}}{\text{mol}}$	\mathcal{D}	\overline{M}_{n} in $\frac{\text{g}}{\text{mol}}$	\mathcal{D}
a	0.5	0.16	0.11	1.45×10^4	1.38	–	–
b	1.0	0.27	–	2.78×10^4	1.31	2.01×10^4	1.24
c	2.0	0.44	–	3.72×10^4	1.32	3.57×10^4	1.22
d	4.0	0.68	0.20	5.43×10^4	1.35	–	–
e	7.0	0.84	–	6.17×10^4	1.38	5.92×10^4	1.39

Although the specific surface S_{m} of $\text{np}_{\text{SiO}_2}\mathbf{v}\text{-2}$ is about 10 times lower than that of the fumed silica $\text{fs}_{\text{SiO}_2}\mathbf{v}\text{-1}$ (significantly higher particle size compared with the primary particles of the fumed silica), the concentration of surface-bound RAFT agent molecules was effectively higher than in polymerization $\text{fs}_{\text{SiO}_2}\mathbf{k}^{2\times}\text{-1}$, owing to the higher RAFT grafting density and the higher particle concentration in polymerization $\text{np}_{\text{si}}\mathbf{k}^1\text{-2}$.

As described in Section 7.1.3, several samples were taken and the conversion was determined gravimetrically by Equation (5.9).

7.2.4 Analysis of the produced nanocomposites

The produced nanohybrids were isolated from the formed polymer in solution by repeated centrifugation and redispersion and analyzed via SEC and TGA as described for samples $\text{fs}_{\text{SiO}_2}\mathbf{k}^{2\times}\text{-1}$. There was only sufficient material to do either TGA ($\text{np}_{\text{si}}\mathbf{k}^1\text{-2a}$ and **d**) or SEC ($\text{np}_{\text{si}}\mathbf{k}^1\text{-2b}$, **c**, and **e**) analysis of the surface-bound polymer. In Table 7.2, all details and results from polymerization $\text{fs}_{\text{SiO}_2}\mathbf{k}^{2\times}\text{-1}$ are listed. Surveying the SEC results from the surface polymer and the solution polymer, it is notable that both possess very similar characteristics, indicative of a frequent exchange between

surface and solution. As opposed to polymerization $^{fs}_{si}\kappa^{2x}-1$, the growth of the radical chains does not proceed in two separate domains, as the radicals can leave the surface here and are then replaced by a radical chain derived from the solution RAFT agent. The slightly higher \overline{M}_n and values in solution are presumably due to the partial dimerization of the sacrificial RAFT agent. The polymer chains on the surface cannot form dimers and are therefore more evenly sized. Secondly, no decrease of the molar masses was observed here and the molar masses grow linearly with the conversion, demonstrating the very high control in the system, which is not only invoked by the presence of the sacrificial solution RAFT agent, but also by the very homogeneously curved surface of the silica particles. All positions are equally exposed and are through the high curvature generally more accessible for incoming radicals from solution. The growing molar masses are in line with the increasing mass fraction of the polymer ω_p in the composites, determined by TGA.

The polymer-functionalized silica nanoparticles $^{fs}_{si}\kappa^{2x}-1$ still formed a stable, semitransparent colloid in organic solvents and the TEM analysis still revealed isolated particles. The equipment of a RAFT agent with a monomethoxysilyl anchor group provided an advanced pathway to silica–polymer core–shell nanocomposites—a material with an imposing homogeneity on the mesoscopic scale. Thanks to the inherent characteristics of the Z-approach, only living chains remain tethered to the surface and constitute the polymer shells.

The polymerizations presented in this chapter illustrate very well how in the already well explored field of surface RAFT polymerizations, still great improvements can be achieved, when the array of solid-supported RAFT agents is expanded by introducing specific modifications in the structure of the anchor RAFT agents, in order to meet the special demands imposed by the type of the solid substrate or the targeted application.

References for Chapter 7

- (1) Rahman, I. A., Padavettan, V., *J. Nanomat.* **2012**, 2012, 15.
- (2) Zou, H., Wu, S., Shen, J., *Chem. Rev.* **2008**, 108 (9), 3893–3957.
- (3) Radhakrishnan, B., Ranjan, R., Brittain, W., *Soft Matter* **2006**, 2 (5), 386–396.
- (4) Pandey, Y. N., Papakonstantopoulos, G. J., Doxastakis, M., *Macromolecules* **2013**, 46 (13), 5097–5106.
- (5) Yu, T., Greish, K., McGill, L. D., Ray, A., Ghandehari, H., *ACS Nano* **2012**, 6 (3), 2289–2301.
- (6) Napierska, D., Thomassen, L. C. J., Lison, D., Martens, J. A., Hoet, P. H., *Part. Fibre Toxicol.* **2010**, 7.
- (7) Osterholtz, F., Pohl, E., *J. Adhes. Sci. Tech.* **1992**, 6 (1), 127–149.
- (8) Arkles, B., *Chem. Tech.* **1977**, 7 (12), 766–778.
- (9) Arkles, B., *Chem. Tech.* **1999**, 29 (12), 7–14.
- (10) Pesek, J., Matyska, M., *Interface Sci.* **1997**, 5 (2-3), 103–117.
- (11) Nguyen, D. H. *RAFT-Polymerisation an Oberflächen*, Ph.D. thesis, Georg-August-Universität Göttingen, **2007**.
- (12) Stöber, W., Fink, A., Bohn, E., *J. Colloid Interface Sci.* **1968**, 26 (1), 62–69.
- (13) Bogush, G., Tracy, M. A., Zukowski IV, C. F., *J. Non-Cryst. Solids* **1988**, 104, 95–106.
- (14) Sadasivan, S., Dubey, A., Li, Y., Rasmussen, D., *English J. Sol-Gel Sci. Technol.* **1998**, 12 (1), 5–14.
- (15) Szekeres, M., Tóth, J., Dékány, I., *Langmuir* **2002**, 18 (7), 2678–2685.
- (16) Ohno, K., Ma, Y., Huang, Y., Mori, C., Yahata, Y., Tsujii, Y., Maschmeyer, T., Moraes, J., Perrier, S., *Macromolecules* **2011**, 44 (22), 8944–8953.
- (17) Fadeev, A. Y., McCarthy, T. J., *Langmuir* **2000**, 16 (18), 7268–7274.
- (18) Huang, X., Appelhans, D., Formanek, P., Simon, F., Voit, B., *Macromolecules* **2011**, 44 (21), 8351–8360.
- (19) Perruchot, C., Khan, M. A., Kamitsi, A., Armes, S. P., Werne, T. von, Patten, T. E., *Langmuir* **2001**, 17 (15), 4479–4481.
- (20) Carrot, G., Diamanti, S., Manuszak, M., Charleux, B., Vairon, J.-P., *J. Polym. Sci., Part A: Polym. Chem.* **2001**, 39 (24), 4294–4301.
- (21) Tsujii, Y., Ejaz, M., Sato, K., Goto, A., Fukuda, T., *Macromolecules* **2001**, 34 (26), 8872–8878.
- (22) Audouin, F., Blas, H., Pasetto, P., Beaunier, P., Boissière, C., Sanchez, C., Save, M., Charleux, B., *Macromol. Rapid Commun.* **2008**, 29 (11), 914–921.
- (23) Blas, H., Save, M., Boissière, C., Sanchez, C., Charleux, B., *Macromolecules* **2011**, 44 (8), 2577–2588.
- (24) Li, C., Benicewicz, B. C., *Macromolecules* **2005**, 38 (14), 5929–5936.
- (25) Calderon, E., Gauthier, M., Decremps, F., Hamel, G., Syfosse, G., Polian, A., *J. Phys. Condens. Matter* **2007**, 19 (43), 436228.
- (26) Zhuravlev, L. T., *Langmuir* **1987**, 3 (3), 316–318.

Chapter 8

Nanohybrids of gold particles

The design and the characterization of the substrate components for this chapter, gold nanocrystals from the *ex-situ* two-phase Brust–Schiffrin synthesis and from reduction with citrate ions $\text{Au}^{\text{ci}}\text{v}-3$, were described in Section 5.1. In the following, it will be outlined how these AuNPs can be functionalized with non-polymeric ligands of different types for stabilization and introduction of functional groups, especially hydroxyl and azido moieties, to which RAFT agents with complementary functionalities could then be coupled, and how they can be coated with the NIPAm RAFT polymers prepared in Section 5.4. Hereby, the binding motifs of ligands bearing trithiocarbonate groups will be the particular focus.

8.1 Different ligands on AuNPs

8.1.1 Functionalization of Brust–Schiffrin gold nanocrystals

AuNPs prepared by the *ex-situ* two-phase Brust–Schiffrin method were presented and their ligand-independent properties were characterized in Section 5.1.3.3 (also see Table 5.2, Section 5.1.5). These nanocrystals are very well suited for functionalization reactions for three major reasons:

- The weakly bound tetraoctylammonium bromide is readily replaced by all ligands that form stronger bonds to the gold surface.
- The sodium borohydride can be completely washed off prior to the addition of the ligand, so that even very reduction-sensitive molecules can be used.
- The arising particle size and shape characteristics are independent of the employed ligand, enabling comparative experiments with different functionalization agents.

In the following, the functionalization reaction with different types of ligands will be discussed. For the reactions, the steps shown in Scheme 5.1 (Section 5.1.3.3) were followed.

8.1.1.1 Functionalization of Brust–Schiffrin AuNPs with 11-mercaptoundecanol

AuNPs $^{2\text{ebs}}_{\text{Au}}\mathbf{V}^{\text{OH}}\text{-9}$ having hydroxyl moieties on their outer surface could be prepared by functionalization with 11-mercaptoundecanol $^{\text{SH}}\lambda^{\text{OH}}\text{-7}$ (chemical structure in Figure 8.5). After the addition of a great excess of $^{\text{SH}}\lambda^{\text{OH}}\text{-7}$, which was carried out under sonication, the AuNPs immediately precipitated from the dispersion in toluene, showing that the ligands were replaced almost instantaneously. The functionalized AuNPs were collected, washed with copious amounts of toluene on a glass frit, and redispersed in DMF. Although the masses of $^{2\text{ebs}}_{\text{Au}}\mathbf{V}^{\text{OH}}\text{-9}$ were not high enough to spin them down with the accessible equipment, centrifugation is a good way to remove potentially formed larger agglomerates with a diameter of more than about 8 nm. In this case, no sedimentation was found after 3 h of centrifugation at 8 603 g, thus proving the absence of aggregates.

Results from the characterization of $^{2\text{ebs}}_{\text{Au}}\mathbf{V}^{\text{OH}}\text{-9}$ were already shown in Section 5.1. See the photograph in Figure 5.2, the size and shape parameters in Table 5.1, the diameter histogram in Figure 5.5, the optical spectrum in Figure 5.8, and the TE micrograph in Figure 5.10. Notably, it had not been possible to produce 11-mercaptoundecanol-functionalized AuNPs by the *in-situ* two-phase Brust–Schiffrin method (see Section 5.1.3.1). Given the fact that the product is stable here, one can only assume that the functional groups exert an interfering effect in the reduction step, even if they are not reduced themselves. In any case, this makes the *ex-situ* protocol extra-valuable. In addition to the 4-mercaptophenol-coated gold nanoclusters $^{1\text{bs}}_{\text{Au}}\mathbf{V}^{\text{OH}}\text{-7}$ from Section 5.1.3.2, now a second type of hydroxyl-functionalized AuNPs, but with approximately ten times higher masses, can be presented here.

Against all expectations, the black precipitate $^{2\text{ebs}}_{\text{Au}}\mathbf{V}^{\text{N}_3}\text{-10}$ could not be redispersed in any solvent, when the 1-azidothiol $^{\text{SH}}\lambda^{\text{N}_3}\text{-9}$ from Section 5.3 was used in an identical reaction. The only reasonable explanations for this finding are that the ligand in some way leads to the irreversible aggregation of the AuNPs, or that the produced material is just insoluble in all common laboratory solvents. In view of the fact that sample $^{2\text{ebs}}_{\text{Au}}\mathbf{V}^{\text{OH}}\text{-9}$ could only be dispersed colloiddally in DMF, the latter explanation seems possible. The solubility problem could potentially be overcome by using a mixture of $^{\text{SH}}\lambda^{\text{N}_3}\text{-9}$ and another ligand or by artificially reducing the surface density with an excess of AuNPs, which is known to lead to a higher entropy-induced solubility.^[1]

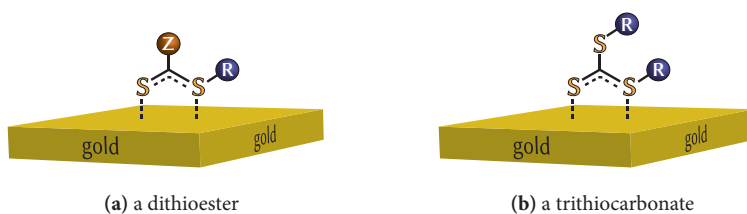


Fig. 8.1: Binding of typical RAFT groups on gold surfaces. The binding modes were elucidated by X-ray photoelectron spectroscopy.^[2,3]

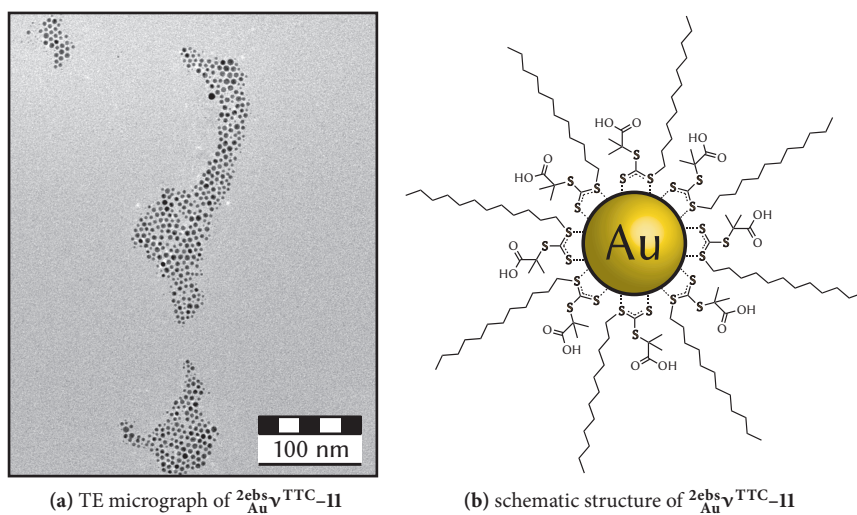


Fig. 8.2: Ex-situ Brust–Schiffrin AuNPs $2^{\text{ebs}}_{\text{Au}} \text{v}^{\text{TTC-II}}$ coated with the trithiocarbonate RAFT agent $\rho\text{-4}$. The TEM image was measured 4 months after performing the experiment. The absence of aggregation shows the high colloidal stability of the particles. No objective aperture had been inserted when taking the micrograph, so that reflections caused by the polycrystallinity of the AuNPs are visible.

8.1.1.2 Coating of Brust–Schiffrin AuNPs by a trithiocarbonate RAFT agent

Although the trithiocarbonate moiety has not received much attention as an anchor to gold surfaces yet, it is well known that this functional group, as well as other sulfur-containing mediating groups in RAFT polymerization, does form stable bonds with gold^[4] with a maximum grafting density comparable to the one which can be obtained with thiols.^[3] X-ray photoelectron spectroscopy indicates a binding motif comprising of two S ··· Au bonds as shown in the schematics in Figure 8.1a for a dithioester and in Figure 8.1b for a trithiocarbonate.^[2,3,5] Dithiocarbamates adsorb on gold in a similar way^[6] and can be used in the synthesis of gold nanoparticles as well.^[7] Furthermore, a crystal structure of a trithiocarbonate–gold(I) complex has been reported.^[8,9]

The mild conditions in the *ex-situ* two-phase Brust–Schiffrin synthesis made it possible to successfully use the trithiocarbonate **p-4** (chemical structure in Figure 5.12, Section 5.2) as AuNP ligand. This commercial RAFT agent had also been used for NIPAm polymerizations in Section 5.4.1. Stable AuNPs $^{2\text{ebs}}_{\text{Au}}\mathbf{v}^{\text{TTC}}\mathbf{-11}$ were obtained that could be stored in dry form for months and still be redispersed in nonpolar organic solvents (toluene, chloroform, not acetone, methanol, or dioxane). The solubility is imparted by the long hydrocarbon chain of **p-4**. The signals in the ¹H-NMR spectrum measured in deuterated chloroform were weak, but signals corresponding to the methyl groups on one side and the C₁₂ chain on the other side of the trithiocarbonate group could be identified, proving its intactness.

Figure 8.2a shows a TE micrograph of $^{2\text{ebs}}_{\text{Au}}\mathbf{v}^{\text{TTC}}\mathbf{-11}$ measured 4 months after the functionalization experiment and Figure 8.2b shows the schematic structure, with the binding mode that involves less steric hindrance, according to Figure 8.1b. The extreme stability of $^{2\text{ebs}}_{\text{Au}}\mathbf{v}^{\text{TTC}}\mathbf{-11}$ demonstrates vividly the high trithiocarbonate–gold binding strength and grafting density.

8.1.1.3 Grafting of multifunctional RAFT agents to Brust–Schiffrin AuNPs

As the last experiment of this series, the polytrithiocarbonate **p^{MB}-8** (chemical structure in Figure 5.12, Section 5.2) was used for the functionalization of the identical *ex-situ* Brust–Schiffrin AuNPs (mass calculated for 1.2 eq. of middle groups per gold atom), giving rise to sample $^{2\text{ebs}}_{\text{Au}}\mathbf{v}^{\text{MB}}\mathbf{-12}$. This multifunctional RAFT agent had been used in Section 5.4.4 for the preparation of NIPAm multiblock polymers.

No solvent was found for the black precipitate $^{2\text{ebs}}_{\text{Au}}\mathbf{v}^{\text{MB}}\mathbf{-12}$. It only formed a very fine and almost transparent dispersion. The coarse dispersion apparently contained

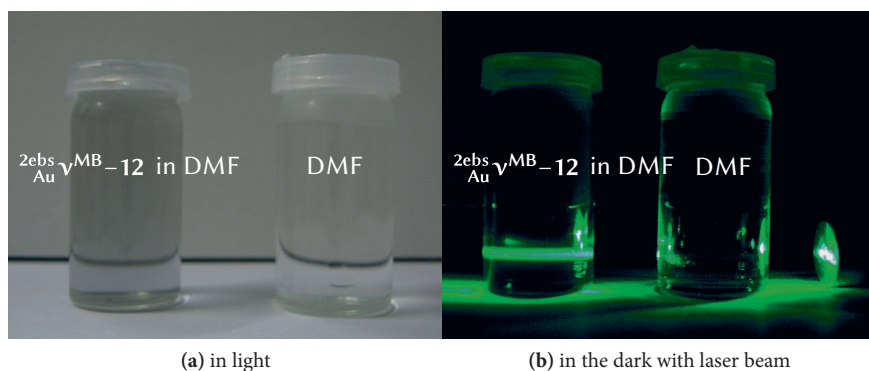


Fig. 8.3: Photographs of AuNPs $2ebs_{Au}^{MB-12}$ coated with polytrithiocarbonate ρ^{MB-8} in solution of DMF. In the dark, the AuNP aggregates can be made visible by Tyndall scattering of the green laser beam.

AuNP aggregates, which were too large to exhibit a localized plasmon resonance effect. In such cases, the particles in the dispersed phase can be made visible by the handy method of Tyndall scattering of a laser beam, demonstrated in Figure 8.3. Photograph 8.3a shows the dispersion of $2ebs_{Au}^{MB-12}$, that only looks marginally darker in comparison to the adjacent vial of pure DMF at light. In photograph 8.3b, taken in the dark, a laser beam passing both vials from right to left is only visible in the left dispersion.

Indeed, TEM analysis of $2ebs_{Au}^{MB-12}$ revealed the presence of large AuNP agglomerates, most likely formed by the interconnection through the multiple trithiocarbonate groups of the employed ligand. One such crosslinked aggregate is shown in micrograph (a) of Figure 8.4. The individual particles are literally glued together in a matrix of ρ^{MB-8} . Although they are kept very close to each other, no real particle fusion is observed as in the case of irreversible AuNP aggregation through the lack of stabilization. A hypothetical schematic drawing of the underlying structure in these superparticles, based on Figure 8.1b, is shown in Figure 8.4b (not drawn to scale).

The finding of these formations constitutes an additional proof for the structure of the multifunctional RAFT agents, as well as for the claim that trithiocarbonate groups firmly attach to gold. Attempts to use these particle networks in radical polymerizations of NIPAm with the goal to extend the interparticle distances in the agglomerates were not successful, although conditions were chosen under which the

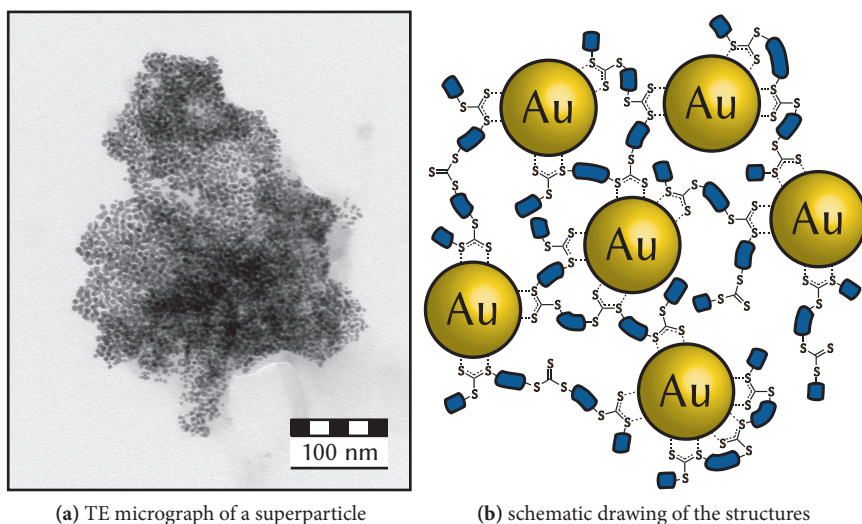


Fig. 8.4: Ex-situ Brust–Schiffrin AuNPs $^{2\text{ebs}}_{\text{Au}}\mathbf{v}^{\text{MB}}\mathbf{-12}$ with the polytrithiocarbonate $\rho^{\text{MB}}\mathbf{-8}$ on the surface. The TEM sample was prepared by drop-casting from DMF. The exact structure of $\rho^{\text{MB}}\mathbf{-8}$ is depicted in Figure 5.12, Section 5.2. The schematic is not drawn to scale.

free RAFT agent $\rho^{\text{MB}}\mathbf{-8}$ did control the radical polymerization (see Section 5.4.4). If this process could be made to work as desired, it would expectedly enable an elegant way to study the RAFT polymerization *in situ* by monitoring the system's color change.

Building on the results from the current section, the studies on the interaction of Brust–Schiffrin AuNPs and multifunctional RAFT agents were continued by Christian Roßner.^[10] He found that controlled structures are formed, when multiblock oligomers were employed in the functionalization.^[11] By the degree of oligomerization, the spatial distances in the produced colloidal superparticles^[12–14] can be fine-tuned.

8.2 Functionalization of citrate-prepared gold nanocrystals

The second, and arguably more important, type of AuNPs on which the focus of this work was directed are those prepared by reduction with citrate ions $_{\text{Au}}^{\text{ci}}\mathbf{v}\mathbf{-3}$ (see

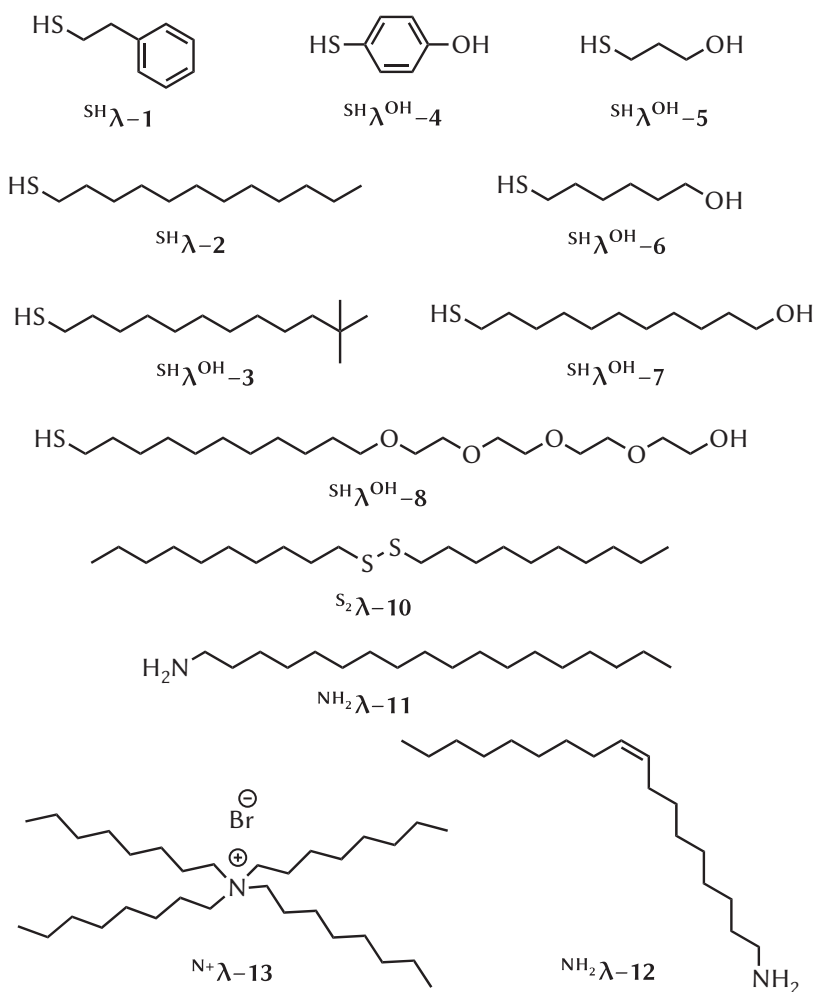
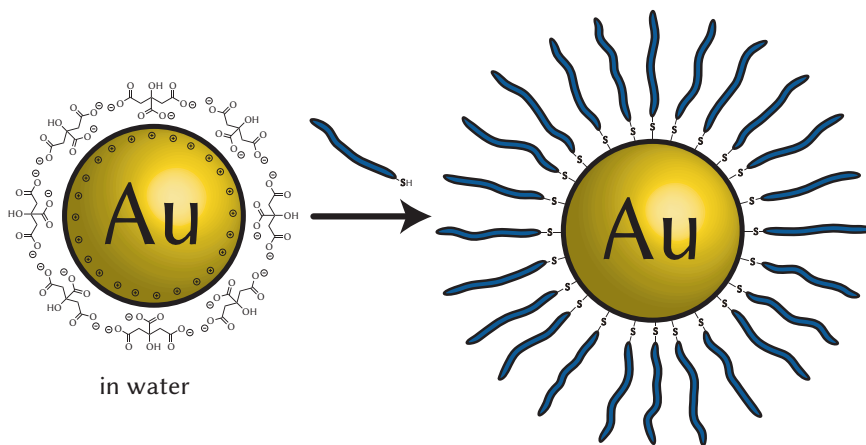


Fig. 8.5: Overview of the structures of all ligands for gold used in the present work (excluding the azidothiol $\text{SH}\lambda^{\text{N}_3}-9$, which was already shown in Scheme 5.5).



Scheme 8.1: General process of the functionalization of citrate-prepared AuNPs $\text{Au}^{\text{ci}}\text{v-3}$ with alkylthiols.

Section 5.1.2). Their extreme lability (electrostatic stabilization) and the restriction of the solvent to water greatly limit their usefulness without any form of surface functionalization.

8.2.1 Non-polymeric ligands onto citrate-prepared AuNPs

In addition to the introduction of functional groups, the coating of the citrate AuNPs $\text{Au}^{\text{ci}}\text{v-3}$ should impart stabilization (see Section 5.1.1) and the possibility to transfer the AuNPs to a solvent other than water. Here, it will be explored to which extent non-polymeric ligands are capable of performing this task.

In Scheme 8.1, the general process that has to be realized is illustrated. Various attempts to implement the functionalization using the thiols $^{\text{SH}}\lambda\text{-1}$, $^{\text{SH}}\lambda\text{-2}$, $^{\text{SH}}\lambda\text{-3}$, $^{\text{SH}}\lambda^{\text{OH}}\text{-4}$, $^{\text{SH}}\lambda^{\text{OH}}\text{-5}$, $^{\text{SH}}\lambda^{\text{OH}}\text{-6}$, $^{\text{SH}}\lambda^{\text{OH}}\text{-7}$ (Figure 8.5), the trithiocarbonate RAFT agent $\rho\text{-4}$ (Figure 5.12) and especially the azidothiol $^{\text{SH}}\lambda^{\text{N}_3}\text{-9}$ (Scheme 5.5) were made in the work for this thesis. Because most of the listed ligands are not water-soluble, different strategies were tried to get them into contact with $\text{Au}^{\text{ci}}\text{v-3}$, the most straightforward one being their addition in solvent which is miscible with water. These functionalization experiments are only described very briefly without going into too much detail here, since, after all, they did not lead to the desired results.

Considering literature reports for this conversion of citrate AuNPs, they appear to belong to a very self-contradictory field. There are a few examples of a successful transformation, but many of these cases, the actual performed procedure is only mentioned in dissatisfying one-liners.^[15–19] At the same time, there are publications which exclusively focus on ways to implement this seemingly very delicate functionalization, for example by using a charged thiol to form a stable intermediate in a two-step method^[20] or by using multidentate thiols^[1] or certain additives.^[21,22] In many cases, the reaction is performed in water with a soluble thiol and the metastable particles are used directly for the next experiment without removing the excess of restant ligands.^[23–27]

For the studies envisaged in this work, it is a necessary prerequisite to be able to isolate the protected AuNPs by centrifugation and redisperse them in organic solvents, which could not be achieved with any of the above listed ligands. As an additionally aggravating factor in this kind of experiments, it is principally difficult to distinguish from TEM images whether kinetic aggregation involving fusion of gold cores through ligand-induced charge equalization has taken place or fully coated nanoparticles have precipitated, which just lack the solubility required for redispersion.

It was especially focused on a one-step transformation method from Baranov and Kadnikova^[28] (2011), with which they functionalized citrate AuNPs with the same water-insoluble azidothiol $^{SH}\lambda^{N_3}$ -**9** as was prepared in this work (see Section 5.3). They reported that the addition of the thiol in a very small amount of DMF under sonication leads to the formation of thiol-coated nanoparticles that could be redispersed in a variety of organic solvents. They proposed that the sonication causes a fine dispersion (analogous to an oil-in-water microemulsion) of the thiol which is beneficial for the reaction, because the microdroplets possess a very large surface and contain the azidothiol in the highest possible concentration. Despite numerous attempts to reproduce this reaction under absolute identical conditions and with the kind support and help of D. Baranov, only non-redispersible particles were obtained every time.

8.2.1.1 Using octadecylamine-coated AuNPs as intermediates for the functionalization of citrate AuNPs

It was also tried to use the octadecylamine-coated AuNPs $_{Au}^{ci}v^{oda}$ -**4** (Section 5.1.2.3) as reactive intermediates. This seemed reasonable since the amine ligands are only very loosely bound and the AuNPs have likely already overcome the most critical step, that is the coating of their surface with any ligand, which then just has to be replaced. Unsuccessful experiments were carried out, where a large excess of

different ligands was added to ${}^{\text{ci}}\text{AuV}^{\text{oda}}\text{-4}$ under various conditions. In light of the fact that thiols first associate weakly to gold while retaining their proton and form the strong thiolate bond only after the proton is lost in the second step,^[29,30] it was also attempted to aid the process by carrying out the functionalization reactions with thiols in the presence of the oxidizing agent 2,3-dichloro-5,6-dicyano-1,4-benzoquinone or, as an alternative, the Dess-Martin periodinane.^[31] This was not successful either, nor was the tentative employment of disulfide $\text{S}_2\lambda\text{-10}$, which does not need to be oxidized (see Section 5.3).

However, there were two clear indications that a replacement reaction on the surface occurred when a ligand was added. The first obvious one was the immediate aggregation in many functionalization attempts. The second one was that in some cases, where the red color of the solution did not vanish at once, the colloid was more stable towards the addition of hydrochloric acid compared with the situation prior to adding the ligand. On the other hand, the octadecylamine-coated nanoparticles themselves could be centrifuged down and redispersed before the functionalization, as opposed to the products of all functionalization attempts with the listed ligands.

As a conclusion drawn from all these experiments, one could likely state that the citrate AuNPs ${}^{\text{ci}}\text{AuV}\text{-3}$ are composed of so many gold atoms that the examined ligands are incapable of holding them in colloidal solution through the energy gain from the interaction with solvent molecules and the entropy gain, when they can assume more conformations. For the smaller ligands in Figure 8.5, that is surely the case. That assumption is in line with the finding that even for the 70 times smaller Brust–Schiffrin AuNPs, the particles ${}^{\text{2ebs}}\text{AuV}^{\text{OH}}\text{-9}$ stabilized with 11-mercaptoundecanol were only soluble in DMF.

A factor that was not considered during the experiments, but might be the cause for the colloidal stability for systems reported in some publications (and for the octadecylamine-coated nanoparticles ${}^{\text{ci}}\text{AuV}^{\text{oda}}\text{-4}$), is the charge state of the nanoparticles. This aspect could potentially be elucidated by performing zeta potential measurements.

The problem with the studied ligands might be that their grafting density is too high, which leads to lower solubility as well, since the interactions with the solvent are lowered and the possible ligand conformations are reduced.^[32] That is the reason why nanoparticles with trithiol ligands, which occupy more space on the surface, have a higher colloidal solubility.^[1] As it is hardly possible to determine the grafting density of a system where aggregation has occurred in the presence of an excess of the ligand, this factor could not be taken into account in comparison with other literature studies. In any case, it appears to be clearly advantageous to employ water-soluble ligands for the functionalization process, if only to assure a maximum of AuNP–ligand contacts and to avoid a ligand mixture on the AuNP surface.

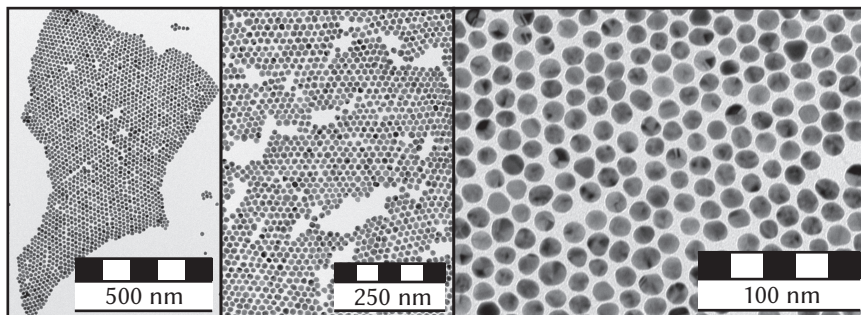


Fig. 8.6: TE micrographs of AuNPs $\text{Au}^{\text{ci}}\text{v}^{\text{OH}}\text{-13}$ with water-soluble long-chain thiol $\text{SH}\lambda^{\text{OH}}\text{-8}$ on the surface.

8.2.1.2 Functionalization of citrate AuNPs with (11-mercaptoundecyl)tetra(ethylene glycol)

Based on the above considerations, an ideally designed ligand for the functionalization of citrate AuNPs $\text{Au}^{\text{ci}}\text{v-3}$ should comprise a thiol group for binding to gold, a very long flexible chain for stabilization and induction of solubility, and it should be soluble in water, so that it can be directly added to the particle sol. It should also carry a functional group as attachment point for further coupling reactions.

(11-Mercaptoundecyl)tetra(ethylene glycol) $\text{SH}\lambda^{\text{OH}}\text{-8}$ (see Figure 8.5) meets all four requirements. And indeed, after adding this thiol in an excess to $\text{Au}^{\text{ci}}\text{v-3}$, the obtained product $\text{Au}^{\text{ci}}\text{v}^{\text{OH}}\text{-13}$ could be centrifuged down, thus purifying it from the excess of ligand molecules, and thereafter be redispersed in a range of solvents. Figure 8.6 shows three TE micrographs with different magnifications of the very homogeneous particles, which assemble into hexagonal lattices with distinct inter-particle spacings as had been observed before (see Section 4.1.3). Absolutely no aggregation could be found.

A drawback of the employment of $\text{SH}\lambda^{\text{OH}}\text{-8}$ as a ligand is that this compound is very expensive. But it should be possible to synthesize it in house from low-priced educts, using a three-step reaction according to a procedure by Canaria *et al.*^[33] (2005) with tetra(ethylene glycol) instead of tri(ethylene glycol) or a strategy by Balinski^[34] (2010). One could also envision the synthesis of an azide equivalent.

The success of the functionalization with $\text{SH}\lambda^{\text{OH}}\text{-8}$ underlines the above-made assumptions that all other examined ligands are just not capable of stabilizing AuNPs of these comparably “large” sizes. Nevertheless, the goal of producing pure, hydroxyl-functionalized AuNPs from $\text{Au}^{\text{ci}}\text{v-3}$ could eventually be achieved. To-

Tab. 8.1: Observations by TEM after functionalization of citrate AuNPs $\text{Au}^{\text{ci}}\text{v}-3$ with different polymers without sulfur-containing groups. The masses of the employed polymer samples were: $\text{Au}^{\text{K}^x}-3$: $\overline{M}_w \approx 3 \times 10^6 \text{ g mol}^{-1}$, $\text{Au}^{\text{K}^x}-4$: $\overline{M}_w \approx 10^5 \text{ g mol}^{-1}$, $\text{Au}^{\text{K}^x}-5$: $M = 570\text{--}630 \text{ g mol}^{-1}$, $\text{Au}^{\text{K}^x}-6$: $\overline{M}_n = 4.0 \times 10^4 \text{ g mol}^{-1}$, $\text{Au}^{\text{K}^x}-7$: $M = 1223 \text{ g mol}^{-1}$, $\text{Au}^{\text{K}^x}-8$: $\overline{M}_n = 5.5 \times 10^4 \text{ g mol}^{-1}$, and $\text{Au}^{\text{K}^x}-9$: $\overline{M}_n = 7.3 \times 10^4 \text{ g mol}^{-1}$.

sample	polymer	after transfer	after 1 month
$\text{Au}^{\text{K}^x}-3$	poly(acrylic acid)	aggregation	–
$\text{Au}^{\text{K}^x}-4$	poly(methacrylic acid)	aggregation	–
$\text{Au}^{\text{K}^x}-5$	poly(ethylene glycol)	aggregation	–
$\text{Au}^{\text{K}^x}-6$	polyvinylpyrrolidone	random distribution	random distribution
$\text{Au}^{\text{K}^x}-7$	polysorbate 20	chainlike structures	chainlike structures
$\text{Au}^{\text{K}^x}-8$	$\pi^x-1\text{c}'$	random distribution	aggregation
$\text{Au}^{\text{K}^x}-9$	$\pi^x-2\text{d}'$	random distribution	aggregation

gether with $\text{Au}^{\text{1bs}}\text{v}^{\text{OH}}-6$ (Section 5.1.3.2) and $\text{Au}^{\text{2ebs}}\text{v}^{\text{OH}}-9$ (Section 8.1.1.1), the nanoparticles $\text{Au}^{\text{ci}}\text{v}^{\text{OH}}-13$ constitute the third representative of this potential component for novel nanostructures in yet another size regime.

8.3 Grafting of polymers to citrate AuNPs

Given the results from the previous section, where successful stabilization of citrate AuNPs $\text{Au}^{\text{ci}}\text{v}-3$ could only be achieved with the longest ligand (see also Section 5.1.1), polymers for the encapsulation and stabilization of AuNPs are the natural and logical next step to induce a maximum of stabilization.^[35] They are indeed ideal candidates, as they are very cheap and can introduce special properties to the nanoparticles, such as thermoresponsivity or just solubility in certain solvents. While citrate AuNPs seem to be toxic,^[36–39] coverage with polymers reduces the nanoparticles' toxicity,^[40,41] enabling medical applications.^[42,43]

Ideally, the polymers are tethered to the AuNP surface via a chemical bond, but first, comparative preliminary experiments were performed using polymers without functional groups that can form links with gold, to be able to assess the importance of the trithiocarbonate group in the later used polymers.

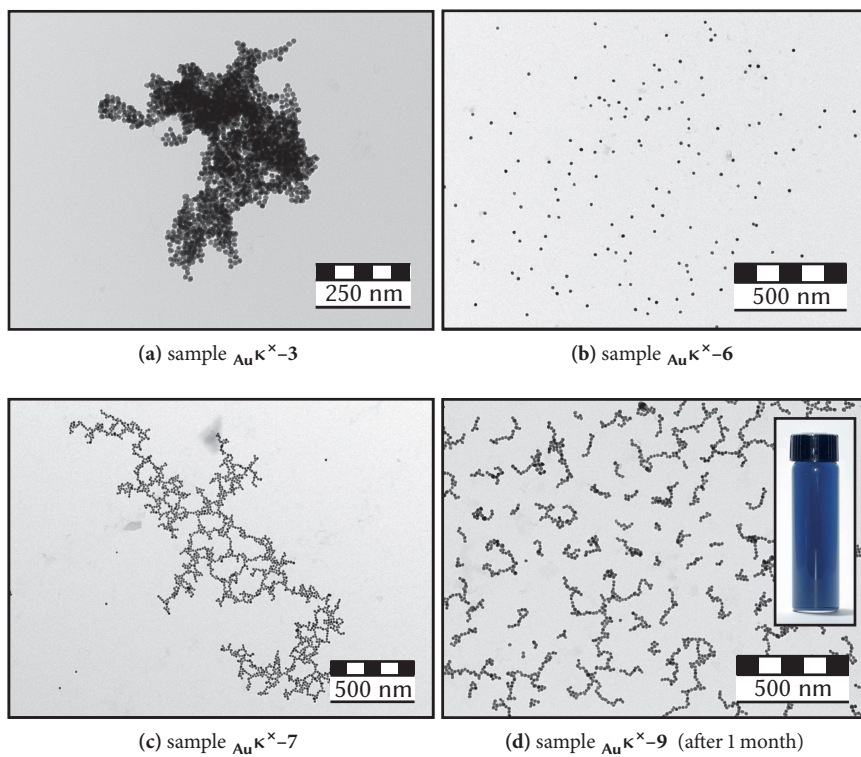


Fig. 8.7: Representative TEM images of citrate AuNPs coated with different polymers without sulfur-containing groups. The inset in c) shows a photograph of the corresponding solution. Sample $\text{Au}\kappa^x\text{-7}$ was drop-cast from DMF.

8.3.1 Grafting of polymers without sulfur to citrate AuNPs

A prerequisite for the surveyed polymers is that they are water-soluble and can thus be directly added to the gold sol $_{\text{Au}}^{\text{ci}}\mathbf{v}-3$. The nonionic polymers poly(acrylic acid) ($\overline{M}_w = 4.5 \times 10^5 \text{ g mol}^{-1}$), poly(vinylpyrrolidone) ($\overline{M}_n = 4.0 \times 10^4 \text{ g mol}^{-1}$), poly(methacrylic acid) ($\overline{M}_w \approx 10^5 \text{ g mol}^{-1}$), poly(acrylic acid) ($\overline{M}_w \approx 3 \times 10^6 \text{ g mol}^{-1}$), poly(ethylene glycol) ($570\text{--}630 \text{ g mol}^{-1}$), and polysorbate 20 (polyethylene glycol sorbitan monolaurate, 1228 g mol^{-1}) were purchased commercially and used as received. The molar masses in parentheses are the respective supplier indications. It can be assumed that all listed polymers do not carry sulfur-containing functional groups, which can form covalent bonds to gold surfaces, so they are only physisorbed. The last polymer in the list, polysorbate 20 (brand name: TWEEN 20), is a neutral polymeric surfactant, composed of four oligomeric polyethylene glycol chains linked to a central sorbitol unit. It can be seen as a branched variant of the also-used linear poly(ethylene glycol). It was chosen, since it had already been used for temporary AuNP stabilization in the literature.^[44–47] The polymer samples $\pi^x\text{--}1\mathbf{c}'$ and $\pi^x\text{--}2\mathbf{d}'$ had been prepared by removal of the trithiocarbonate group from synthesized RAFT polymers with AIBN (see Section 5.4.5 and Table 5.3). These samples were perfectly suited for a comparative experiment, as they only differ from the original RAFT polymers examined in the next section in the absence of the trithiocarbonate group. Polymers with high molar masses were chosen for the defunctionalization reaction, since those should supposedly exert the highest stabilizing effect.

Experimentally, an aqueous solution of an excess of the polymer sample was added to the gold sol $_{\text{Au}}^{\text{ci}}\mathbf{v}-3$ under sonication. This led in no case to immediate particle aggregation, evidenced by the retained red color of the colloidal solution. The mixture was incubated overnight in the dark and then isolated from the excess polymer and sodium citrate by three centrifugation steps with redispersion in methanol. With the used equipment, it took approximately 8 h for the AuNPs to be completely spun down. The sediments at the bottom of the centrifuge tubes were not completely solid and dry, but rather a very concentrated dispersion, that, however, could be isolated by careful decantation.

In Table 8.1, the sample denominations and the observations made by TEM analysis of the functionalized AuNPs directly after the functionalization process and after one month are listed. Aggregation of AuNPs, shown exemplarily for sample $_{\text{Au}}\mathbf{K}^x-3$ in micrograph (a) of Figure 8.7, went along with the color of the colloidal solution turning blue. For $_{\text{Au}}\mathbf{K}^x-3$, $_{\text{Au}}\mathbf{K}^x-4$, and $_{\text{Au}}\mathbf{K}^x-5$, the color change was already observed after the first centrifugation step. The three respective polymers are not capable of the stabilization of this type of nanoparticles. The other four

samples $\text{AuK}^{\times}-6$, $\text{AuK}^{\times}-7$, $\text{AuK}^{\times}-8$, and $\text{AuK}^{\times}-9$ remained visually unchanged. The analysis via TEM revealed a completely random distribution of AuNPs with arbitrary interparticle spacings.

An exemplary micrograph of sample $\text{AuK}^{\times}-6$ is shown in Figure 8.1b. The stabilization capacity of the respective polymers must presumably be due to different structural properties in comparison to the first three polymers. Polyvinylpyrrolidone and pNIPAm comprise nitrogen atoms, which might play a role. Indeed, for pNIPAm, it was reported that it can form weak bonds to gold over the constitutive amide groups (Au–N and Au–O and unconventional N–H...Au bonds).^[48–50] This interaction is strong enough to stabilize small AuNPs with diameters of 1–5 nm over longer periods of time.^[51] In the case of polysorbate 20, the branched structure might be an important factor. Notably, the AuNPs decorated with these polymers self-arranged into large chain-like aggregates after deposition on the TEM films (see Figure 8.1c)—an opposite effect to the observed formation of lattices. These structures must have been formed in the deposition process, since the colloid was still red.

The AuNPs encapsulated with the defunctionalized pNIPAm samples ($\text{AuK}^{\times}-8$ and $\text{AuK}^{\times}-9$) were not stable over time. A gradual color change to blue was observed. Figure 8.1d shows a micrograph of $\text{AuK}^{\times}-9$ taken after about one month and a photograph of the corresponding blue colloidal solution as inlay. The presence of many short-chain aggregates indicates a step-growth aggregation process. Given the observed gradual agglomeration over time, it can be concluded that the performed purification by centrifugation, which did not adulterate these samples, is very mild.

The above results show that it is possible to weakly stabilize citrate AuNPs $\text{Au}^{\text{ci}}\text{v}-3$ with particular water-soluble polymers without anchor groups. The stabilizing power of pNIPAm—the central polymer of this thesis—was not sufficient.

8.3.2 Grafting of polymers with trithiocarbonate groups to citrate AuNPs

In the following, the untreated RAFT polymers from Section 5.4 will be combined with the citrate AuNPs $\text{Au}^{\text{ci}}\text{v}-3$ in a grafting-to approach, in order to produce (smart) core-shell nanocomposites.^[52] The especially well defined samples selected for this task were already listed in Table 5.3.

RAFT polymers are often used in this context^[53,54] because RAFT groups can easily be reduced to thiols—the most prominent group for linkage to gold surfaces.^[55–59] But this transformation is not even necessary in most cases because the RAFT groups themselves can function as anchors for the AuNPs (see Figure 8.1). This has been demonstrated by the high stability of the trithiocarbonate-coated AuNPs

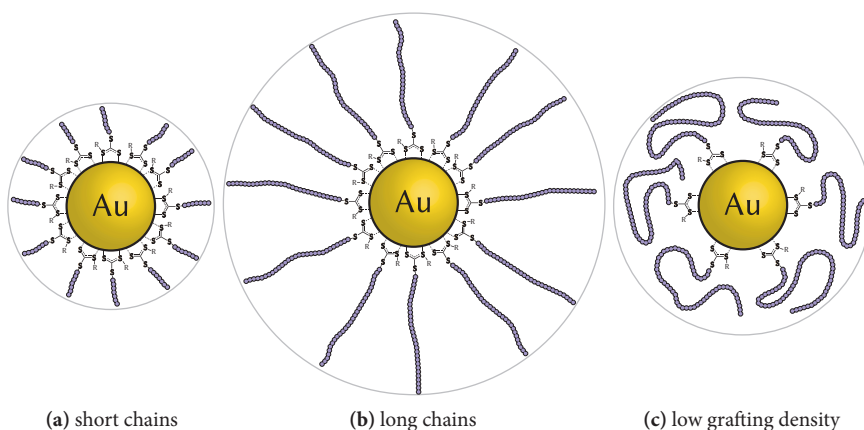


Fig. 8.8: Conventional nanohybrids produced by coating of citrate AuNPs $\text{Au}^{\text{cit}}\text{V-3}$ with NIPAm polymers of defined lengths carrying a trithiocarbonate group at the terminal end. (R: rest of the RAFT agents' stabilizing group). The polymer shells occupy more space when the macromolecules are longer or the grafting density is higher. These illustrations are schematics not drawn to scale.

$2\text{ebs}_{\text{Au}}\text{V}^{\text{TTC}}\text{-11}$ in Section 8.1.1.2. Polymers with incorporated trithiocarbonate groups have already been applied to cover gold surfaces^[2,4,60–65] and appear to be able to create even denser polymer layers on the surface than thiol-capped polymers.^[5] When the trithiocarbonate group is in the middle of the polymer chain, V-shaped polymer brushes are formed by the adsorption.^[66,67]

The direct addition was used preferentially in this work. Not only because it entails less effort and would thus lead to a cheaper scaled-up industrial process, but also because otherwise, it would just be impossible to implement the strategy using the multiblock polymers with multiple trithiocarbonate groups along their backbone. Reduction of the trithiocarbonate groups would split these polymers into the individual blocks, as has been demonstrated in Section 5.4.5.

8.3.2.1 Grafting of polymers with single trithiocarbonate groups to citrate AuNPs

First, a series of structurally equivalent conventional pNIPAm samples with a single trithiocarbonate group at the terminal chain end, but with different chain lengths, were used, in order to systematically evaluate the influence of the chain length

Tab. 8.2: Results from the TEM-image evaluation of all conventional nanohybrid samples: the sample identifiers for the nanohybrids and the polymers used for their production, the polymers' \overline{M}_n and dispersity D values from the SEC analysis (DMAc, RI detector), the total number of evaluated TEM images, the total number of measured distances, and the determined interparticle spacing d . (Data in this table reprinted with permission from a previous publication.^[69] Copyright 2013 American Chemical Society.)

sample	polymer	\overline{M}_n in $10^4 \frac{\text{g}}{\text{mol}}$	D	no. micro- graphs	no. dis- tances	d in nm
$\text{AuK}^{\text{TTC}}\text{-9}$	$\pi\text{-8b}$	1.49	1.20	16	561	11.6 ± 2.6
$\text{AuK}^{\text{TTC}}\text{-10}$	$\pi\text{-8c}$	2.20	1.21	15	865	16.6 ± 2.1
$\text{AuK}^{\text{TTC}}\text{-11}$	$\pi\text{-8d}$	2.58	1.15	11	834	17.2 ± 2.1
$\text{AuK}^{\text{TTC}}\text{-12}$	$\pi\text{-7a}$	3.79	1.14	8	510	23.7 ± 3.4
$\text{AuK}^{\text{TTC}}\text{-13}$	$\pi\text{-2a}$	4.74	1.15	17	743	30.1 ± 4.1
$\text{AuK}^{\text{TTC}}\text{-14}$	$\pi\text{-1c}$	5.48	1.19	7	232	34.8 ± 5.3
$\text{AuK}^{\text{TTC}}\text{-15}$	$\pi\text{-2b}$	6.77	1.19	11	281	38.8 ± 6.2
$\text{AuK}^{\text{TTC}}\text{-16}$	$\pi\text{-2d}$	7.44	1.22	15	609	40.9 ± 6.8

on the functionalization process. The SEC traces of these samples are shown in Figure 5.15 in Section 8.3.2.1.

An excess of the polymers was added to the citrate sol $\text{Au}^{\text{ci}}\text{v-3}$ in aqueous solution and the extant macromolecules were removed by repeated centrifugation and redispersion as described in Section 8.3.1. That way, the nanohybrids $\text{AuK}^{\text{TTC}}\text{-9}$ to $\text{AuK}^{\text{TTC}}\text{-16}$, which will be referred to as “conventional nanohybrids” in the following and are sketched schematically in Figure 8.8, were obtained as red dispersions (absorption maximum around 521 nm in methanol) free of excess polymer, citrate ions, oxidation products and the very small gold clusters, which are known to remain from the synthesis process in low concentrations.^[68] To be absolutely certain that the polymers remain in solution during the centrifugation, a pNIPAm sample with a very high molar mass (sample $\pi\text{-4a}$) was centrifuged for 5 d at full speed. No sedimented polymer was found thereafter.

In contrast to the nanohybrids $\text{AuK}^{\times}\text{-8}$ and $\text{AuK}^{\times}\text{-9}$ from the defunctionalized pNIPAm samples, no color change was found for dispersions of the nanohybrids $\text{AuK}^{\text{TTC}}\text{-9}$ to $\text{AuK}^{\text{TTC}}\text{-16}$, even after storing them for months. The presence of a trithiocarbonate anchor group is crucial for the long-term stabilization of the nanocomposites.

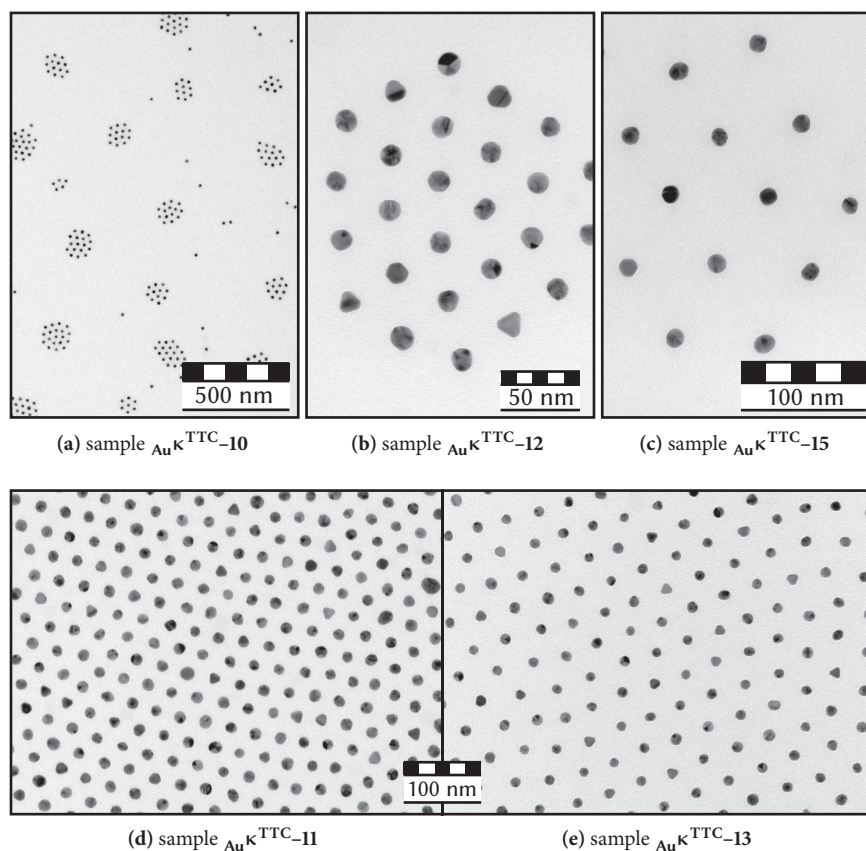


Fig. 8.9: Typical regions of hexagonally arranged cores, taken from the TE micrographs of different conventional nanohybrid samples. As visible in (a), not all particles are ordered in lattices, but there is always a minimum distance between them, caused by the surrounding, electron-transparent polymer shell. (Micrographs a, d, and e reprinted with permission from a previous publication.^[69] Copyright 2013 American Chemical Society.)

TEM analysis For the analysis of the nanohybrids via TEM, all specimens were prepared by drop-casting from methanol rather than water, in order to be sure that the elongation of the pNIPAm chains would not be influenced by the temperature or additives. However, the TEM results turned out to be solvent-independent in later comparative experiments.

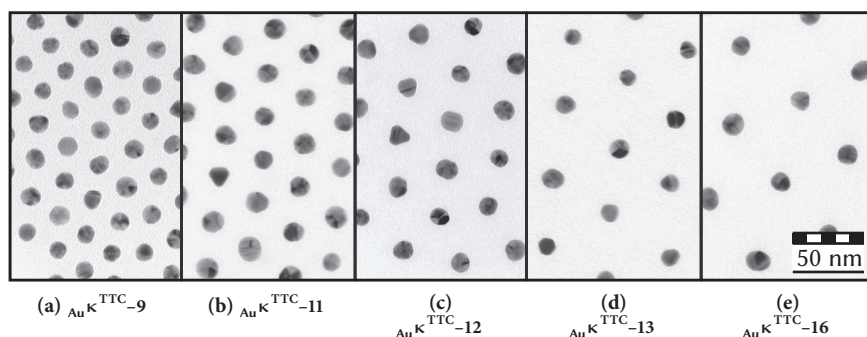


Fig. 8.10: TE micrographs taken with the same magnification in order to illustrate the growing interparticle spacing with \bar{M}_n of the decorating polymers for five conventional nanohybrid samples. (Reprinted and adapted with permission from a previous publication.^[69] Copyright 2013 American Chemical Society.)

The micrographs in Figure 8.9 show representative spots found by the TEM analysis of the conventional nanohybrids, exemplarily selected for five different samples. The gold cores can be visualized directly and it is seen that no AuNPs are fused together and that their size distribution has not changed as a result of the functionalization process. Regions of different sizes are visible where the AuNPs assembled into regular hexagonal patterns,^[70–72] which demonstrates the high homogeneity and the round shape of the nanohybrids. (Read the possible explanations for this “islanding” behavior in Section 4.1.3.) This effect occurred spontaneously when the specimens were prepared by drop-casting using a regular glass pipette which should not affect the self-assembly.^[73] No annealing was performed. The polymer shells cannot be seen directly in high magnifications, as would be the case with larger nanohybrids^[74] or cores of materials with less electron-interaction,^[75] but their presence causes the gold cores to be evenly spaced from each other.* The size of the hexagonal domains varied and not all particles were assembled in ordered lattices, but no AuNPs closer together than a constant minimum distance were found. These distinct spacings between the gold cores are clearly caused by the polymer brushes, since no other substances are present in the solution. An electrostatic effect^[77] can be excluded, because pNIPAm-coated AuNPs are completely uncharged, as shown by zeta potential measurements.^[78]

* At lower magnifications, the polymer shells can be vaguely seen as blurred shadows. They could not be successfully visualized by staining with ammonium molybdate.^[76]

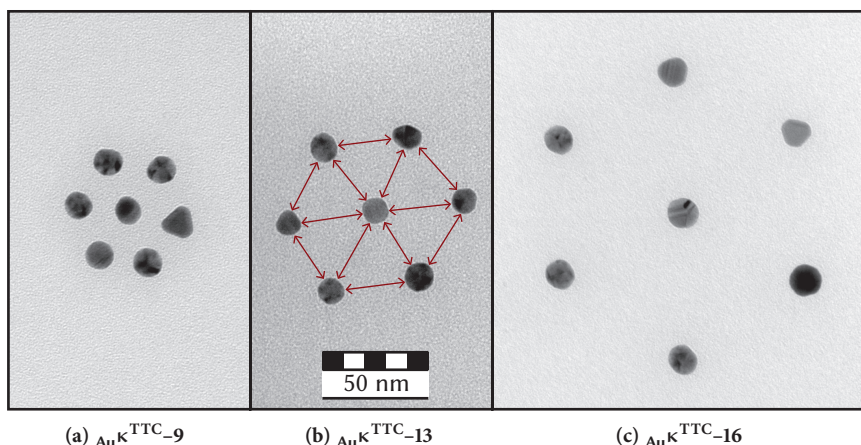


Fig. 8.11: TE micrographs taken with the same magnification, which feature the same structural motif of an isolated hexagon. The increasing interparticle spacings are clearly visible. In image (b), it is demonstrated with red arrows how the distances were measured during the evaluation. (Micrograph c reprinted and adapted with permission from a previous publication.^[69] Copyright 2013 American Chemical Society.)

Comparing micrographs 8.9d and 8.9e, taken with the same magnification, the different interparticle distances in the visible hexagonal regions are evident. It was observed that these distances increased with growing \overline{M}_n of the polymers as is shown in 8.10 for samples $\text{AuK}^{\text{TTC-9}}$, $\text{AuK}^{\text{TTC-11}}$, $\text{AuK}^{\text{TTC-12}}$, $\text{AuK}^{\text{TTC-13}}$, and $\text{AuK}^{\text{TTC-16}}$. The micrographs have the same magnification and are arranged by the lengths of the decorating polymer chains. (Figure 8.6 shows even shorter distances in an analogous lattice with the non-polymeric ligand $^{\text{SH}}\lambda^{\text{OH-8}}$.) The three micrographs in Figure 8.11 show the increasing particle distances for the isolated typical hexagonal motif. The same phenomenon had already been reported on a smaller scale with AuNPs coated with alkyl thiols.^[79] With growing length of the alkyl chain from C_6 to C_{12} , the interparticle distance increased from 1.4 nm to 2.3 nm. Nishi and Kobatake^[32] (2012) also observed increasing distances in the TEM images of citrate AuNPs coated with polystyrene with different chain lengths, but did not measure the distances between the gold cores systematically. Ohno *et al.*^[80] (2003) produced arrays of polymer-decorated AuNPs with increasing distances for longer polymer chains by depositing the nanohybrids with a special Langmuir

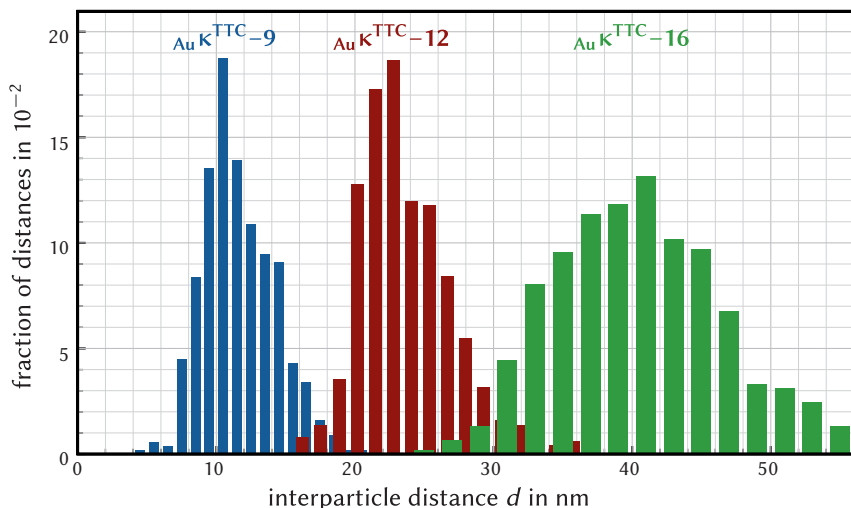


Fig. 8.12: Interparticle spacing d histograms for three conventional nanohybrid samples. The binning steps for the histograms are 1 nm for $\text{Au}\kappa^{\text{TTC-9}}$, 1.3 nm for $\text{Au}\kappa^{\text{TTC-12}}$, and 2 nm for $\text{Au}\kappa^{\text{TTC-16}}$. (Reprinted and adapted with permission from a previous publication.^[69] Copyright 2013 American Chemical Society.)

trough equipped with a compression barrier. Earlier in this work, a similar effect could also be seen in Figure 5.10, although on an overall smaller scale.

On the basis of these findings, the distances between the particle cores should be correlated with the \overline{M}_n values of the decorating polymers. To this end, the average interparticle spacing d was determined by measuring a large number of shortest distances between the gold cores in several TEM images with resolutions from 9.40 pixels nm^{-1} to 3.26 pixels nm^{-1} (corresponding to magnifications from 660 000-fold to 230 000-fold on the native TEM screen) using the software IMAGEJ. Only all twelve distances in complete hexagons were measured and averaged (illustrated in Figure 8.11b), in order to compensate for lattice distortions. Performing this analysis by hand was inevitable, since by automated processes, it is very difficult to selectively single out the ordered regions. Also, the lattice regularity was not high enough to find clear reflexes in the TEM diffraction mode.^[81] The measuring results are listed in Table 8.2, along with the properties of the corresponding polymers. The distances d are strictly increasing, from sample $\text{Au}\kappa^{\text{TTC-9}}$ to sample $\text{Au}\kappa^{\text{TTC-16}}$ almost by a factor of 4. For the samples with the shortest polymers, the deviation from the average value is mainly due to the nanoparticles' shapes, and for

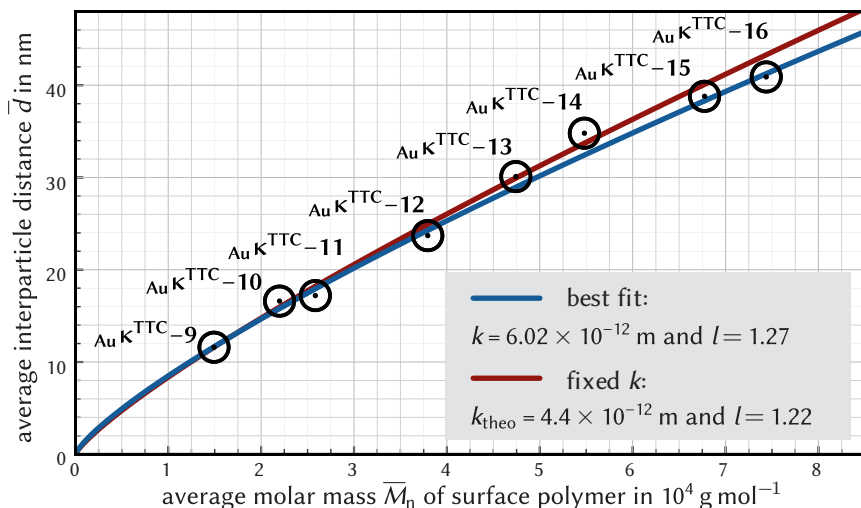


Fig. 8.13: Plot of the average interparticle spacing \bar{d} as a function of the \bar{M}_n values of the polymers in the shell of the conventional nanohybrids. The lines are fits by Equation 8.1. (Reprinted and adapted with permission from a previous publication.^[69] Copyright 2013 American Chemical Society.)

the samples with longer polymers, the deviation is mainly caused by the deformation of the hexagons. The interparticle spacing histogram for samples AuK^{TTC}-9, AuK^{TTC}-12, and AuK^{TTC}-16 is plotted exemplarily in Figure 8.12. The measured d values are plotted as a function of the polymers' average molar masses in Figure 8.13. When employing polymers with even higher \bar{M}_n values, such as polymer π -4c, nanohybrids featuring hexagonal lattices with even larger spacings were obtained, but the distances differed too much from region to region, so that these samples could therefore not be included in this study.

A reasonable function relating the measured interparticle spacings d to the polymer's \bar{M}_n values was then sought to be fitted to the obtained data. If it is assumed that the \bar{M}_n dependence of d does not increase with \bar{M}_n itself, the most simple, yet rational, correlation function that goes through the origin and then steadily increases with \bar{M}_n has the form:

$$\bar{d} = k \times [\bar{M}_n]^{\frac{1}{l}}. \quad (8.1)$$

Here, k represents the polymer lengths per molar mass and l can be interpreted physically as describing the profile of the increase. The limiting values for l , which

is strictly related to the grafting density, are $l = 1$ (linear growth, perfect polymer brush, Figure 8.8a to Figure 8.8b) and $l = 2$ (growth with square root, isolated polymer coils, Figure 8.8c).^[82] For dense polymer brushes on flat surfaces, low l values can be expected, while high l values would indicate a low grafting density and/or high curvature of the surface.^[83] The best fit is obtained with the parameters $k = 6.02 \times 10^{-12}$ m and $l = 1.27$ and is shown as the blue line in 8.13. Theoretically, the parameter k should be equal to twice the contour length (length of maximum elongation) of pNIPAm per g mol^{-1} . It can be estimated to be approximately $k_{\text{theo}} = 2 \times 2.2 \times 10^{-12}$ m = 4.4×10^{-12} m,^[84,85] which is very close to the value derived from the best fit. Alternatively, only the parameter l can be adjusted to make 8.1 fit to the data, setting k to the fixed theoretical value. This way, an even lower value of $l = 1.22$ is obtained. The corresponding curve, which describes the data almost as well, is the red line in Figure 8.13. It can be seen that the function describes the data quite well, although the underlying model does not take into account uncertain factors like the fact that longer polymer chains could influence l more than shorter ones. The very good agreement of the theoretical k value with the one obtained from the best fit indicates that ligand intercalation/interpenetration, usually referred to as “interdigitation” of the ligands,^[86,87] which was verified for alkyl thiols on small silver nanocrystals,^[88] only occurs to a very low degree, when macromolecules are on the surface. Although the presented approach is a grafting-to strategy, where the polymer grafting density is expected to be controlled by the space of the polymer, rather than the availability of reactive positions on the surface, the profile of the function describing the dependence of the coating polymers’ molar masses on the interparticle spacings is more similar to the profile expected for growing polymer brushes than to the expected profile for the growth of isolated macromolecules, which might indicate that the polymer coating on the AuNPs is close to the polymer brush regime.

One could also envision utilizing the obtained calibration function in the opposite way to produce nanohybrid lattices with selectively targeted spacings by employing RAFT polymers with the respectively needed molar masses. By pyrolysis and evaporation of the polymer at high temperatures, even and fine-tuned AuNP arrays could thus be obtained.^[89]

AFM analysis AFM is complementary to TEM, as it yields the topography of the sample.^[90] It is preferable to SEM in this case, because the resolving power is higher and the samples can be measured without pretreatment.^[91] Since it was impossible to use the TEM specimens for the AFM measurements as well, new specimens were prepared by spin-coating the nanohybrids on glass disks from solution in methanol.

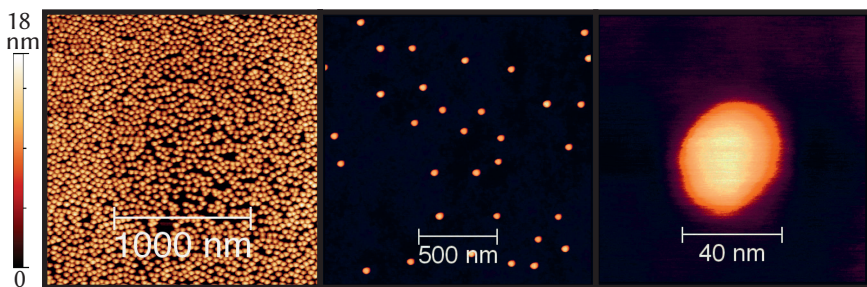


Fig. 8.14: AFM analysis of the conventional nanohybrid sample $\text{Au}\kappa^{\text{TTC}}\text{-14}$. The three images are from specimens spin-coated with different nanohybrid concentrations.

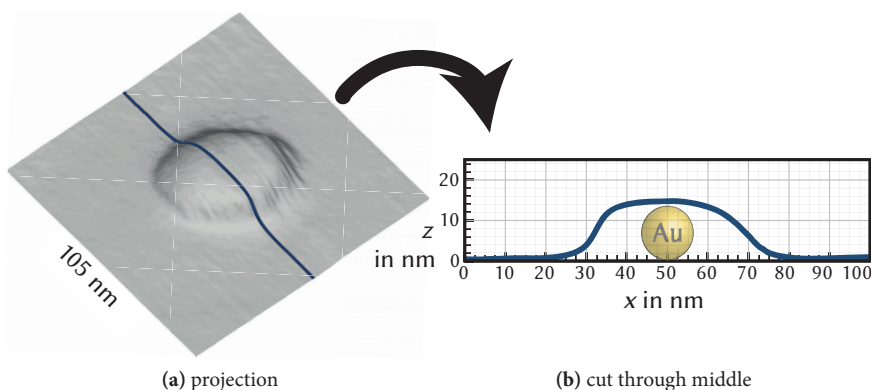


Fig. 8.15: AFM analysis of the topography of a single conventional nanohybrid from sample $\text{Au}\kappa^{\text{TTC}}\text{-14}$. Image (a) was created as described in Section 4.2. The diagram in (b) shows the height profile, when the object in (a) is cut along the blue line. The semitransparent AuNP has a diameter of 13.6 nm—the average value determined for $\text{Au}\nu\text{-3}$ in Section 5.1.2.3.

By this preparation method, no close-packed lattices arose. Three AFM images of sample $\text{Au}\kappa^{\text{TTC}}\text{-14}$, which is at the upper end of the conventional nanohybrids regarding the interparticle spacing, are shown in Figure 8.14. Here, the outside of the polymer shells is visualized, rather than the gold cores. Remarkably, all nanohybrids are very homogeneous and completely isolated. Their slightly elliptic shape is no measuring artifact—it was retained even when the scanning direction was rotated by 90° and is presumably due to the deposition by spin-coating.

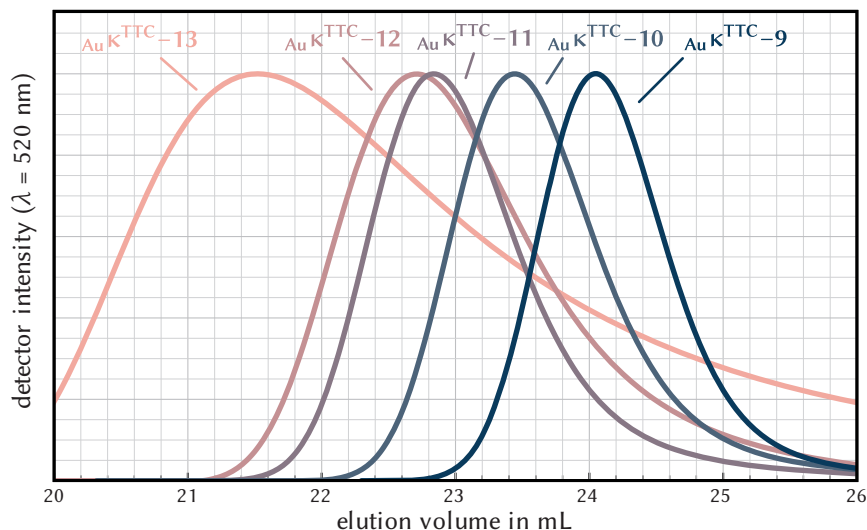


Fig. 8.16: Elution chromatograms of the five conventional nanohybrid samples with the shortest macromolecules on the surface: samples $\text{AuK}^{\text{TTC}-9}$, $\text{AuK}^{\text{TTC}-10}$, $\text{AuK}^{\text{TTC}-11}$, $\text{AuK}^{\text{TTC}-12}$, $\text{AuK}^{\text{TTC}-13}$. A shift to lower elution volumes and a significant broadening of the SEC traces are observable. The samples coated with even longer conventional polymers were excluded. (Reprinted and adapted with permission from a previous publication.^[69] Copyright 2013 American Chemical Society.)

Figure 8.15a shows the projection of one random single nanohybrid from sample $\text{AuK}^{\text{TTC}-14}$. The image was created using the workflow described in Section 4.2. Figure 8.15b shows the height profile along the blue line in Figure 8.15a. A single semitransparent AuNP projection with a diameter of 13.6 nm (see Section 5.1.2.3) is drawn in the middle of this cut. It can be seen that the polymer shell is only slightly higher than the AuNP, but extends farther on both sides. The polymer chains lie mainly around the individual AuNPs. The thus induced compression could explain the low l parameter. (Compare the solid silica nanoparticles $\text{SiO}_2^{\text{NP}}\text{v}-2$ in Figure 4.8, where the width exactly coincides with the height.)

In this particular case, the diameter of the analyzed nanohybrid coincides very well with the corresponding interparticle spacing from the TEM analysis ($d = 34.8 \pm 5.3$ nm), but to make a truly meaningful comparison, a large number of randomly selected nanohybrids would have to be measured this way—an extremely tedious and time-consuming task.

SEC analysis All trithiocarbonate-nanohybrid samples were subjected to SEC analysis with the same DMAc-setup which had also been used for the pure polymers. To this end, the purification by centrifugation was performed with redispersion in DMAc instead of methanol. A well suited gold concentration for the SEC measurements was approximately 1 g L^{-1} . This concentration was determined based on the optical attenuation at 520 nm, assuming that the functionalization and the different solvent have no major effect on the attenuation behavior (see Figure 5.9). Correspondingly, the SEC elution behavior was traced with the UV detector set to the plasmon-resonance wavelength of the AuNPs at 520 nm. This signal can be used, because of the high homogeneity of the encapsulated AuNPs, and had a much higher signal-to-noise ratio, but was otherwise practically identical to the RI detector output. All obtained SEC traces feature a unimodal signal and no remaining unbound polymer could be found, showing the success of the applied purification. The SEC traces were almost unaffected by the concentration of the examined nanohybrids. For want of any calibration data for this type of nanocomposites, the raw elution chromatograms are taken into consideration here, without converting them into molar mass distributions. Figure 8.16 shows the SEC traces of samples $\text{AuK}^{\text{TTC}}\text{-9}$, $\text{AuK}^{\text{TTC}}\text{-10}$, $\text{AuK}^{\text{TTC}}\text{-11}$, $\text{AuK}^{\text{TTC}}\text{-12}$, and $\text{AuK}^{\text{TTC}}\text{-13}$. As expected for larger objects, the signals are observed at lower elution volumes than for the respective pure polymers. (Going from 31.6 mL for $\pi\text{-8b}$ to 26.4 mL for $\pi\text{-2a}$.) With higher chain lengths of the encapsulating polymers, the elution volumes further decrease. Decreasing elution volumes in SEC for nanostructures with identical gold cores but increasing shell thickness have already been reported in literature, although with smaller dimensions for both cores and shells than examined here.^[92,93] Additionally, it can be seen in Figure 8.16 that the signals become broader with higher chain length of the coating polymers. While the signal for sample $\text{AuK}^{\text{TTC}}\text{-9}$ is still very narrow—applying the same PMMA calibration as for the analysis of the pure polymers would yield a dispersity of $\bar{D} = 1.09$, for example—the width of the signal increases approximately exponentially with the coating polymers' chains lengths, making the peak for $\text{AuK}^{\text{TTC}}\text{-13}$ already so broad that the samples with longer polymers had to be excluded here. A possible explanation for this broadening is the formation of aggregates of different sizes by the entanglement of the coating polymers. In these agglomerates, the nanohybrids would be temporarily immobilized in parts of the SEC setup, leading to higher retention times. For longer coating macromolecules, one would also expect a higher degree of entanglement. In addition to the higher width, an increasing skewing can be observed for the samples with higher \bar{M}_n values, the main cause for this probably being the SEC experiment itself, since it has been shown that larger particles lead to higher SEC skewing.^[94,95]

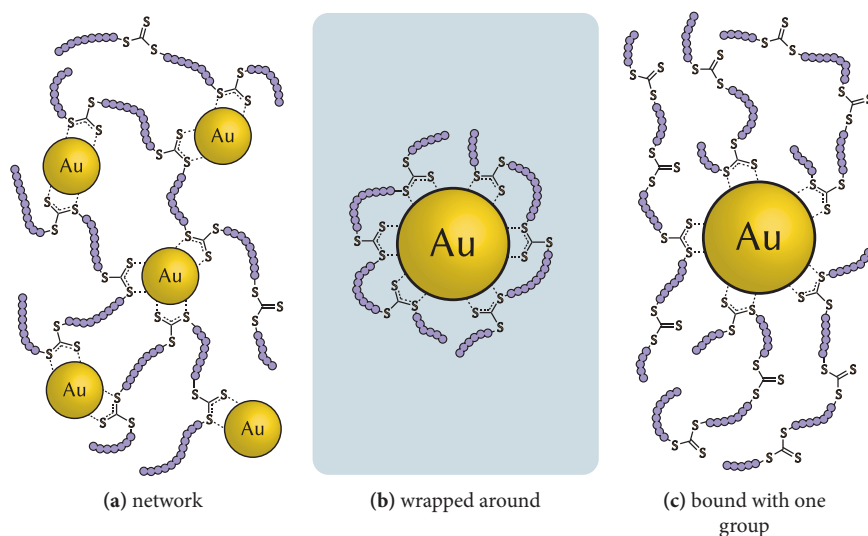


Fig. 8.17: In principle conceivable binding schemes for nanohybrids composed of AuNPs in the core and shells of macromolecules with multiple trithiocarbonate groups along their backbone: (a) The trithiocarbonate groups bind to different AuNPs which are thus interconnected and a network is formed. (b) The polymer chains are wrapped around the AuNPs, forming loops linked with multiple sites. (c) The macromolecules couple only with a single trithiocarbonate group. The results from the presented study show that (b) is the actual structure. All illustrations are schematics not drawn to scale.

Lin *et al.*^[96] (2009) reported strong skewing even when examining AuNPs with diameters below 2 nm coated with dihydrolipoic acid on a SEPHACRYL column.

8.3.2.2 Grafting of polymers with multiple trithiocarbonate groups to citrate AuNPs

It is an especially intriguing question which kind of nanostructures are formed, when the NIPAm multiblock polymers with several trithiocarbonate groups along their backbone (see Section 5.4.4) are employed in the same functionalization process. These samples will be denoted “multiblock nanohybrids” in the following.

Figure 8.17 shows the different binding schemes which could in principle be expected: The multiblock polymers could connect with their binding groups to different AuNPs, forming a network (Figure 8.17a), they could be wrapped around

Tab. 8.3: Results from the TEM-image evaluation of all multiblock nanohybrid samples: the sample identifiers for the nanohybrids and the polymers used for their production, the polymers' \overline{M}_n and dispersity D values from the SEC analysis (DMAc, RI detector), the average number of trithiocarbonate groups per polymer $\overline{N}_{\text{TTC}}$ calculated via Equation (5.20) (Section 5.4.5), the total number of evaluated TEM images, the total number of measured distances, and the determined interparticle spacing d . (Data in this table reprinted with permission from a previous publication.^[69] Copyright 2013 American Chemical Society.)

sample	polymer	\overline{M}_n in $10^4 \frac{\text{g}}{\text{mol}}$	\bar{g}	no. micro- graphs	no. dis- tances	d in nm
$\text{AuK}^{\text{MB}}\text{-17}$	$\pi^{\text{MB}}\text{-15c}$	4.38	3.00	17	554	12.6 ± 3.8
$\text{AuK}^{\text{MB}}\text{-18}$	$\pi^{\text{MB}}\text{-17b}$	5.41	4.50	27	1748	13.0 ± 3.4
$\text{AuK}^{\text{MB}}\text{-19}$	$\pi^{\text{MB}}\text{-18a}$	5.95	3.20	11	966	13.7 ± 4.2
$\text{AuK}^{\text{MB}}\text{-20}$	$\pi^{\text{MB}}\text{-16a}$	7.11	1.90	16	713	16.8 ± 3.9
$\text{AuK}^{\text{MB}}\text{-21}$	$\pi^{\text{MB}}\text{-11b}$	9.08	2.00	21	540	14.6 ± 4.1

the AuNPs, linked to the same particle at multiple sites and forming loops on the nanoparticles' surface (Figure 8.17b), or they could bind to the AuNPs with only a single trithiocarbonate moiety, leaving the rest unreacted (Figure 8.17c). Du *et al.*^[97,98] (2008, 2010) used trithiocarbonate-group containing multiblock copolymers as capping agents in the synthesis of AuNPs of lower sizes than those of citrate particles and did not observe interconnection of the thus synthesized AuNPs, but it was not possible to elucidate if loops on the surfaces had formed. At the same time, it is known that AuNPs are fused into a covalently bonded network by α - ω -dithiols with short alkyl-chains.^[99,100] Given the results from Section 8.1.1.3, the assumption of particle crosslinking (Figure 8.17c) would arguably first be made.

The multiblock nanohybrids $\text{AuK}^{\text{MB}}\text{-17}$ to $\text{AuK}^{\text{MB}}\text{-21}$ were produced from citrate AuNPs $\text{Au}^{\text{ci}}\text{v-3}$ and the multiblock polymer samples listed in Table 5.3 in an identical way as reported for the conventional nanohybrids above. The resulting red dispersions in methanol did not differ in appearance from those with the conventional nanohybrids, although their redispersion tended to need some more time and sonication. The fact that no precipitation was observed already makes the theory that the AuNPs would be crosslinked by the multiblock polymers very unlikely (Figure 8.17c).

TEM analysis The multiblock nanohybrids exhibited the same minimum spacing and ordering when examined via TEM as had been observed for the conventional

nanohybrids before, although the formed lattices were slightly more irregular. Figure 8.18 shows four exemplary micrographs of different samples. The fact that all particles are found next to each other and no stacking was seen up until very high concentrations constitutes more evidence that the gold cores are in no way held together by the covering multiblock polymers. AuNP aggregates of gold cores were found in no case.

The distances were measured in the same way as for the conventional nanohybrids (see Figure 8.11b). The results are listed in Table 8.3, along with the assignment of sample identifiers and the characteristics of the encapsulating polymers, taken from Table 5.3. It can be seen that the d values deviate slightly more from the average than in the case of the conventional nanohybrids, which reflects that the lattices were less regular here. This could indicate that the polymer shells in the multiblock nanohybrids are less homogeneous in shape. But most notably, the interparticle spacings are approximately the same for all five examined samples $\text{AuK}^{\text{MB}}\text{-17}$, $\text{AuK}^{\text{MB}}\text{-18}$, $\text{AuK}^{\text{MB}}\text{-19}$, $\text{AuK}^{\text{MB}}\text{-20}$, and $\text{AuK}^{\text{MB}}\text{-21}$ and lie distinctly under the values for the conventional nanohybrids (also compare with Figure 8.18d with the hexagons in Figure 8.11), independent of the polymer chain length and the number of trithiocarbonate groups, as can be seen in the plot of the measured average d values as a function of \overline{M}_n together with the previously determined calibration function for the conventional nanohybrids in Figure 8.19. It can be assumed that the \overline{M}_n values are comparable for the conventional and the multiblock polymers, since the components of multifunctional RAFT agent only constitute a small part of the whole multiblock polymers. The \overline{M}_n values are mainly interpreted relative to each other here, so that it would not matter much if, by the used SEC calibration, slightly inaccurate masses had been obtained. But the spacings are still all higher than for $\text{AuV}^{\text{OH}}\text{-13}$ with the water-soluble thiol $\text{SH}\lambda^{\text{OH}}\text{-8}$ (Figure 8.6) or for the conventional nanohybrid $\text{AuK}^{\text{TTC}}\text{-9}$. This shows that there is undoubtedly polymer on the AuNP surfaces.

The observed behavior demonstrates that the multiblock polymers are indeed wrapped around the AuNPs as depicted in Figure 8.17b. If the multiblock polymers were only connected via one single group (Figure 8.17c), one would still expect that the distances increase from $\text{AuK}^{\text{MB}}\text{-17}$ to $\text{AuK}^{\text{MB}}\text{-21}$. However, it cannot be elucidated from this analysis whether the spacing is influenced more by the looped middle blocks or the (smaller) end blocks (see Section 5.4.4.1). It also remains to be further explored if the constant value of approximately 14 nm reflects an ideal distance for the linkage points of the polymer loops on the AuNP surface and if it is a coincidence that this spacing almost exactly coincides with the average AuNP diameter.

Tab. 8.4: Results from the SEC analysis of gold-pNIPAm nanohybrids. All nanohybrid samples with the sample identifier of the coating polymers, the coating polymers' \overline{M}_n values from the SEC analysis (DMAc, RI detector), the average number of blocks per polymer \overline{b}_{cl} calculated via (5.20) (Section 5.4.5), the interparticle spacing d from the evaluation of TEM images, and the maximum elution volume $V_{\max, \text{SEC}}$ and the full width at half maximum w_{SEC} of the SEC traces of the nanohybrids (UV detector at 520 nm). The corresponding elution chromatograms can be seen in Figures 8.16 and 8.20. (Data in this table reprinted with permission from a previous publication.^[69] Copyright 2013 American Chemical Society.)

sample	polymer	\overline{M}_n in $10^4 \frac{\text{g}}{\text{mol}}$	\overline{b}_{cl}	d in nm	$V_{\max, \text{SEC}}$ in mL	w_{SEC} in mL
$\text{AuK}^{\text{TTC}}\text{-9}$	$\pi\text{-8b}$	1.49	1.2	11.6 ± 2.6	24.04	1.09
$\text{AuK}^{\text{TTC}}\text{-10}$	$\pi\text{-8c}$	2.20	1.2	16.6 ± 2.1	23.45	1.25
$\text{AuK}^{\text{TTC}}\text{-11}$	$\pi\text{-8d}$	2.58	1.2	17.2 ± 2.1	22.83	1.27
$\text{AuK}^{\text{TTC}}\text{-12}$	$\pi\text{-7a}$	3.79	1.1	23.7 ± 3.4	22.71	1.67
$\text{AuK}^{\text{TTC}}\text{-13}$	$\pi\text{-2a}$	4.74	1.2	30.1 ± 4.1	21.52	3.17
$\text{AuK}^{\text{MB}}\text{-17}$	$\pi^{\text{MB}}\text{-15c}$	4.38	4.0	12.6 ± 3.8	24.32	1.32
$\text{AuK}^{\text{MB}}\text{-18}$	$\pi^{\text{MB}}\text{-17b}$	5.41	5.5	13.0 ± 3.4	23.76	1.44
$\text{AuK}^{\text{MB}}\text{-19}$	$\pi^{\text{MB}}\text{-18a}$	5.95	4.2	13.7 ± 4.2	24.51	1.38
$\text{AuK}^{\text{MB}}\text{-20}$	$\pi^{\text{MB}}\text{-16a}$	7.11	2.9	16.8 ± 3.9	24.39	1.23
$\text{AuK}^{\text{MB}}\text{-21}$	$\pi^{\text{MB}}\text{-11b}$	9.08	3.0	14.6 ± 4.1	24.35	1.26

AFM analysis AFM images of the multiblock nanohybrids were comparable to those of the conventional nanohybrids shown in Figure 8.14. The nanohybrids were found evenly distributed on the prepared specimens and in no way preferentially associated to each other—another proof that interparticle linking is present to no extent in these nanostructures.

SEC analysis As was shown above for the conventional nanohybrids, the multiblock nanohybrids were now subjected to SEC analysis in an identical way. Figure 8.18 shows the five obtained elution chromatograms for samples $\text{AuK}^{\text{MB}}\text{-17}$ to $\text{AuK}^{\text{MB}}\text{-21}$. The semitransparent SEC traces of the conventional nanohybrid samples $\text{AuK}^{\text{TTC}}\text{-9}$ to $\text{AuK}^{\text{TTC}}\text{-13}$ are taken from Figure 8.16. The broadness and to some extent the position of their peaks can be used as an internal reference.

In order to quantify this kind of evaluation, the position of the maximum $V_{\max, \text{SEC}}$ and the full width at half maximum w_{SEC} of the signals are listed for all examined nanohybrid samples in Table 8.3. Inspecting the results for the multiblock nanohy-

brids $\text{AuK}^{\text{MB}}\text{-17}$ to $\text{AuK}^{\text{MB}}\text{-21}$, it stands out that all signals are very similar, appear at high elution volumes and are relatively narrow, in the range of the conventional samples $\text{AuK}^{\text{TTC}}\text{-10}$ and $\text{AuK}^{\text{TTC}}\text{-11}$. This shows that all nanoparticles are well separated from each other and are not interconnected by the multiblock polymers. Furthermore, as seen before with TEM, also the SEC results prove that the multiblock nanohybrids all have approximately the same size and are considerably smaller than would have been expected by the molar masses of the decorating polymers, providing even more evidence that the multiblock polymers are wrapped around the AuNPs.

Conclusions on the binding motif Based on the results from analysis of the multiblock nanohybrids, a very clear answer could eventually be given to the seemingly intricate initial question regarding which way polymers with multiple trithiocarbonate groups would bind to gold nanocrystals from reduction with citrate: by interconnection of different AuNPs (Figure 8.17a), by wrapping around the nanoparticles (Figure 8.17b), or by binding to the AuNPs with only one trithiocarbonate group (Figure 8.17c).

Crosslinking of the AuNPs by the coating multiblock polymers could be directly ruled out, mainly because of four findings:

- The position of the plasmon-resonance peak of the prepared nanohybrids was not shifted to longer wavelengths, which would have been expected in the case of aggregation.
- No stacking or twinning of nanoparticles was observed with TEM. All particles were well isolated.
- Evenly distributed deposited nanohybrids on the specimen were also found by AFM.
- A single and relatively narrow signal was observed in the SEC traces.

The conventional nanohybrids $\text{AuK}^{\text{TTC}}\text{-9}$ to $\text{AuK}^{\text{TTC}}\text{-16}$ could be used as a reference in TEM and SEC measurements to decide between the remaining two possibilities shown in Figure 8.17b and Figure 8.17c. Although the employed multiblock polymers possess different chain lengths and numbers of trithiocarbonate groups, all of their nanohybrids with the AuNPs showed approximately the same distances of on average 14 nm in the self-assembled hexagonal lattices that were found by TEM in all cases. Moreover, these distances are clearly lower than those from the previously obtained calibration function for the conventional nanohybrids,

which is a clear indication that the multiblock polymers are indeed wrapped around the nanoparticles and not only bound with one or a low number of their trithiocarbonate groups. This was confirmed by SEC: While the traces of the conventional nanohybrids feature a signal which is shifted to lower elution volumes and broadens approximately exponentially with increasing chain length of the decorating polymers, the signals of the multiblock nanohybrids appear at higher elution times and are smaller than one would expect in comparison. The revealed true structure of the multiblock nanohybrids is highlighted by the blue background in Figure 8.17.

Using polymers with multiple trithiocarbonate groups is therefore a second novel and straightforward way to prepare polymer loops on nanosurfaces, in addition to the approach shown in Section 7.1. The produced multiblock nanohybrids are promising candidates for applications where stable gold nanocrystals are needed. Whether the found binding motif gives rise to special properties and whether their binding trithiocarbonate groups are still accessible for further functionalization reactions, are worthwhile topics for further investigations.

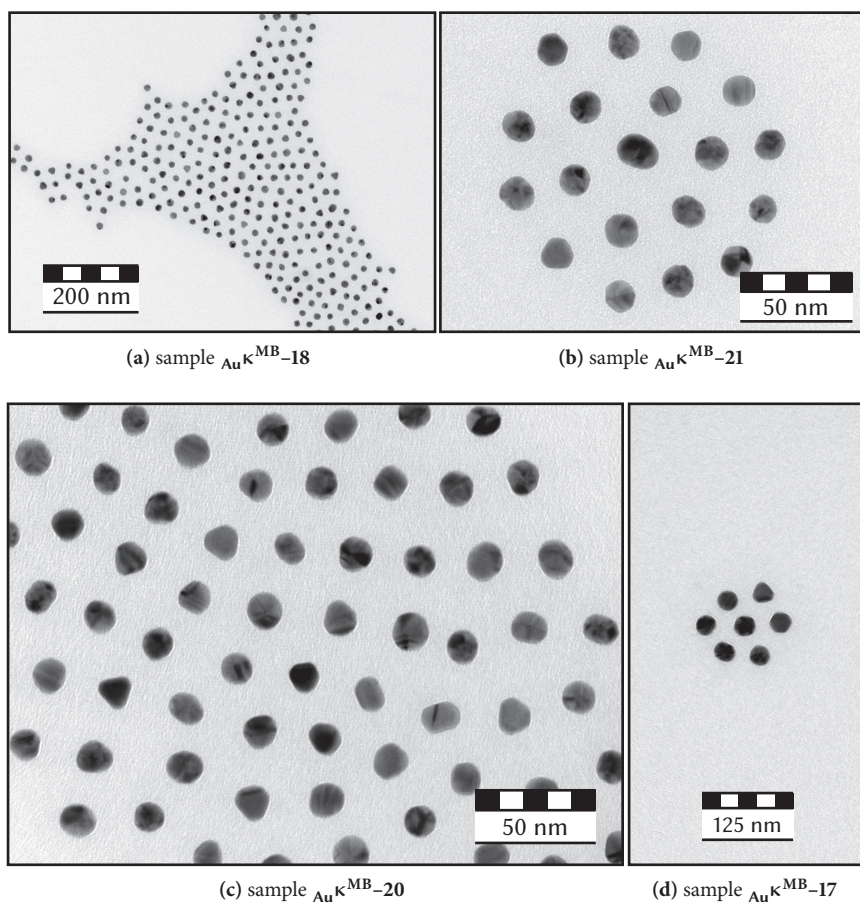


Fig. 8.18: Typical hexagonally arranged gold-core structures, taken from the TE micrographs of different multiblock nanohybrid samples. The structures are comparable to those of the conventional nanohybrids (Figure 8.9). Compare image (d) with the hexagons in Figure 8.11. (Micrograph c reprinted and adapted with permission from a previous publication.^[69] Copyright 2013 American Chemical Society.)

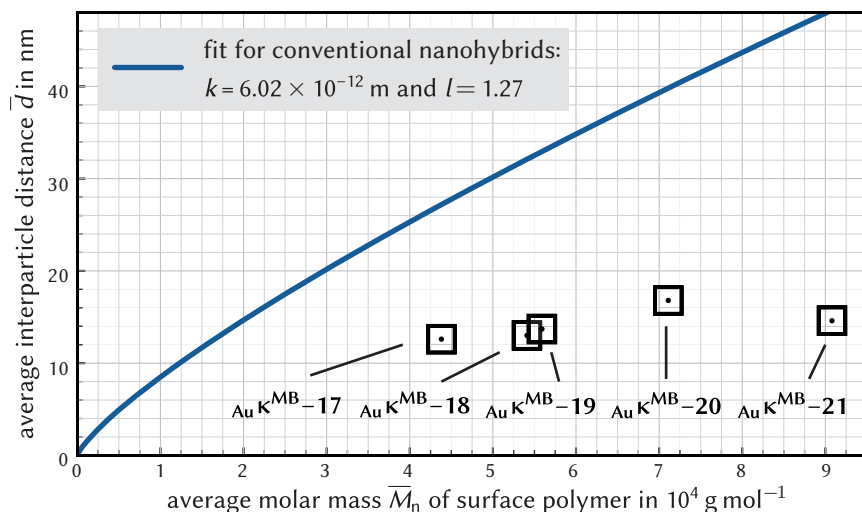


Fig. 8.19: Plot of the average interparticle spacing \bar{d} as a function of the \bar{M}_n values of the polymers in the shell of five multiblock nanohybrids in comparison to the calibration curve obtained for the conventional nanohybrids (Equation 8.1 with $k = 6.02 \times 10^{-12} \text{ m}$ and $l = 1.27$). The distances in the structures formed by the multiblock nanohybrids lie distinctly under this calibration curve and are almost independent of the polymers' molar masses. (Reprinted and adapted with permission from a previous publication.^[69] Copyright 2013 American Chemical Society.)

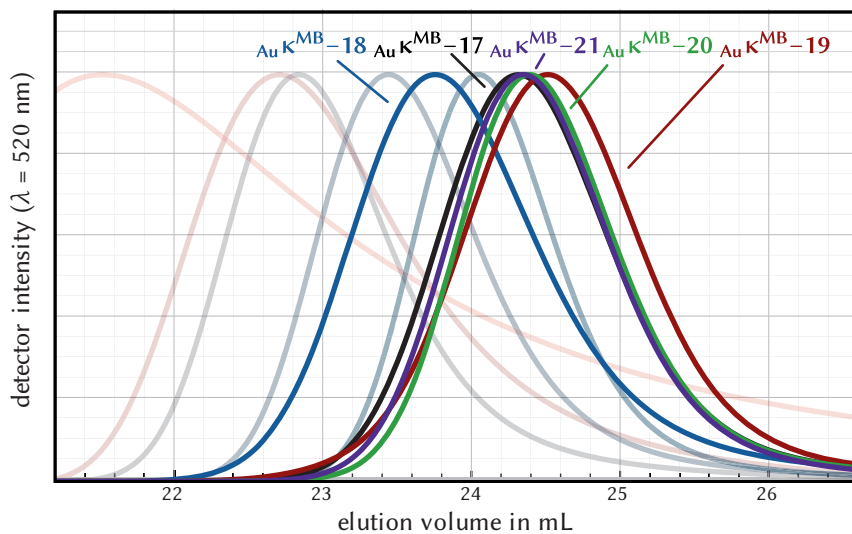


Fig. 8.20: Elution chromatograms of the multiblock nanohybrid samples. The semitransparent traces of the five conventional nanohybrid samples with the shortest macromolecules on the surface from Figure 8.16 are shown for comparison. (Reprinted and adapted with permission from a previous publication.^[69] Copyright 2013 American Chemical Society.)

References for Chapter 8

- (1) Zhang, S., Leem, G., Srisombat, L.-o., Lee, T. R., *J. Am. Chem. Soc.* **2008**, *130* (1), 113–120.
- (2) Duwez, A.-S., Guillet, P., Colard, C., Gohy, J.-F., Fustin, C.-A., *Macromolecules* **2006**, *39* (8), 2729–2731.
- (3) Fustin, C.-A., Duwez, A.-S., *J. Electron Spectrosc. Relat. Phenom.* **2009**, *172* (1–3, Sp. Iss. SI), 104–106.
- (4) Fustin, C.-A., Colard, C., Filali, M., Guillet, P., Duwez, A.-S., Meier, M. A. R., Schubert, U. S., Gohy, J.-F., *Langmuir* **2006**, *22* (15), 6690–6695.
- (5) Slavin, S., Soeriyadi, A. H., Voorhaar, L., Whittaker, M. R., Becer, C. R., Boyer, C., Davis, T. P., Haddleton, D. M., *Soft Matter* **2012**, *8* (1), 118–128.
- (6) Almeida, I., Ferreira, V., Montemor, M., Abrantes, L., Viana, A., *Electrochim. Acta* **2012**, *83*, 311–320.
- (7) Vickers, M. S., Cookson, J., Beer, P. D., Bishop, P. T., Thiebaut, B., *J. Mater. Chem.* **2006**, *16* (2), 209–215.
- (8) Vicente, J., Chicote, M.-T., Gonzalez-Herrero, P., Jones, P. G., *J. Chem. Soc., Chem. Commun.* **1995**, (7), 745–746.
- (9) Guo, Y.-R., Pan, Q.-J., Fang, G.-Z., Liu, Z.-M., *Chem. Phys. Lett.* **2005**, *413* (1–3), 59–64.
- (10) Rossner, C. *Tuning the interaction of RAFT polymers with gold nanoparticles*, thesis, Georg-August-Universität Göttingen, **2013**.
- (11) Rossner, C., Ebeling, B., Vana, P., *ACS Macro Lett.* **2013**, *2*, 1073–1076.
- (12) Wang, T., LaMontagne, D., Lynch, J., Zhuang, J., Cao, Y. C., *Chem. Soc. Rev.* **2013**, *42* (7), 2804–2823.
- (13) Frankamp, B. L., Boal, A. K., Rotello, V. M., *J. Am. Chem. Soc.* **2002**, *124* (51), 15146–15147.
- (14) Lim, I.-I. S., Vaiana, C., Zhang, Z.-Y., Zhang, Y.-J., An, D.-L., Zhong, C.-J., *J. Am. Chem. Soc.* **2007**, *129* (17), 5368–5369.
- (15) Huang, S., Minami, K., Sakaue, H., Shingubara, S., Takahagi, T., *J. Appl. Phys.* **2002**, *92* (12), 7486–7490.
- (16) Briñas, R. P., Maetani, M., Jr., J. J. B., *J. Colloid Interface Sci.* **2013**, *392*, 415–421.
- (17) Lian, X., Jin, J., Tian, J., Zhao, H., *ACS Appl. Mater. Interfaces* **2010**, *2* (8), 2261–2268.
- (18) Li, J. F., Huang, Y. F., Ding, Y., Yang, Z. L., Li, S. B., Zhou, X. S., Fan, F. R., Zhang, W., Zhou, Z. Y., Wu, D. Y., Ren, B., Wang, Z. L., Tian, Z. Q., *Nature* **2010**, *464* (7287), 392–395.
- (19) Xie, W., Walkenfort, B., Schluecker, S., *J. Am. Chem. Soc.* **2013**, *135* (5), 1657–1660.
- (20) Lin, S.-Y., Tsai, Y.-T., Chen, C.-C., Lin, C.-M., Chen, C.-h., *J. Phys. Chem. B* **2004**, *108* (7), 2134–2139.
- (21) Chen, K., Robinson, H., *J. Nanopart. Res.* **2011**, *13* (2), 751–761.
- (22) Lee, H. B., Yoo, Y. M., Han, Y.-H., *Scripta Mater.* **2006**, *55* (12), 1127–1129.
- (23) Kalimuthu, P., John, S. A., *Mater. Chem. Phys.* **2010**, *122* (2–3), 380–385.
- (24) Zhang, J., Wang, X., Yang, X., *Analyst* **2012**, *137* (12), 2806–2812.

- (25) Wang, Y., Zeiri, O., Neyman, A., Stellacci, F., Weinstock, I. A., *ACS Nano* **2012**, 6 (1), 629–640.
- (26) Guarise, C., Pasquato, L., Scrimin, P., *Langmuir* **2005**, 21 (12), 5537–5541.
- (27) Nooney, R., Dhanasekaran, T., Chen, Y., Josephs, R., Ostafin, A., *Adv. Mater.* **2002**, 14 (7), 529–532.
- (28) Baranov, D., Kadnikova, E. N., *J. Mater. Chem.* **2011**, 21 (17), 6152–6157.
- (29) Matthiesen, J. E., Jose, D., Sorensen, C. M., Klabunde, K. J., *J. Am. Chem. Soc.* **2012**, 134 (22), 9376–9379.
- (30) Ansar, S. M., Perera, G. S., Jiang, D., Holler, R. A., Zhang, D., *J. Phys. Chem. C* **2013**, 117 (17), 8793–8798.
- (31) Dess, D. B., Martin, J. C., *J. Am. Chem. Soc.* **1991**, 113 (19), 7277–7287.
- (32) Nishi, H., Kobatake, S., *Dyes Pigm.* **2012**, 92 (2), 847–853.
- (33) Canaria, C. A., Smith, J. O., Yu, C., Fraser, S. E., Lansford, R., *Tetrahedron Lett.* **2005**, 46 (28), 4813–4816.
- (34) Balinski, A. *Improved Synthesis of Tetraethylene Glycol-Derived Thiol for Monolayer-Protected Gold Nanoparticles*, thesis, Vanderbilt University, Nashville, Tennessee, **2010**.
- (35) Gibson, M. I., O'Reilly, R. K., *Chem. Soc. Rev.* **2013**, 42 (17), 7204–7213.
- (36) Sabella, S., Brunetti, V., Vecchio, G., Galeone, A., Maiorano, G., Cingolani, R., Pompa, P., *J. Nanopart. Res.* **2011**, 13 (12), 6821–6835.
- (37) Wang, S., Lawson, R., Ray, P. C., Yu, H., *Toxicol. Ind. Health* **2011**, 27 (6), 547–554.
- (38) Vecchio, G., Galeone, A., Brunetti, V., Maiorano, G., Sabella, S., Cingolani, R., Pompa, P. P., *PLoS ONE* **2012**, 7 (1), e29980.
- (39) Freese, C., Ubaldi, C., Gibson, M., Unger, R., Weksler, B., Romero, I., Couraud, P.-O., Kirkpatrick, C., *Part. Fibre Toxicol.* **2012**, 9 (1), 23.
- (40) Sabella, S., Galeone, A., Vecchio, G., Cingolani, R., Pompa, P. P., *J. Nanosci. Lett.* **2011**, 1 (3), 145–165.
- (41) Treuel, L., Malissek, M., Grass, S., Diendorf, J., Mahl, D., Meyer-Zaika, W., Epple, M., *J. Nanopart. Res.* **2012**, 14 (9), 1–12.
- (42) Zhang, X.-D., Wu, H.-Y., Wu, D., Wang, Y.-Y., Chang, J.-H., Zhai, Z.-B., Meng, A.-M., Liu, P.-X., Zhang, L.-A., Fan, F.-Y., *Int. J. Nanomed.* **2010**, 5, 771–781.
- (43) Zhang, X.-D., Wu, D., Shen, X., Liu, P.-X., Yang, N., Zhao, B., Zhang, H., Sun, Y.-M., Zhang, L.-A., Fan, F.-Y., *Int. J. Nanomed.* **2011**, 6, 2071–2081.
- (44) Aslan, K., Pérez-Luna, V. H., *Langmuir* **2002**, 18 (16), 6059–6065.
- (45) Chakraborty, S., Bishnoi, S. W., Pérez-Luna, V. H., *J. Phys. Chem. C* **2010**, 114 (13), 5947–5955.
- (46) Shen, C.-C., Tseng, W.-L., Hsieh, M.-M., *J. Chromatogr. A* **2012**, 1220, 162–168.
- (47) Zhang, Z., Zhang, J., Qu, C., Pan, D., Chen, Z., Chen, L., *Analyst* **2012**, 137 (11), 2682–2686.
- (48) Kryachko, E., Remacle, F., *Chem. Phys. Lett.* **2005**, 404 (1–3), 142–149.
- (49) Kryachko, E. S., Remacle, F., *Nano Lett.* **2005**, 5 (4), 735–739.
- (50) Kryachko, E. S., Remacle, F., *J. Phys. Chem. B* **2005**, 109 (48), 22746–22757.

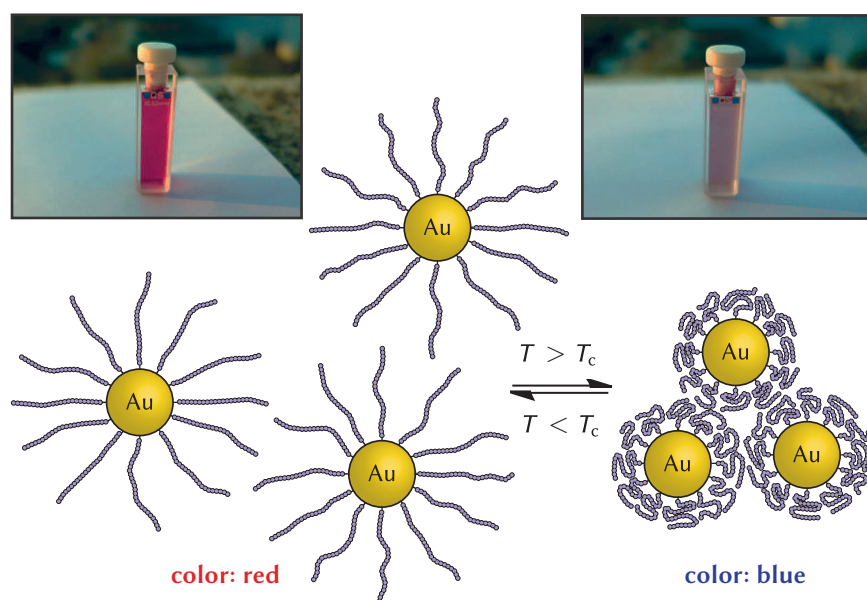
- (51) Aqil, A., Qiu, H., Greisch, J.-F., Jérôme, R., Pauw, E. D., Jérôme, C., *Polymer* **2008**, 49 (5), 1145–1153.
- (52) Li, D., He, Q., Li, J., *Adv. Colloid Interface Sci.* **2009**, 149 (1–2), 28–38.
- (53) Beija, M., Marty, J.-D., Destarac, M., *Prog. Polym. Sci.* **2011**, 36 (7), 845–886.
- (54) Boyer, C., Stenzel, M. H., Davis, T. P., *J. Polym. Sci., Part A: Polym. Chem.* **2011**, 49 (3), 551–595.
- (55) Lowe, A. B., Sumerlin, B. S., Donovan, M. S., McCormick, C. L., *J. Am. Chem. Soc.* **2002**, 124 (39), 11562–11563.
- (56) Sumerlin, B. S., Lowe, A. B., Stroud, P. A., Zhang, P., Urban, M. W., McCormick, C. L., *Langmuir* **2003**, 19 (14), 5559–5562.
- (57) Han, D.-H., Pan, C.-Y., *J. Polym. Sci., Part A: Polym. Chem.* **2008**, 46 (1), 341–352.
- (58) Gibson, M. I., Danial, M., Klok, H.-A., *ACS Comb. Sci.* **2011**, 13 (3), 286–297.
- (59) Glaria, A., Beija, M., Bordes, R., Destarac, M., Marty, J.-D., *Chem. Mater.* **2013**, 25 (9), 1868–1876.
- (60) Hotchkiss, J. W., Lowe, A. B., Boyes, S. G., *Chem. Mater.* **2007**, 19 (1), 6–13.
- (61) Boyer, C., Whittaker, M. R., Luzon, M., Davis, T. P., *Macromolecules* **2009**, 42 (18), 6917–6926.
- (62) Boyer, C., Whittaker, M. R., Nouvel, C., Davis, T. P., *Macromolecules* **2010**, 43 (4), 1792–1799.
- (63) Liu, J., Setijadi, E., Liu, Y., Whittaker, M. R., Boyer, C., Davis, T. P., *Aust. J. Chem.* **2010**, 63 (8), 1245–1250.
- (64) Liang, M., Lin, I.-C., Whittaker, M. R., Minchin, R. F., Monteiro, M. J., Toth, I., *ACS Nano* **2010**, 4 (1), 403–413.
- (65) Lin, I.-C., Liang, M., Liu, T.-Y., Ziora, Z. M., Monteiro, M. J., Toth, I., *Biomacromolecules* **2011**, 12 (4), 1339–1348.
- (66) Wang, Z.-L., Xu, J.-T., Du, B.-Y., Fan, Z.-Q., *J. Colloid Interface Sci.* **2011**, 360 (2), 350–354.
- (67) Wang, Z.-L., Xu, J.-T., Du, B.-Y., Fan, Z.-Q., *J. Colloid Interface Sci.* **2012**, 384 (1), 29–37.
- (68) Uppal, M. A., Kafizas, A., Ewing, M. B., Parkin, I. P., *New J. Chem.* **2010**, 34 (12), 2906–2914.
- (69) Ebeling, B., Vana, P., *Macromolecules* **2013**, 46 (12), 4862–4871.
- (70) Whitesides, G. M., Grzybowski, B., *Science* **2002**, 295 (5564), 2418–2421.
- (71) Grzelczak, M., Vermant, J., Furst, E. M., Liz-Marzán, L. M., *ACS Nano* **2010**, 4 (7), 3591–3605.
- (72) Moffitt, M. G., *J. Phys. Chem. Lett.* **2013**, 4, 3654–3666.
- (73) Qian, L., Zhai, S., Jiang, Y., Das, B., *J. Mater. Chem.* **2012**, 22 (11), 4932–4937.
- (74) Contreras-Cáceres, R., Sánchez-Iglesias, A., Karg, M., Pastoriza-Santos, I., Pérez-Juste, J., Pacifico, J., Hellweg, T., Fernández-Barbero, A., Liz-Marzán, L. M., *Adv. Mater.* **2008**, 20 (9), 1666–1670.
- (75) Karg, M., Pastoriza-Santos, I., Liz-Marzán, L. M., Hellweg, T., *Chem. Phys. Chem.* **2006**, 7 (11), 2298–2301.
- (76) Chen, H. Y., Abraham, S., Mendenhall, J., Delamarre, S. C., Smith, K., Kim, I., Batt, C. A., *ChemPhysChem* **2008**, 9 (3), 388–392.
- (77) Sashuk, V., Hołyst, R., Wojciechowski, T., Górecka, E., Fiałkowski, M., *Chem.—Eur. J.* **2012**, 18 (8), 2235–2238.

- (78) Boyer, C., Whittaker, M. R., Chuah, K., Liu, J., Davis, T. P., *Langmuir* **2010**, 26 (4), 2721–2730.
- (79) Martin, J. E., Wilcoxon, J. P., Odinek, J., Provencio, P., *J. Phys. Chem. B* **2000**, 104 (40), 9475–9486.
- (80) Ohno, K., Koh, K., Tsujii, Y., Fukuda, T., *Angew. Chem., Int. Ed.* **2003**, 42 (24), 2751–2754.
- (81) Picco, A. S., Zelaya, E., Azzaroni, O., Ceolín, M., *J. Colloid Interface Sci.* **2013**, 397, 206–209.
- (82) Gnanou, Y., Fontanille, M., *Organic and Physical Chemistry of Polymers*; Wiley Interscience: New York: **2008**.
- (83) Ohno, K., Koh, K.-m., Tsujii, Y., Fukuda, T., *Macromolecules* **2002**, 35 (24), 8989–8993.
- (84) Goodman, D., Kizhakkedathu, J. N., Brooks, D. E., *Langmuir* **2004**, 20 (8), 3297–3303.
- (85) Nykänen, A., Nuopponen, M., Hiekkataipale, P., Hirvonen, S.-P., Soininen, A., Tenhu, H., Ikkala, O., Mezzenga, R., Ruokolainen, J., *Macromolecules* **2008**, 41 (9), 3243–3249.
- (86) Badia, A., Singh, S., Demers, L., Cuccia, L., Brown, G. R., Lennox, R. B., *Chem.—Eur. J.* **1996**, 2 (3), 359–363.
- (87) Kim, J. Y., Raja, S., Stellacci, F., *Small* **2011**, 7 (17), 2526–2532.
- (88) Wang, Z. L., Harfenist, S. A., Whetten, R. L., Bentley, J., Evans, N. D., *J. Phys. Chem. B* **1998**, 102 (17), 3068–3072.
- (89) Vogel, N., Fernández-López, C., Pérez-Juste, J., Liz-Marzán, L. M., Landfester, K., Weiss, C. K., *Langmuir* **2012**, 28 (24), 8985–8993.
- (90) Duner, G., Thormann, E., Dedinaite, A., Claesson, P. M., Matyjaszewski, K., Tilton, R. D., *Soft Matter* **2012**, 8 (32), 8312–8320.
- (91) Hlawacek, G., Ahmad, I., Smithers, M. A., Kooij, E. S., *Ultramicroscopy* **2013**, 135, 89–94.
- (92) Al-Somali, A. M., Krueger, K. M., Falkner, J. C., Colvin, V. L., *Anal. Chem.* **2004**, 76 (19), 5903–5910.
- (93) Sperling, R. A., Liedl, T., Duhr, S., Kudera, S., Zanella, M., Lin, C.-A. J., Chang, W. H., Braun, D., Parak, W. J., *J. Phys. Chem. C* **2007**, 111 (31), 11552–11559.
- (94) Wolpers, A., Russell, G. T., Vana, P., *Macromol. Theory Simul.* **2011**, 20 (8), 667–674.
- (95) Busnel, J., Foucault, F., Denis, L., Lee, W., Chang, T., *J. Chromatogr. A* **2001**, 930 (1–2), 61–71.
- (96) Lin, C.-A. J., Yang, T.-Y., Lee, C.-H., Huang, S. H., Sperling, R. A., Zanella, M., Li, J. K., Shen, J.-L., Wang, H.-H., Yeh, H.-I., Parak, W. J., Chang, W. H., *ACS Nano* **2009**, 3 (2), 395–401.
- (97) Du, B., Zhao, B., Tao, P., Yin, K., Lei, P., Wang, Q., *Colloids Surf., A* **2008**, 317 (1–3), 194–205.
- (98) Du, B., Chen, X., Zhao, B., Mei, A., Wang, Q., Xu, J., Fan, Z., *Nanoscale* **2010**, 2 (9), 1684–1689.
- (99) Wallner, A., Jafri, S. H. M., Blom, T., Gogoll, A., Leifer, K., Baumgartner, J., Ottosson, H., *Langmuir* **2011**, 27 (14), 9057–9067.
- (100) Vitale, F., Fratoddi, I., Battocchio, C., Piscopiello, E., Tapfer, L., Russo, M., Polzonetti, G., Gianini, C., *Nanoscale Res. Lett.* **2011**, 6 (1), 1–9.

Chapter 9

Future perspectives

In this chapter, selected experiments are presented which are seminal for more detailed systematic examinations. Also, possible future studies building upon concepts presented in this work are discussed.



Scheme 9.1: Reversible aggregation of aqueous solutions of pNIPAM–AuNP nanohybrids with 50 mmol L^{-1} NaCl at the cloud temperature T_c of pNIPAm. The illustration shows conventional nanohybrids, but the effect was also verified for multiblock nanohybrids. Also compare Scheme 1.4 in Section 1.2.2.1. The two inlays show photographs of an aqueous solution of $\text{AuK}^{\text{TTC}}\text{-II}$ at 22 °C (left) and approximately 40 °C (right).

In Section 8.3.2, the multiresponsive pNIPAm samples (Section 5.4) were coated on AuNPs $_{\text{Au}}^{\text{ci}}\mathbf{v-3}$ from reduction with citrate (Section 5.1.2), yielding the water-soluble nanohybrids $_{\text{Au}}\mathbf{K^{TTC-9}}$ to $_{\text{Au}}\mathbf{K^{MB-21}}$. The thermochromic properties of these nanohybrids at atmospheric pressure were not examined systematically in this work, since the observed behavior did not differ notably from that of similar systems already studied in literature.^[1,2] Yusa *et al.*^[1] (2007) showed by quasi-elastic light scattering that the pNIPAm shells of nanohybrids with AuNP cores collapse reversibly and the hydrodynamic radius shrinks, when the aqueous solution is heated above the cloud temperature. However, the color of the colloidal solution remains red, because the nanohybrids remain metastably dispersed. This effect might be caused by the very low polymer concentration in these dispersions. At higher concentrations, the system is too intensely colored, so that it will appear black, regardless of the aggregation state (see the photos in Figure 1.7, Section 1.2.3.2). Yusa *et al.* showed that the kinetic barrier of aggregation can be overcome by adding the small amount of 50 mmol L⁻¹ NaCl to the solution.^[1,3] This is only 1/40 of the concentration used in the measurement shown in Figure 6.8 (Section 6.4.1.1) and should not have a significant effect on the cloud-point curve. After addition of NaCl, the nanohybrids aggregate instantly, as soon as the cloud temperature is exceeded, a bathochromic shift* of the plasmon resonance band is observed (compare Section 1.2.3.2) and the color of the dispersion turns from red to blue. This process is illustrated in Scheme 9.1. Such thermochromic properties were found for both the conventional and the multiblock nanohybrids. No indication was found for the assumption that the number of switching cycles would be limited by any effect. In future studies, the thermochromic behavior of all samples could be studied systematically, after different organic are added to the aqueous systems.

After the exciting findings regarding the effect of high pressures on the phase behavior of aqueous solution of the pure pNIPAm samples in Section 6, the next logical step was to find out if the results obtained in this chapter can be transferred to nanohybrids comprising of the same polymers. Unlike planned, this turned out to be impossible with the used high-pressure apparatus, because of the limitation that the borescope camera provided only a black and white image (see Figure 6.2 in Section 6.2) and the color change from red to blue was not accompanied by a visible clouding of the solution. If the concentration was raised, the red color became so intense (compare the photos in Figure 1.7) that the solution always appeared completely dark in the borescope camera's image. The only way to get around these experimental limitations would be the modification of the set-up, either by

* Change of spectral band position in the absorption, reflectance, transmittance, or emission spectrum of a molecule to a longer wavelength.

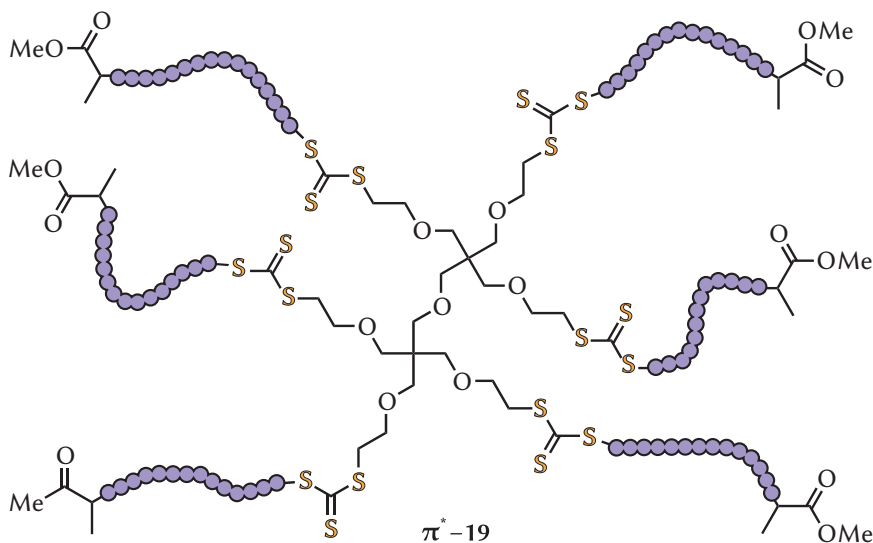


Fig. 9.1: Chemical structure of the used NIPAm star polymer π^*-19 ($\overline{M}_n = 2.07 \times 10^5 \text{ g mol}^{-1}$). The pNIPAm blocks are represented by the purple “strings of beads”.

integrating a color camera or by reducing the path length of the cell. However, with the used set-up, it could be proven that the nanohybrids at least survive the high pressures of up to 3 000 bar without any disintegration. The examined dispersions remained red and transparent. This shows that the pNIPAm–gold nanohybrids are in principle applicable in high-pressure sensing or catalysis applications.

A model system which mimics the basic structure of the produced nanohybrids, but is however colorless, is the 6-arm star polymer π^*-19 ($\overline{M}_n = 2.07 \times 10^5 \text{ g mol}^{-1}$), also composed of pNIPAm and produced using a multifunctional RAFT agent. Its structure is shown schematically in Figure 9.1. The only structural differences are the lack of the gold core and the lower number of arms, but the major feature that the polymer chains are in close proximity to each other in the center is identical. Figure 9.2 shows a cloud-point curve of an aqueous solution of π^*-19 in comparison with the curve of an aqueous solution of the linear pNIPAm sample $\pi-7a$, having an average molar mass approximately coinciding with the mass of each arm of π^*-19 . They were measured as described in Section 6, but with a lower polymer concentration of $c = 1.0 \text{ g mol}^{-1}$ in both cases, since the available material of π^*-19 was limited. Being in line with results obtained by other groups at atmospheric

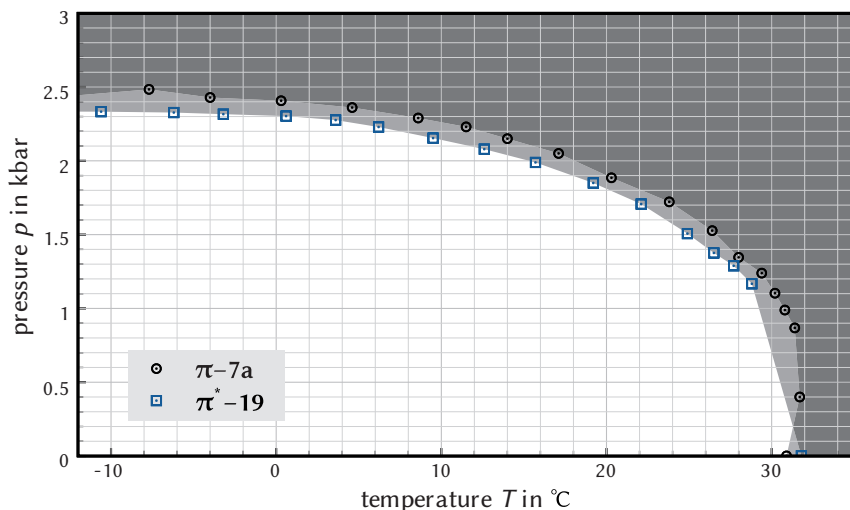


Fig. 9.2: Cloud-point curves of the NIPAm star polymer π^*-19 and the linear pNIPAm sample $\pi-7a$ with a molar mass corresponding approximately to the mass of the star polymer's arms. The polymer concentration is $c = 1.0 \text{ g mol}^{-1}$ for both systems.

pressure,^[4,5] both curves in Figure 9.2 are very similar. The small shift is presumably due to the higher hydrophilicity of the star polymer's end groups,^[6] which also explains the converse behavior in the high-temperature and in the low-temperature region (see Section 6.3.2). These findings are a clear indicator for the assumption that the results obtained in Chapter 6 can also be applied to the conventional pNIPAm–gold nanohybrids $\text{Au}\kappa^{\text{TTC}}-9$ to $\text{Au}\kappa^{\text{TTC}}-16$, presumably—but with less certainty—also to the multiblock nanohybrids $\text{Au}\kappa^{\text{MB}}-17$ to $\text{Au}\kappa^{\text{MB}}-21$ prepared in this work.

Other properties of the produced nanohybrids could also be studied in future. For example, one could expect that the multiblock nanohybrids are more stable than the conventional ones, thanks to the multiple polymer–gold junction points. The stability could be surveyed by slow addition of dithiothreitol^[7] or iodine^[8] to the dispersions, while monitoring their optical spectrum in a spectrophotometer. It seems also reasonable to expect that the polymer loops on the surface of the multiblock polymers exhibit a lower shielding effect towards small molecules and thus render the nanohybrids more active in catalysis applications. The samples produced in this work, conventional nanohybrids with increasing shell thickness and multiblock nanohybrids, are an excellent basis for comparative experiments.

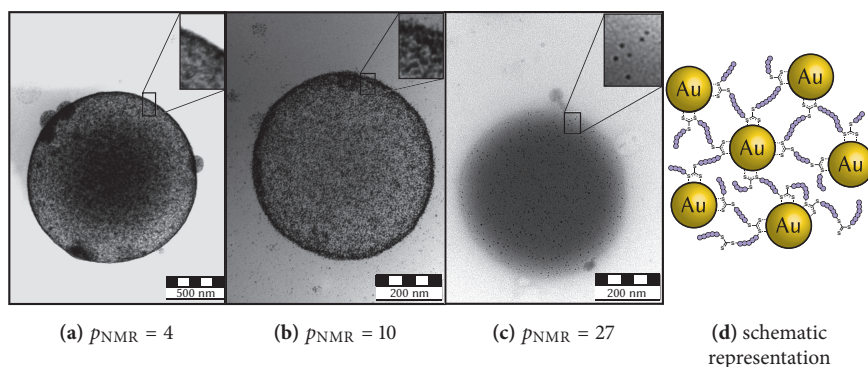


Fig. 9.3: Spherical AuNP assemblies interconnected by styrene multiblock polymers with 5.7 trithiocarbonate groups and different degrees of polymerization p_{NMR} . (Reprinted and adapted with permission from a previous publication.^[9] Copyright 2013 American Chemical Society.)

It should also be mentioned at this point that a part of the studies presented here was continued by Christian Roßner.^[9–11] He grafted multiblock styrene polymers with low molar masses (prepared as in Section 5.4.4) to ex-situ Brust–Schiffrin AuNPs (Section 5.1.3.3) and obtained stable spherical AuNP superstructures dispersed in toluene. By the degree of polymerization p_{NMR} (referring to the individual blocks and determined by NMR spectroscopy) and thus the lengths of the oligomeric blocks interconnected by the trithiocarbonate groups, the interparticle distances in these assemblies could be finely tuned. Figure 9.3 shows three TE micrographs of these spherical superparticles with different p_{NMR} values (Figure 9.3a–c). The interparticle distances increase visibly. Figure 9.3d shows a schematic representation of these structures. Colloidal superparticles of this type are useful for a range of applications^[12–21] and it seems very worthwhile to continue the studies of these hybrid structures.^[22]

New advanced nanohybrid structures could also be formed in future studies by employing polymers of other architectures in the presented functionalization protocol for citrate AuNPs $\text{Au}^{\text{ci}}\mathbf{v-3}$ (Section 8.3.2). A first candidate could be the pNIPAm star polymer $\pi^*\mathbf{-19}$ in Figure 9.1. In $\pi^*\mathbf{-19}$, the trithiocarbonate groups are in the middle of the star polymer, but one could also prepare a star polymer with peripheral trithiocarbonate groups using a modified RAFT agent to this end. It is hard to predict if the employment of such an R-RAFT star polymer would lead to interparticle crosslinking in the AuNP functionalization process. It seems also

promising to produce water soluble multisegmented copolymers (as outlined in Section 5.4.4), use them in the functionalization process, and examine whether the products possess particular properties. An alternative approach could be to employ the multiblock nanohybrids $\text{Au}\kappa^{\text{MB}}\text{-17}$ to $\text{Au}\kappa^{\text{MB}}\text{-21}$ produced in this work in a second radical polymerization. The anchoring trithiocarbonate groups (or a fraction of them) might be still accessible as mediating groups.

The several building blocks presented in this work could also be used for the production of novel nanohybrids in different modular combinations. As an example, the RAFT agent $\text{fsP}^{2\text{x}}\text{-1}$ with two anchor groups, which was used for polymerizations on fumed silica in Section 7.1, could be employed to form an interconnected network of the hydroxyl-functionalized AuNPs $\text{Au}\nu^{\text{OH}}\text{-9}$ or $\text{Au}\nu^{\text{OH}}\text{-13}$ on a silicon surface.^[23] After a RAFT polymerization of NIPAm, the AuNPs would be very evenly dispersed within the polymer matrix, because the polymer links would all possess the same chain length, which is moreover specifically tunable by the polymerization time. Since the polymer links are constantly rearranged in the RAFT polymerization, no strain would be present in the resulting very stable structure. Highly miniaturized multiresponsive sensors could thus be created.^[24–27]

References for Chapter 9

- (1) Yusa, S.-i., Fukuda, K., Yamamoto, T., Iwasaki, Y., Watanabe, A., Akiyoshi, K., Morishima, Y., *Langmuir* **2007**, 23 (26), 12842–12848.
- (2) Hermes, J. P., Sander, F., Peterle, T., Cioffi, C., Ringler, P., Pfohl, T., Mayor, M., *Small* **2011**, 7 (7), 920–929.
- (3) Zhang, Z., Maji, S., Antunes, A. B. d. F., De Rycke, R., Zhang, Q., Hoogenboom, R., De Geest, B. G., *Chem. Mater.* **2013**, 25 (21), 4297–4303.
- (4) Plummer, R., Hill, D. J. T., Whittaker, A. K., *Macromolecules* **2006**, 39 (24), 8379–8388.
- (5) Lambeth, R. H., Ramakrishnan, S., Mueller, R., Poziemski, J. P., Miguel, G. S., Markoski, L. J., Zukoski, C. F., Moore, J. S., *Langmuir* **2006**, 22 (14), 6352–6360.
- (6) Furyk, S., Zhang, Y., Ortiz-Acosta, D., Cremer, P. S., Bergbreiter, D. E., *J. Polym. Sci., Part A: Polym. Chem.* **2006**, 44 (4), 1492–1501.
- (7) Anderson, M., Torres-Chavolla, E., Castro, B., Alocilja, E., *J. Nanopart. Res.* **2011**, 13 (7), 2843–2851.
- (8) Kim, J.-B., Bruening, M. L., Baker, G. L., *J. Am. Chem. Soc.* **2000**, 122 (31), 7616–7617.
- (9) Rossner, C., Ebeling, B., Vana, P., *ACS Macro Lett.* **2013**, 2, 1073–1076.
- (10) Rossner, C., *Tuning the interaction of RAFT polymers with gold nanoparticles*, thesis, Georg-August-Universität Göttingen, **2013**.
- (11) Rossner, C., Ebeling, B., Vana, P., *ACS Symp. Ser.* **2015**, in press.
- (12) Wang, L., Xu, L., Kuang, H., Xu, C., Kotov, N. A., *Acc. Chem. Res.* **2012**, 45 (11), 1916–1926.
- (13) Wang, T., LaMontagne, D., Lynch, J., Zhuang, J., Cao, Y. C., *Chem. Soc. Rev.* **2013**, 42 (7), 2804–2823.
- (14) Elghanian, R., Storhoff, J. J., Mucic, R. C., Letsinger, R. L., Mirkin, C. A., *Science* **1997**, 277 (5329), 1078–1081.
- (15) Nam, J., La, W.-G., Hwang, S., Ha, Y. S., Park, N., Won, N., Jung, S., Bhang, S. H., Ma, Y.-J., Cho, Y.-M., Jin, M., Han, J., Shin, J.-Y., Wang, E. K., Kim, S. G., Cho, S.-H., Yoo, J., Kim, B.-S., Kim, S., *ACS Nano* **2013**, 7 (4), 3388–3402.
- (16) Frankamp, B. L., Boal, A. K., Rotello, V. M., *J. Am. Chem. Soc.* **2002**, 124 (51), 15146–15147.
- (17) Hao, E., Schatz, G. C., *J. Chem. Phys.* **2004**, 120 (1), 357–366.
- (18) DeVries, G. A., Brunnbauer, M., Hu, Y., Jackson, A. M., Long, B., Neltner, B. T., Uzun, O., Wunsch, B. H., Stellacci, F., *Science* **2007**, 315 (5810), 358–361.
- (19) Maye, M. M., Chun, S. C., Han, L., Rabinovich, D., Zhong, C.-J., *J. Am. Chem. Soc.* **2002**, 124 (18), 4958–4959.
- (20) Zhang, C., Macfarlane, R. J., Young, K. L., Choi, C. H. J., Hao, L., Auyeung, E., Liu, G., Zhou, X., Mirkin, C. A., *Nat. Mater.* **2013**, 12 (8), 741–746.
- (21) Schreiber, R., Do, J., Roller, E.-M., Zhang, T., Schuller, V. J., Nickels, P. C., Feldmann, J., Liedl, T., *Nat. Nano.* **2014**, 9 (1), 74–78.
- (22) Boal, A., Ilhan, F., DeRouchey, J., Thurn-Albrecht, T., Russell, T., Rotello, V., *Nature* **2000**, 404 (6779), 746–748.

-
- (23) Srivastava, S., Agarwal, P., Archer, L. A., *Langmuir* **2012**, 28 (15), 6276–6281.
 - (24) Dahlin, A. B., *Sensors* **2012**, 12 (3), 3018–3036.
 - (25) Tokarev, I., Minko, S., *Soft Matter* **2012**, 8 (22), 5980–5987.
 - (26) Lange, H., Juárez, B. H., Carl, A., Richter, M., Bastús, N. G., Weller, H., Thomsen, C., von Klitzing, R., Knorr, A., *Langmuir* **2012**, 28 (24), 8862–8866.
 - (27) Szunerits, S., Boukherroub, R., *Chem. Commun.* **2012**, 48 (72), 8999–9010.

Chapter 10

Conclusions

With a view back to the initial goals of the work presented here (Section 5), it can be stated that for the production of polymer–inorganic nanohybrids, the special features of RAFT polymerization could indeed be utilized to full capacity in this work.

Although the concept of the mechanistically unique Z-RAFT polymerization has already been quite widely applied, it could be shown how special modifications in the structure of Z-RAFT agents can make them specifically adapted for different types of silica substrates. The performed polymerizations illustrate that nanohybrids composed of the same components (silica and polymers) can still have completely different structures and properties.

The findings that the effect of cononsolvents added to aqueous solutions of pNIPAm is literally turned upside down when high pressures are applied added a completely new aspect to the multiresponsive behavior of these systems. The results could be reasonably explained using both models which are currently discussed in the scientific community: It is disputed whether polymer–solvent interactions or solvent–solvent interactions are the main driving force behind the effect of cononsolvency. The observations made here could not definitely elucidate which model is better suited to describe the phenomenon. However, either way, the assumption could be reaffirmed that the mechanisms of the temperature-induced clouding (at low pressures) and the pressure-induced clouding (at low temperatures) are substantially different.

It was found that using the trithiocarbonate groups in conventional RAFT polymers as anchor groups for the coating of citrate AuNPs was a more convenient method than reducing the trithiocarbonate groups to thiols in a preceding step, while not yielding polymer–gold nanohybrids of a lower quality. On the contrary, the increasing interparticle spacings in the hexagonal lattices observed via TEM analysis indicated a very high grafting density. The high strength of the bond between the trithiocarbonate group and gold could be demonstrated by the exceptionally

high stability of *ex-situ* Brust–Schiffrin AuNPs covered with a trithiocarbonate RAFT agent and by the fact that citrate AuNPs stabilized with polymers without trithiocarbonate groups did not exhibit long-term stability.

RAFT polymerization also enabled the very straightforward synthesis of polymers with multiple trithiocarbonate groups incorporated along their backbone chain. A clear answer could eventually be given to the initially posed question as to which nanostructures would form when these multiblock polymers are employed for the functionalization of AuNPs. In the case of citrate AuNPs, it could be proven by the unexpectedly short and constant interparticle distances found by TEM and the very narrow SEC traces that the multiblock polymers are wrapped around the individual gold nanocrystals, connected to the gold core through multiple junctions. Along with the use of a doubly anchored RAFT agent, yet another pathway for polymer loops on surfaces was thus found. On the other hand, the addition of multiblock styrene polymers to the smaller and less reactive AuNPs from the *ex-situ* two-phase Brust–Schiffrin synthesis led to spherical superstructures of interconnected AuNPs. The reasons for these different behaviors remain to be elucidated.

Based on the results of this work, it can be concluded that nanohybrids of polymers and AuNPs are better prepared by grafting-to methods, rather than following a grafting-from strategy, due to the reactive surface and the high lability of AuNPs. Nevertheless, although they were not used for the production of nanohybrids with polymers, the initial goal of producing hydroxyl-functionalized AuNPs could be achieved as well. They were obtained in three different size dimensions, having approximately 10^2 , 10^3 , and 10^5 gold atoms in the core. These AuNPs could potentially be used as building blocks for the assembly of nanohybrids with preformed macromolecules.

The combination of the responsive properties of pNIPAm and the special optical features of gold nanocrystals led indeed to a material with thermochromic and most likely piezochromic properties. The results of this work indicate that the optical response of the smart nanohybrids to temperature and pressure variation can moreover be fine-tuned by the addition of organic solvents.

Appendices

The appendices comprise the full code of the conversion script which has been presented in Section 4.2, the index, and finally information about the author of this work.

Appendix A

Code of the conversion script

This is the code of the PYTHON-script explained in Section 4.2 which can be used to convert the “.txt” output files from GWYDDION (z-value matrix) to “.obj” files that can be read with MeshLab. The script can also be downloaded as extra material from <http://extras.springer.com/>.

```
1  #!/usr/bin/env python
2
3  # convert.py -- converts z-value matrix files of AFM scans
   into OBJ files for use with MeshLab or Blender
4  # created for python 2.7
5  # Copyright (C) 2012--2014 Martin Eggers & Bastian Ebeling
6
7  # This program is free software: you can redistribute it
   and/or modify
8  # it under the terms of the GNU General Public License
   version 3, as published by
9  # the Free Software Foundation.
10
11 # This program is distributed in the hope that it will be
   useful,
12 # but WITHOUT ANY WARRANTY; without even the implied
   warranty of
13 # MERCHANTABILITY or FITNESS FOR A PARTICULAR PURPOSE. See
   the
14 # GNU General Public License for more details.
15
16 # <http://www.gnu.org/licenses/>
17
18 import argparse # for parsing command line arguments
19 import os.path # for extension splitting
20 import sys      # for command line
21
22 # write a string to a text file
23 def write_file(text,filename):
24     fh_write=open(filename,"w")
25     fh_write.write(text)
```

```

26     fh_write.close()
27
28     # read file to a string
29     def read_file(filename):
30         fh_read=open(filename,'r')
31         input=fh_read.read()
32         return input
33
34     # strip extension from filename
35     def strip_extension(filename):
36         return os.path.splitext(filename)[0]
37
38     # replaces substrings in string with strings from list
39     def replace(string, list):
40         result=string
41         for couple in list:
42             result = result.replace(couple[0],couple[1])
43         return result
44
45     # class for the converter
46     class Converter:
47         def __init__(self, filename=''):
48             self.vdlist=[]
49             self.fdlist=[]
50             self.ndlist=[]
51             self.sources=[]           #each source creates vd/fd and
52                                     adds to list
53             self.sinks=[]
54             if filename != '':
55                 self.add_source(filename)
56
57         def add_source(self, filename):
58             ext = os.path.splitext(filename)[1]
59             if ext == '.obj':
60                 self.sources.append(MeshInput(filename))
61             elif ext == '.txt':
62                 self.sources.append(TextInput(filename))
63
64         def add_sink(self, type):
65             if type == 'MESH':
66                 self.sinks.append(MeshOutput())
67
68         def read(self):
69             for source in self.sources:
70                 source.parse()
71                 self.vdlist.append(source.vd)
72                 self.fdlist.append(source.fd)
73                 self.ndlist.append(source.nd)

```

```

74     def write(self):
75         assert len(self.vdlist) == len(self.fdlist)
76         for sink in self.sinks:
77             for idx,vd in enumerate(self.vdlist):
78                 sink.write(self.sources[idx].filename, self.vdlist[
                    idx], self.fdlist[idx], self.ndlist[idx])
79
80     class TextInput:
81         def __init__(self, filename):
82             self.filename = filename
83             self.vd=VertexData()
84             self.fd=None
85             self.nd=None
86
87         def parse(self):
88             fh_read=open(self.filename,"r")
89             input=fh_read.readlines()
90             cml = 0
91             for idx1,line in enumerate(input):
92                 # ignore file header, commented with hash
93                 if line.split(" ")[0]=="#":
94                     cml=cml+1
95                     continue
96                 linesplit = line.rstrip("\n").split("\t")
97                 for idx2,element in enumerate(linesplit):
98                     vec = [float(idx1-cml),float(idx2),float(element)]
99                     self.vd.add(vec)
100             fh_read.close()
101
102             # generate face data
103             self.fd=FaceData(self.vd.xcount(),self.vd.ycount())
104
105     class MeshInput:
106         def __init__(self, filename):
107             self.filename = filename
108             self.vd=VertexData()
109             self.fd=FaceData()
110             self.nd=NormalData()
111
112         def parse(self):
113             fh_read=open(self.filename,"r")
114             input=fh_read.readlines()
115             cml = 0
116             for line in input:
117                 split = line.split(" ")
118                 if split[0] == 'v': #vertex
119                     self.vd.add([float(split[1]),float(split[2]),float(
                        split[3])])
120                 elif split[0] == 'F': #face

```

```

121         vec = []
122         for element in split:
123             if element != 'F' and element.split('/')[-1] == -1:
124                 vec.append(int(element))
125             elif element != 'F' and element.split('/')[-1] !=
126                 -1:
127                 vec.append(int(element.split('/')[-1]))
128         self.fd.add(vec)
129         elif split[0] == 'vN': #vertex normal
130             vec = []
131             for element in split:
132                 if element != 'vN':
133                     vec.append(float(element))
134             self.nd.add(vec)
135         fh_read.close()
136
137     class MeshOutput:
138         def write(self, filename, vectors, faces, normals=None):
139             string=''
140             ext='.OBJ'
141             fn=strip_extension(filename)+ext
142             string += vectors.string('MESH')
143             string += faces.string('MESH')
144             write_file(string, fn)
145
146     # class for the vertex which is read directly from the text
147     file
148     # the file contains a N x M matrix of z-Values
149     class VertexData:
150         def __init__(self):
151             self.list=[]
152             self.max=[0,0,0]
153             self.count=[0,0]
154
155         def size(self):
156             return len(self.list)
157
158         def updmax(self, vec):
159             for idx,element in enumerate(vec):
160                 if element > self.max[idx]:
161                     self.max[idx] = element
162
163         def xcount(self):
164             return self.count[0]
165
166         def ycount(self):
167             return self.count[1]

```



```

168 def xmax(self):
169     return self.max[0]
170
171 def ymax(self):
172     return self.max[1]
173
174 def zmax(self):
175     return self.max[2]
176
177 def scale(self, vec):
178     if vec == [1,1,1]:
179         return
180     self.max=[0,0,0]
181     for idx1,vertex in enumerate(self.list):
182         assert(len(vertex) == len(vec))
183         tmp = []
184         for idx2,element in enumerate(vertex):
185             tmp.append(element*vec[idx2])
186         self.list[idx1] = tmp
187         self.updmax(tmp)
188
189 def translate(self, vec):
190     if vec == [0,0,0]:
191         return
192     self.max=[0,0,0]
193     for idx1,vertex in enumerate(self.list):
194         assert(len(vertex) == len(vec))
195         tmp = []
196         for idx2,element in enumerate(vertex):
197             tmp.append(element+vec[idx2])
198         self.list[idx1] = tmp
199         self.updmax(tmp)
200
201 def recenter(self):
202     self.translate([-self.xmax()/2,-self.ymax()/2,0])
203
204 def add(self, vec):
205     self.list.append(vec)
206     self.updmax(vec)
207     self.count=[self.max[0],self.max[1]]
208
209 def string(self, format):
210     assert(format == 'MESH')
211     result=''
212     if format == 'MESH':
213         result+='# List of vertices: \n'
214         for vertex in self.list:
215             result+='%v'
216             for element in vertex:

```

```

217         result+=', '+str(element)
218     result+=', '+1.0'\n'
219     return result
220
221
222 class FaceData:
223     def __init__(self, xmax=0, ymax=0):
224         self.list=[]
225         if xmax != 0 and ymax != 0:
226             self.generate(xmax,ymax)
227
228     def size(self):
229         return len(self.list)
230
231     def generate(self, xmax, ymax):
232         self.list=[]
233         xi = int(xmax)+1
234         yi = int(ymax)+1
235         for x in range(0,xi-1):
236             for y in range(0,yi-1):
237                 self.list.append([x*yi+1+y,(x+1)*yi+1+y,x*yi+2+y])
238             for y in range(0,yi-1):
239                 self.list.append([x*yi+2+y,(x+1)*yi+1+y,(x+1)*yi+2+
240                                 y])
241
242     def add(self, vec):
243         self.list.append(vec)
244
245     def string(self, format):
246         assert(format == 'MESH')
247         result=''
248         if format == 'MESH':
249             result+='# List of faces: \n'
250             for face in self.list:
251                 result+="F"
252                 for element in face:
253                     result+=', '+str(element)
254             result+='\n'
255         return result
256
257 # done with functions and classes; main program starts here
258
259 # command line arguments
260 parser = argparse.ArgumentParser(description='CONVERT RAW
261 DATA FROM AN AFM SCAN TO WAVEFRONT .OBJ FORMAT.')
262 parser.add_argument('FILENAME', nargs='*', type=str,help=
263     'NAME OF THE FILE CONTAINING THE RAW DATA.')
264 scaling = parser.add_mutually_exclusive_group()

```

```

262 scaling.add_argument('--SCALE','-s', metavar='s',nargs='?',
    default=1.00,type=float,help='SCALING FACTOR TO BE
    APPLIED TO DATA IN Z DIRECTION TO MATCH X/Y.')
263 scaling.add_argument('--SIZE','-z', metavar='z',nargs='?',
    type=float,help='SIZE OF THE BROADER EDGE OF THE AFM
    SCAN IN M TO CALCULATE SCALE.')
264 parser.add_argument('--RECENTER','-r',action='STORE_TRUE',
    help='ADJUST ORIGIN TO MATCH THE CENTER OF THE CREATED
    MESH VERTICES.')
265 parser.add_argument('--OUTPUT','-o', metavar='o',nargs='*',
    default=['MESH'], type=str, help='OUTPUT TYPE, SUPPORTS
    ONLY "MESH" SO FAR.')
266 args=parser.parse_args()
267
268 # converter
269 cv = Converter()
270
271 # display help if no filename is given
272 if len(args.filename) == 0:
273     parser.print_help()
274
275 # add output methods
276 for mode in args.output:
277     cv.add_sink(mode)
278
279 # add input files
280 for file in args.filename:
281     cv.add_source(file)
282
283 # read sources
284 cv.read()
285
286 # go over all the data
287 for vd in cv.vdlist:
288     # re-center data
289     if args.recenter:
290         vd.recenter()
291     # compute maximum
292     print "MAXIMUM Z-VALUE: "+str(vd.zmax())+" m"
293     # compute scaling
294     if args.size:
295         xymax=max(vd.xmax(),vd.ymax())
296         scale = xymax/args.size
297     else:
298         scale = args.scale
299     # scale the data (in z direction)
300     print "SCALING DATA WITH FACTOR "+str(scale)+" FOR
        DISPLAY."
301     vd.scale([1,1,scale])

```

```
302
303 # write all files
304 if len(args.filename) > 0:
305     print 'WRITING FILE(S).'
306     cv.write()
```

Appendix B

Index

- acknowledgements, vii–ix
- AFM, *see* atomic force microscopy
- anionic polymerization, 9
- applications
 - of colloidal supercrystals, 259
 - of gold nanoparticles, v, 31, 34, 117, 127, 137, 138
 - of gold–polymer nanohybrids, 34, 226, 246, 257, 258
 - of multisegmented copolymers, 152
 - of nanohybrids, 35, 200
 - of nanomaterials, 3, 27
 - of poly(isopropylacrylamide), 19, 23, 145, 173, 193
 - of polymers, 7
 - of silica nanoparticles, 4, 199, 200
 - of smart polymers, 4
- aqua regia, 86, 116, 119
- atom transfer radical polymerization, 10
- atomic force microscopy
 - creation of 3D meshes, vii, viii, 110–113, 239, 267–274
 - instrumental details, 60–61
 - of gold–polymer nanohybrids, vii, viii, 238–239, 244
 - of silica nanoparticles, 112
 - working principle, 110
- ATRP, *see* atom transfer radical polymerization
- AuNPs, *see* gold nanoparticles
- azidothiol, 72, 143–144, 216, 221–223

- Beer plot, 128, 129
- Beer–Lambert law, 128
- binning, 109, 124, 125, 134, 236

- binodal curve, *see* coexistence curve
- block copolymers, v, 9, 12, 13, 23, 36–38
- bottom-up approach, 28, 116
- Brunauer-Emmett-Teller method, 109
- calibration, 238, 243, 246, 248
 - for optical attenuation of gold nanoparticles, 135
 - of size-exclusion chromatography, 18, 56, 151, 153, 240
 - of TEM diffraction mode, 98
- calorimetry, 24
- catalysis, 3, 10, 34, 257, 258
 - phase-transfer catalyst, 14, 130, 131, 133
- cationic polymerization, 9
- centrifugation, 76, 88–90
 - instrumental details, 55
 - of gold nanoparticles, 121, 128, 131, 133, 136, 137, 216, 223
 - of gold–polymer nanohybrids, 228–231, 239
 - of polymer, 146, 150
 - of silica nanoparticles, 207, 209
 - of silica–polymer nanohybrids, 211
- chain-growth polymerization, 7, 15
- chain-length distribution function, 15
- Cheerios effect, 103
- chemisorption, 5, 36, 226
- Clausius–Clapeyron equation, 177
- click chemistry, 142
- cloud points, 22–24, 263
 - accessible range, 176–179
 - addition of alcohols, 181, 187–192
 - addition of salts, 172, 185–187, 256
 - definition, 22
 - determination at atmospheric pressure, 57, 179–181
 - determination at high pressures, 57–60
 - effect of ethanol concentration, 189–192, 194
 - effect of polymer concentration, 181–183
 - effect of polymer's molar mass, 173, 183–185
 - experimental set-up, 175–176, 179, 256
 - of star polymer, 257, 258
 - photographs, 177

- state of the art, 171–175
- cloud-point curves of aqueous pNIPAm solutions, *see* cloud points
- coexistence curve, 19
- colloidal supercrystals, 220, 259, 264
- column chromatography, 17, 55, 144
- computed tomography, 34
- cononsolvency
 - other polymers, 26–27
 - poly(isopropylacrylamide), 24–26, 175, 181, 187–194, 256, 263
 - possible explanations, 25–26
- controlled radical polymerization, *see* reversible-deactivated radical polymerization
- conventional radical polymerization, 7–9, 11, 172
 - elementary reactions, 8
 - kinetic coefficients, 8
- coordinative polymerization, 9
- correlation infrared spectroscopy, 174
- cosolvency, 23
- crystal structure, 30, 31, 130, 218
- Damascus steel, 27
- deep-sea science, 193
- dispersity
 - calculation, 16
 - definition, 16
 - of conventional polymers, 56, 77–81, 147, 151, 185, 204, 212, 235
 - of gold nanoparticles, 124, 125
 - of gold–polymer nanohybrids, 240, 243, 244
 - of multiblock polymers, 82–85, 147, 153–157, 243
 - of the Poisson distribution, 16
- disulfide, 14, 130, 131, 144, 157, 158, 224
- dithiobenzoates, 139
- dithiocarbamates, 11, 218
- dithioesters, 10, 217, 218
- DNA, 7, 22, 95
- drop-casting, 61, 96, 102, 121, 126, 134, 220, 227, 231, 232
- EDX, *see* energy-dispersive X-ray spectra
- electrophoresis, 137
- elemental analysis, 210

- experimental details, 60
 - of gold nanoparticles, 132
 - of RAFT agents, 143
- energy-dispersive X-ray spectra, 61, 98, 99
- entropy of mixing, 20
- environmentally sensitive polymers, *see* smart properties
- face-centered cubic lattice, 97, 98, 126
- Fourier transform infrared spectroscopy, 173, 174
- free enthalpy of mixing, 20
- free radical polymerization, *see* conventional radical polymerization
- Fresnel fringe, 105
- fumed silica, 68, 200, 203–205, 209
 - scanning electron microscopy, 201
- Gaussian distribution, *see* normal distribution
- gel-permeation chromatography, *see* size-exclusion chromatography
- general remarks on this work, ix
- glovebox, 63
- gold ions, 116, 117, 130, 135, 136
- gold nanoparticles
 - alteration in the TEM, 101
 - amine functionalization, 121–127, 223–225
 - applications, v, 31, 34, 117, 127, 137, 138
 - dark-field TEM images, 101
 - depletion stabilization, 116
 - diffraction pattern, 98
 - dispersity, 124, 125
 - electrostatic stabilization, 115, 121, 222, 233
 - energy-dispersive X-ray spectra, 99
 - functionalization protocol, 87–90
 - general synthesis strategies, 116–117
 - gold nanoclusters, 28–33, 86–87, 127, 130–132, 137, 138, 230
 - green synthesis, 116–117
 - NMR spectroscopy, 131, 218
 - optical photospectroscopy, 130, 134
 - optical properties, *see* localized plasmon resonance effect
 - optical spectrum, 32, 127–130
 - overview of used ligands, 221, 222

- photographs, 32, 33, 118, 131, 219
- properties, 28–31
- staining, 28–30
- steric stabilization, 116
- synthesis protocols, 86–89
- thiol functionalization, 222
- transmission electron microscopy, 121, 123–125, 133, 134, 136, 217, 218, 220, 225
- trithiocarbonate functionalization, 217
- types of stabilization, 115–116
- via one-phase Brust–Schiffrin, 118, 127, 131–132
- via reduction with an amine, 118, 127, 134–136
- via reduction with citrate, 117–130, 136–138, 220–246, 259
- via seed-growth synthesis, 119
- via two-phase Brust–Schiffrin, 118, 121, 123, 124, 127, 129–138, 215–220, 259, 264
- with multifunctional trithiocarbonates, 218–220
- gold nanorods, 29, 33, 110, 116
- gold nanospheres, *see* gold nanoparticles
- gold nanowires, 119
- gold–polymer nanohybrids, 56, 263
 - applications, 34, 226, 246, 257, 258
 - atomic force microscopy, 238–239, 244
 - conventional, 230–241, 248, 249, 255–258
 - multiblock, 241–249, 256–258, 264
 - optical photospectroscopy, 230, 242, 258
 - photographs, 227, 255
 - size-exclusion chromatography, 239–241, 244–246, 249, 264
 - stability, 229, 231, 242, 258, 264
 - superparticles, 220, 259
 - synthesis protocols, 89–90
 - transmission electron microscopy, 227–229, 231–238, 242–244, 246, 264
 - without sulfur-containing groups, 226–229
- gold–thiolate bond, 30, 31, 117, 121, 130, 222–223, 225–226, 230
- GPC, *see* size-exclusion chromatography
- grafting density, 35–37, 209–211, 218, 224, 225, 230, 231, 236, 237, 263
- grafting-from approach, 5, 34–37, 199, 264
 - RAFT R-approach, 34, 36–38, 141, 203, 206, 210, 259
 - RAFT Z-approach, 5, 34, 36–38, 138–141, 199, 200, 202–203, 206, 210–212, 263
- grafting-through approach, 34, 35
- grafting-to approach, 34–36, 38, 115, 230, 237, 264

- gravimetry, 69, 148, 150, 151, 202, 211
gray goo, 27
group-transfer polymerization, 9
- hexagonal close-packed lattice, 126
high-pressure cell, 57, 59, 173, 175
 technical sketch, 58, 176
high-pressure cloud points of aqueous pNIPAm solutions, *see* cloud points
Hofmeister series, 23
hydrogen bonds, 21, 25, 110, 116, 174, 187, 229
- immunogold staining, 34
inhibitor, 8, 67
iniferters, 9
initiator, 8, 10–12, 35, 36, 67, 76–85, 145, 146, 158, 202, 203, 206, 210, 211
intelligent polymers, *see* smart properties
interdigitation, 237
interparticle spacing, 124, 219, 225, 229, 233–235, 237, 239, 243, 244, 248
 histogram, 235, 236
islanding, *see* self-assembly of nanoparticles
- laser-ablation, 116
LCST, *see* lower critical solution temperature
lithographic etching, 28
living polymerization, v, 9
living radical polymerization, *see* reversible-deactivated radical polymerization
localized plasmon resonance effect, vi, 3, 29, 31–34, 96, 98, 127, 128, 130, 134, 136–138, 219, 239, 245, 256
 schematic illustration, 32
lower critical solution temperature, vi, 19–22, 24, 27, 191
Lycurus cup, 29, 30
- MADIX polymerization, 10
magic numbers, 29, 30, 137
Mark–Houwink parameters, 18, 56, 151
mass spectrometry, 60, 137, 140, 141
methoxysilyl groups, 199
 monomethoxysilyl group, 65, 66, 140, 141, 208–212
 trimethoxysilyl group, 36, 65, 67, 138–140, 200–202, 208, 209

- microchips, 28
- microemulsion, 223
- microscopy
 - atomic force microscopy, *see* atomic force microscopy
 - light microscopy, 95
 - resolution, 95
 - scanning electron microscopy, *see* scanning electron microscopy
 - transmission electron microscopy, *see* transmission electron microscopy
- molar volume isotope effect, 173
- molar-mass distribution, 9, 11, 12, 14–15, 17, 18, 156
 - characterization, 15–17
 - of multiblock polymers, 153–157
- molecular-weight distribution, *see* molar-mass distribution
- motivation, *see* scientific goals of this work
- multiblock copolymers, *see* multisegmented copolymers
- multiblock polymers, 5, 146, 152, 230, 259, 264
 - block distribution, 153–157
 - cleavage, 76–81, 147, 153, 157–159, 228, 230
 - dispersity, 82–85, 147, 153–157
 - ideal dispersity, 156
 - NMR spectroscopy, 259
 - on gold nanoparticles, 241–249
 - overview of samples, 147
 - size-exclusion chromatography, 147, 153, 157–159, 243
 - synthesis, 151–153
 - synthesis protocols, 75–76, 82–85
- multisegmented copolymers, 152
 - applications, 152
- nanohybrids, v, 3, 5
 - applications, 35, 200
 - of gold and polymers, *see* gold–polymer nanohybrids
 - of silica and polymers, *see* gold–silica nanohybrids
 - special properties, 4
- nanomaterials, v, 27
 - applications, 3, 27
 - toxicity, 27
- nitroxide mediated radical polymerization, 10
- NMR spectroscopy, 66, 144, 150

- instrumental details, 62
- of conventional polymers, 149, 172
- of gold, 131
- of gold nanoparticles, 131, 218
- of multiblock polymers, 259
- of multifunctional RAFT agents, 153
- of RAFT agents, 140, 141, 143
- normal distribution, 109, 124, 134
- nuclear magnetic resonance, *see* NMR spectroscopy
- nucleophilic substitution, 14, 139, 141, 144
- optical photospectroscopy, 57
 - for cloud-point determination, 179–181
 - instrumental details, 62
 - of gold nanoparticles, 32, 96, 127–130, 134
 - of gold–polymer nanohybrids, 230, 242, 258
- organotellurium-mediated radical polymerization, 10
- orientation entropy, 20
- osmosis, 15
- parameters for nanoparticle characterization, 103–110, 123
- particle-size histogram, 124, 134, 216
- PDI, *see* dispersity
- pH value, 22, 35, 120, 121, 132, 173
 - determination, 60
- phase diagram
 - of a typical polymer solution, 19, 22
- physisorption, 4, 35, 206
- plasmon coupling, 34, 229, 255, 264
- plasmon resonance, *see* localized plasmon resonance effect
- pNIPAm, *see* poly(isopropylacrylamide)
- Poisson distribution, 15–17
- poly(isopropylacrylamide)
 - applications, 19, 23, 145, 173, 193
 - cloud points of aqueous solutions, *see* cloud points
 - coil-to-globule transition, 21–23, 26, 27, 255
 - cononsolvency, *see* cononsolvency
 - contour length, 236
 - general, v, 4, 18–19

- hydrogels, 23–25, 172, 173, 193
- microgels, 174
- monomer, 144
- NMR spectroscopy, 149
- on gold nanoparticles, 226–246
- overview of samples, 147
- size-exclusion chromatography, 150–151
- synthesis, 144–153
- temporal development of publications, 18
- polycondensation, 157
- polydispersity index, *see* dispersity
- polygon mesh, 111–113
- polymer brushes, v, 4, 35, 37, 203, 230, 233, 236, 237
 - synthesis strategies, 34–36
- polymer loops, v, 6, 37, 38, 139, 140, 200, 202–207, 241, 242, 244, 246, 258, 264
- pressure-induced clouding, 173, 186, 187, 192, 263
- proteins, 4, 7, 22, 23, 174, 182, 193
 - protein adhesion, 4, 34, 35
- pyrogenic silica, *see* fumed silica
- quantum dots, 32
- quasi-elastic light scattering, 256
- quasi-elastic neutron scattering, 174
- radical polymerization, *see* conventional radical polymerization
- RAFT agent, v, 10–12, 67–68
 - R group, 10–13, 34, 36, 37, 139–142, 203
 - Z group, 5, 10–13, 34, 36, 37, 139, 141, 199, 203, 231
 - clickable, 142–143
 - doubly anchored, 138–140, 200–203, 260
 - elemental analysis, 143
 - monofunctional anchor, 140–142, 208–210
 - multifunctional, 56, 152, 154, 156, 218–220
 - NMR spectroscopy, 141, 143
 - sacrificial, 34, 36, 202, 210, 212
 - structural formulas, 145
 - synthesis protocols, 69–72
- RAFT polymerization
 - agent, *see* RAFT agent

- conditions, 11
 - elementary reactions, 11–12
 - expected molar masses, 13
 - from surfaces, 36–38, 199
 - general, v, 4, 10–13
 - main equilibrium, 11–13, 154
 - net reaction, 13
 - of poly(isopropylacrylamide), 144–153
 - pre-equilibrium, 11, 12
 - unique features, 5
 - with multifunctional agents, 154
- refractive index, 33
- reversible chain transfer, 4, 10
- reversible termination, 10
- reversible-deactivated radical polymerization, v, 4, 9–10, 24, 35
- ring-opening polymerization, 9
- scanning electron microscopy, 96
 - instrumental details, 62
 - of fumed silica, 201
 - of silica–polymer nanohybrids, 205, 206
- Schultz–Flory distribution, 154, 156, 157
- scientific goals of this work, 5–6, 263
- SEC, *see* size-exclusion chromatography
- self-assembly of nanoparticles, 102–103, 121, 123, 125, 126, 134, 225, 229, 232–235, 242, 247
- self-organization, *see* self-assembly of nanoparticles
- SEM, *see* scanning electron microscopy
- semi-automatic particle analysis, 104, 124, 133
- sensors, vi, xxii, 4, 6, 34, 193, 255, 257, 260
- silanol number, 108
- silica nanoparticles, 36, 69, 199, 207–209
 - alteration in the TEM, 100–102
 - applications, 4, 199, 200
 - atomic force microscopy, 112
 - characteristic parameters, 110
 - functionalization, 208
 - functionalization protocol, 88, 90
 - particle-size histogram, 104

- transmission electron microscopy, 207, 210
- silica–polymer nanohybrids, 199, 202–207, 210–212, 263
 - scanning electron microscopy, 205, 206
 - size-exclusion chromatography, 204
 - synthesis protocols, 90
 - thermogravimetric analysis, 202, 204, 206, 211
 - transmission electron microscopy, 208, 212
- size-exclusion chromatography, 90
 - calibration, 17, 18, 56, 151, 153, 240
 - general principle, 17–18
 - instrumental details, 55–56
 - of conventional polymers, 147, 150–151, 202, 211, 230, 235
 - of gold–polymer nanohybrids, 239–241, 244–246, 249, 264
 - of multiblock polymers, 147, 153, 156–159, 243
 - of multifunctional RAFT agents, 152
 - of silica–polymer nanohybrids, 204
- small-angle neutron scattering, 173
- smart polymers, *see* smart properties
- smart properties, 18, 22, 171, 199, 255, 264
- solubility of polymers, 19–21
- Soxhlet extraction, 90, 203, 207, 209
- spin-coating, 60, 112, 238, 239
- spinodal curve, 19, 22
- sputter coating, 62
- Stöber process, 207
- standard deviation, 109
- star polymers, v, 9, 68, 146, 257–259
- static light scattering, 16
- step-growth polymerization, 7
- stimuli-responsive polymers, *see* smart properties
- substance identifiers, xix
- supercrystals, *see* colloidal supercrystals
- superlattices, *see* self-assembly of nanoparticles
- TEM, *see* transmission electron microscopy
- temperature-induced clouding, 172, 173, 186, 187, 192, 263
- TERP, *see* organotellurium-mediated radical polymerization
- TGA, *see* thermogravimetric analysis
- thermogravimetric analysis, 62, 202, 204, 206, 211

- thin-layer chromatography, 56
- TLC, *see* thin-layer chromatography
- top-down approach, 28, 116
- transmission electron microscopy
 - alteration of samples, 100–102
 - analysis of AuNPs, 96, 98
 - diffraction pattern of AuNPs, 98
 - drying artifacts, 119
 - gold nanoparticles, 123
 - imaging modes, 100, 101
 - instrumental details, 61
 - micrographs for particle analysis, 103–105
 - of gold nanoparticles, 86, 121–127, 133, 134, 136, 217, 218, 220, 225
 - of gold–polymer nanohybrids, 227–229, 231–238, 242–244, 246, 264
 - of silica nanoparticles, 207, 210
 - of silica–polymer nanohybrids, 208, 212
 - operation modes, 97
 - resolution, 95
 - sample preparation, 61, 96
 - selective spot problem, 103
 - self-assembled structures, *see* self-assembly of nanoparticles
 - semi-automatic particle analysis, 103–109, 122–125
 - staining, 34
 - working principle, 95–97
- trithiocarbonates, 4–6, 10, 11, 13, 130, 139, 180
 - binding to gold, 132, 216–218, 226, 230, 231, 241, 258, 263
 - cleavage, 76–81, 147, 153, 157–159, 228, 230
 - cyclic, 152
 - distribution in multiblock polymers, 153–157
 - multifunctional, 152
 - synthesis, 13–14
- Tyndall scattering, 219
- UCST, *see* upper critical solution temperature
- ultrasonication, 120, 216, 223, 228, 242
 - instrumental details, 63
- upper critical solution temperature, 19, 20, 25, 27, 174, 189, 191
- UV/vis spectroscopy, *see* optical photospectroscopy

- van-der-Waals forces, 35, 103, 192
- volume phase transition temperature, 23
- water purification, 63, 66, 119, 120
- Wittelsbach cup, 30
- X-ray diffraction, 30, 130
- X-ray photoelectron spectroscopy, 217, 218
- xanthates, 10, 11

About the author

Bastian Ebeling, * October 8, 1982, Utrecht, Netherlands.



Curriculum vitae

2002 *Abitur (final secondary-school examinations)*, Gymnasium Burgdorf, Germany, final grade: “1,6”.

2002–2003 *German mandatory national service (Zivildienst)*, Deutsches Rotes Kreuz (German Red Cross), Kreisverband Burgdorf, Germany.

2003 *Attendant care worker*, Deutsches Rotes Kreuz (German Red Cross), Kreisverband Burgdorf, Germany.

2003–2009 *Chemistry at the Georg–August–Universität Göttingen*, Germany.

2005 *Vordiplom (intermediate examinations)*, Georg–August–Universität Göttingen, final grade: “sehr gut”.

2006–2008 *Teaching assistant*, Institut für Organische und Biomolekulare Chemie, Georg–August–Universität Göttingen.

2007 *Research project*, Dipartimento di Chimica Organica “Ugo Schiff”, Università degli Studi di Firenze (Florence), Italy. “Sintesi stereoselettiva di derivati dell’acido 1,2,7-triidrossioctaidroindolizin-8-carbossilico” (“Stereoselective Synthesis of Derivatives of 1,2,7-Trihydroxyoctahydroindolizine-8-carboxylic Acid”) (6 months) in the group of Prof. Dr. Alberto Brandi, granted by the EU within the ERASMUS programme.

2009–2014 *Teaching assistant*, Institut für Physikalische Chemie, Georg–August–Universität Göttingen.

2009 *Diplom (final degree)*, Georg–August–Universität Göttingen, final grade: “sehr gut”, diploma thesis: “Multiblock-Copolymere durch RAFT-Polymerisation” (“Multiblock Copolymers via RAFT Polymerization”) in the group of Prof. Dr. Philipp Vana.

2010–2014 *Promotion (PhD student)*, Georg–August–Universität Göttingen, final grade: “summa cum laude”, supervisor: Prof. Dr. Philipp Vana, awarded the Richard-Zsigmondy Prize for the best chemistry thesis in 2014.

since 2014 *Post-doctoral researcher*, École Supérieure de Chimie Physique Électronique de Lyon, Laboratoire C2P2, Équipe LCPP, Villeurbanne, France. “Multi-stimuli responsive assemblies in water”.

Publications

Parts of the work presented here has already been published in the following publications:

- “Ideal Molecular Weight Distributions of Multiblock Copolymers Prepared via RAFT Polymerization”
B. Ebeling, M. Eggers, P. Vana, *Macromolecules* **2010**, 43(24), 10283–10290.
- “Multiblock Copolymers of Styrene and Butyl Acrylate via Polytrithiocarbonate-Mediated RAFT Polymerization”
B. Ebeling, P. Vana, *Polymers* **2011**, 3(2), 719–739.
- “RAFT-Polymers with Single and Multiple Trithiocarbonate Groups as Uniform Gold-Nanoparticle Coatings”
B. Ebeling, P. Vana, *Macromolecules* **2013**, 46(12), 4862–4871.
- “Spherical Gold-Nanoparticle Assemblies with Tunable Interparticle Distances Mediated by Multifunctional RAFT Polymers”
C. Rossner, B. Ebeling, P. Vana, *ACS Macro Letters* **2013**, 2, 1073–1076.
- “Oberflächen nach Maß”
B. Ebeling, F. Ehlers, P. Vana, *Nachrichten aus der Chemie* **2014**, 62, 24–28.
- “Flipping the Pressure- and Temperature-Dependent Cloud-Point Behavior in the Cononsolvency System of Poly-(*N*-isopropylacrylamide) in Water and Ethanol”
B. Ebeling, S. Eggers, M. Hendrich, A. Nitschke, P. Vana, *Macromolecules* **2014**, 47(4), 1462–1469.
- “Comparison of Monomethoxy-, Dimethoxy-, and Trimethoxysilane Anchor Groups for Surface-Initiated RAFT Polymerization from Silica Surfaces”
D. Hübner, V. Koch, B. Ebeling, J. Mechau, J. E. Steinhoff, P. Vana, *Journal of Polymer Science, Part A: Polymer Chemistry* **2014**, 53(1), 103–113.

- “Design Strategies for the Fabrication of Tailored Nanocomposites via RAFT Polymerization”
C. Rossner, B. Ebeling, P. Vana, *ACS Symposium Series* **2015**, in press.

Contributions to conferences and workshops

The author has presented some of the results from this thesis at the following conferences or workshops:

- “Molecular Weight Distribution of Multiblock Polymers Prepared via RAFT Polymerization”
Poster, Bunsen-Kolloquium “Kinetics of Radical Polymerization: The Foundation of Novel Materials and Processes”, Göttingen, **April 2010**.
- “Molecular Weight Distribution of Multiblock Polymers Prepared via RAFT Polymerization”
Poster, 43rd IUPAC World Polymer Congress, “Macro2010”, Glasgow, UK, **July 2010**.
- “Multiblock Copolymers via RAFT Polymerization”
Talk, 16th Workshop Physical & Chemical Graduate School (DFG GRK 782), Hesse, **September 2010**.
- “Tailored Polymer Films on Surfaces via RAFT Polymerization”
Poster, Workshop “Funktionalisierung von Oberflächen”, Measurement Valley, Göttingen, **February 2011**.
- “Functionalized gold nanoparticles for surface-confined RAFT polymerizations”
Poster, 17th Workshop Physical & Chemical Graduate School (DFG GRK 782), Göttingen, **March 2011**.
- “Bio-inspired materials with H-bonded nanodomains via living polymerization techniques”
Poster, XIX. International Conference on “Horizons in Hydrogen Bond Research”, Göttingen, **September 2011**.
- “Microscopic Analysis of RAFT-Polymer Coated Gold Nanoparticles”
Poster, Göttingen ETEM Workshop on Heterogeneous Catalysis, Surface Science and Energy Research, Göttingen, **July 2012**.

- “Tailored Polymer Films on Surfaces via RAFT Polymerization”
Poster, Sartorius-College Forschungsforum “Verbindungen (wieder)entdecken und stärken”, Göttingen, **October 2012**.
- “RAFT-Polymers with Single and Multiple Trithiocarbonate Groups as Uniform Gold-Nanoparticle Coatings”
Poster, Göttinger Chemie-Forum 2013, Göttingen, **June 2013**.
- “Polymers with single or multiple trithiocarbonate groups as capping agents for gold nanocrystals”
Poster, European Polymer Congress, “EPF 2013”, Pisa, Italy, **June 2013**.

